

Meinen Eltern Dieter und Christine

Danksagung

Mein erster Dank gilt beiden meiner Doktoreltern

Dr. habil. Nathalie Kunkel und **Prof. Dr. Thomas Fässler**.

Dr. habil. Nathalie Kunkel danke ich für die Möglichkeit, diese Arbeit anfertigen zu können, für die interessante Themenstellung, für ihre Hilfsbereitschaft und für die stets angenehme Zusammenarbeit über den gesamten Zeitraum

und

Prof. Dr. Thomas Fässler danke ich für die unkomplizierte und kompromisslose Aufnahme in seinen Arbeitskreis, die angenehme Zusammenarbeit und die fachliche aber auch persönliche Betreuung.

Mein Dank gilt zudem allen, die mich während den letzten drei Jahren unterstützt haben und ohne deren Hilfe diese Arbeit nicht möglich gewesen wäre. Daher danke ich besonders:

Meinem Doktorgroßvater **Prof. Dr. Holger Kohlmann** für die fachliche Betreuung, die vielen netten und hilfreichen Gespräche und auch für die sehr angenehme Zusammenarbeit mit ihm und seinem Arbeitskreis.

Prof. Dr. Antti Karttunen für die tolle Zusammenarbeit, die vielen Hilfestellungen bei quantenchemischen Rechnungen und die freundliche Aufnahme in Helsinki.

Prof. Dr. Tom Nilges für die Kristallographiekurse, die entspannten Gespräche und seine stets aufmunternde Unterstützung.

Manuela Donaubauer für die unermüdliche Hilfe bei allen organisatorischen Angelegenheiten und ihre unglaubliche Zuverlässigkeit.

Meinem Kollegen **Dr. Thomas Wylezich** für etliche Hilfestellungen, die vielen Messungen und die angenehme Zusammenarbeit seit der Masterarbeit.

Meinem Masteranden **Samuel Merk**, meinen Praktikanten **Johanna Haimerl**, **Lukas Bichlmaier**, **Leonidas Brunk** und meiner Hilfswissenschaftlerin **Annika Schulz** für die engagierte und motivierte Mitarbeit und Hilfe bei meinen Forschungsprojekten.

Meinen Bürokollegen **Vincent Daiber** und **Manuel Botta** für die vielen unterhaltsamen Gespräche und die tolle, stets lustige Arbeitsatmosphäre.

Dem gesamten **Arbeitskreis Fässler** danke ich für die angenehme Arbeitsatmosphäre und die unterhaltsamen Unternehmungen.

Prof. Dr. Andries Meijerink für die nette Aufnahme an der Universität Utrecht und die Bereitstellung seines Equipments. **Dr. Atul Sontakke** für die Unterstützung der Lumineszenzmessungen und Diskussion derer Ergebnisse in Utrecht und darüber hinaus.

Dr. Gregor Kieslich für die wissenschaftliche Unterstützung, viele weitere Hilfestellungen und bereichernde Diskussionen. Seiner Mitarbeiterin **Silva Kronawitter** danke ich für temperaturabhängige XRD Messungen.

Dr. Gabriele Raudaschl-Sieber für die NMR Messungen und die vielen unterhaltsamen Gespräche beim Rotorpacken.

PD. Dr. Marko Bertmer, Dr. Guy Bernard und **Prof. Dr. Vladimir Michaelis** für die unkomplizierten NMR Messungen und die Diskussion derer Ergebnisse.

Sophia Wandelt und der **Arbeitsgruppe Schnick** für die spannende Zusammenarbeit und die Adoption in ihren Arbeitskreis am HäKo in Bayreuth.

Dem **ATUMS** Projekt danke ich für die finanzielle Unterstützung dieser Promotion.

Auch möchte ich mich bei allen meinen **Freunden** bedanken, die mich teilweise bereits seit der Grundschule oder sogar schon eher begleiten. Die vielen Freizeitunternehmungen waren immer ein toller Ausgleich zu der Arbeit. Ohne euch wäre diese Zeit nicht annähernd so toll und bereichernd gewesen.

Ein besonderer und letzter Dank gilt meiner **Familie**, insbesondere meinen **Eltern**. Ohne euch wäre das alles nicht möglich gewesen. Ihr habt immer alles Erdenkliche gemacht und mir immer den Rücken freigehalten. Das, obwohl ihr selbst immer mehr als genug Anderes zu erledigen hattet. Auf euch konnte ich mich immer verlassen. **Danke!**

Abstract

Tailoring of the anion chemistry has become an important part for the design of new functional materials. By the incorporation of different anions within a single chemical compound, the different inherent characteristics of the involved species can be combined and utilized. In this way, materials properties can be selectively tuned and new materials are accessible. In particular, this heteroanionic approach led to the emergence of the promising compound class of the heteroanionic hydrides with many remarkable functionalities attributed to themselves. Fast ionic conduction or remarkable optical properties are just few examples of those. Despite recent advances made in this particular research field, numerous heteroanionic hydrides remain unexplored and many further important insights and materials properties are to be gained and discovered.

In this regard, the full hydride fluoride solid solutions series **RbCaH_xF_{3-x}** and **CsCaH_xF_{3-x}** were synthesized and investigated regarding their structures and optical properties. The structures were elucidated by X-ray and neutron diffraction. Both solid-solutions series follow Vegard's law and the cubic perovskite structure with disordered anions is formed by all compounds throughout the whole series. The europium doped solid-solution series **CsCaH_xF_{3-x}:Eu²⁺** shows remarkable luminescent behaviour. Bright and tunable luminescence glow can be observed upon UV light excitation. Differently to previous investigated luminescent hydride fluorides, a new type of redshift was detected herein. With increasing hydride content, new, narrow emission bands emerge at the lower energy region, causing the perceivable redshift. The findings are highly advantageous for the design of new red emitting narrow band phosphors. However, many anion combinations are unrealized to date and further, likely desirable properties remain hidden. In this work, attempts were made to establish further unprecedented anion combinations. Herein, by a sophisticated thermal synthesis under controlled conditions, **Na₃SO₄H** could be obtained. To the best of our knowledge, the first compound to contain sulfate anions next to hydride ions. The structure was solved from X-ray powder diffraction and corroborated by neutron diffraction of the deuterated analogue. **Na₃SO₄H** was determined to crystallize in a tetragonal antiperovskite-like structure. Several independent methods, including vibrational spectroscopy, MAS NMR, elemental analysis in combination with quantum chemical calculations unambiguously prove the abundance of hydride ions. With the insights obtained from the sulfate hydride, another unprecedented anion combination could be accomplished within this work. Herein the four compounds **A₃MO₄H** (*A* = Rb, Cs; *M* = Mo, W) are introduced as the first solid-state structures to contain both complex transition oxometalate and hydride anions. The compounds were synthesized by a similar sophisticated thermal approach expedient for the sulfate hydride. The structures of the newly formed phases were solved ab-initio from X-ray powder diffraction. With neutron diffraction of the deuterium analogues, the structural models were completed. All compounds show antiperovskite-like architectures. Particularly the structure of **Rb₃WO₄H** is to be highlighted. This compound shows a new perovskite-like variant that has not been observed before. Furthermore, **Rb₃WO₄H** undergoes a phase transition near room temperature, adding further structural peculiarities.

With Raman and ^2H MAS NMR spectroscopy the hydridic character of the four new samples was proven. Quantum chemical calculations additionally support the experimental findings. All samples reveal interesting electronic properties. Direct transitions between the hydride and metalate states are predicted for all phases. From the insights obtained by these compounds semiconductors may be improved.

Lastly, investigations on the lighter alkaline homologues yielded a further compound with the assumed stoichiometry $\text{K}_3\text{MoO}_4\text{H}$, proving the sophisticated synthesis method suitable for further materials alike.

This thesis concerns the general syntheses strategies and properties of yet unknown heteroanionic hydrides. A special emphasis is placed on luminescent properties and the exploration of new anionic combinations. Hereby, the understanding of structure property relations of heteroanionic hydrides is enhanced. Eventually, synthesis routes to new classes of heteroanionic hydrides are provided and analytical methods for the improved detection thereof are exemplarily shown which will be of importance for future works.

Kurzzusammenfassung

Das Anpassen der Anionenchemie ist ein wichtiger Bestandteil für die Entwicklung neuer, funktioneller Materialien geworden. Durch die Kombination ungleicher Anionen innerhalb einer chemischen Verbindung, können die unterschiedlichen Eigenschaften dieser genutzt und verbunden werden. Materialeigenschaften lassen sich so gezielt verändern und neue Materialien sind so zugänglich. Aus diesem heteroanionischen Ansatz entwickelte sich im Speziellen die vielversprechende Materialklasse der heteroanionischen Hydride. Eigens mit bedeutenden Funktionalitäten. Schnelle Ionenleitfähigkeiten oder bemerkenswerte optische Eigenschaften sind nur wenige Beispiele dieser Funktionalitäten. Trotz jüngster Fortschritte in diesem Forschungsgebiet sind noch zahlreiche heteroanionische Hydride unerforscht und unentdeckt. Viele weitere Erkenntnisse sowie bedeutende Materialeigenschaften dieser können noch gewonnen und entdeckt werden.

So wurden im Rahmen dieser Arbeit die vollständigen Mischreihen der Hydridfluoride **RbCaH_xF_{3-x}** und **CsCaH_xF_{3-x}** dargestellt und hinsichtlich ihrer Strukturen und optischer Eigenschaften untersucht. Die Strukturen wurden anhand Röntgen- und Neutronenbeugung aufgeklärt. Beide Mischreihen folgen der Vegard'schen Regel und Verbindungen kristallisieren im gesamten Phasenbereich in der kubischen Perowskitstruktur mit ungeordneten Anionen. Die europiumdotierte Mischreihe CsCaH_xF_{3-x}:Eu²⁺ weist bemerkenswerte Lumineszenz auf. Intensives und einstellbares Lumineszenzleuchten ist durch Anregung mit UV-Licht erkennbar. Anders als in zuvor untersuchten lumineszierenden Hydridfluoriden, ist hier eine neue Art der Rotverschiebung entdeckt worden. Mit steigendem Hydridgehalt innerhalb der Mischreihe, erscheinen neue, schmalbandige Emissionsbanden im niedrigerenergetischen Bereich, welche für die visuell erkennbare Rotverschiebung verantwortlich sind. Diese Erkenntnisse sind besonders vorteilhaft, um neue schmalbandige und rotemittierende Leuchtstoffe zu konzipieren.

Viele weitere Anionenkombinationen sind bis dato jedoch noch unverwirklicht und weitere, möglicherweise wünschenswerte Eigenschaften bleiben verborgen. So wurde in dieser Arbeit das Erschließen neuer Anionenkombinationen angestrebt. Hierbei konnte **Na₃SO₄H**, unseres Wissens nach, die erste Verbindung, welche sowohl Sulfat-, als auch Hydridionen beinhaltet, mittels einer ausgefeilten thermischen Route unter kontrollierten Bedingungen erhalten werden. Die Struktur wurde anhand Röntgenpulverdiffraktometrie gelöst und durch Neutronendiffraktometrie des Deuteriumanalogon Na₃SO₄D vervollständigt. Weitere unabhängige Methoden, wie Vibrationsspektroskopie, Festkörper NMR, Elementaranalyse und quantenchemische Rechnungen beweisen eindeutig die Präsenz von Hydridionen. Mit den Erkenntnissen, welche durch das Sulfathydrid gewonnen wurden, konnte im Rahmen dieser Arbeit eine weitere, unseres Wissens nach, zuvor unerreichte Anionenkombination erschlossen werden. Hier werden die vier Verbindungen **A₃MO₄H** (*A* = Rb, Cs, *M* = Mo, W) als erste Festkörperstrukturen vorgestellt, welche sowohl komplexe Übergangsoxometallat- als auch Hydridanionen beinhalten. Die Verbindungen konnten wiederum durch eine ausgefeilte thermische Route, welche sich zuvor bei dem Sulfathydrid als zielführend erwies, dargestellt werden. Die Strukturen der neu gebildeten Phasen wurden ab initio durch

Röntgenpulverdiffraktometrie gelöst. Neutronenbeugung der Deuteriumanalogen vervollständigten die Strukturmodelle. Alle Verbindungen zeigen antiperowskitähnliche Architekturen. Besonders $\text{Rb}_3\text{WO}_4\text{H}$ ist hier hervorzuheben. Diese Verbindung zeigt ein neues perowskitähnliches Strukturmotiv, welches in dieser Form noch nicht beobachtet wurde. Darüber hinaus zeigt $\text{Rb}_3\text{WO}_4\text{H}$ eine Phasenumwandlung nahe Raumtemperatur und fügt so weitere strukturelle Besonderheiten hinzu. Durch Ramanspektroskopie und ^2H Festkörper NMR konnte der hydridische Charakter der Verbindungen bewiesen werden. Quantenchemische Rechnungen unterstützen die experimentellen Ergebnisse. Alle Proben offenbaren interessante elektronische Eigenschaften. Für alle Phasen werden direkte Übergänge zwischen Hydrid- und Metallatzuständen vorhergesagt. Mittels dieser Erkenntnisse könnten beispielsweise Halbleiter verbessert werden. Zuletzt ergaben Untersuchungen an den leichteren Alkalianalogen eine weitere Phase mit der ungefähren Zusammensetzung $\text{K}_3\text{MoO}_4\text{H}$. Das zeigt auf, dass solch verfeinerte Synthesemethoden für das Finden neuer, ähnlicher heteroanionischer Hydride geeignet sind.

Diese Dissertation behandelt die grundlegenden Synthesestrategien und Eigenschaften bislang unbekannter heteroanionischer Hydride. Ein besonderes Augenmerk wird dabei auf die lumineszenten Eigenschaften sowie das Erkunden neuer Anionenkombinationen gelegt. Damit wird das Verständnis der Struktur-Eigenschaft Beziehung heteroanionischer Hydride verbessert. Es werden schließlich Syntheserouten zu neuen, bislang unbekannt Materialklassen aufgezeigt und analytische Methoden zum besseren Nachweis derer beispielhaft veranschaulicht, welche in Zukunft von Nutzen sein werden.

List of Abbreviations

A.U.	Atomic unit
ATR	attenuated total reflection
CB	conduction band
<i>ccp</i>	cubic close packing
DFT	density functional theory
DFT-PBE	density functional theory – Perdew–Burke–Ernzerhof
DSC	differential scanning calorimetry
FT-IR	Fourier-transform infrared
FWHM	full width at half maximum
<i>hcp</i>	hexagonal close packing
LED	light emitting diode
LT	low temperature
MAS	magic angle spinning
NIR	near-infrared
NMR	nuclear magnetic resonance
OT*	set oven temperature
p-XRD	powder X-ray diffraction
PL	photoluminescence
PLE	photoluminescence excitation
RT	room temperature
S.o.f.	site occupation factor
USPP	ultra-soft pseudopotential

UV	ultraviolet
VB	valence band
VIS	visible

Note

This dissertation is based on selected articles published in peer reviewed journals. The associated work was carried out between July 2019 and June 2022. The relevant publications are embedded in chapter 7. The content and outline of the respective publications are shortly summarized in advance. Contributions of all authors and reproduction permissions of the publications are also explicitly stated herein.

The theoretical background, the motivation and relevance of this work are compiled in chapter 1 as introductory part. Experimental details on the synthesis and analytical methods are given in chapter 2. The most important results of the embedded publications and further topic relevant information are discussed in chapter 3 and 4. The summary and outlook of this thesis are given in chapter 5. A complete list of publications, conference contributions and press releases produced within the scope of this work are listed in chapter 8.

Table of Contents

Abstract.....	I
Kurzzusammenfassung.....	III
List of abbreviations	V
1 Introduction	1
1.1 Metal hydrides	1
1.1.1 The polarizability and ionic radius of the hydride ion	3
1.2 Heteroanionic hydrides.....	4
1.2.1 Elemental heteroanionic hydrides	4
1.2.2 Hydrides in combination with complex anions	7
1.3 The perovskite structure	12
1.3.1 Distorted variants and the Goldschmidt tolerance factor	12
1.3.2 The antiperovskite structure	14
1.3.3 Antiperovskites with complex anions.....	15
1.4 Photoluminescence	16
1.4.1 Eu^{2+} -activated luminescence	17
1.4.2 Eu^{2+} -activated luminescence in metal hydrides.....	20
1.4.3 Energy transfer	22
1.5 Aims	24
2 Experimental details	25
2.1 Chemicals	25
2.2 Solid-state reactions.....	26

2.3	Reactions under hydrogen pressure	27
2.4	Mechanochemical reactions	28
2.5	Powder X-ray diffraction	29
2.6	Powder neutron diffraction	29
2.7	Rietveld refinement	30
2.8	Photoluminescence spectroscopy	30
2.9	Magic-angle spinning NMR spectroscopy	31
2.10	Fourier-transform infrared spectroscopy	31
2.11	Raman spectroscopy	32
2.12	UV-Vis absorption spectroscopy	32
2.13	Elemental analysis	32
2.14	Differential scanning calorimetry	33
2.15	Density functional theory calculations	33
3	New hydride fluorides crystallizing in the ideal perovskite structure	35
3.1	$M\text{CaH}_x\text{F}_{3-x}:\text{Eu}^{2+}$ ($M = \text{Rb}, \text{Cs}$) – a different type of red shift	35
4	New heteroanionic hydrides with complex oxoanions	43
4.1	$\text{Na}_3\text{SO}_4\text{H}$ – the first sulfate hydride	43
4.2	Hydrides in combination with transition oxometalate anions	50
4.2.1	$A_3\text{MO}_4\text{H}$ ($A = \text{Rb}, \text{Cs}; M = \text{Mo}, \text{W}$) as the first transition oxometalate anions ...	50
4.2.2	Low temperature phase transition of $\text{Rb}_3\text{WO}_4\text{H}$	60
4.2.3	$\text{K}_3\text{MoO}_4\text{H}$ as a further transition oxometalate hydride	63
5	Summary and conclusion	67
6	References	71

7	Publications and manuscripts.....	85
7.1	MCaH _x F _{3-x} (M = Rb, Cs): Synthesis, Structure, and Bright, Site-Sensitive Tunable Eu ²⁺ Luminescence.....	85
7.2	Na ₃ SO ₄ H—The First Representative of the Material Class of Sulfate Hydrides...	105
7.3	Expanding the hydride chemistry: antiperovskites A ₃ MO ₄ H (A = Rb, Cs; M = Mo, W) introducing the transition oxometalate hydrides	131
8	List of Publications.....	177
9	List of Figures.....	179
10	List of Tables	185
11	Appendix	187
11.1	Rietveld refinement plots and additional crystallographic data	187
11.2	Statutory declaration.....	200

1 Introduction

1.1 Metal hydrides

With hydrogen being a ubiquitous and highly abundant element,^[1–4] the variety of different chemical compounds containing hydrogen is inordinate. However, combinations of hydrogen with metals are one kind of their own, owed to their dissimilar characteristics and functionalities when compared to the molecular, covalent bonded compounds of hydrogen with nonmetals. Generally, the combination of metals with hydrogen are referred to as *metal hydrides*. An umbrella term that subsumes three fundamental types of metal hydrides, the molecular, the interstitial, and the salt-like metal hydrides.^[5,6] *Molecular or covalently bonded metal hydrides* occur predominantly by the combination of hydrogen with metals or semi metals of the main group such as Si, Ge or Sn or also with late transition metals of the groups 11 and 12. Usually, compounds alike form simple gaseous molecules e.g. GeH_4 or SbH_3 . These are built analogously to their lighter nonmetal homologues, are hazardous, very reactive, and have the tendency to build polymeric units.^[6–8] The metal-hydride bond herein can be described as a typical covalent bond with, depending on the bonding partner, positive or negative partial charges on the hydrogen atoms which in turn directly determines the reactivity. Widely associated with the term metal hydride is the combination of hydrogen with transition or lanthanide metals or alloys thereof. This distinctive type of metal hydrides is however more precisely described by the expression *interstitial hydrides*. Here, hydrogen dissolves into the metal and occupies the interstitial sites of the host lattice. It is then located within tetrahedral or octahedral gaps of the *ccp* or *hcp* arrangement of the metal lattice. Depending on the occupancies of the respective polyhedral gaps, generally non-stoichiometric compositions of MH_x with $0 < x < 3$ are formed. The bonding situation herein is yet to be fully clarified. The dihydrogen molecules fully dissolve into the lattice, break up homolytically and might either donate their electrons to the conduction band or accept electrons of the conduction band in order to be part of the metallic scaffold. Thus, a hydrogen atom following after can have a positive or negative (partial) charge. An alloy-like situation as ‘dissolved’ hydrogen atoms within the lattice is also discussed.^[5–8] These type of metal hydrides are, contrary to the earlier discussed molecular constituted compounds, rather unreactive but also stable against air and moisture. While the crystal structures are mostly uninfluenced by the uptake of hydrogen, the physical properties usually change explicitly. Insulating materials may become conductive and vice versa or even superconductivity might be observed after insertion of hydrogen.^[9,10] Due to the possibility to uptake large amounts of hydrogen, (intermetallic) interstitial hydrides have been widely investigated is hydrogen storage materials.^[5,6,11,12] Schematics of a molecular bonded and a interstitial metal hydride are depicted in **Figure 1.1**.

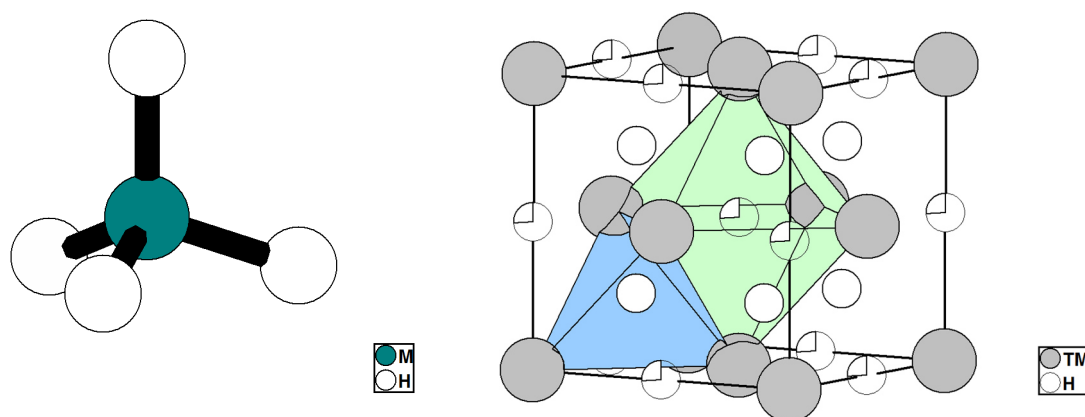


Figure 1.1. A covalently bonded metal hydride MH_4 (left) with M consisting of a main group (semi)metal. In contrast on the right: an interstitial metal hydride. TM is equal to a transition or lanthanide metal. In this exemplification the hydrogen atoms are incorporated in the *ccp* of the transition metal atoms. The tetrahedra sites (blue) are fully occupied and the octahedra sites (lime) are statistically occupied by approx. 25% (partially filled spheres), resulting in a non-stoichiometric hypothetical sum formula of $TMH_{2.25}$.

The metal hydrides of the third, the salt-like type, are equally as distinctive in their chemical and physical behaviour. In combination with highly electropositive elements, hydrogen is able to uptake an electron, fulfilling the duplet rule ($1s^2$) to form the unattached hydride anion H^- . It is then considered as a negatively charged anion with no or only very minor covalent interactions with its bonding partners. Thus, compounds built with this instance are referred to as *salt-like* or *saline hydrides*. Hydride anions are mostly observed in combination with the electropositive alkaline metals, earth alkaline metals except beryllium and some lanthanide metals e.g. europium. Characteristically, these compounds react heavily with moisture to form the hydroxide analogues under release of hydrogen gas. Also typical for salt-like representatives is their low thermal stability, with only very few examples stable enough to reach its melting point before decomposition.^[5–8] Introducing further anions in hydridic materials has shown that resistance against moisture and temperature of such hydrides can be improved. This will be discussed in chapter 1.2.

Salt-like hydrides can also occur in the form of complex (metal) hydrides. This is usually the case when salt-like metal hydrides forming elements are in combination with elements forming a different type of metal hydride. Here, complex, negatively charged hydrido metalate anions are formed where hydrogen is coordinated or covalently bonded to a central cation, either an interstitial- or a molecular-type element. Prominent examples of complex metal hydrides are e.g. K_2ReH_9 with tricapped trigonal prismatic $[ReH_9]^{2-}$ units or $MgNiH_4$ with tetrahedral $[NiH_4]^{2-}$ units. Moreover, nonmetal type complex hydrido anions e.g. the borohydrides BH_4^- , amides NH_2^- or larger molecules belonging to the borane family $B_yH_x^{n-}$ are also ascribed to the complex hydrides.^[5–7,13] Complex hydrides of the latter type find application as hydrogen storage materials and have been recently investigated as ionic conductors.^[14–21] **Figure 1.2** shows typical structures of a salt-like hydride and a complex hydride with molecular hydrido anions.

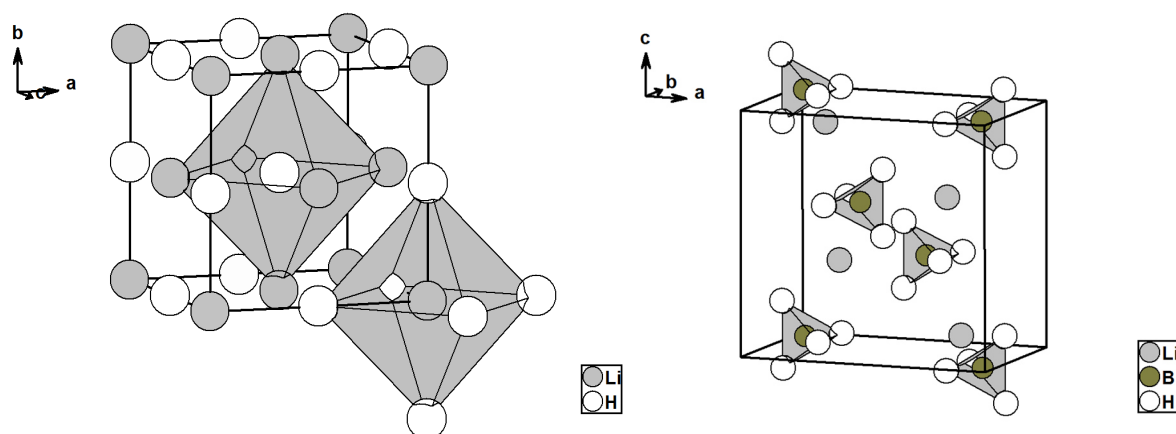


Figure 1.2 Rock salt-type LiH (left) consisting of Li^+ and H^- ions as an example for an ionic, salt-like hydride. A complex hydride LiBH_4 (right) with molecular BH_4^- units next to Li^+ ions as an example of a complex hydride.

Even when only considering combinations of metals with hydrides, the diversity is vast among this composition type. A differentiation into the above introduced categories is not always straightforward as intermediate cases are formed frequently and strict borders between the types are difficult to draw. Anyway, this work only concerns the lastly introduced type of metal hydrides, the salt-like representatives. The hydride ions are considered to be unequivocally present as elemental, anionic species for all cases discussed henceforth.

1.1.1 The polarizability and ionic radius of the hydride ion

The hydride ion fulfils the noble gas configuration and therefore is considered as a stable ionic species. With its moderate electronegativity (2.2 Pauling scale^[22]) and only one single proton to electrostatically bind the surplus electron, the electrons are not strictly bonded to the nucleus. This eventuality results in a ‘soft’ hydride anion with a high polarizability and correlated varying ionic radii, strongly dependent on the chemical environment it is located in.^[23–25] One could assume the hydride is adjusting to its surroundings chameleon-like. Hence, many discussions about the actual ionic radius of the hydride ion emerged. Pauling, among the first, suggested a rather large ionic radius of 208 pm.^[26] Later works more precisely suggest smaller ionic radii in the range of approx. 110 - 150 pm,^[5,7,27–30] with the latter values similar to the ionic radius of the fluoride ion (133 pm in sixfold coordination sphere).^[30] This similarity and the matching charge of both anions result in the phenomenon that many salt-like hydrides crystallize isostructural to their fluoride counterparts, generally denoted as the hydride-fluoride analogy.^[29] This can be paradigmatically observed for instance in binary (earth) alkaline hydrides and fluorides or in ternary alkaline/earth alkaline perovskites.^[31] As the structures of compounds formed by both anions are similar, the physical properties differ largely which can be directly derived from the polarizable nature of the hydride ion. This overall polarizability does not only, as mentioned before, influence the ionic radius but also leads to a special bonding situation. Due to polarization of the hydride and the assumed ionic metal-hydride bond, an ionic bonding situation with covalent contributions is formed (**Figure 1.3**).

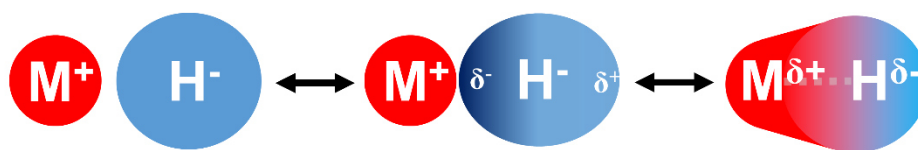


Figure 1.3 Schematic of the bonding situation in salt-like hydrides. Left: pure ionic interaction; middle: the polarized hydride ion with partially charged domains and right: covalent interaction between the metal and hydride with negative and positive partial charges.

Even though the hydride ion is generally considered to be an ionic species, a non-negligible amount of covalent interactions with its bonding partners exist.^[6] This described polarizable and covalent nature of the metal-hydride bond can be directly observed for instance in Eu^{2+} doped hydrides and will be explained in detail in chapter 1.4.2.

1.2 Heteroanionic hydrides

For the synthesis of new functional solid-state materials many approaches are applicable. From the bottom-up synthesis of nanostructured materials to post-synthetic modifications, many strategies can be exploited to optimize old and to find new functional materials.^[32,33] However, from the beginning of the last decade, a different approach of materials design has been established by combining different anionic species within one compound. While heteroanionic compounds have been widely known before, a particular emphasis is nowadays placed on the modification of the anionic composition, contrary to the common modification of the cationic counterparts. Through the combination of different types of anions, new materials can be obtained. Different electronegativities, polarizabilities and anionic radii can be introduced, allowing for an alteration of the material's properties at will.^[34–36]

This concept has been successfully applied to metal hydrides and heteroanionic hydrides emerged as an own class of materials with intriguing properties themselves. Widely desired characteristics such as superconductivity,^[37,38] hydride ion conduction,^[39–44] or tuneable optical properties^[45–50] were observed that accumulated the interest of many and induced this research field.

In the following chapters, a fundamental overview regarding several established subclasses of the heteroanionic hydride family discovered to date will be introduced and discussed.

1.2.1 Elemental heteroanionic hydrides

The simplest and most researched hydridic heterostructures belong to simple combination of hydrides with further elemental anions, such as fluoride, oxide and nitride anions. Especially the combinations of hydrides with elemental anions of the second periodic row are well researched and will be presented below.

Hydride halides

The halide hydrides are a well-researched and investigated composition type among the combinations of hydrides with monoatomic anionic species. The most prominent and most represented class within the halide hydrides to date is set by the hydride fluorides. As already mentioned, the hydride fluoride analogy enables the easy substitution of the two anions with one another.^[29] Consequently, many phase systems were obtained by starting from pure fluorides and stepwise increasing the hydride amount through targeted substitution. Solid-solution series with general stoichiometries of e.g. MH_xF_{y-x} with $0 \leq x \leq y$ are easily accessible. While some phase systems herein show limits or miscibility gaps, complete solid-solution series are observed frequently, especially if the pure fluorides and hydrides exist with the same crystal structure and similar lattice parameters.^[46,47,51–56] Such solid-solution systems of hydride fluorides have been found to be easily adjustable host and model systems for Eu^{2+} -luminescence, due to the inherent higher polarizable character of the hydride anions compared to fluoride anions.^[46,47,54] Hydride halides of the heavier halides are known as well. The first representatives thereof were already reported in 1956 by Ehrlich *et al.* in the form of $AEHX$ ($AE = \text{Ca, Sr, Ba, } X = \text{Cl, Br, I}$), all crystallizing in the PbFCl Matlock-type.^[57–59] Overall, these were the first and only reported halide hydrides for the time being. To date, further hydride (heavy) halides are reported numerous.^[41,60–68] Anyway, the ionic radius of the heavier halogenides progressively differ from the ionic radius of the hydride and solid-solution series of this composition type are uncommon. Instead, ordered compounds are observed. Such anion-ordered hydride halides as $\text{Ba}_{2-\delta}\text{H}_{3-2\delta}\text{X}$ ($\delta \sim 0.2$; $X = \text{Cl, Br, and I}$) have been recently discussed as fast hydride ion conductors.^[41]

Oxide hydrides^a

Oxide hydrides or often also simplified ‘oxy hydrides’ are another frequently synthesized and investigated type of heteroanionic hydrides. Even though the first oxide hydrides LaHO , CeHO and PrHO were reported by Carter in 1962,^[69] the general interest in such compounds was rather low for the time being. With the finding of $\text{LaSrCoH}_{0.7}\text{O}_3$ (**Figure 1.4**) and its high magnetic ordering temperature of 350 K in the early 2000s,^[70] the research on the still unexplored field of oxide hydrides picked up momentum. Numerous similar compounds have been discovered subsequently and multiple desirable, interesting characteristics were exposed within this standalone subclass of heteroanionic hydrides itself.^[71] Magnetic ordering at high temperatures,^[72–77] electronic and ionic conductivities^[43,44,78–80] or superconductivity^[38,81] are only some of the properties detected. Furthermore, resistance against moisture and air is observed frequently.^[45,48,82,83] These promising properties justify the ongoing as well as growing research and interest in this class of materials. Several different synthesis routes were found to be expedient in synthesizing oxide hydrides. While some compounds are accessible by topotactic reactions of oxides with hydridic reactants, others can be synthesized by

^a To be consistent with the nomenclature used in the own publications, compounds of this particular compound class will be denoted as oxide hydrides. In sum formulas, hydride is stated before the single atomic oxide ion to avoid confusion with hydroxide ions (OH^-).

conventional solid-state reactions with or without applied hydrogen pressure.^[71] Mechanochemical reactions were also found to be applicable.^[78] Anyway, two cases of oxide hydrides are to be distinguished. A case with ordered arrangement of the anions and secondly, a disordered arrangement of hydrides and or oxides with mixed occupations. The oxide anion O^{2-} has a similar ionic radius as the hydride ion.^[30] A substitution of oxides by hydride anions and vice versa similar to the hydride fluoride analogy is possible. This was often demonstrated in e.g. perovskite titanates such as $BaTiH_xO_{3-x}$.^[79,80,84] However, full substitutions or complete solid-solutions are inaccessible due to missing charge compensations.

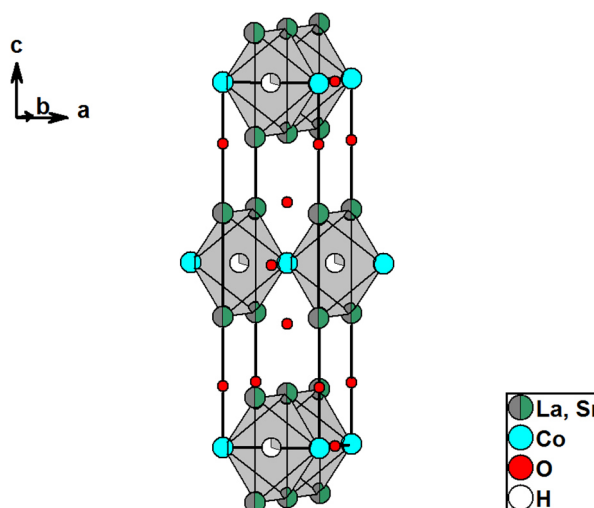


Figure 1.4. Crystal structure of the transition metal containing oxide hydride $LaSrCoH_{0.7}O_3$. The coordination sphere of hydride is depicted as a grey octahedron.

Sulfide hydrides and the heavier homologue chalcogenide hydrides are reported as well, yet remain an underrepresented group. Examples are the antiperovskites A_3HCh ($A = Li, Na; Ch = S, Se, Te$)^[85], the hydride selenides $MHTe$ ($M = Y, La-Nd, Gd-Er, Lu$)^[86,87] and hydride tellurides $MHTe$ ($M = Y, La-Nd, Gd-Er$)^[88] as well as the recently reported lanthanum selenide hydrides La_2H_2Se, La_2H_3Se and La_2H_4Se .^[89]

Hydride nitrides

The simple combination of the nitride anions N^{3-} with hydrides has also attracted the attention of many. One of the first compounds of this composition type was discovered by Brice *et al.* in 1976 in the form of Ca_2HN .^[90] This ternary hydride nitride is accessible by the hydrogenation reaction of Ca_2N under N_2 and H_2 gas-flow at $300\text{ }^\circ\text{C}$.^[91] Ca_2HN crystallizes in a particular cubic structure where the Ca^{2+} ions form two penetrating supertetrahedra as shown in **Figure 1.5**. The hydride ions are, equally as the nitride ions, located within calcium octahedra. Further examples of hydride nitrides are Li_4HN ^[92], Ba_2HN ^[93] or the quaternary $LiSr_2H_2N$.^[94,95] Hydride nitrides are investigated as candidates for hydride ion conduction and also as ammonia catalysts.^[91,93,96–98]

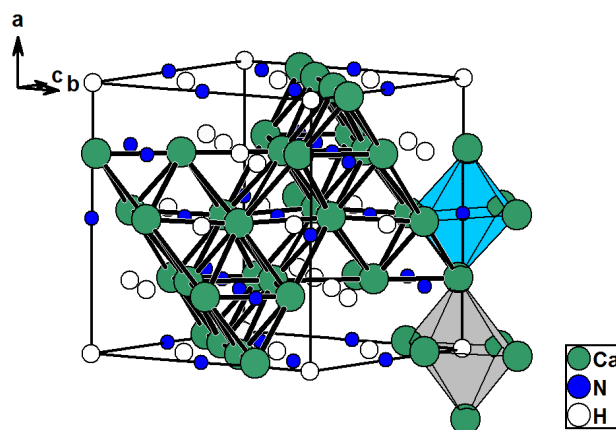


Figure 1.5. Crystal structure of Ca_2HN with the penetrating Ca-supertetrahedra. The coordination sphere of hydride is depicted as a grey octahedron, nitride in light blue.

Beyond the previously discussed elemental heteroanionic hydrides, examples of hydride carbides^[99–107] and hydride silicides^[108–115] are known, whereas compounds of the latter class are often rather ascribed to so-called Zintl-phase hydrides.^[116]

Hydrides in combination with two further anions

Heteroanionic structures with three or more different anions are rare and even more so with hydride anions being part of the anionic constituents. Only few examples were discovered to date. In 2017 $\text{LiEu}_2\text{HOCl}_2$ was introduced as the first hydride oxide chloride. Synthetically accessible by the reduction of Eu_2O_3 in a LiH/LiCl flux, $\text{LiEu}_2\text{HOCl}_2$ shows bright, yellow luminescence, owing to the Eu(II) cations.^[117] Very recently, Zapp *et. al.* introduced $\text{SmH}_{0.78}\text{OF}_{0.22}$ as a hydride oxide fluoride. Starting from Sm_2O_3 , SmOF was eventually formed after the reaction with polytetrafluoroethylene, which was subsequently converted to $\text{SmOF}_{0.22}\text{H}_{0.78}$ by metathesis reactions with LiH , NaH , or CaH_2 .^[118] Further noteworthy instances of this kind are the multinary $\text{Sr}_2\text{TiH}_{0.48}\text{O}_3\text{F}$,^[119] the hydride oxide nitrides $\text{Sr}_{0.9}\text{La}_{0.1}\text{H}_{0.11}\text{N}_{0.1}\text{O}_{2.79}$ ^[120] and $\text{BaTiH}_{0.3}\text{N}_{0.2}\text{O}_{2.5}$ ^[121] and also the hydride oxide iodide $\text{Ba}_5\text{H}_2\text{O}_2\text{I}_{3.9(2)}$ reported by Reckeweg in 2011.^[67]

1.2.2 Hydrides in combination with complex anions

Previously, heteroanionic compounds with only single atomic anions were discussed. Heteroanionic hydrides where additionally complex anions, *i.e.* anions with covalent, molecular building units are abundant, were also discovered. However, the reductive nature of hydrogenation reactions often reduces the complex anion and prevents the formation of new compounds with this composition type. Suitable synthesis routes are often missing and only a handful of these hydride-to-anion combinations are known hitherto. The first and most important representatives with complex oxide- or nitridoanions reported to date will be discussed further on.

Aluminate hydrides

One of the first heteroanionic hydrides with complex anions reported are the aluminate hydrides, with complex tetrahedral $[\text{AlO}_4]^{5-}$ units next to hydride ions. The first reported representative thereof is $\text{Ba}_3\text{AlO}_4\text{H}$ and was described by Huang and Corbet in 1998. Accessible by a solid-state reaction of BaH_2 , BaO and Al_2O_3 under hydrogen atmosphere, $\text{Ba}_3\text{AlO}_4\text{H}$ crystallizes in a structure related to the orthorhombic Ba_3GeO antiperovskite-type. In **Figure 1.6** the crystal structure is depicted where the complex aluminate ions (blue) occupy the voids of the three-dimensional, strongly distorted HBa_6^b octahedra network.^[122] The (anti)-perovskite structure and derivatives with complex anions will be discussed in detail in chapter 1.3 later on.

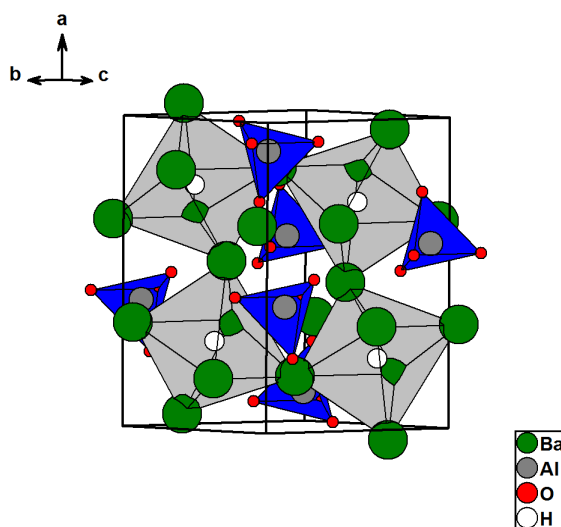


Figure 1.6. Crystal structure of $\text{Ba}_3\text{AlO}_4\text{H}$. The silicate ions are depicted as blue tetrahedra, HBa_6 octahedra are depicted grey.

As further aluminate hydrides, the mixed cationic series $\text{Sr}_{1-x}\text{A}_x\text{AlO}_4\text{H}$ ($\text{A} = \text{Ca}, \text{Ba}; x = 0, 1$) were reported by Wu *et al.* and obtained by applying the same synthesis method of the earlier reported barium analogue. The three reported compounds were found to crystallize also in antiperovskite-like structures but with a more symmetrical tetragonal build-up. Additionally, for the first time, Ce^{3+} luminescence in a hydridic host material was reported herein.^[49]

Silicate hydrides

Gehlhaar *et al.* were able to synthesize $\text{LiSr}_2\text{SiO}_4\text{H}$ and thus, opened up the compound class of the silicate hydrides. $\text{LiSr}_2\text{SiO}_4\text{H}$ is synthetically accessible by a solid-state reaction of LiH with Sr_2SiO_4 in quartz glass ampules without any applied hydrogen pressure or hydrogen atmosphere. It crystallizes isostructural to the corresponding fluoride in the monoclinic space group $P2_1/m$ (11) with the cell parameters $a = 6.5863 \text{ \AA}$, $b = 5.4236 \text{ \AA}$, $c = 6.9501 \text{ \AA}$ and $\beta = 112.5637^\circ$. The hydride ions are located within face-sharing Li_2Sr_4 octahedra that form infinite strands along the b-axis as illustrated in **Figure 1.7**.

^b To avoid confusion with complex, molecular anions, charges of coordination polyhedra will be neglected.

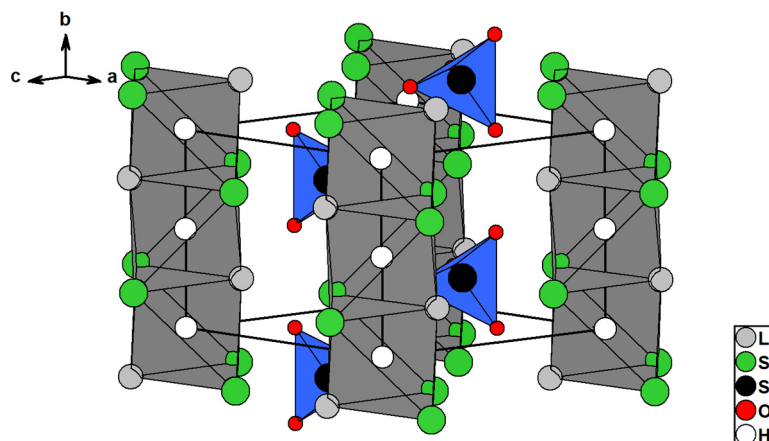


Figure 1.7. Crystal structure of $\text{LiSr}_2\text{SiO}_4\text{H}$.

Despite the hydridic character, $\text{LiSr}_2\text{SiO}_4\text{H}$ shows remarkable resistance against moisture, is stable in air and also only starts to decompose at temperatures above 550 K. Beyond that, it shows only slow dissociation in diluted acid. When doped with Eu^{2+} , bright yellow-green luminescence is observed, indicating the suitability as host material for luminescence.^[48] $\text{LiSr}_2\text{SiO}_4\text{H}$ remains the only silicate hydride reported to date.

Phosphate hydrides

Hydrides in combination with phosphate ions were firstly observed after a topotactic reduction of $\text{Ca}_5(\text{PO}_4)_3\text{OH}$ with TiH_2 . Only small, non-stoichiometric amounts of hydride ions, comparable with dopant concentrations could be detected.^[123] Eventually, $\text{Sr}_5(\text{PO}_4)_3\text{H}$ was obtained as the first, fully-substituted phosphate hydride by a mechanochemical reaction of SrH_2 with $\text{Sr}_3(\text{PO}_4)_2$. The novel phosphate hydride crystallizes in the hexagonal apatite-structure $P6_3/m$ (176) with the cell parameters $a = 9.7169 \text{ \AA}$ and $c = 7.2747 \text{ \AA}$. Similar to the elemental anions in apatite-structures and types alike, the hydride ions are located within trigonal channels, set up by the earth alkaline metals, as in this case strontium ions.^[124]

This finding did not only open a path to the phosphate hydrides, it also expanded the apatite family by a further anion. The heavier barium analogue could be synthesized *via* the same synthesis route. A full structural characterization is yet pending.^[125]

Borate hydrides

The first borate hydride was introduced shortly after the earlier discovered phosphate hydride and is closely related thereto. $\text{Sr}_5(\text{BO}_3)_3\text{H}$ is the first representative of this novel class of materials and accessible by the same synthesis route successfully deployed for the phosphate hydride. $\text{Sr}_5(\text{BO}_3)_3\text{H}$ crystallizes in a distorted orthorhombic apatite-like structure in the space group $Pnma$ (62) with the cell parameters $a = 7.1982 \text{ \AA}$, $b = 14.1461 \text{ \AA}$ and $c = 9.8215 \text{ \AA}$. The hydride anions are again located within trigonal channels of strontium ions, yet slightly off-centred in this lower symmetric apatite variant as shown in comparison with the hexagonal perovskite structure in **Figure 1.8**. When doped with Eu^{2+} , the compound shows red-orange luminescence, demonstrating that borate hydrides might be suitable as host materials for

europium-activated luminescence. Similar to the earlier discussed silicate hydride, it only shows slow dissociation after contact with dry air, uncommon for salt-like hydrides.^[45]

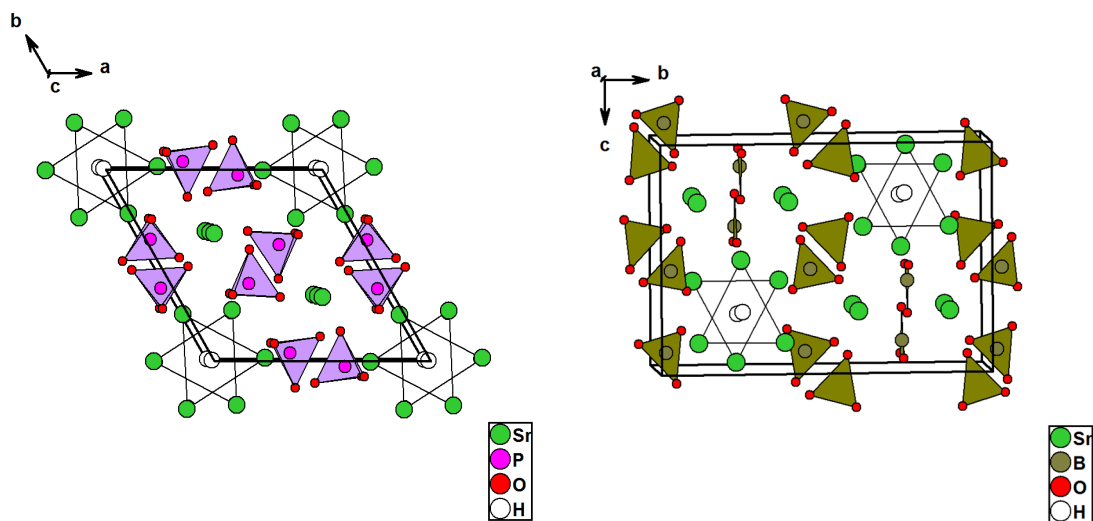


Figure 1.8. Crystal structures of $\text{Sr}_5(\text{PO}_4)_3\text{H}$ with lilac phosphate tetrahedra (left) and $\text{Sr}_5(\text{BO}_3)_3\text{H}$ with trigonal planar olive borate ions (right). The coordination sphere of hydride is shown as colourless trigonal planar species respectively.

Nitridoborate hydrides

Most complex anions next to hydride ions are oxide-based anions, yet further complex anions, such as nitride-based anions in combination next to hydrides are also known. In this regard, a nitridoborate hydride has been reported in the form of $\text{Ca}_2\text{BN}_2\text{H}$, crystallizing in the orthorhombic space group $Pnma$ (62), isostructural to the corresponding fluoride. $\text{Ca}_2\text{BN}_2\text{H}$ can be synthesized by the solid-state reaction of Ca_3N_2 with CaH_2 and BN under inert conditions. As in **Figure 1.9** illustrated, the HCa_4 tetrahedra are edge sharing to form infinite strands. Further nitridoborate hydrides are yet to be discovered.^[126]

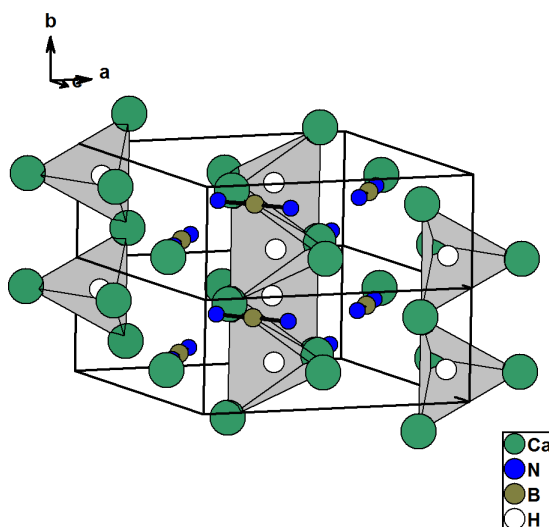


Figure 1.9. Crystal structure of $\text{Ca}_2\text{BN}_2\text{H}$. HCa_4 tetrahedra are illustrated grey.

Nitridochromate hydrides

Also, $\text{Ca}_6\text{Cr}_2\text{N}_6\text{H}$ was reported as a nitridochromate hydride in 2003 by Bailey *et alii*. $\text{Ca}_6\text{Cr}_2\text{N}_6\text{H}$ can be synthesized by the solid-state reaction of CaH_2 , CrN and Ca_3N_2 in steel ampules by heating the powders at 1000 °C. This structure contains ethane-like complex nitridochromate dimeric units $[\text{Cr}_2\text{N}_6]^{11-}$, consisting of mixed valent Cr(III) and Cr(IV) that are located between isolated HCa_6 -octahedra.^[127]

As a related nitridochromate hydride, $\text{Ba}_3\text{CrN}_3\text{H}$ with trigonal planar $[\text{Cr}(\text{IV})\text{N}_3]^{5-}$ anions was obtained by a similar synthesis method. Hydride ions are located within face-sharing, one dimensional strands of Ba_6 octahedra and the complex $[\text{CrN}_3]^{5-}$ -units are located in between.^[128] Such complex nitride hydride are discussed as catalysts for ammonia synthesis.^[129] The structures of both nitridochromate hydrides are shown in **Figure 1.10**.

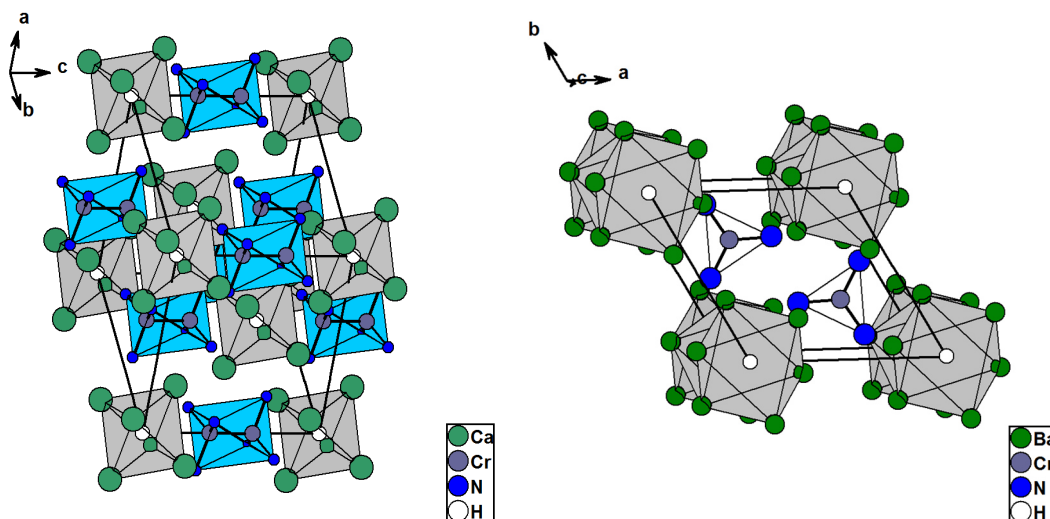


Figure 1.10. Crystal structures of $\text{Ca}_6\text{Cr}_2\text{N}_6\text{H}$ (left) and $\text{Ba}_3\text{CrN}_3\text{H}$ (right). The coordination sphere of hydrogen is depicted as grey polyhedra respectively. $[\text{Cr}_2\text{N}_6]^{11-}$ ions are light blue, $[\text{CrN}_3]^{5-}$ ions are shown as colourless, trigonal planar units.

It is apparent that encapsulating hydride anions within highly electropositive cations is key to stabilize such heteroanionic structures. However, the synthetic strategies towards obtaining new heteroanionic hydrides differ. In many cases, a successful formation of the desired compounds need a high activation barrier to be overcome. This again requires high reaction temperatures that inadvertently activate the hydride ions which in turn facilitate the early decomposition and reductions of reactants. This altogether results in undesired phases. Especially oxide-based anions with highly charged central cations are prone to reduction by hydrogen and present hydride ions. New ways are yet to be explored to avoid these hurdles and to access further, new unprecedented materials. Heteroanionic hydrides with complex anions are by far the least investigated and explored kind of hydrides in general. Furthermore, many combinations to several complex anions, e.g. carbonates or nitrates are yet to be discovered and established.

1.3 The perovskite structure

Often occurring structures of inorganic and also increasingly hybrid inorganic-organic compounds can be derived from or ascribed to the perovskite structure. In general, two basic building principles exist that can be deduced from either a cubic or a hexagonal aristotype. Structures belonging to the hexagonal perovskite family will be discussed later in the subsequent chapter 1.3.1. The cubic perovskite structure (**Figure 1.11**), also often referred to as the 'ideal' perovskite structure, crystallizes in the space group $Pm\bar{3}m$ (221). This structure is built from the ReO_3 structure (herein described as BX_3) by filling the cuboctahedra voids with a further cation (A), resulting in the general stoichiometry ABX_3 . In a different perspective, AX_3 together form a cubic close packing where every octahedral gap is occupied by the cation B .^[5] Commonly, the lower valent and thus larger cation (A) is generally expected to occupy the cuboctahedral voids, while the smaller, higher valent cation (B) is coordinated octahedrally.

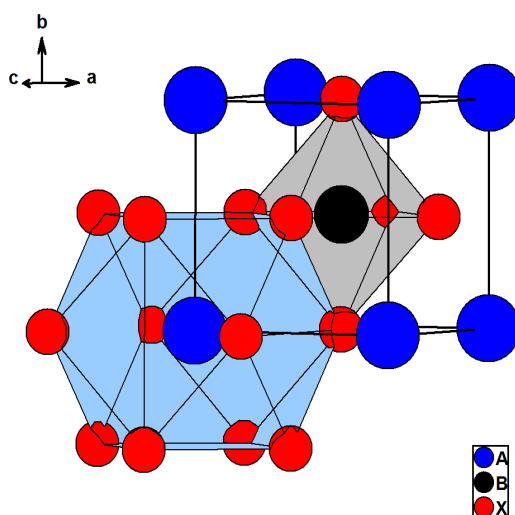


Figure 1.11. Crystal structure of the ideal cubic perovskite structure with AX_{12} cuboctahedron (light blue) and BX_6 octahedron (grey).

There are exceptions where the perovskite structure is adopted with inverse coordination spheres of the cations, usually observed when the higher valent cation has a significantly larger ionic radius. This is then indicated as the inverse perovskite structure. Prominent examples of inverse perovskites are LiBaF_3 or the analogue hydride LiBaH_3 where the markedly larger Ba^{2+} ion is demanding more space in comparison with the smaller Li^+ ions, ultimately resulting in inverse coordination spheres.^[130–132] The expression 'inverse perovskite' is used inconsistently in literature. The term is also often ascribed to structures that are additionally classified as antiperovskites. Anyway, antiperovskite structures are to be distinguished therefrom and will be introduced and discussed later on in chapter 1.3.2.

1.3.1 Distorted variants and the Goldschmidt tolerance factor

Compounds with the composition ABX_3 show a large structural variety, especially regarding perovskite related structures. This is already reflected by the eponymous mineral with the

chemical composition CaTiO_3 . This compound adapts a distorted orthorhombic variant at room temperature which would even suggest a different structure type associated to this name.^[5] To estimate and explain distortions of perovskite structures or derivatives, Goldschmidt introduced the tolerance factor of the same name.^[133] The tolerance factor compares the ionic radii of the involved species and gives a qualitative explanation for structural adaptations. Ideally, A and X ions are approximately of the same size, as both ions form a cubic close packing.^[5] Simply put, if the tolerance factor is ~ 1 , the ideal cubic perovskite structure is formed. If the tolerance factor deviates too far from 1, distorted variants occur. Usually, orthorhombic-rhombohedral variants are formed for $t < 1$ and tetragonal-hexagonal variants for $t > 1$. The Goldschmidt-tolerance factor can be formulated as follows:^[133]

$$t = \frac{r_A + r_X}{\sqrt{2}(r_B + r_X)} \quad (1.1)$$

with r_A, r_B and r_X , being the ionic radii of the involved species in respect to their coordination spheres. The distortion of the CaTiO_3 structure is now easily explained by the Goldschmidt tolerance factor. The Ca^{2+} ions are too small in comparison with O^{2-} and Ti^{4+} . With its deficient size, the Ca^{2+} ions are unable to fill the cubooctahedral voids properly and the TiO_6 octahedra show an activated tilt towards the Ca^{2+} ions. The determined tolerance factor is accordingly below the ideal value of 1.

Distortions of perovskite structures are often generally recognizable and categorized by tilting and twisting of the octahedra coordinating the B-site cation. In **Figure 1.12** such examples with twisted octahedra tilted octahedra are shown.

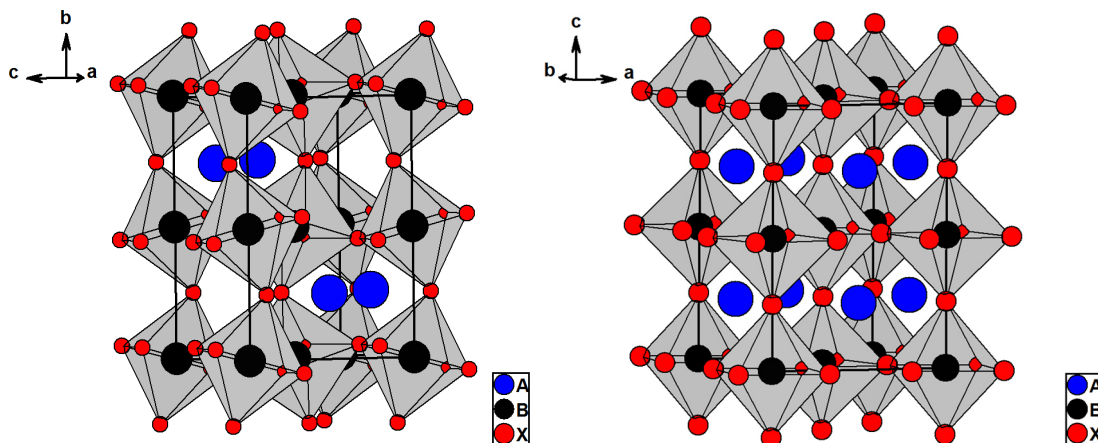


Figure 1.12. Left: orthorhombic perovskite structure (FeGdO_3 -type) in the space group $Pnma$ (62) and right: a tetragonal perovskite structure in the SrZrO_3 -type ($I4/mcm$, 140).

As mentioned before, perovskite structures related to the cubic aristotype are in principle built by the cubic close packing of AX_3 , resulting in a variety of structures with twisted, tilted or also distorted corner-sharing octahedra. Variants with additionally face-sharing interconnection of the octahedra also exist. Structures alike then belong to the second perovskite architecture with a hexagonal building principle. These perovskites, also denoted as stacking polytypes, are built of both cubic close packing as well as hexagonal close packing of the ions.^[5,134] Atomic layers

with hexagonal close packing (*hcp*) of the ions result in face-sharing octahedra whereas cubic close packing (*ccp*) layers result in corner-sharing octahedra. The particular stacking polytype can be classified as the Jagodzinski-notation by the order and number of *ccp* or *hcp* layers.^[5,134] The sum of distinct hexagonal ($\triangleq h$) and cubic layers ($\triangleq c$) within a unit cell are given by a prefix *n* with an indication to the crystal system of the respective structure; e.g. R for rhombohedral or H for hexagonal crystal systems. A prominent example of such a stacking variant is represented by the 6H stacking polytype, the aristotype of the hexagonal perovskite family. In this hexagonal structure, two octahedra are condensed and face-sharing. These condensed octahedra are then interconnected corner-sharing to three further octahedra each. The corresponding Jagodzinski-notation herein is cch_2 ($\triangleq cchcch$). Another example of a stacking perovskite variant is the rhombohedral 9R-type ($\triangleq (hhc)_3$). Here, units of three face-sharing octahedra form a three-dimensional network by the corner-sharing interlinking of these units. Both examples of the above mentioned hexagonal type perovskite structures are depicted in **Figure 1.13** with an illustration of the respective *hcp* and *ccp* layers. Non-stacking, cubic-related perovskite variants can equally be described as 3C-types (*ccc*).

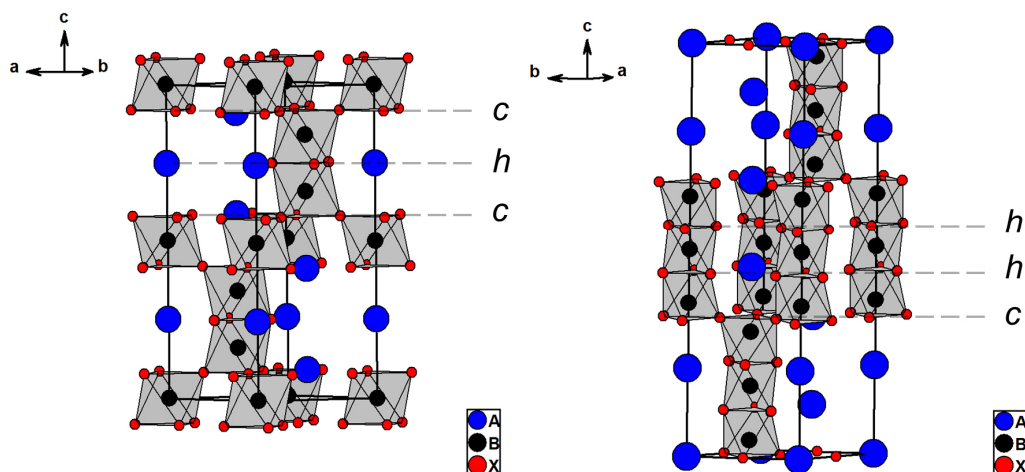


Figure 1.13. Left: 6H-stacking polytype perovskite $P6_3/mmc$ (194), right: 9R-stacking polytype perovskite $R\bar{3}m$ (166). The hexagonal and cubic close packing layers are marked with *h* and *c* respectively.

1.3.2 The antiperovskite structure

As counterpart to the traditional ABX_3 -like composition, a reversed set-up of the ions is possible, describable as A_3BX . A refers now to a usually monovalent cation, while *B* and *X* are both different and aliovalent anions, in many cases mono and divalent. As suggested by the twisted composition, compounds alike are denoted as antiperovskites. The physical properties of these materials often differ from ‘classic’ perovskites. Due to the possibility to introduce high amounts of e.g. alkaline metal cations, high ionic conductivity is observed frequently within this class of materials.^[135] This is investigated for instance in oxide-based antiperovskites such as A_3OX or ($A = \text{Li, Na, K; } X = \text{Cl, Br, I}$).^[136]

1.3.3 Antiperovskites with complex anions

The *B*- and *X*-site anions may also be in the form of complex anions, mostly tetrahedral anions, such as SO_4^{2-} , SiO_4^{4-} , or PO_4^{3-} or BH_4^- anions. The charges are then equivalent to the respective elemental anion the complex anion substitutes. These compounds form structures very similar to perovskites and its distorted representatives.^[137] The complex anions, equal to the cations of the ‘normal’ perovskite structure, either occupy the cuboctahedral or octahedral voids of the cationic network. The tolerance factor for antiperovskite structures, also regarding structures containing complex anions, can still be used to estimate the structural modification:^[138,139]

$$t_{AP} = \frac{r_B + r_A}{\sqrt{2}(r_X + r_A)} \quad (1.2)$$

If the *B* or *X*-site is occupied by a complex ion, the ionic radius of the respective complex ion is used (bond length plus ionic radius of the decentral bonding partner). However, due to the often rather large ionic radius of the complex anions, an ideal tolerance factor of ~ 1 is hard to fulfil. To date, only few examples of structures with complex anions are known to crystallize comparable with an ideal cubic (anti)perovskite-like architecture. Examples are $\text{K}_3\text{SO}_4\text{F}$ which adapts the ideal cubic perovskite structure at temperatures above 858 K^[140] or the natural occurring mineral Sulphohalite $\text{Na}_3\text{SO}_4\text{F}_{0.5}\text{Cl}_{0.5}$ as a representative of the elpasolite-structure, the doubled perovskite.^[141] Beyond that, Na_3OBH_4 with the relatively small complex borohydride ion BH_4^- is another example known to crystallize in the cubic perovskite variant.^[142]

An often observed antiperovskite structure type with complex anions at the *B*-site is the $\text{K}_3\text{SO}_4\text{F}$ -type,^[140] closely related to the above discussed tetragonal SrZrO_3 -type. Another tetragonal type is represented by the $\text{Ag}_3\text{CrO}_4\text{Cl}$ -type.^[143] Both structures illustrated with a perovskite-like build-up are shown in **Figure 1.14**.

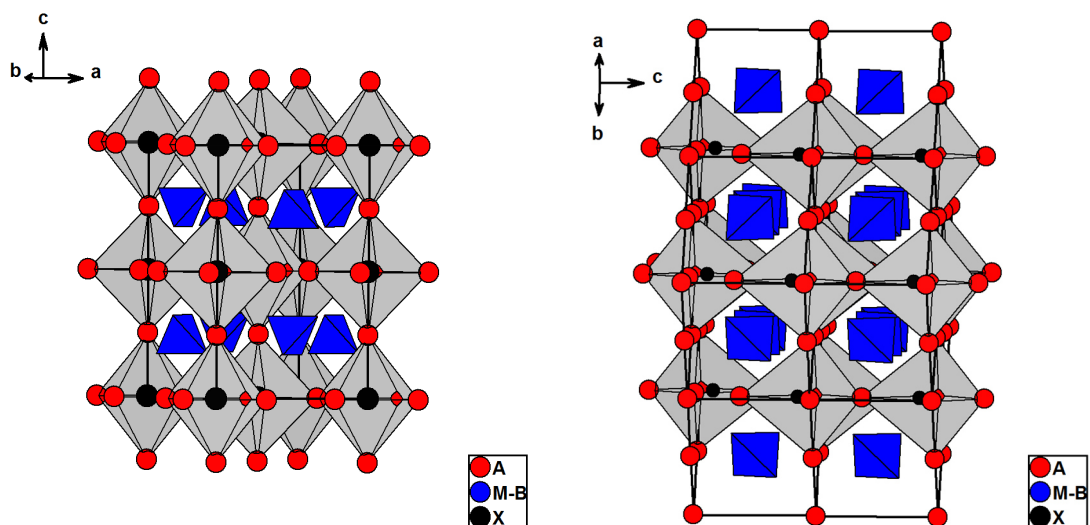


Figure 1.14. Crystal structure of tetragonal antiperovskites with complex anions. Left tetragonal $\text{K}_3(\text{SO}_4)\text{F}$ -type ($I4/mcm$, 140), right tetragonal $\text{Ag}_3\text{CrO}_4\text{Cl}$ -type ($P4/nmm$, 129, O2). The complex anions are depicted as blue tetrahedra. The colour codes are kept identical to the normal perovskite structure, illustrating the analogy of the octahedra.

Stacking polytypes are also observed often.^[137] For instance, the mineral Kogarkoite $\text{Na}_3\text{SO}_4\text{F}$ crystallizes in a monoclinic 9R stacking-type (**Figure 1.15**)^[144,145] while the silicate $\text{Ca}_3\text{SiO}_4\text{O}$ crystallizes in the rhombohedral 9R-type.^[146]

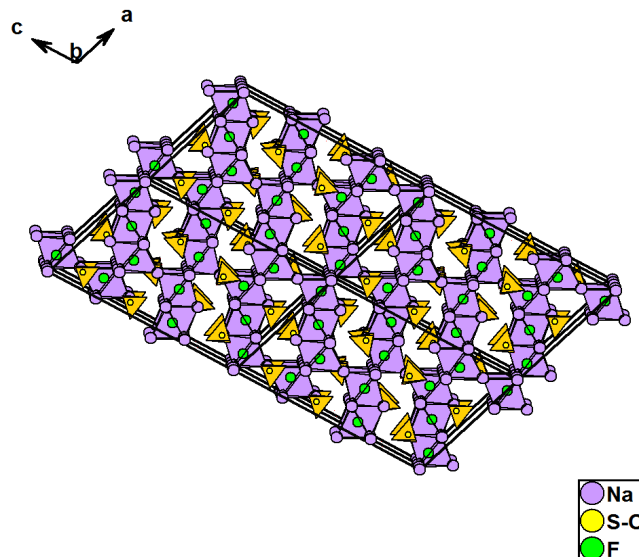


Figure 1.15. Crystal structure of the mineral Kogarkoite, $\text{Na}_3\text{SO}_4\text{F}$, space group $P2_1/m$ (11), depicted as a 4x4 supercell to point out the 9R-stacking perovskite polytype analogy. SO_4^{2-} tetrahedra are depicted yellow, FNa_6 octahedra purple.

1.4 Photoluminescence

Optical materials for light generation are indispensable in daily life. From smartphone screens to traffic lights, all artificial lighting devices are based on materials able to emit photons of desired wavelengths. While earliest artificial lighting was based on incandescent generation of light, the norm has now shifted towards luminescent materials.^[147,148] Luminescent materials are per definition solids which are able to convert energy predominantly in electromagnetic radiation rather than thermal energy or thermal radiation. If a luminescent process is induced by electromagnetic radiation (mostly UV or visible light), it is then denoted as photoluminescence. Hence, a photoluminescent material is able to convert electromagnetic radiation of certain energy into electromagnetic radiation of different, lower energy. A simplistic macroscopic schematic of the processes arising in a photoluminescent material is depicted in **Figure 1.16**. An activator ion **A**, embedded in a solid-state matrix, is excited by electromagnetic radiation. Upon vibrational transitions, part of the excitation energy is transferred *via* nonradiative processes to the host matrix, eventually resulting in heat transferred to the host system. Electromagnetic radiation of certain wavelength is emitted subsequently.^[149]

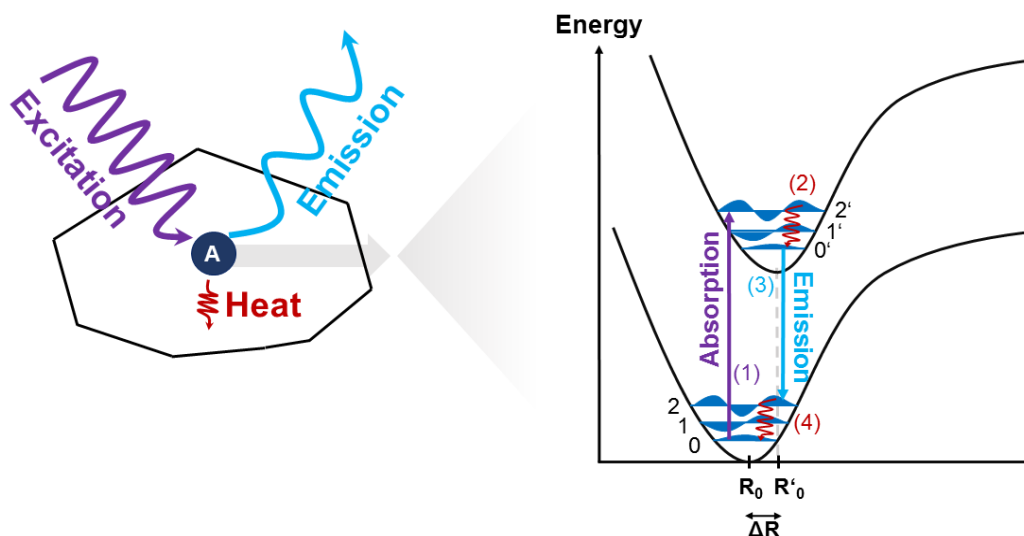


Figure 1.16. A macroscopic depiction of a luminescent particle (left) and the detailed luminescence process arising in the activator ion depicted as configurational coordinate diagram (right), modified after^[149].

In a more detailed view, the luminescence process arising in the activator ion can be broken down into four steps. First, an electron in the ground state gets excited to a state of higher energy. In terms of photoluminescence, this excitation occurs by the absorption of a photon. In the second step, the electron undergoes nonradiative vibrational relaxations to reach the lowest vibrational level of the excited state. Afterwards the electron relaxes spontaneously by the emission of a photon to reach the electronic ground state. In the last step, again vibrational relaxations occur before the electron finally reaches the initial electronic and vibrational ground state. The overall time needed for the emission to occur accounts to 10^{-9} s to 10^{-6} s.^[150] Due to the multiple nonradiative vibrational relaxations, energy is transferred from the activator ion to the surroundings, usually the host material and mostly in the form of heat. This energy ‘loss’ is ultimately noticeable in the luminescence spectrum. The observed emission appears always at lower energy as the absorption (excitation energy). This energy difference is called the Stokes shift.^[149]

With their partly filled f -shells, lanthanide ions are frequently used as activator ions, as f - f or d - f transitions are often within the range of visible light. Some d -metal ions such as manganese or chromium ions or several main group ions can also serve as activator ion for luminescent materials. Important activator ions for the application in luminescent materials are e.g. the trivalent Ce^{3+} cation or the divalent europium Eu^{2+} owed to their capability to undergo d - f transitions.^[149] The luminescent properties of the latter activator ion will be discussed more in detail in the following chapter.

1.4.1 Eu^{2+} -activated luminescence

Among the lanthanides, europium stands out as a special ion. Due to its electron configuration ($[\text{Xe}] 4f^7 6s^2$), europium can form two stable ions: a trivalent (+III) and also a divalent (+II)

ion. The empty s -shell and half-filled f -shell ($[Xe] 4f^7$) are the cause of the stable oxidation state +II, uncommon for lanthanides which form preferably trivalent or tetravalent oxidation states.^[151] Regarding the luminescent properties of the aliovalent europium ions, the two differ from each another. In its trivalent state, europium is best known for a characteristic red-orange line emission (ca. 610 nm), arising from interconfigurational $f-f$ transitions. Electronic $f-f$ transitions in general are forbidden by the parity rule, although the rules might not strictly apply in solids as mixing of wave functions may occur. Therefore, some, often less intense luminescence can still be observed.^[149,151,152] In consequence, for the design of efficient phosphors with varying emission wavelengths, the lower valent Eu^{2+} ion is utilized. The divalent Eu^{2+} ion, contrary to its oxidized counterpart, is capable of $f-f$ and also $d-f$ transitions. Electronic $d-f$ transitions are parity allowed and, due to the unshielded d -orbitals, dependent on the chemical environment which now allows for the alteration of the emitted wavelength. In **Figure 1.17** the two possible luminescent transitions of the Eu^{2+} ion are depicted. **Figure 1.17 a)** shows the $f-f$ transition (as Russel-Saunders term symbols: ${}^6P_{7/2} \rightarrow {}^8S_{7/2}$) of the Eu^{2+} ion. In this case the excited $4f^7$ state is energetically lower than the $4f^65d^1$ state, resulting in $f-f$ transitions with a characteristic line emission at ca. 360 nm. In **Figure 1.17 b)**, a typical $d-f$ transition is shown. The energy levels of the excited $4f^65d^1$ state are now situated below the excited $4f^7$ states; thus, an electron is excited to the $4f^65d^1$ state resulting in allowed $d-f$ transition. A band emission, with a wavelength depending on the host materials the activator ion is embedded in, is now observed.

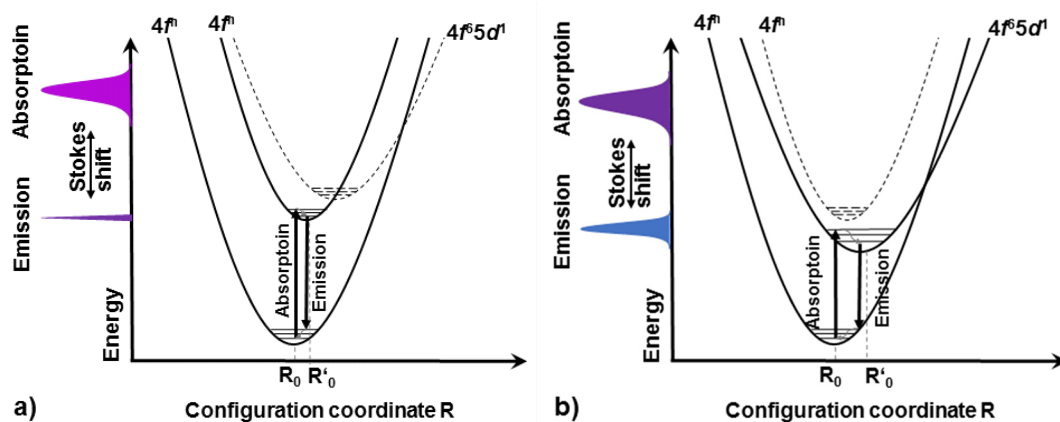


Figure 1.17 a) configurational coordinate diagram of $f-f$ transitions; b) configurational coordinate diagram of $d-f$ transitions.

From **Figure 1.17** it can be qualitatively explained why $f-f$ transitions in general show line emissions, whereas $d-f$ transitions show band emissions. Electrons of the $4f$ -orbitals are near the atomic core and consequently these f -orbitals barely participate in the chemical bonding, contrary to the $5d$ and $6s$ orbitals which are directly involved.^[153] Therefore, the energetic position of the excited $4f$ state is almost uninfluenced by the chemical environment. ΔR in the configuration coordinate diagram is correspondingly small and the emissions appear as sharp line emissions. The $5d$ orbitals are, as mentioned before, actively participating in the chemical

bonding, ΔR is consequently larger and $4f^65d^1 - 4f^7$ emissions appear accordingly as band emissions.^[149]

Previously, the electronic $f-f$ and $d-f$ transitions of the Eu^{2+} ion were explained that ultimately may result in detectable luminescence. Yet, for some cases, due to own dissimilar characteristics, a third distinctive type of Eu^{2+} activated luminescence is discussed and denoted as anomalous luminescence. This type of luminescence is ascribed to when following three criteria are observed: (1) An anomalous large Stokes shift and large FWHM of the emission band, (2) anomalous temperature dependencies and decay times and (3) unexpected luminescent properties, not derivable from simple host-guest relations. This type of luminescence is however only observed for Eu^{2+} and Yb^{2+} as activator ions, as for other divalent lanthanide ions (e.g. Sm^{2+} and Tm^{2+}), f -levels are probably interfering and inducing quenching mechanisms.^[154] The suggested mechanism as configurational coordinate diagram of the anomalous luminescent process is depicted in **Figure 1.18**.

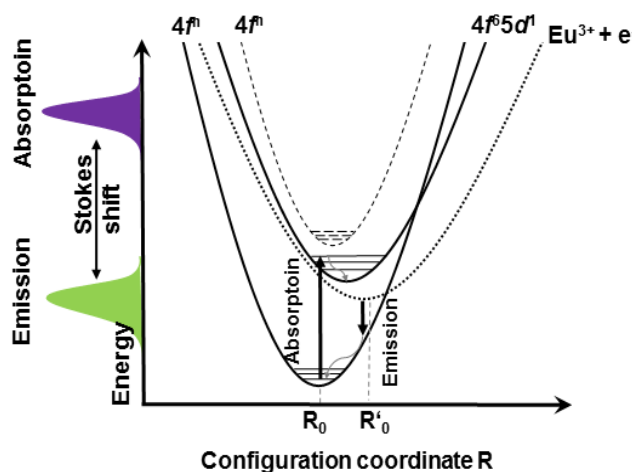


Figure 1.18. Configurational coordinate diagram of an anomalous luminescence process of Eu^{2+} according to ^[154].

First, an electron is excited to the $4f^65d^1$ state similarly to the normal $d-f$ transition. Through autoionization, a Eu^{3+} -centre is formed that generates a new energetic state below the $4f^65d^1$ state (herein denoted as ' $\text{Eu}^{3+} + e^-$ '). By recombination of the electron with the Eu^{3+} impurity, a photon is emitted and the initial ground state is retrieved.^[154]

The newly formed state ' $\text{Eu}^{3+} + e^-$ ' can be exemplified with the model of the impurity trapped exciton with contributions of the conduction band (CB) as shown in **Figure 1.19**. First, the electron is excited to the $5d$ state, energetically below the conduction band. By autoionization, the electron is then excited into the conduction band, a localized Eu^{3+} -centre is formed and the now unoccupied $5d$ -state is energetically raised to the conduction band. On a local level, the newly formed Eu^{3+} -centre, smaller in cationic size than the Eu^{2+} centre, attracts the surrounding anions (red) through the higher electrostatic charge. The electron is now trapped in the surrounding M^{2+} cations with a reduced Madelung potential. In combination with the higher coulombic attractions of the electron to the Eu^{3+} -centre, the newly formed excitonic state presumably has a lower energetic state compared to the $5d$ state of the Eu^{2+} ion.^[154,155]

Materials where anomalous Eu^{2+} luminescence is discussed are e.g. $\text{BaF}_2:\text{Eu}^{2+c}$,^[155] $\text{CsCaF}_3:\text{Eu}^{2+}$,^[156,157] and $\text{LiBaF}_3:\text{Eu}^{2+}$.^[154,158]

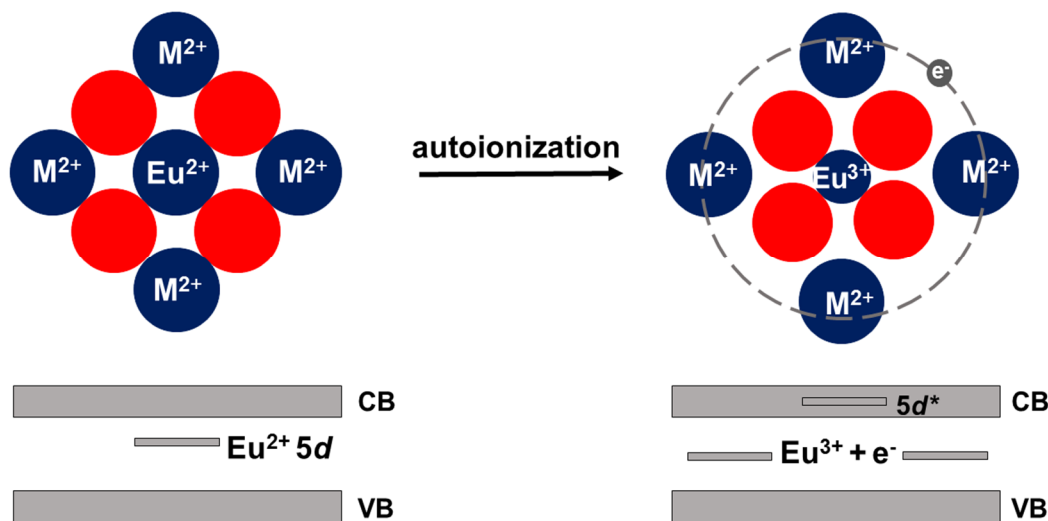


Figure 1.19. Formation of an impurity trapped exciton with a Eu^{3+} centre according to ^[154].

1.4.2 Eu^{2+} -activated luminescence in metal hydrides

As discussed above, the emitted wavelength is always of lower energy as the excitation wavelength's energy. While a certain amount of energy is 'lost' due to internal vibrational relaxations (Stokes effect), further effects also contribute considerably to a lowering of the energy levels of the excited states. Another influence is governed by the crystal field splitting, according to the symmetry of the atomic site where the activator ion is located at. More precisely, the energy levels of degenerate orbitals, upon involving in a chemical bond, split accordingly to the coordination sphere surrounding the activator ion. The stronger the crystal field splitting effects are, the lower the energy levels of the excited d -state.^[159–161] Yet another effect is also strongly determining the energy levels of the excited states which is deduced from the covalency of the metal ligand bond, described by the nephelauxetic effect (from greek: *cloud-expanding*). This can be simply put as follows: the higher the polarizable character of a ligand bonded to a metal centre, the lower the energy of the resulting molecular orbital. Correspondingly, with polarizable ligands, a rather covalent metal-ligand bonding situation is formed. Covalent molecular orbitals are larger compared to more confined, rather ionic molecular orbitals. The overall electronic repulsion is reduced in the larger, covalent molecular orbital and the energy level of the orbitals are lowered.^[162–164] A schematic of all contributions to the total energy level is shown in **Figure 1.20**.

^c A sum formula with an added ' $:M^{n+}$ ' indicates that a chemical compound is doped with an activator ion, as in this case divalent Eu^{2+} . This can be analogously written as $\text{Ba}_{1-x}\text{Eu}_x\text{F}_2$ for the example of $\text{BaF}_2:\text{Eu}^{2+}$.

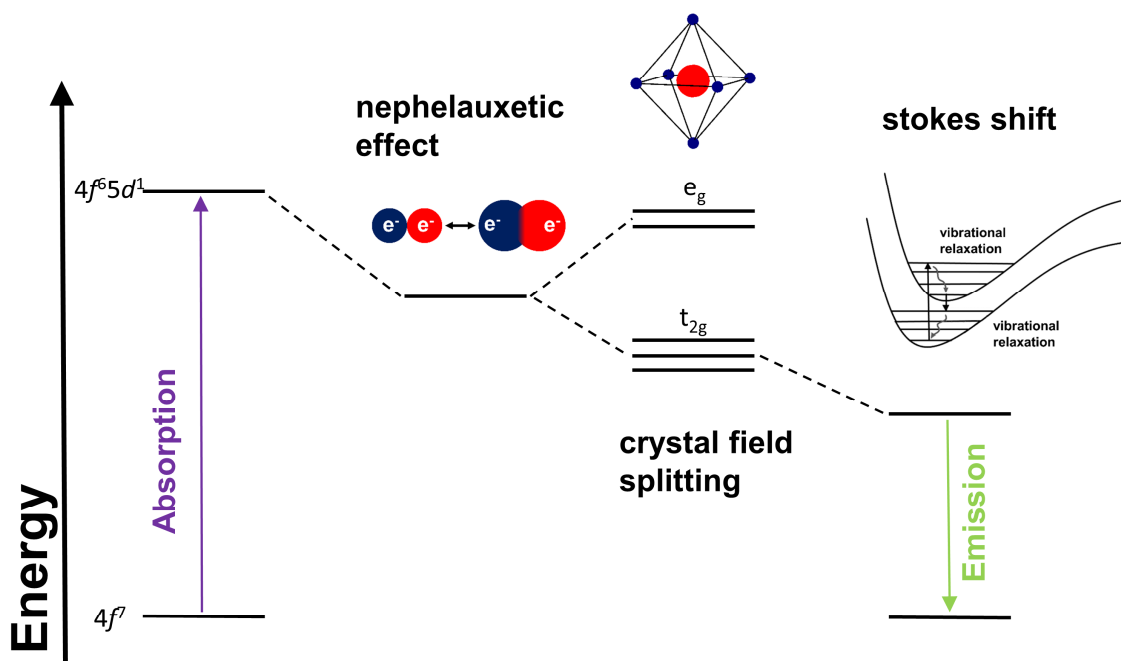


Figure 1.20. Schematic illustration of the contributions to the energetic level of the $4f^6 5d^1$ state in transitions of Eu^{2+} . An octahedral coordination sphere of Eu^{2+} is illustrated to demonstrate the crystal field splitting effect. Energy levels are not representative of realistic energy levels.

This effect is pronounced recognizable in hydridic host materials. As discussed in chapter 1.1.1, the hydride ion is polarizable and consequently the metal-hydride bond has a high degree of covalency. However, europium luminescence in a hydride as host material was only described a decade ago. Kunkel *et al.* were the first to systematically study Eu^{2+} luminescence in hydridic host materials. Here, very red-shifted europium luminescence was observed in the binary alkaline earth hydrides $\text{AEH}_2:\text{Eu}^{2+}$ ($\text{AE} = \text{Ca}, \text{Sr}, \text{Ba}$).^[165] Shortly after, bright, efficient luminescence was observed in the ternary perovskites $\text{LiSrH}_3:\text{Eu}^{2+}$ and $\text{LiBaH}_3:\text{Eu}^{2+}$, proving the suitability of hydridic materials to host europium activated luminescence.^[166] Applying the approach of heteroanionic materials design and with the aid of the hydride fluoride analogy, heteroanionic hydride fluoride solid-solutions were investigated. As a result, tunable europium luminescence was observed in $\text{EuH}_x\text{F}_{2-x}$.^[54] Here, by increasing the hydride content, the luminescence could be selectively redshifted. Further solid-solution series emerged where tunable Eu^{2+} -luminescence was reported. Further examples are the solid-solution series $\text{KMgH}_x\text{F}_{3-x}:\text{Eu}^{2+}$, $\text{RbMgH}_x\text{F}_{3-x}:\text{Eu}^{2+}$ ^[46] and $\text{NaMgH}_x\text{F}_{3-x}:\text{Eu}^{2+}$.^[47] Not only does this introduce the possibility to tune the emission wavelength at will, but these easily adjustable systems are also suited as model systems to investigate europium luminescence and improve existing phosphors. Beyond hydrides or hydride fluorides, further heteroanionic hydrides were discovered that exhibit luminescent properties. $\text{Sr}_5(\text{BO}_3)_3\text{H}:\text{Eu}^{2+}$,^[45] $\text{LiSr}_2\text{SiO}_4\text{H}:\text{Eu}^{2+}$ ^[48] or $\text{Sr}_3\text{AlO}_4\text{H}:\text{Eu}^{2+}$ ^[49] are archetypical examples. For all systems, the emitted wavelength is always of lower energy compared to the emitting non hydridic, in many cases fluoridic, counterparts. This eventuality is always traced back to the pronounced nephelauxetic effect introduced by the hydride ions.

1.4.3 Energy transfer

As mentioned before, an excited luminescent centre usually relaxes to the ground state via radiative and nonradiative transitions. However, a further mechanism can take place where energy is transferred from the excited centre S^* to another, excitable centre A. Following after, emission from the other, now excited centre A^* occurs. The energy transfer process can be written synoptically as following: $S^* + A \rightarrow S + A^*$. As S^* is considered to be a sensitizer, it is referred herein and in the following as S. The second luminescent centre is considered as the activator or acceptor and referred to as A. Anyway, A^* may also relax non radiative and thus, can be a quencher of S. The process in the luminescent particle in analogy to **Figure 1.16** can be seen in **Figure 1.21 a)**.^[149]

With the assumption that both optical centres are in proximity of each other, such that interactions are non-vanishing, two further basic conditions must be fulfilled for energy transfer to occur: (1) sufficient interactions between the two distinct centres exist and (2) the energy difference between the ground and excited states of S and A are equal (resonance condition). Interactions can either be exchange interactions (wave function overlap) or *via* allowed multipole interactions (electronic or magnetic). The resonance condition is usually examinable by the spectral overlap between the emission band of S with the absorption band of A, as seen in **Figure 1.21 b)**.^[149]

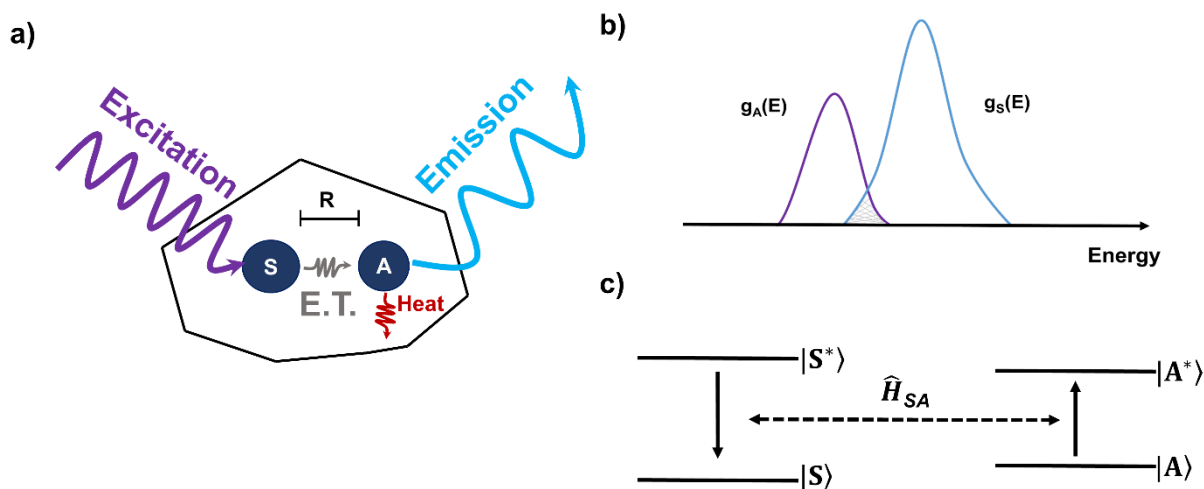


Figure 1.21. Energy transfer (E.T.) process in a luminescent particle between S and A with a distance R; b) spectral overlap between the emission $g_S(E)$ of the sensitizer and the absorption $g_A(E)$ of the activator; c) energy level schemes of the involved states according to ^[149].

In consideration of both conditions, the transfer rate (P_{SA}) can be formulated with equation (1.3).

$$P_{SA} = \frac{2\pi}{\hbar} |\langle S, A^* | \hat{H}_{SA} | S^*, A \rangle|^2 \cdot \int g_S(E) \cdot g_A(E) dE \quad (1.3)$$

The matrix term of the equation describes the interaction of the initial states with the final states, whereby \hat{H}_{SA} refers to the interaction Hamiltonian. The integral element represents the spectral

overlap as normalized optical line shape functions, $g_S(E)$ for the sensitizer and $g_A(E)$ of the activator. From this equation it is apparent that high transfer rates are only feasible if the interactions (multipolar or exchange type) are efficient as well allowed and also the resonance *i.e.* the spectral overlap (**Figure 1.21 b**) is high. Anyway, the interaction part of P_{SA} is additionally depended on the distance R between the involved activator species. Multipole type interactions follow an R^{-n} dependency, with n corresponding to the respective multipole-multipole interaction type. Exchange type interactions follow an exponential dependency, as these kind of interactions require wave function overlap. When multipolar interactions are forbidden, the distance is reduced from e.g. 30 Å to 5-6 Å, as only wave function overlap remains as interaction part and atomic orbitals must be in proximity to each other. Whether a luminescence process is dictated by energy transfers can be detected by measuring the photoluminescence decay curves. A typical experimentally obtained decay curve is illustrated in **Figure 1.22**. Normally, the lifetime of an excited state follows an exponential decay of first order. If a second luminescent centre is involved, the profile of the decay curve deviates from the first order and higher orders of an exponential decay are observed. The radiative decay for an isolated activator ion is given by equation (1.4).^[149]

$$I(t) = I_0 \exp(-\gamma t) \quad (1.4)$$

Where $I(t)$ refers to the detectable intensity at a certain time (t), I_0 to the intensity at $t = 0$ and γ to the radiative rate. If now S^*-A transfer occurs, the decay gets more complex. Assuming that only S^*-A transfers and no additional S^*-S transfers occurs, equation (1.4) can be formulated as follows:^[149]

$$I(t) = I_0 \exp(-\gamma t - Ct^n) \quad (1.5)$$

C is now introduced as a factor for the A concentration and the S^*-A interaction, n refers to the multipolar interaction type.

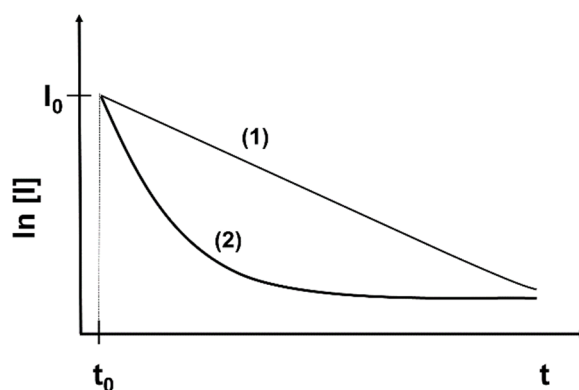


Figure 1.22. Typical decay curves on a logarithmic scale with an exponential decay (1) and a decay curve influenced by energy transfers (2).

With energy transfer between two centres, the luminescence decay does not follow a normal exponential behaviour anymore. Energy transfer happens on a much faster timescale as the lifetime of the excited states; thus, detectable luminescence decays faster. After no S^* to A energy transfers occur anymore, exponential behaviour is observed again. There are further cases possible e.g. where S^*-S and S^*-A transfers occur simultaneously amongst others which do even more impact the decay properties. All these processes are easily detectable by measuring the lifetime of the excited states.^[149]

1.5 Aims

The aim of the present work is to establish further synthetic strategies and to improve analytical methods towards new hydridic materials, especially unprecedented hydride-to-anion combinations. New materials are then primarily investigated in structural and optical properties. Despite the recent attention heteroanionic hydrides have gained, this particular research on this class of materials is still in its infancy. The fundamental challenge to synthesize hydridic materials stalls the realization of novel, likely and predicted stable compounds. Furthermore, hydrogen is basically invisible by the means of X-ray diffraction - the gold-standard of laboratory structure determination. This drastically impedes structural elucidation and analytical evidence of hydride abundance in new materials. As a result, many hydridic compounds and new combinations of hydrides with different anions are yet to be discovered which leaves a vast field of materials with potentially desirable features unexplored.

Structure determination of potentially new phases is carried out by Rietveld refinement of powder X-ray diffraction and neutron diffraction data. MAS NMR and vibrational spectroscopy is applied, which in combination with DFT calculations, provides a complementary tool to corroborate and locate hydride ions within unsolved structures. The structures and physical properties of obtained new hydrides are investigated and, if possible, compared with the fluoride counterparts which will enhance the understanding of the polarizable character introduced by the hydride ions. In case of successfully doping new compounds with Eu^{2+} ions, the luminescent behaviour is investigated which is utilized as a local probe to gain further understandings at the local atomic structure in heteroanionic hydrides. Simultaneously, such luminescent hydrides can be utilized as easy tunable host systems to enhance the understanding of luminescent processes arising in rare earth doped phosphors.

2 Experimental details

Syntheses and manipulations of air and moisture sensitive reactants as well as all reaction products were carried out within gloveboxes (*MBraun*) under argon atmosphere. The O₂ and H₂O concentrations were monitored and kept below 0.5 ppm respectively. Glass ware, agate mortars and metallic laboratory equipment were dried in an oven at 120 °C for at least one hour before use to remove traces of surface water.

2.1 Chemicals

Chemicals used in this thesis are listed in **Table 2.1**.

Earth alkaline hydrides were synthesized by the direct hydrogenation of the respective elements. The general procedure of a hydrogenation reaction is described in chapter 2.3. Alkaline, alkaline earth metals, and europium were freed from oxide layers mechanically before use. Sodium deuteride (NaD) was synthesized from NaH by an isotope exchange reaction. Thereto, NaH is heated under 80 bar pressure of deuterium gas. This is repeated a total of 5 times to reach an estimated enrichment of approx. 95%. KH was washed several times with hexane and then dried under vacuum. Commercially acquired chemicals in form of powders were dried thoroughly before use. For this purpose, the powders were transferred into a Schlenk tube and then dried at 200 °C for 24 hours under dynamic vacuum. All further chemicals were used without any further purification steps.

Table 2.1. List of chemicals used in this thesis.

Chemical	Chemical formula	Form	Manufacturer	Purity [%]
Calcium	Ca	granules	Alfa aesar	99.5
Calcium fluoride	CaF ₂	powder	Alfa aesar	99.95
Calcium hydride	CaH ₂	powder	Own synthesis	-
Calcium deuteride	CaD ₂	powder	Own synthesis	-
Cesium	Cs	lumps	Alfa aesar	99.8
Cesium carbonate	Cs ₂ CO ₃	powder	Alfa aesar	>99.9
Cesium fluoride	CsF	powder	chemPUR	99.99
Cesium molybdate	Cs ₂ MoO ₄	powder	Own synthesis	-
Cesium tungstate	Cs ₂ WO ₄	powder	Alfa aesar	99
Deuterium	D ₂	gas	Air liquide	99.98
Europium	Eu	granules	Alfa aesar	99.9
Europium (II) fluoride	EuF ₂	powder	Alfa aesar	99.9
Europium hydride	EuH ₂	powder	Own synthesis	-

Table 2.1 continued.

Chemical	Chemical formula	Form	Manufacturer	Purity [%]
Hydrogen	H ₂	gas	Westfalen AG	99.9
Molybdenum(VI)oxide	MoO ₃	powder	Alfa aesar	99.5
Potassium	K	pieces	Unknown origin	-
Potassium hydride	KH	powder	Alfa aesar	35 wt.% solution in paraffin
Potassium molybdate	K ₂ MoO ₄	powder	Sigma aldrich	98
Potassium tungstate	K ₂ WO ₄	powder	VWR	≥ 99.95
Rubidium	Rb	lumps	Alfa aesar	99.9
Rubidium carbonate	Rb ₂ CO ₃	powder	chemPUR	99.9
Rubidium fluoride	RbF	powder	abcr	99.9
Rubidium molybdate	Rb ₂ MoO ₄	powder	own synthesis	-
Rubidium tungstate	Rb ₂ WO ₄	powder	chemPUR	99.9
Sodium hydride	NaH	powder	Sigma aldrich	90
Sodium deuteride	NaD	powder	own synthesis	-
Sodium sulfate	Na ₂ SO ₄	powder	Alfa aesar	99

2.2 Solid-state reactions

Solid-state synthesis with air-stable reactants and reactions with gaseous by-products were conducted under ambient conditions. Hereto, the powders were mixed and ground thoroughly in an agate mortar under air atmosphere for approximately 10 minutes. The homogenized mixture was then transferred into corundum crucibles and placed in a muffle furnace (*Nabertherm*). Afterwards a temperature program was set and started to induce the reactions. The purity of the obtained products was determined by powder X-ray diffraction. The compounds, if used as further reactants, were then dried as described in chapter 2 and stored under inert-gas atmosphere.

Non-hydridic but air and moisture sensitive compounds were synthesized in sealed metal ampoules, as shown in **Figure 2.1**.



Figure 2.1. Picture of an encapsulated and sealed Ni-alloy ampoule, ready to be placed in an oven. Stone wool is placed as buffer between the quartz glass and the ampoule.

There to, the reactants were ground thoroughly in an agate mortar under inert-gas atmosphere. This reaction mixture is transferred in nickel alloy ampoules (NiCu₃₀Fe, *Eugen-Geyer GmbH*) which are then sealed via arc welding. The sealed ampoules are additionally jacketed within evacuated quartz glass to avoid oxidation of the ampoule material. The air-tight ampoules were placed vertically into a muffle furnace (*Nabertherm*) and an appropriate temperature program is started. The ampoules were opened after the reaction under inert-gas atmosphere and characterized by X-ray diffraction.

2.3 Reactions under hydrogen pressure

Reactions that require hydrogen pressure or hydrogen atmosphere were conducted in an in-house built autoclave consisting of a hydrogen resistant, nickel-based alloy (Boehler steel L718). The alloy of the autoclave was hardened once pre-use *via* a special temperature program under flow of argon gas. This processing ensures a complete hydrogen resistivity also at elevated temperatures. The respective temperature program is depicted below in **Figure 2.2**.

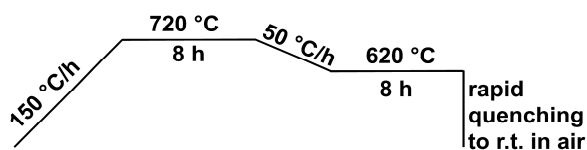


Figure 2.2 Annealing temperature program for the hardening process of the autoclaves.

After hardening, reactions can take place with temperatures up to 823 K and applied hydrogen pressures of up to 150 bar. A picture of the unassembled, hardened autoclave with all additional required setup is seen on the left side in **Figure 2.3**.

The reaction chamber of the autoclave has a diameter of approx. 1.5 cm and a depth of 9 cm so the empty reaction volume adds up to approx. 15.90 cm³. Up to three reaction crucibles (inner height 2.5 cm, inner diameter 1 cm) can be placed inside. So in total, reactants with a volume of up to 6 cm³ can be placed inside the crucibles and reacted at once. For the general synthesis procedure, the reactants were handled and processed accordingly and placed within the crucibles which were then put inside of the reaction chamber of the autoclave. Afterwards, the autoclave was assembled and sealed pressure and air-tight *via* a copper gasket and six screws (**Figure 2.3** middle). The sealed autoclave was then filled with hydrogen pressure by a gas valve and placed in a tube furnace (*Carbolite Gero*), as in **Figure 2.3** right. A temperature program was set and then started to initiate the reaction. The exact reaction conditions (gas pressure, temperature program) of the individual reactions are discussed in the respective chapters. The set temperatures for the reactions are given in both the oven temperature and the approximated temperature within the autoclave (~ 0.71 of set temperature; determined by calibration).

Reactions temperatures will be stated with the approximated temperature within the autoclave. The set oven temperature is indicated aside as OT*.



Figure 2.3. Picture of the disassembled autoclave (left) for reactions under hydrogen pressure. The assembled autoclave with the crucibles and reactants inside is depicted in the middle, ready to be loaded with hydrogen pressure. The hydrogen-loaded autoclave, placed in a tube furnace with stone wool for isolation is depicted on the right. A burst protection is adjusted in front.

2.4 Mechanochemical reactions

Formation of reactive mixtures or mechanochemical reactions with hydridic samples were conducted in a planetary micro mill (Pulverisette 7 Premium Line, *Fritsch*) with either WC or ZrO₂ beakers. The beakers were filled with 10 balls (10 mm Ø) of the respective beaker material together with the reactants. A picture of the beakers and mill is shown in **Figure 2.4**.



Figure 2.4. Tungsten carbide (grey) and zirconium dioxide (yellow) beakers with 10 balls each for mechanochemical reactions. Placed beaker in the planetary mill, ready to be started.

As the beakers are designed to handle inside-pressures up to 20 bar, the total amount of hydridic reactants was set to not exceed this pressure by an assumed complete decomposition thereof. One milling cycle, depending on the sample, usually consisted of 2-3 minutes milling with consecutive pausing for 2-10 minutes to avoid overheating. Additionally, the rotation direction was reversed after each cycle to ensure a homogenous distribution of the sample within the beaker.

After milling, thermal annealing was applied to increase the samples crystallinity either in fused quartz ampoules or with hydrogen pressure in the autoclave at 300 – 550 °C for 2 - 10 days.

2.5 Powder X-ray diffraction

Powder X-ray diffraction data were collected on a Stoe Stadi P diffractometer (*Stoe & Cie GmbH*) in transmission geometry with a curved Ge(111) monochromator and Mythen1K (*DECTRIS*) detector. Measurements were conducted either at Cu-K $_{\alpha 1}$ ($\lambda = 1.54059 \text{ \AA}$) or Mo-K $_{\alpha 1}$ ($\lambda = 0.70930 \text{ \AA}$) radiation, depending on the absorption and fluorescence behaviour of the to be measured samples. For measurements, small amounts of the well-ground polycrystalline samples were transferred into glass capillaries of 0.1 - 0.3 mm diameter and 0.01 mm wall thickness which are then sealed air-tight by sealing with capillary wax. Samples with strong X-ray absorbing elements were measured in flatbed transmission geometry. Thereto, small amounts of the samples were mixed together with grease (glisseal HV, *Borer Chemie*) and fixated air-tight between X-ray amorphous capton foil. Measurements of approx. 15 - 30 minutes in a scattering range from 5° - 80° 2θ (Cu-K $_{\alpha 1}$) or 2° - 40° 2θ (Mo-K $_{\alpha 1}$) were performed to analyse phase purity. Measurements for Rietveld refinements were performed in similar scattering ranges but with longer exposure time and smaller measuring steps. In total, diffraction patterns for refinement were measured over time periods ranging from 12 h to 3 d. Silicon (NIST 640c) was applied as an external standard for zero shift calibration.

Temperature dependent X-ray diffraction data was collected likewise on a Stoe Stadi P diffractometer with Mo-K $_{\alpha 1}$ radiation. The capillaries of the respective samples were fixated within a cryofurnace. Patterns were collected in a temperature range of 100 – 400 K with individual temperature steps of 20 K. Each pattern was collected over the span of 1 hour.

Collected XRD data was evaluated by the software package WinXPOW^[167] and the implemented Inorganic Crystal Structure Database ICDD. Further evaluation was done with Pearson's crystal data,^[168] the web services of Springer Materials^[169] and Materials Project.^[170]

2.6 Powder neutron diffraction

Powder neutron diffraction data was acquired from D2B^[171] at the Institut Laue Langevin (ILL) in Grenoble, France or from SPODI^[172] at the Heinz Maier-Leibnitz Forschungsreaktor (FRM II) in Garching, Germany. Thereto, large quantities of deuterated samples (approx.

3 - 5 g) were synthesized which are required to ensure sufficient data quality. The polycrystalline samples were enclosed in vanadium cylinders of 9 mm diameter under argon atmosphere and sealed air-tight with an indium wire. Diffraction patterns were recorded in a range of 0° - $160^\circ 2\theta$ with neutron wavelengths of 1.594 Å (D2B) or 1.548 Å (SPODI) over the course of 5 hours.

Measurements at 4 K to reduce thermal displacement parameters were recorded at the D2B by the use of a cryofurnace. Here, a background measurement of the empty cryofurnace was done which is then used for a manual background correction.

2.7 Rietveld refinement

Crystal structure refinements based on the Rietveld method^[173] of powder X-ray or powder neutron diffraction data were done with the program packages of Fullprof^[174] or Jana2006^[175] and the fundamental parameter approach.^[176] The cell parameters, three form factors (Caglioti parameters U , V , W), and two (neutron diffraction data) or four asymmetry (X-ray diffraction data) parameters were refined. For X-ray diffraction data obtained by Mo- $K_{\alpha 1}$ radiation, axial divergence with two coefficients was additionally introduced to fit the reflection asymmetry. The reflection profile was fitted using the pseudo-Voigt approximation and the ratio of Gaussian to Lorentzian contributions (η). The background was fitted using either a linear interpolation of background points with refineable heights or Chebyshev polynomials. Lastly, atomic parameters, occupations and isotropic, or if applicable, anisotropic thermal displacement parameters were refined.

2.8 Photoluminescence spectroscopy

Preliminary photoluminescence emission spectra were recorded in-house on an AvaSpec-ULS2048 (*MountainPhotonics*) spectrometer of samples encapsulated in evacuated quartz glass (length ≤ 40 mm, 5-6 mm \varnothing , wall thickness 1 mm). A mercury lamp with short-wave UV-light ($\lambda = 254$ nm) and long wave UV-light ($\lambda = 376$ nm) or LEDs with wavelengths of 340 nm or 375 nm were used for excitation.

High quality luminescence emission, excitation spectra and decay measurements were acquired at Utrecht University on a Horiba a FLS920 spectrofluorometer (*Edinburgh Instruments*). The samples are likewise encapsulated in quartz glass for measurement. Photoluminescence spectra were recorded with a 450 W Xe-lamp as excitation source and a R928 photomultiplier tube (*Hamamatsu photonics*) for detection. For the excitation beam, a double monochromator according to Czerny–Turner with 300 nm blaze was used. For emission a monochromator with 500 nm blaze was used. The spectra were corrected for lamp intensity and detector response. Decay measurements were recorded with a pulsed diode laser (376.8 nm, *Edinburgh Instruments*) as excitation source and a H74220 60 photomultiplier tube (*Hamamatsu*

photonics) for detection.

For measurements at 4.2 K, samples were cooled down within an *Oxford Instruments* liquid He flow cryostat with an external temperature control unit. For temperature dependent measurements in the range of 4.2–500 K, the temperature was adjusted *via* the temperature control unit.

Additional luminescence emission and excitation spectra were recorded at the University of Göttingen on a *Fluorolog* FL322 equipped with 450 W Xenon lamp as excitation source and double monochromator for the excitation beam (1200 l/mm, 300 nm blaze) and double monochromator (1200 l/mm, 500 nm blaze) for the emission. Emission was detected by a R928P photomultiplier tube (*Hamamatsu photonics*).

2.9 Magic-angle spinning NMR spectroscopy

In-house measurements of ^1H MAS NMR spectra were carried out on a *Bruker* AV300 spectrometer with samples in 4 mm ZrO_2 rotors at a frequency of 300.13 MHz, spinning frequencies of 8.0 or 15.0 kHz, single pulse excitation and recycle delays of 10 s. Adamantane (1.85 ppm to TMS) was used for external referencing.

Further ^1H and ^{23}Na MAS NMR spectra were recorded at the University of Alberta in Edmonton, Canada on a *Bruker* Avance III 400 HD NMR spectrometer. For ^1H MAS NMR measurements, the samples were enclosed in 4 mm ZrO_2 rotors measured a frequency of 400.3 MHz with 4.0 μs 90° pulses ($\nu_{\text{rf}} = 62.5$ kHz). Recycle delays were 180 s and spinning frequency was set to 10.0 kHz. As external standard adamantane (1.85 ppm to TMS) was used.

^{23}Na NMR spectra were acquired at a frequency of 106.9 MHz, using a 4.0 μs solid 90° excitation pulse and a 5 s recycle delay. Spinning frequency was set to 10.0 kHz. The Spectra were referenced to NaNO_3 (-7.1 ppm under MAS).

^2H MAS NMR spectra were recorded at the University of Leipzig on a *Bruker* Avance 750 spectrometer at a frequency of 114.88 MHz, single pulse excitation and recycle delays of 2000 s. Magic angle spinning rotation speed was set to 5.0 kHz. The spectra were referenced indirectly to TMS or d-TMS *via* the ^1H shift of a sample to PDMS (0.07 ppm to TMS).

2.10 Fourier-transform infrared spectroscopy

FT-IR spectra were recorded on a *Bruker* Alpha-P FT-IR spectrometer with an ATR unit. The spectrometer is stored and operated within a glovebox to avoid air and moisture contact of the samples. Small amounts of the samples were directly placed on the spectrometer and fixated by a diamond pressure cell without further treatment. The spectra were recorded in a range of 4000 - 400 cm^{-1} with a spectral resolution of 2 cm^{-1} .

2.11 Raman spectroscopy

For the acquisition of Raman spectra, polycrystalline samples were sealed in glass capillaries (0.3 Ø, 0.01mm wall thickness). The spectra were recorded on a *Renishaw* inVia Reflex Raman System equipped with a charge-coupled device detector. Wavelengths of the laser were chosen to be either $\lambda = 532$ nm or $\lambda = 785$ nm depending on the samples.

2.12 UV-Vis absorption spectroscopy

Experimental determination of band gaps were determined *via* solid-state UV-Vis absorption spectroscopy according to the Tauc-method.^[177] For measurement, a thin film of the polycrystalline sample was placed between two quartz glass slides. The glass slides were sealed air-tight with vacuum grease. The UV-Vis absorption of the polycrystalline samples were recorded on a *Shimadzu* UV-3600 Plus UV-Vis-NIR spectrophotometer. To finally estimate the band gap, the experimental absorption spectrum is transformed by formula (2.1) to plot the absorption α of the material in dependency of the energy with respect to the expected transition (r):

$$E \text{ (eV)} = \frac{1240}{\lambda \text{ (nm)}} (\alpha h\nu)^{\frac{1}{r}} \quad (2.1)$$

r was set to 1/2 for expected direct allowed transitions (direct band gap). Lastly, the band gap can be determined by the x-abcissa of a linear fit of the transition area.

2.13 Elemental analysis

Elemental analysis was conducted by the in-house technicians Ulrike Ammari and Bircan Dilki of the microanalytics laboratory at the Catalysis research Center, TUM. Hydrogen contents of the samples were determined *via* a CHNS (= Carbon, Hydrogen, Nitrogen, Sulfur) analysis conducted on a Vario El microanalyzer (*elementar*). Thereto, ~3-5 mg of the samples were packed as air-tight as possible inside small tin foil boats beforehand.

Molybdenum and tungsten contents were determined *via* alkaline pulping and consecutive photometric analysis of the respective substances. For the measurement, 5 mg of molybdenum-containing compounds or 12 mg of tungsten-containing compounds were packed and folded within aluminium-foil boats to avoid air and moisture contamination *pre* analytics.

2.14 Differential scanning calorimetry

Low temperature thermal analysis was conducted on a *Netzsch* DSC 200 F3 Maja calorimeter. For the measurement 30 mg of the sample were sealed air-tight inside of aluminium crucibles. An empty sealed crucible was used as reference. The measurement was performed under nitrogen flow of 100 mL/min in a temperature range from 153 – 373 K with a rate of 10 K/min. Two consecutive cycles were performed. The DSC data was processed using the Protheus Thermal Analysis software.

2.15 Density functional theory calculations

In order to study the geometries, electronic and vibrational properties of the compounds, density functional theory calculations were conducted with the CRYSTAL17 program package.^[178] The PBE0 hybrid density functional method with Gaussian-type basis sets was used.^[179,180] The basis sets (split valence polarized and triple zeta valence polarized) have been derived previously from the molecular Karlsruhe def2 basis sets^[181] and prior works.^[45,182–185] The reciprocal space was sampled using Monkhorst-Pack-type k-meshes^[186] which were set, when multiplied with the real space primitive cell edges, to be above 30 Å. Truncation criteria of the bielectronic (Coulomb and exchange) integrals were evaluated by tightened tolerance factors (TOLINTEG) of 8, 8, 8, 8 and 16. The optimal geometry of the experimentally determined crystal structures was elaborated by fully optimizing the atomic positions and the lattice parameters within the constraints set by the space group symmetry. If the optimized cell edges did not differ more than 3% in comparison with the experimental values, the input crystal geometry and the obtained optimized structure were assumed to be of sufficient merit. The band paths in the reciprocal space for the determination of the electronic band structures were obtained by the Seek-path webservice.^[187,188]

Harmonic frequencies, Raman- and IR-intensities were simulated by using computational schemes implemented in the CRYSTAL17 program package.^[189–191] If the optimized structure did not exhibit imaginary frequencies, the optimized structure was confirmed to be a true local energetic minimum. If imaginary frequencies were detected, the optimized crystal structure was distorted along the imaginary modes. A reiteration of the frequencies was then conducted and investigated if the applied distortion resulted in diminishing of the imaginary modes. If an imaginary mode was still detected, further distortions were applied. For the simulation of Raman- and IR spectra, temperature and Raman laser wavelength were set according to the experimental setup. Peak profiles of the final spectra were simulated using pseudo-Voigt profiles (50:50 - Lorentzian:Gaussian) and FWHM of 8 cm⁻¹.

3 New hydride fluorides crystallizing in the ideal perovskite structure

3.1 $M\text{CaH}_x\text{F}_{3-x}\cdot\text{Eu}^{2+}$ ($M = \text{Rb}, \text{Cs}$) – a different type of red shift

See chapter 7.1 *MCaH_xF_{3-x} (M = Rb, Cs): Synthesis, Structure, and Bright, Site-Sensitive Tunable Eu²⁺ Luminescence*, A. Mutschke, T. Wylezich, A. D. Sontakke, A. Meijerink, M. Hoelzel, N. Kunkel*, *Adv. Optical Mater.* **2021**, *9*, 2002052

To date, several luminescent hydride fluoride solid-solution series doped with divalent europium were reported. For all cases, the Eu^{2+} luminescence is gradually redshifted by the stepwise substitution of fluoride with hydride ions. This can be traced back to the nephelauxetic effect introduced by the polarizable hydride ions and the sensitivity of the $4f^65d^1 - 4f^7$ transitions to the local environment.^[46,47,50,54] So far, no Eu^{2+} doped luminescent hydride fluoride has been reported where the europium ion is supposed to substitute a calcium site. For both calcium containing perovskites RbCaF_3 and CsCaF_3 europium activated luminescence is reported,^[156,192,193] making an investigation and alteration of these compounds intriguing. In this context the corresponding hydride fluoride solid solution series $\text{RbCaH}_x\text{F}_{3-x}$ and $\text{CsCaH}_x\text{F}_{3-x}$ were synthesized and investigated regarding their crystal structures and luminescent properties upon doping with divalent europium.

The solid-solution series of $\text{RbCaH}_x\text{F}_{3-x}$

RbCaF_3 and RbCaH_3 both crystallize in the ideal cubic perovskite structure in the space group $Pm\bar{3}m$ (221). Even though heteroanionic hydride-fluoride phases are likely in consideration of the hydride-fluoride analogy, no such phases were reported before.

In this sense, the complete solid-solution series of $\text{RbCaH}_x\text{F}_{3-x}$ was synthesized and characterized by Rietveld refinement of X-ray diffraction data, elemental analysis and Raman spectroscopy. For the synthesis of $\text{RbCaH}_x\text{F}_{3-x}$, rubidium metal was mixed together in an agate mortar with appropriate stoichiometric amounts of $\text{CaH}_2/\text{CaF}_2$ and/or RbF . The respective compounds were then formed by the in-situ formation of RbH in an autoclave at 390 °C (550 °C OT*) under 50 bar hydrogen pressure for approx. 2 days. The pure fluoride is obtained by a solid-state reaction of RbF with CaF_2 at 800 °C for 12 hours in arc-welded Ni-alloy ampoules. The X-ray diffraction patterns obtained for each respective synthesized phase are depicted in

Figure 3.1. The cell parameters and hydride to fluoride ratios for mixed phases were determined by Rietveld refinement. An exemplary Rietveld refinement plot of the mixed phase RbCaHF_2 is depicted in the appendix in **Figure 11.1**.

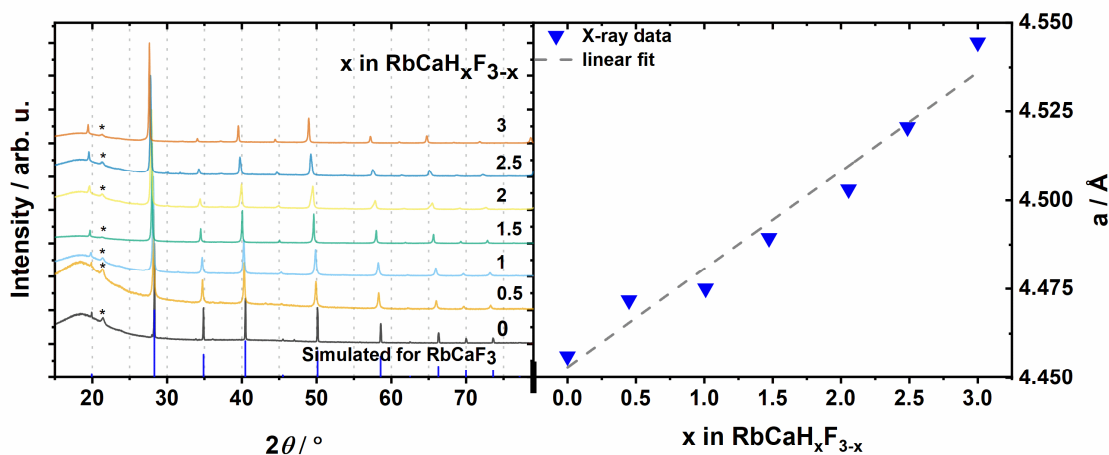


Figure 3.1. X-ray diffraction patterns of $\text{RbCaH}_x\text{F}_{3-x}$ and the refined cell parameters a plotted in dependency of the hydride content x in the mixed phase. Background reflections caused by the grease to fixate the samples within the capton foils are marked with an asterisk.

As shown in **Figure 3.1**, the solid-solution series evidently follows Vegard's law and the following equations regarding the cell parameter a and the volume V in respect to the hydride content x can be derived:

$$a = 0.028(3)x \text{ \AA} + 4.453(5) \text{ \AA} \quad (3.1)$$

$$V = 1.7(1)x \text{ \AA}^3 + 88.2(2) \text{ \AA}^3 \quad (3.2)$$

A distortion of the crystal lattice and a lowered symmetry by e.g. local ordering of the distinct anion species can be excluded by Raman spectroscopy. Here, no signals were detectable that hinted to a lowering of the Raman-inactive octahedral symmetry (O_h^1) of the cubic perovskite structure. Thus, it can be assumed that the ideal cubic perovskite structure is preserved for the complete solid-solution series.

Doping RbCaF_3 with Eu^{2+} by the addition of 1 mol% EuF_2 , weak blue luminescence was detected as reported by Sommerdijk and Bril.^[192] However, for the mixed phases $\text{RbCaH}_x\text{F}_{3-x}:\text{Eu}^{2+}$ with $x > 0$ no luminescence could be detected, even for very low amounts of hydride and also not at liquid nitrogen temperatures. Further attempts varying the dopant concentrations did not enhance the luminescent properties. Different dopant methods, for instance using EuH_2 as dopant or predoped $\text{CaH}_2:\text{Eu}^{2+}$ (prepared by hydrogenation of a $\text{Ca}_{0.99}\text{Eu}_{0.01}$ alloy), also did not result in detectable luminescence for hydridic phases. By the introduction of hydrides in RbCaF_3 , the band gap might be reduced and the $4f^65d^1$ state is then be situated in the conduction band. Respective $4f^7$ to $4f^65d^1$ excitations are then unfavourable.

The solid-solution series of $\text{CsCaH}_x\text{F}_{3-x}$

CsCaF_3 and CsCaH_3 , equally to the rubidium analogues, crystallize in the ideal cubic perovskite structure and again, a mixed hydride fluoride solid-solution series is likely.^[194,195] This has already been shown by Park *et al.* in 1988 where they synthesized mixed phases in the system $\text{CsCaH}_x\text{F}_{3-x}$ and determined an upper limited of $x \approx 1.7$ for this system.^[52] However, as they only utilized CsF and $\text{CaH}_2/\text{CaF}_2$ for their syntheses, the phase limit was already set to $x = 2$ by the stoichiometry of the reactants. Herein, this system was reinvestigated and the previous limit could be removed by using elemental cesium and in-situ formed cesium hydride as the required, beforehand missing last hydride source. The complete solid-solution series $\text{CsCaH}_x\text{F}_{3-x}$ was synthesized analogously to the solid solution series of $\text{RbCaH}_x\text{F}_{3-x}$. Cesium metal was mixed together with appropriate stoichiometric amounts of $\text{CaH}_2/\text{CaF}_2$ and CsF in an agate mortar. The reaction was then carried out in an autoclave under 50 bar hydrogen pressure and a reaction temperature of 390 °C (550 °C OT*) for approx. 2 days. For compounds with $x \geq 2$, a higher reaction temperature of 426 °C (600 °C OT*) was required to ensure phase pure samples. The pure fluoride CsCaF_3 was synthesized by solid-state reaction of CsF and CaF_2 in arc-welded Ni-alloy ampoules at 800 °C for 12 hours.

The obtained X-ray diffraction data and by Rietveld refinement determined cell parameters as well as hydride-to-fluoride ratios are depicted in **Figure 3.2**. The solid solution follows a linear trend in dependency of x and thus follows Vegard's law.

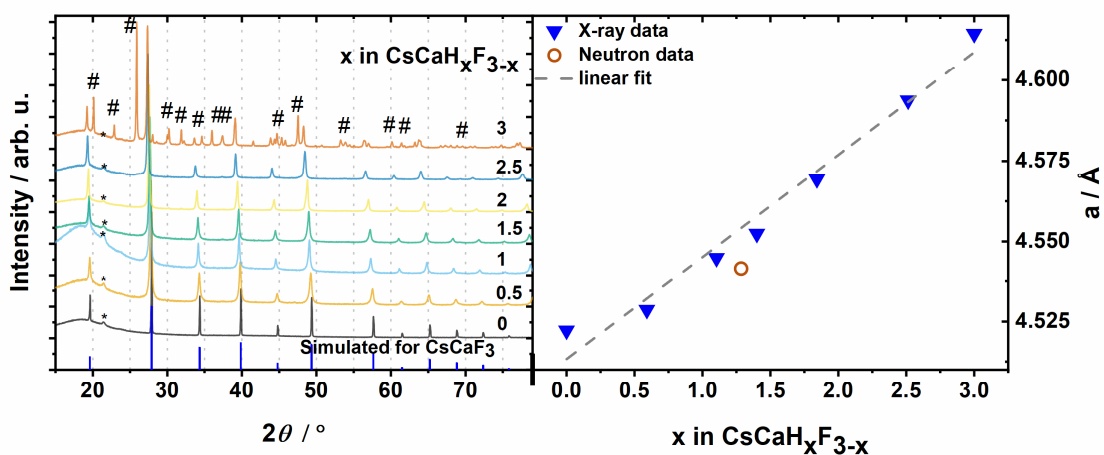


Figure 3.2. X-ray diffraction patterns of $\text{CsCaH}_x\text{F}_{3-x}$ and the refined cell parameters a plotted in dependency of the hydride content x in the mixed phase. Background reflections caused by the grease to fixate the samples within the capton foils are marked with an asterisk, reflections originating from Cs_2CaH_4 are marked with a rhombus.

Following equations can be derived regarding the cell parameter a and the Volume V in dependency of the hydride content x :

$$a = 0.032(2)x \text{ \AA} + 4.513(4) \text{ \AA} \quad (3.3)$$

$$V = 2.0(2)x \text{ \AA}^3 + 91.0(3) \text{ \AA}^3 \quad (3.4)$$

Pezat *et al.* suspected a distortion of the F/H octahedra surrounding the calcium and even suggested a lowered crystal symmetry which they explained by ^{19}F NMR spectroscopy.^[196] However, Rietveld refinement of neutron diffraction data of the mixed phase $\text{CsCaD}_{1.5}\text{F}_{1.5}$, obtained at the SPODI at the FRMII, shows that the ideal perovskite structure is preserved with disordered anions. Also, Raman spectroscopy does not show signals corresponding to a distortion of the ideal octahedral symmetry. It is therefore apparent that the ideal perovskite structure is preserved throughout the complete solid solution. The refinement plot of $\text{CsCaD}_{1.5}\text{F}_{1.5}$ based on neutron diffraction data is depicted in **Figure 3.3** and the corresponding crystallographic data is listed in **Table 3.1**.

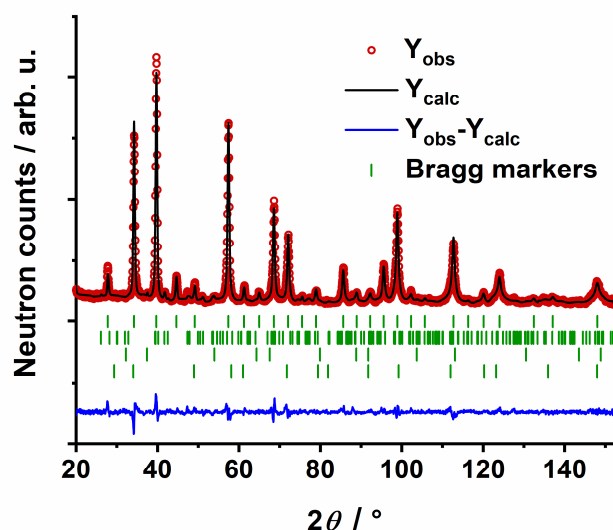


Figure 3.3. Rietveld refinement plot of $\text{CsCaD}_{1.5}\text{F}_{1.5}$ based on co-refinement of neutron and X-ray diffraction data. Bragg markers from top to bottom: $\text{CsCaD}_{1.5}\text{F}_{1.5}$ (97.04(7) wt%), CaD_2 , (2.15(9) wt%), CaO (0.43(20) wt%), CaF_2 (0.39(22) wt%). $R_p = 5.10\%$, $R_{wp} = 6.53\%$, $R_{\text{Bragg}} = 3.15\%$, $\chi^2 = 4.97$.

Table 3.1. Crystallographic data of $\text{CsCaD}_{1.28}\text{F}_{1.72}$ obtained by joint Rietveld refinement of neutron and X-ray diffraction data.

Cell parameter						
$a = 4.5416(3) \text{ \AA}$, $V = 93.68(1) \text{ \AA}^3$						
$Pm\bar{3}m$ (221)						
Atom	Wyckoff position	x	y	z	$U_{iso} (\text{Å}^2)$	S.o.f.
Cs	1a	0	0	0	0.0184(5)	1
Ca	1b	$\frac{1}{2}$	$\frac{1}{2}$	$\frac{1}{2}$	0.0110(8)	1
F	3c	0	$\frac{1}{2}$	$\frac{1}{2}$	0.0111(4)	0.57(1)
D	3c	0	$\frac{1}{2}$	$\frac{1}{2}$	0.0111(4)	0.43(1)

A phase pure synthesis of CsCaH_3 was not possible by the available means. A mixture of Cs_2CaH_4 and a maximum of ca. 30 wt.% CsCaH_3 could only be obtained by adding 100%

excess of CaH_2 . This reflects previous synthesis attempts which initially mistook Cs_2CaH_4 for CsCaH_3 .^[197,198] Gingsl *et al.* eventually synthesized CsCaH_3 , still with Cs_2CaH_4 as impurity, only with applied hydrogen pressures of 200 bar.^[194] The Rietveld refinement plot of the product mixture obtained by the attempted synthesis of CsCaH_3 is depicted in the appendix in **Figure 11.2**.

The europium doped samples $\text{CsCaF}_{3-x}\text{H}_x\text{:Eu}^{2+}$ show bright luminescence upon irradiation with UV light. With increasing hydride content x in the solid solution, the emission colour is gradually redshifted, ranging from cyan-green ($\text{CsCaF}_3\text{:Eu}^{2+}$) to red ($\text{CsCaH}_{2.5}\text{F}_{0.5}\text{:Eu}^{2+}$), clearly noticeable with the bare eye. A picture of the encapsulated samples under daylight and the same samples under UV-light excitation is shown in **Figure 3.4**.

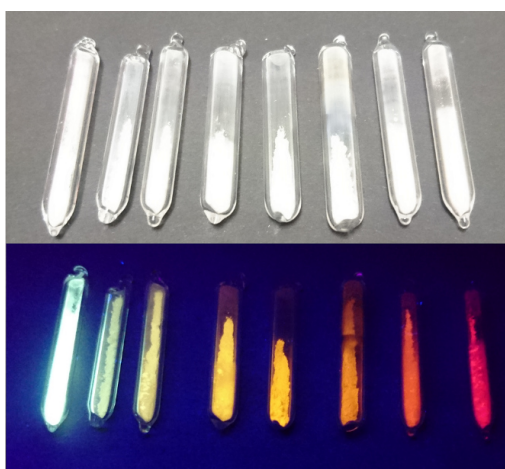


Figure 3.4. Pictures of encapsulated samples of $\text{CsCaH}_x\text{F}_{3-x}\text{:Eu}^{2+}$ ($x \leq 2.5$). Top shows the ampoules under daylight and the bottom picture the corresponding luminescence upon 376 nm UV irradiation. From left to right: $x = 0, 0.25, 0.5, 0.75, 1.0, 1.5, 2.0,$ and 2.5 .

The visible redshift is due to new emission bands emerging with increasing hydride content and their intensity ratio towards each other as clearly recognizable in the PL spectrum depicted in **Figure 3.5**.

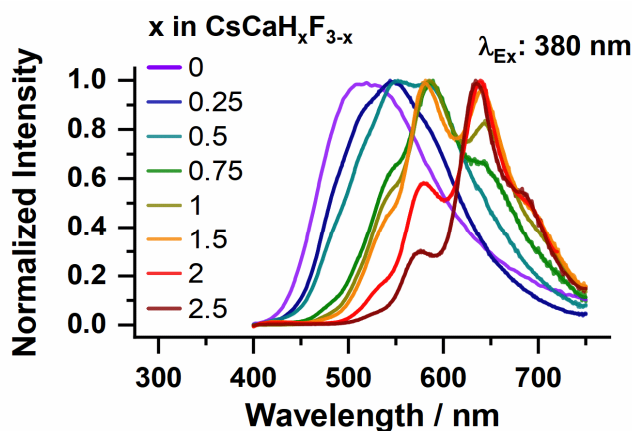


Figure 3.5. PL spectra of $\text{CsCaH}_x\text{F}_{3-x}\text{:Eu}^{2+}$ at an excitation wavelength of 380 nm.

This is in strong contrast to previous studies on europium doped mixed halide hydrides where a redshift of the luminescence was caused by the gradual redshift of a single emission band.^[46,47,54] The new emerging emission bands can be tentatively assigned to distinct emissive Eu^{2+} centres and their respective first coordination sphere, ranging from distinct EuF_6 to EuH_6 octahedra, with all possible intermediates in between. With increasing hydride coordinated to the Eu^{2+} centre, the particular emission band appears at lower energy sites caused by the nephelauxetic effect introduced by the hydride ions. In addition, the new emerging emission bands, show narrow bands with e.g. 35 nm FWHM for the 635 nm emission site. This can be attributed to the confined space for the europium ions at the slightly too small calcium site. That the emission bands originate from distinct luminescent centres can be determined by lifetime measurement of the excited states, where the monitored emission bands show individual lifetimes of the excited states (**Figure 3.6**).

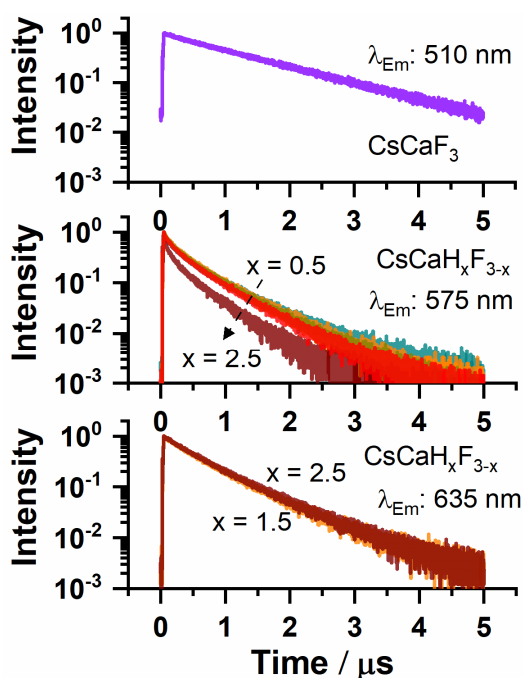


Figure 3.6. Decay curves of $\text{CsCaH}_x\text{F}_{3-x}:\text{Eu}^{2+}$ monitored at several emission maxima wavelengths with excitation wavelength of 375 nm. Whereas $\text{CsCaF}_3:\text{Eu}^{2+}$ shows a monoexponential behaviour, the decay curves of monitored emission bands of the mixed phases deviate from a monoexponential behaviour.

Also noteworthy, with increasing hydride content, the lifetimes of the excited states corresponding to a monitored high energy emission band (575 nm emission band) continually decrease. This and the non-exponential behaviour of the decay curves indicate energy transfer from the high to low energy emission sites. The intensity ratios therefore generally deviate from a Gaussian distribution, since high energy sites are partly quenched and feed red emitting sites.

Investigations on the ideal dopant concentration revealed a further interesting effect. With higher dopant (Eu^{2+}) concentrations, the luminescence glow is noticeable further redshifted. This is shown by PL spectra in **Figure 3.7**. Here, the phase with the stoichiometry $\text{CsCaH}_2\text{F}:\text{Eu}^{2+}$ with several different dopant concentrations was examined. PL spectra of samples with higher dopant concentrations show a quenching of high energy emission bands

whereas emission bands at the lower energy site appear with higher intensity.

As discussed above, energy transfer between luminescent centres of high energy emission sites to low energy emission sites occurs. Thus, with more fluoride-rich sites populated, more efficient energy transfer to the hydride rich sites is feasible. This can be also monitored by measuring the PL decay curves of the respective emission bands. With higher dopant concentrations, the PL of the high energy emission sites (fluoride-rich sites) is quenched as energy transfer, faster in time, to the hydride rich sites occurs.

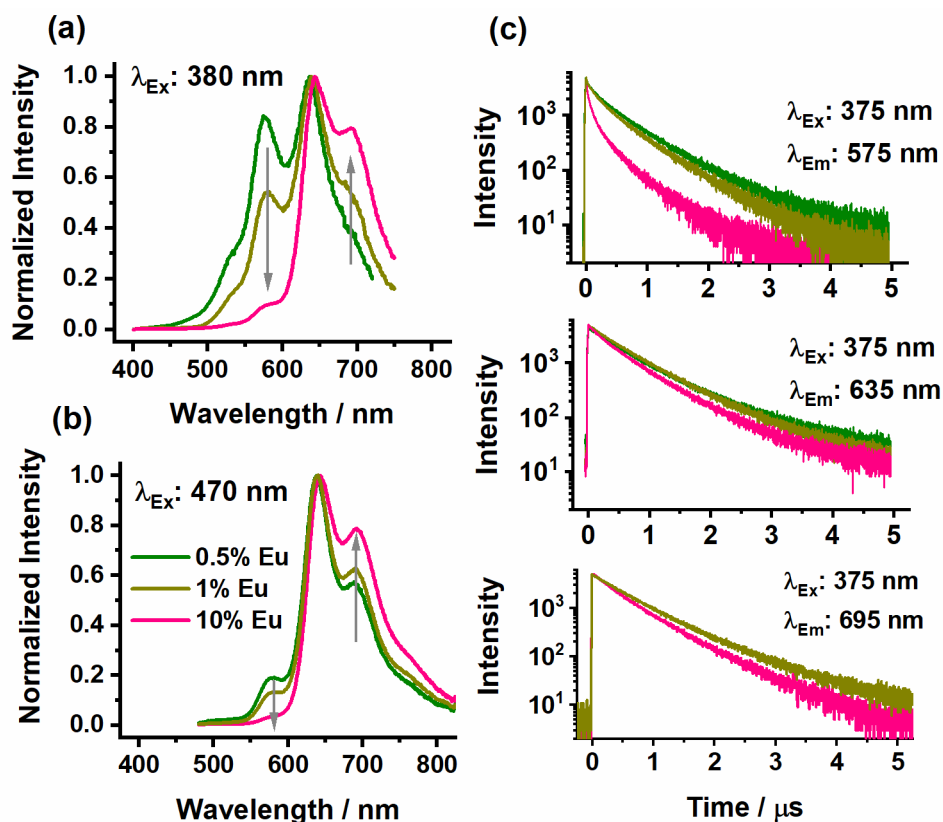


Figure 3.7. a) and b): PL spectra of CsCaH₂F:Eu²⁺ with several different dopant concentrations (0.5 mol%, 1 mol% and 10 mol% in respect to Ca²⁺). Arrows mark the intensity change of the emission bands with increasing dopant concentrations. c) monitored decay curves of different emission bands of the samples with varying dopant concentrations. The colour codes are kept the same as depicted for the PL spectra.

Lastly, different dopant methods, *i.e.* different ways to introduce divalent europium ions in the host material, were tested. Two methods were applied: either adding EuF₂ during the preparation of the reactive mixture or using already doped CaH₂:Eu²⁺ (prepared by hydrogenation of a Ca_{0.99}Eu_{0.01} alloy) as a reactant. Here, a further effect can be observed. Samples prepared with predoped CaH₂:Eu²⁺ show a further redshifted emission compared to samples with the same compositions prepared by adding EuF₂ during the synthesis. By adding CaH₂:Eu²⁺, the europium ions are already in a hydrogen rich environment and therefore are also more likely to be situated at the hydride rich sites in the final host material. This is shown in **Figure 3.8** where it is clearly noticeable that the high energy emission site at 575 nm is completely quenched in the CsCaH₂F:Eu²⁺ samples prepared with CaH₂:Eu²⁺.

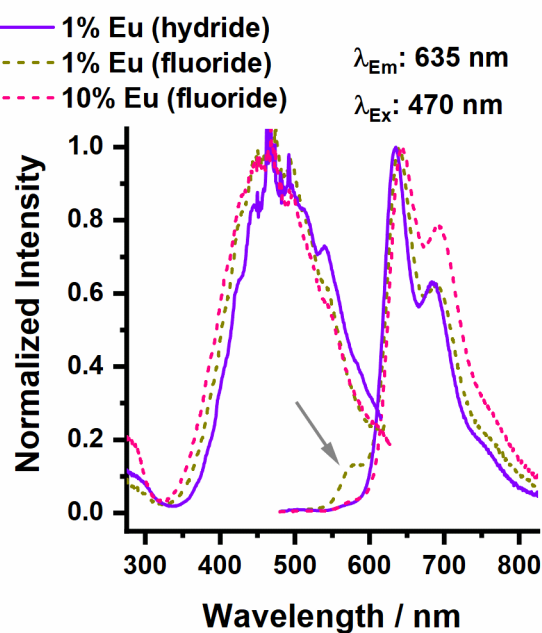


Figure 3.8. PL and PLE spectra of $\text{CsCaH}_2\text{F}:\text{Eu}^{2+}$ prepared by both dopant methods in comparison to the PL and PLE spectrum of $\text{CsCaH}_2\text{F}:\text{Eu}^{2+}$ doped with 10 mol% Eu^{2+} . The arrow marks the vanishing emission band.

Unfortunately, $\text{CsCaH}_3:\text{Eu}^{2+}$ did not exhibit luminescent properties. The impurity phases obtained in the product mixture (Cs_2CaH_4 and CaH_2) likely disturb PL measurements. It is also likely that the low energy emission sites are purely feed through energy transfer from high energy emission sites. These sites are completely missing in the pure hydride CsCaH_3 and therefore even pure samples of $\text{CsCaH}_3:\text{Eu}^{2+}$ do not exhibit luminescent properties.

In summary, $\text{CsCaH}_x\text{F}_{3-x}$ is proven to be an ideal host system for spectral tuning. Three different ways to selectively tune the emission colours are possible. Either by varying the hydride content, varying the dopant concentration or using different Eu^{2+} precursors. In contrast to the previous luminescent heteroanionic hydride fluorides, the spectral tuning herein is possible due to adjusting the intensity ratios of new emerging emission bands instead of the shift of a single emission band.

Motivated by these findings, attempts were made finding further, different heteroanionic hydrides with yet unreported compositions. Beyond the hydride fluorides, other heteroanionic hydrides, such as silicate hydrides and borate hydrides have been demonstrated to be suited as host materials for rare earth activated luminescence.^[45,48,49,199] Aside from investigating possible new heteroanionic hydrides as host materials for lanthanide activated luminescence, such heteroanionic compounds may have further advantageous and unforeseen properties yet to be explored. The biggest challenge herein is to establish suitable synthesis routes to realize new materials of this kind.

This will be discussed in the subsequent chapter.

4 New heteroanionic hydrides with complex oxoanions

4.1 Na₃SO₄H – the first sulfate hydride

See chapter 7.2 *Na₃SO₄H – The First Representative of the Material class of Sulfate Hydrides*, A. Mutschke, G. M. Bernard, M. Bertmer, A. J. Karttunen, C. Ritter, V. K. Michaelis, N. Kunkel*, *Angew. Chem. Int. Ed.* **2021**, 60, 5683-5687

In chapter 1.2.2 heteroanionic hydrides were introduced that contain complex anions next to hydrides. This particular composition type of heteroanionic hydrides is by far the least investigated among the variety of heteroanionic hydrides found to date. Overall, the amount of such structures is scarce and more importantly, many simple hydride-to-anion combinations are still unexplored. Specifically, simple complex anions as e.g. carbonates, nitrates and also sulfates are reported in combination with hydrides. Among these, sulfates might provide a promising anion partner for hydrides. Heteroanionic sulfates share some valuable materials properties such as ion conduction,^[200,201] luminescent properties^[151,202,203] but also non-linear optics.^[204] Consequently, combinations of sulfates with hydrides might in turn provide a fruitful approach for materials design.

Following a typical autoclave synthesis as described in the experimental section, Na₃SO₄H can be synthesized by the solid-state reaction of dry Na₂SO₄ with 10% excess NaH or NaD for neutron diffraction. Thereto, NaH/NaD and Na₂SO₄ are thoroughly ground in an agate mortar and furthermore shortly homogenized in a planetary ball mill. The reaction mixture is then heated in an autoclave under 10 bar hydrogen pressure with a reaction temperature of 328 °C (462 °C OT*) for 2 days. Na₃SO₄H is obtained as a crystalline, colourless, air and moisture sensitive powder. The exact reaction temperature is of particular importance for this synthesis. Overall, only a small temperature window of approx. 10 °C was found to be feasible in order to achieve crystalline phase pure samples. A too low reaction temperature (5 °C and more below 328°C) drastically prolongs the reaction time and large amounts of reactants are yet visible in the product mixture. Especially large quantities of Na₂SO₄ in the metastable orthorhombic polymorph (phase III, *Cmcm*)^[205,206] are visible. In turn, if the reaction temperature was set too high (5°C and more above 328 °C), the hydride ions are activated and start to reduce the sulfate anions, impeding the synthesis of a sulfate hydride. In this case, Na₂S is observed as a main side phase along with heavily strained reflections of decomposing Na₃SO₄H along further

unassignable and unindexable impurity phases. p-XRD measurements of the respective synthesis products are shown in **Figure 4.1**.

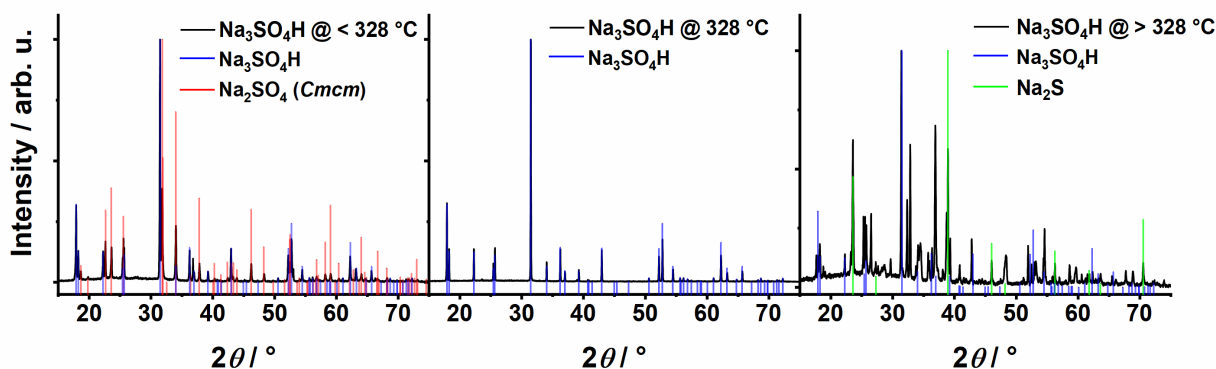


Figure 4.1. p-XRD patterns of the synthesis products with the respective set autoclave temperatures. The vertical bars represent simulated Bragg reflections: blue $\text{Na}_3\text{SO}_4\text{H}$, red Na_2SO_4 (*Cmcm*) and green Na_2S .

The structure of $\text{Na}_3\text{SO}_4\text{H}$ was solved ab-initio from powder X-ray diffraction patterns and complemented by neutron diffraction of the deuterated analogue. The respective Rietveld refinement plot is shown in **Figure 4.3**. $\text{Na}_3\text{SO}_4\text{H}$ crystallizes in the tetragonal space group $P4/nmm$ (129, O2) with the cell parameters $a = 7.00530(5)$ Å, $c = 4.85822(4)$ and adopts the $\text{Ag}_3\text{CrO}_4\text{Cl}$ structure type.^[143] Full crystallographic data can be found in **Table 4.1**. This structure can be described as an antiperovskite-like build-up. HNa_6 octahedra form a three-dimensional network *via* shared corners in which the sulfate tetrahedra occupy the cuboctahedra voids as illustrated in **Figure 4.2**.

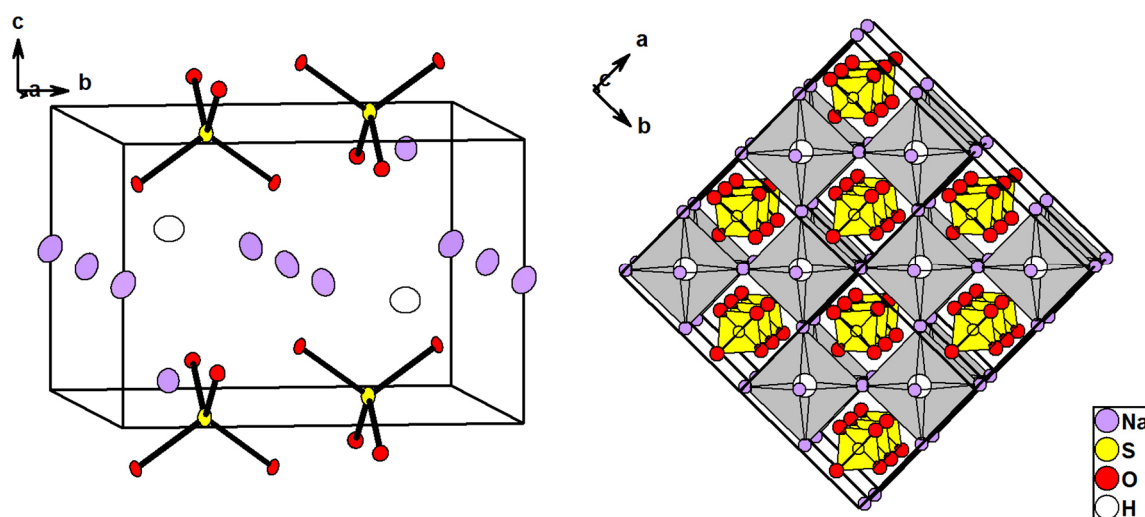


Figure 4.2 Crystal structure of $\text{Na}_3\text{SO}_4\text{H}$. Simplistic unit cell with ellipsoids (90% probability) left and depiction with Na_6H octahedra as an antiperovskite-like structure right. Sulfate tetrahedra are depicted yellow.

Unexpectedly, considering the hydride fluoride analogy, this compound crystallizes differently than the corresponding fluoride $\text{Na}_3\text{SO}_4\text{F}$ that crystallizes in a monoclinic structure resembling

a 9R stacking antiperovskite-like variant.^[144] Instead, Na₃SO₄H crystallizes isostructural to the predicted structure of the yet unreported chloride analogue Na₃SO₄Cl.^[207] This underlines the polarizability of the hydride ion which presumably acquires a larger ionic radius comparable with the chloride anion herein. The crystallographic data determined by Rietveld refinement of neutron diffraction data of the deuteride analogue Na₃SO₄D data can be found in **Table 4.1**.

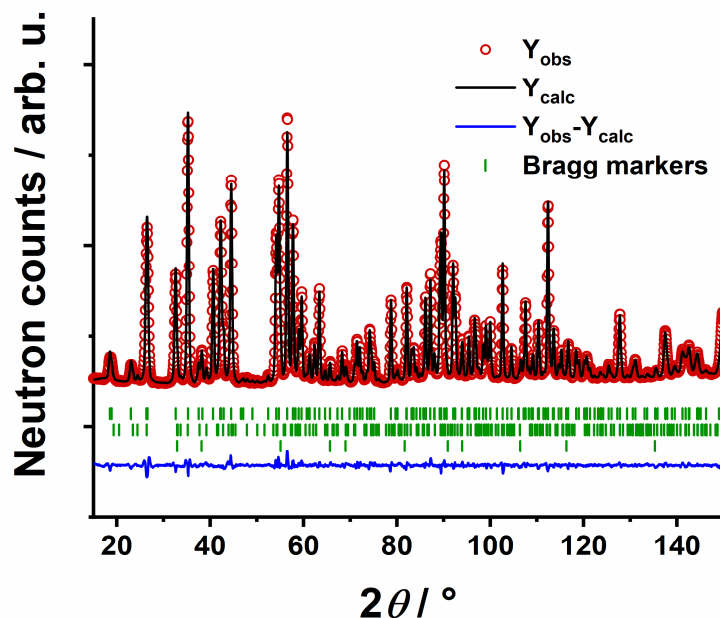


Figure 4.3. Rietveld refinement of Na₃SO₄D. Diffraction data acquired at the D2B at the ILL. Bragg markers from top to bottom Na₃SO₄D (92.2(9) wt.%), Na₂SO₄ (*Cmcm*) (6.3(7) wt.%), NaD (1.5(2) wt.%). $R_p = 1.70\%$ $R_{wp} = 3.63\%$ $R_{exp} = 3.63\%$ $\chi^2 = 1.00$.

The Rietveld refinement parameters corresponding to this refinement are listed in **Table 11.1** in the appendix.

Na₃SO₄D was synthesized by the use of NaD instead of NaH. This has been synthesized beforehand from an isotopic exchange reaction starting from NaH. Residual amounts of hydride ions in within the as-synthesized NaD were expected and thus, the refinement of Na₃SO₄D was carried out with split occupations of the deuteride sites.

Table 4.1 Crystallographic data of Na₃SO₄D obtained by Rietveld refinement of neutron diffraction data.

Cell parameters						
a = 7.0034(2) Å c = 4.8570(2) Å, V = 238.227(13) Å ³						
P4/nmm (129, O2)						
Atom	Wyckoff position	Site	x/a	y/b	z/c	S.o.f.
D1	2c	4mm	1/4	1/4	0.5991(4)	0.950(4)
H1	2c	4mm	1/4	1/4	0.5991(4)	0.050(4)
Na1	4e	2/m	0	0	1/2	1
Na2	2c	4mm	1/4	1/4	0.0621(7)	1
S1	2a	-4m2	3/4	1/4	0	1
O1	8i	m	1/4	0.92123(13)	0.1766(2)	1

Table 4.1 continued.

Anisotropic displacement parameters in \AA^2						
Atom	U_{11}	U_{22}	U_{33}	U_{12}	U_{13}	U_{23}
D1	0.0281(8)	0.0281(8)	0.0201(14)	0.00000	0.00000	0.00000
H1	0.0281(8)	0.0281(8)	0.0201(14)	0.00000	0.00000	0.00000
Na1	0.0172(8)	0.0172(8)	0.0231(14)	0.0031(12)	0.0046(7)	0.0046(7)
Na2	0.0145(11)	0.0145(11)	0.0175(16)	0.00000	0.00000	0.00000
S1	0.0058(10)	0.0058(10)	0.0102(18)	0.00000	0.00000	0.00000
O1	0.0175(5)	0.0089(5)	0.0177(5)	0.00000	0.00000	-0.0041(5)

In general, the exact atomic positions of hydrogen atoms in crystalline compounds are determinable by neutron diffraction of the deuterium analogues. However, a lot of isotopes of different elements share similar bound coherent scattering lengths close to the ^2H isotope and thus, neutron diffraction rather locates a certain isotope but does not reliably differentiate between isotopes.^[208] To unambiguously prove that indeed hydride ions are incorporated in this structure and that also sulfate anions are additionally present, vibrational spectroscopy was applied. Vibrational spectroscopy is not only suited to prove the abundance of complex tetrahedral ions such as the sulfate anions but in combination with DFT calculations can also be a powerful tool to prove the hydride abundance. The experimental FT-IR and Raman spectra with corresponding simulated spectra at the DFT-PBE0 level of theory are depicted in **Figure 4.4**.

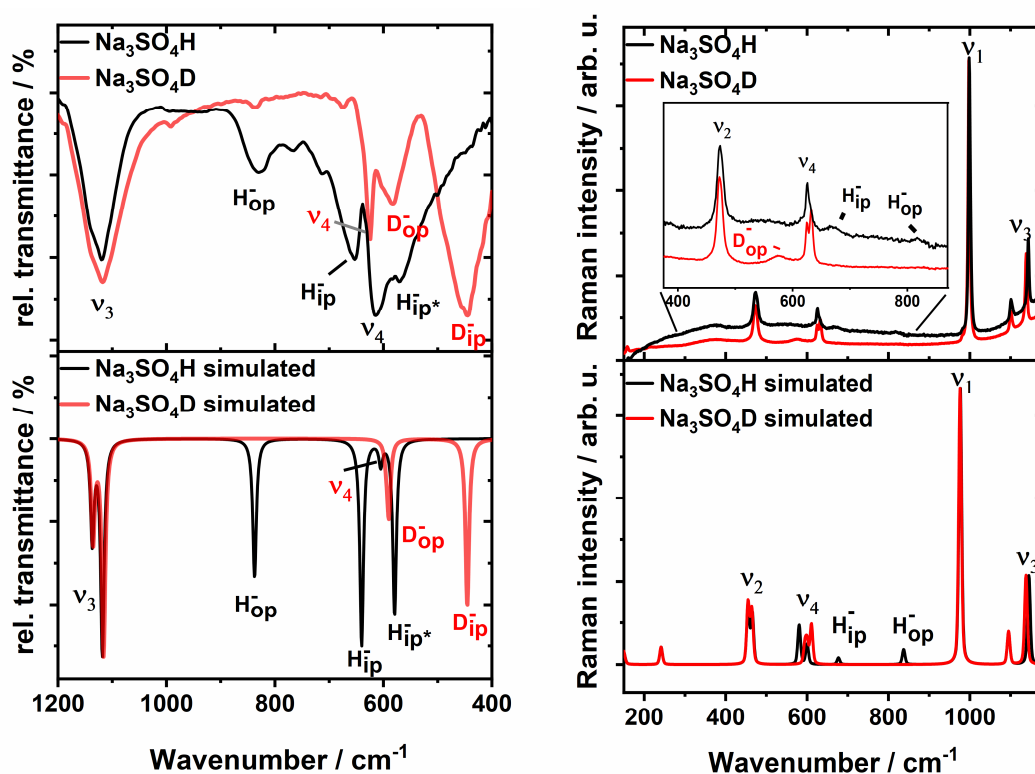


Figure 4.4. Left: FT-IR spectra of $\text{Na}_3\text{SO}_4\text{H}$ and $\text{Na}_3\text{SO}_4\text{D}$ with simulated spectra (DFT-PBE0 level of theory) below. Right: Raman spectra of $\text{Na}_3\text{SO}_4\text{H}$ and $\text{Na}_3\text{SO}_4\text{D}$ with the corresponding simulated spectra (DFT-PBE0 level of theory) below.

FT-IR spectroscopy on $\text{Na}_3\text{SO}_4\text{H}$ shows the for sulfate ions expected asymmetric bending modes but also pronounced bands that originate from certain vibrational modes of the hydride ions. The experimental spectrum is in good agreement with the simulated spectrum obtained by DFT calculations at the DFT-PBE0 level of theory. FT-IR spectroscopy on the deuteride $\text{Na}_3\text{SO}_4\text{D}$ is also in good agreement with the simulated spectrum. Additionally, hydride vibrational modes are now shifted by a factor of $\sqrt{2}$ to lower wave numbers originating from the now doubled mass of the deuteride ion. This can be explicitly seen for the hydride-out-of-plane (H_{op}^-) and the hydride-in-plane (H_{ip}^-) modes appearing at 840 cm^{-1} and 640 cm^{-1} respectively. These modes appear for the corresponding deuteride modes D_{op}^- and D_{ip}^- at 590 cm^{-1} and 450 cm^{-1} respectively.

The Raman spectra of $\text{Na}_3\text{SO}_4\text{H}$ and $\text{Na}_3\text{SO}_4\text{D}$ are also in good agreement with the simulated spectra. The bending and stretching vibrations $\nu_1 - \nu_4$ of the sulfate anions are readily visible as predicted. The hydride bands are simulated to be of weak intensity which is also reflected in the experimental spectrum. Similar as for the FT-IR spectra, an isotopic shift between the hydride and deuteride modes is noticeable, altogether supplement the FT-IR spectroscopy and proving the hydride abundancy.

To also complement the wide range structure determined by the diffraction techniques, the structure at a local level was determined by magic angle spinning NMR spectroscopy on the ^1H and ^{23}Na nuclei. The respective NMR spectra are shown in **Figure 4.5**.

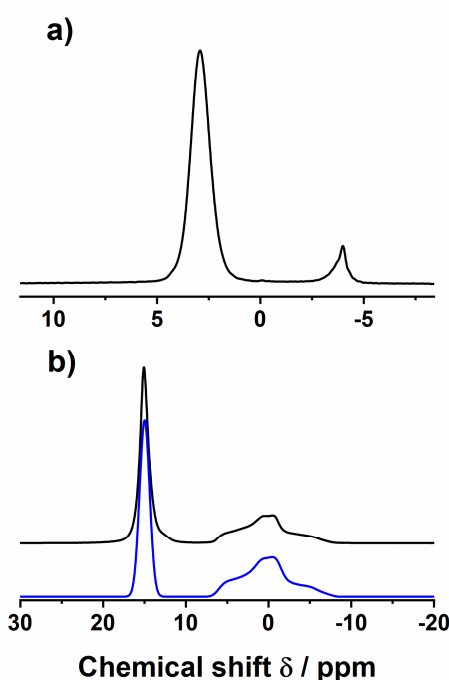


Figure 4.5. a) Room temperature ^1H MAS NMR spectrum of $\text{Na}_3\text{SO}_4\text{H}$, acquired with a spinning frequency of 10.0 kHz, $B_0 = 9.4\text{ T}$, b) ^{23}Na NMR spectrum of $\text{Na}_3\text{SO}_4\text{H}$, the deconvolution is traced in blue below the experimental spectrum.

A single sharp peak at $\delta_{\text{iso}} = 2.9$ is obtained for the ^1H NMR measurement corresponding to the single crystallographic position for the hydride ion. A further asymmetric signal can be seen in the ^1H NMR spectrum which can be traced back to impurities from the starting materials and/or amorphous side phases not visible in the diffraction patterns. Calculations at the DFT-PBE/USPP level of theory predict a value of $\delta_{\text{iso}} = 4.3$ ppm for the chemical shift of the hydride. This does not perfectly match the experimental value but lies within the same range. Furthermore, the chemical shift found is within the range typically found for hydride ions, in summary proving the presence of hydride anions within the structure^[45,48,124]. ^{23}Na NMR spectroscopy shows two peaks, a sharp signal at $\delta = 15$ ppm and an asymmetric signal at $\delta = 6.2$ ppm. This is in good agreement with the two distinct sodium positions. The symmetric peak corresponds to the Na2 position with the higher symmetric environment, whereas the asymmetric peak corresponds to the Na1 position with a lower symmetric environment and quadrupolar interactions. DFT-PBE/USPP calculations on the chemical shift predicts $\delta_{\text{iso}} = -2.5$ for the for Na1 position and $\delta_{\text{iso}} = 7.7$ ppm for the for Na2 position. Whereas the predicted chemical shift slightly deviates from the experimental values, the difference between the shifts is accurately predicted with 9.9 ppm in comparison with the experimental value of 8.8 ppm.

Electronic band structure calculations (**Figure 4.6**) reveal an insulating character of $\text{Na}_3\text{SO}_4\text{H}$ with an indirect band gap of ca. 7.4 eV and is in line with the colourless appearance of the polycrystalline samples.

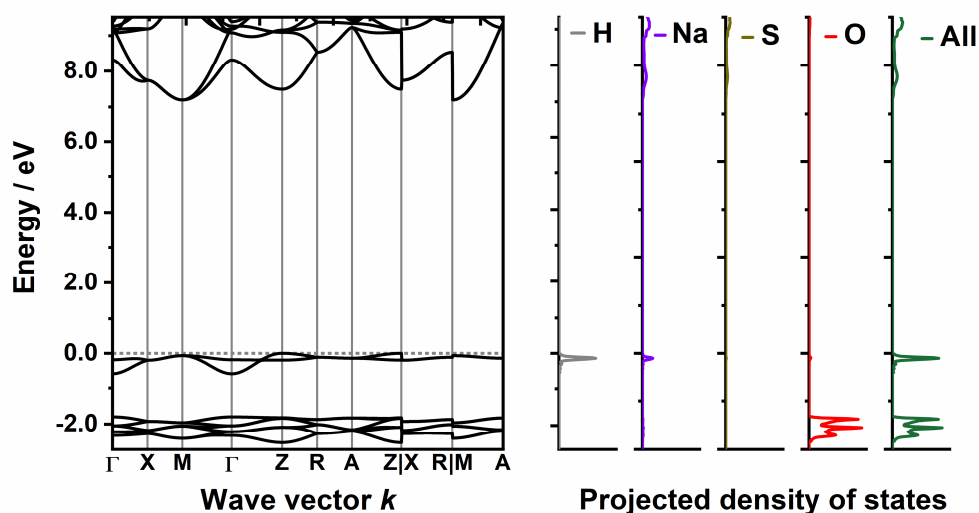


Figure 4.6. Electronic band structure of $\text{Na}_3\text{SO}_4\text{H}$ and projected density of states at the DFT-PBE0 level of theory.

Hydride states are located at the topmost of the valence band with only small contributions of the other atoms. This is a reoccurring observation for heteroanionic hydrides where hydride states are always projected to be located at the topmost valence band, as e.g. for $\text{Sr}_5(\text{BO}_3)_3\text{H}$ or $\text{LiSr}_2\text{SiO}_4\text{H}$. This can be traced back to the high polarizable character of the hydride anion.^[45,48]

Doping $\text{Na}_3\text{SO}_4\text{H}$ with Eu^{2+} ions did not result in noteworthy luminescence. Due to a missing divalent site for the Eu^{2+} ions, an incorporation thereof in this particular host lattice is unlikely. Also, the Na^+ -sites, as the only available cation sites might be too narrow, as Eu^{2+} is ca. 0.15 Å larger than Na^+ ions in equal coordination spheres.^[30] Testing further activator ions with smaller ionic radii, e.g. Ce^{3+} or Pr^{3+} also did not result in detectable luminescence. Future studies may synthesize divalent or trivalent sulfate hydrides based in these findings and test lanthanide activated luminescence in these host materials.

4.2 Hydrides in combination with transition oxometalate anions

See chapter 7.3 *Expanding the hydride chemistry: antiperovskites A_3MO_4H ($A = Rb, Cs$; $M = Mo, W$) introducing the transition oxometalate hydrides*, A. Mutschke*, A. Schulz, M. Bertmer, C. Ritter, A. J. Karttunen, G. Kieslich, N. Kunkel*, *Chem. Sci.* **2022**, *13*, 7773-7779

Oxide hydrides of transition metals are undoubtedly a fascinating class of materials. Many desirable materials properties were detected herein. Ionic and electronic conductivities,^[43,79,209–214] magnetic ordering at elevated temperatures^[72–76] and superconductivity^[38,215] are only few of the reported properties. However, all of these materials consist of isolated oxide and hydride ions. Likewise, as several other hydride-to-anion combinations, heteroanionic hydrides with complex transition oxometalate ions, e.g. chromates, molybdates or tungstates are among the unrealized compositions. This and the multiple reported properties of the oxide hydride based materials makes an investigation of this field intriguing. In this regard, many simple quasi ternary fluorides exist which provide conceptual compositions that, according to the hydride fluoride analogy, might also exist in its hydridic form. In 1951 Schmitz-Dumont and Weeg reported several alkaline chromate, molybdate and tungstate fluorides, providing a small library of simple compounds worth investigating in this context.^[216] In this work, the four compounds A_3MO_4H ($A = Rb, Cs$; $M = Mo, W$) could be synthesized as the corresponding hydrides. These are the first compounds to simultaneously host complex transition oxometalate and hydride anions.

4.2.1 A_3MO_4H ($A = Rb, Cs$; $M = Mo, W$) as the first transition oxometalate anions

The syntheses of the transition oxometalate hydrides follow a typical autoclave synthesis route, as described in the experimental sections. Similar to the presently discussed sulfate hydride, a thermal synthesis route with controlled conditions is necessary to prepare the samples. Moreover, only small temperature windows are found to be feasible, especially for the molybdate hydrides. For the synthesis of these, alkaline metal (rubidium or cesium) is mixed together with the quasi-binary molybdate salts. This reaction mixture is then heated under 10 bar hydrogen pressure at 255 °C (360 °C OT*) for 48 hours. In-situ formed alkaline hydride readily reacts with the oxometalate salt and the respective molybdate hydride forms. At reaction temperatures of already 260 °C and above, the usually colourless polycrystalline products are obtained as greyish-black powders, hinting at the starting reduction of the molybdate ions towards elemental molybdenum. This is confirmed by X-ray diffraction patterns of the as obtained production mixtures where reflections corresponding to molybdenum are plainly visible (**Figure 4.7**). RbH/CsH reflections are then also detectable which hints to decompositions of the molybdate hydride phases.

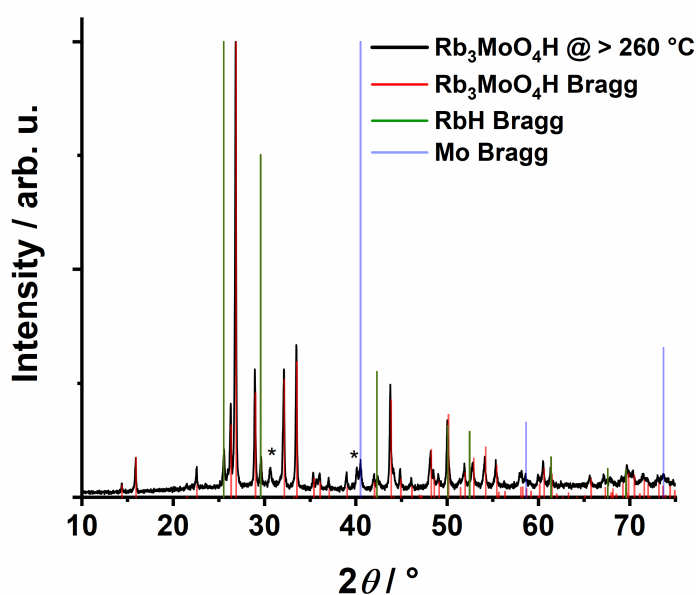


Figure 4.7. p-XRD pattern of Rb₃MoO₄H obtained after a synthesis attempt at too high reaction temperatures. The vertical bars represent simulated Bragg reflections: red Rb₃MoO₄H, blue Molybdenum and green RbH. Asterisks mark a further not assignable side phase.

Too low reaction temperatures overall yield incomplete reactions with the reactants still largely visible in the p-XRD patterns, as exemplarily shown in **Figure 4.8** for a synthesis attempt of Cs₃MoO₄H. In summary, a temperature window of approx. 15 °C was determined to deliver molybdate hydride samples of sufficient merit.

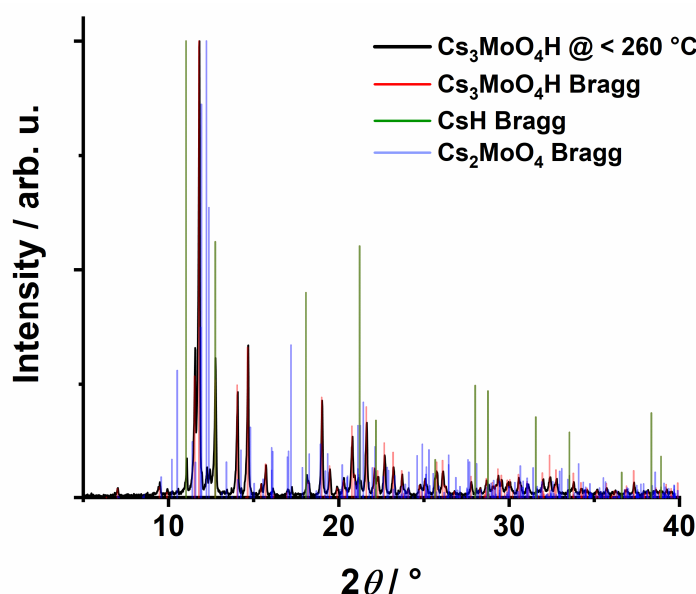


Figure 4.8. p-XRD pattern of Cs₃MoO₄H obtained after a synthesis attempt at a too low reaction temperature. The vertical bars represent simulated Bragg reflections of the indexable compounds: red Cs₃MoO₄H, blue Cs₂MoO₄, and green CsH.

The preparation of the tungstate hydrides follows the same procedure described for the molybdate hydrides. However, the samples can be synthesized at higher temperatures and within a wider temperature range of ca. 60 °C. The optimal reaction temperature herein was

found to be 327 °C (460 °C OT*). Adapting the other synthesis conditions applied for the molybdate hydrides, crystalline pure samples with no remaining reactants or decomposition products visible in X-ray diffraction patterns were obtained. Only at reaction temperatures above 345 °C, greyish, instead of otherwise colourless powders are obtained. X-ray diffraction pattern of products synthesized at these temperatures appear noisier, with larger background and unassignable impurity reflections start to emerge as shown in **Figure 4.9**.

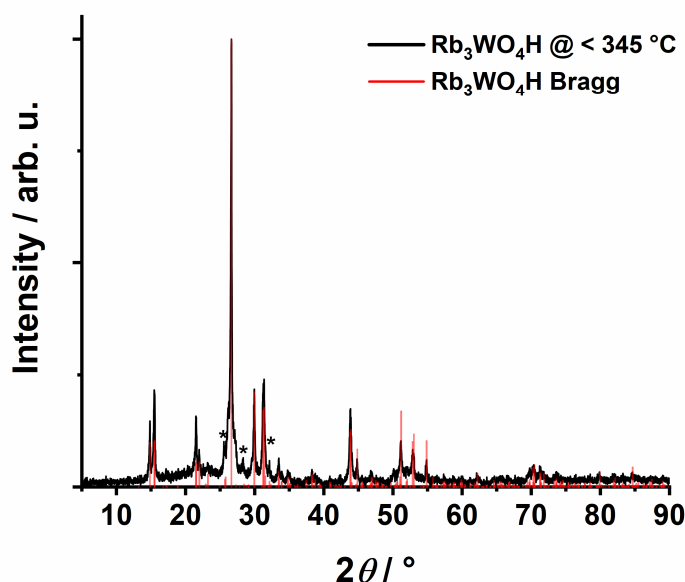


Figure 4.9. p-XRD pattern of $\text{Rb}_3\text{WO}_4\text{H}$ obtained after a synthesis attempt at a too high reaction temperature. The vertical bars represent simulated Bragg reflections of $\text{Rb}_3\text{WO}_4\text{H}$, asterisks marks unassignable impurities.

As no crystallographic data of the corresponding, likely isostructural fluorides is reported, the structures of the newly formed phases were solved ab-initio from powder diffraction data. Early structural models were obtained by X-ray diffraction data and corroborated by Rietveld refinement of neutron diffraction data of deuterated samples. All refinement plots and full crystallographic data of the new phases can be found in the appendix. The four compounds assemble in two distinct structures. $\text{Rb}_3\text{MoO}_4\text{H}$, $\text{Cs}_3\text{MoO}_4\text{H}$ and $\text{Cs}_3\text{WO}_4\text{H}$ crystallize in the tetragonal $\text{K}_3\text{SO}_4\text{F}$ -type each with the space group $I4/mcm$ (140), whereas $\text{Rb}_3\text{WO}_4\text{H}$ shows a different, orthorhombic structure with the space group $Pbca$ (61). A schematic of the tetragonal phases is depicted in **Figure 4.10**. This structure can be described as an antiperovskite-like structure, very related to the SrZrO_3 -type, a tetragonal perovskite variant. Corner sharing HA_6 ($A = \text{Rb}, \text{Cs}$) octahedra with an activated tilt along the c -axis build a three dimensional framework. The complex oxometalate anions are located in between and occupy the cuboctahedra voids. This is an often reoccurring structure type regarding compounds with the general composition A_3MX where M consists of a complex, tetrahedral anion.^[49,135,217,218]

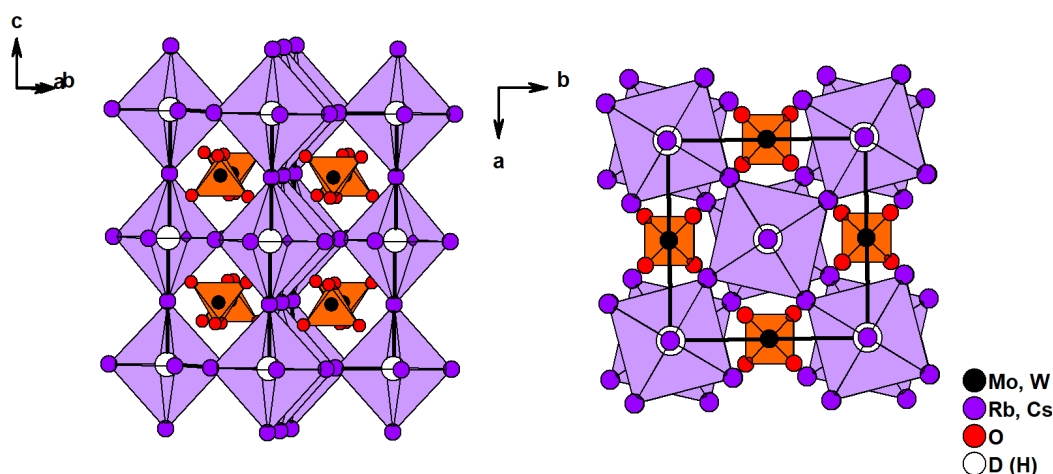


Figure 4.10. Schematic of the tetragonal phases with the K_3SO_4F structure type along the c -axis (left) and a/b -plane (right). A_6H octahedra are depicted lilac, the oxometalate tetrahedral orange.

Solely Rb_3WO_4H forms an orthorhombic structure. Again, an antiperovskite-like arrangement is observed with corner sharing HRb_6 octahedra and tungstate ions occupying cuboctahedra voids. Contrary to the tetragonal counterparts, the HRb_6 octahedra are now also distorted in addition to activated tilts. Additionally, the tungstate anions within the cuboctahedra voids are slightly tilted towards one another in all crystallographic directions. These multiple slight distortions and tilts yield a pseudo-tetragonal arrangement ($a/b = 1.0464$, $b/c = 0.9955$, $c/a = 0.9600$). In sum, a new structure type is formed and, considering the antiperovskite-like composition, an unprecedented perovskite variant can be observed that differs from all further perovskite and antiperovskite structures. A summary of the crystal structures of the four respective compounds can be found in **Table 4.2**. The crystal structure of Rb_3WO_4H is depicted in **Figure 4.11**.

Table 4.2. Overview of the crystal structures.

	Rb_3MoO_4D	Cs_3MoO_4D	Cs_3WO_4D	Rb_3WO_4D
Space group	$I4/mcm$ (140)	$I4/mcm$ (140)	$I4/mcm$ (140)	$Pbca$ (61)
Phase prototype	K_3SO_4F	K_3SO_4F	K_3SO_4F	Own structure type
Lattice parameter (Å)	$a = 7.8620(3)$ $c = 12.2998(5)$	$a = 8.2113(2)$ $c = 12.7893(4)$	$a = 8.2331(2)$ $c = 12.8289(3)$	$a = 11.9262(3)$ $b = 11.3972(5)$ $c = 11.4492(5)$
Formular units (Z)	4	4	4	8
Glazer tilt notation	$a^0a^0c^-$	$a^0a^0c^-$	$a^0a^0c^-$	not applicable ^d

^dDue to the slight distortions of the $D(H)Rb_6$ octahedra, the Glazer tilt notation is not applicable. Removing the distortions yields the same Glazer tilt notation as for the tetragonal phases.

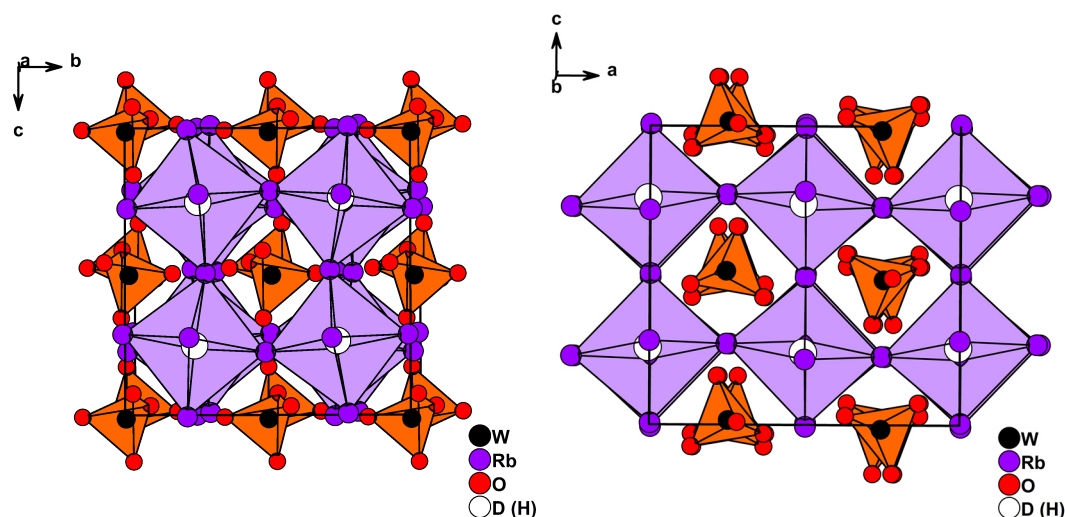


Figure 4.11. Crystal structure of $\text{Rb}_3\text{WO}_4\text{H}$ in a -direction (left) and b -direction (right). HRb_6 octahedra are depicted lilac, tungstate tetrahedra orange.

A structural comparison with the fluoride analogues, reported by Schmitz-Dumont and Weeg was not possible as no structural data is given. Only assumptions of the cell symmetries are given.^[216] Synthesis attempts of the fluorides were unsuccessful, as also no experimental methods thereto are given. Although, by comparison with their sketched reflection scheme, a similar arrangement of reflections is notable for the tetragonal crystallizing phases, whereas discrepancies between $\text{Rb}_3\text{WO}_4\text{F}$ and $\text{Rb}_3\text{WO}_4\text{H}$ are perceivable. It is noteworthy that, similar to the present case, it was determined that also in the analogous fluoride system $\text{Rb}_3\text{WO}_4\text{F}$ crystallizes distinctly to the molybdate analogue.

To understand why $\text{Rb}_3\text{WO}_4\text{H}$ shows a distinct structure and in particular differs from its molybdate analogue, the total energies at 0K and the Gibbs free energies at ambient conditions (1 atm and 298 K) of the compounds $\text{Rb}_3\text{MoO}_4\text{H}$ and $\text{Rb}_3\text{WO}_4\text{H}$ were calculated at the DFT-PBE0 level of theory. Both compositions were calculated in both structure types. The calculated energies are given in A.U. per formula units (Z) within the unit cell and are listed in **Table 4.3**. The energy difference between the obtained energy values ($\Delta E = E_{\text{orthorhombic}} - E_{\text{tetragonal}}$) were converted from Hartree to kJ/mol for easier comparison.

Table 4.3. Calculated total and Gibbs free energies of $\text{Rb}_3\text{MoO}_4\text{H}$ and $\text{Rb}_3\text{WO}_4\text{H}$ at the DFT-PBE0 level of theory in both crystallographic modifications.

$\text{Rb}_3\text{MoO}_4\text{H}$	$I4/mcm$ (140)	$Pbca$ (61)	ΔE (kJ/mol)
Total energy 0K	-442.1082 A.U.	-442.1084 A.U.	-0.5
Gibbs free energy	-442.1062 A.U.	-442.1065 A.U.	-0.7
$\text{Rb}_3\text{WO}_4\text{H}$	$I4/mcm$ (140)	$Pbca$ (61)	ΔE (kJ/mol)
Total energy 0K	-441.0154 A.U.	-441.0150 A.U.	1.0
Gibbs free energy	-441.0140 A.U.	-441.0144 A.U.	-1.1

Unexpectedly, DFT calculations suggest that $\text{Rb}_3\text{MoO}_4\text{H}$ is presumably more stable in the orthorhombic structure according to the total energies and the Gibbs free energy. Moreover, $\text{Rb}_3\text{WO}_4\text{H}$ is determined to be more stable in the tetragonal structure type according to the total

energies – the complete opposite to what is experimentally observed. Only in terms of Gibbs free energy, $\text{Rb}_3\text{WO}_4\text{H}$ is more stable in its experimentally determined orthorhombic structure. However, the energy differences for all determined values are minor and conclusively, DFT calculations do not provide a satisfactory answer to as why $\text{Rb}_3\text{WO}_4\text{H}$ crystallizes solely in an own, distinct structure type.

A simpler approach to understand the structural modifications was exerted by determining the Goldschmidt tolerance factor t . In consideration of the antiperovskite-like build up, formula (4.1) was used thereto. Ionic radii were taken from Shannon.^[30] The experimental determined bond lengths plus the ionic radius of the covalently bonded oxide is used to estimate the ionic radius of the complex metalate ion.

$$t = \frac{r_{\text{MO}_4^{2-}} + r_{\text{A}^+}}{\sqrt{2} (r_{\text{H}^-} + r_{\text{A}^+})} \quad (4.1)$$

The determined tolerance factors are listed in **Table 4.4**. By this simple approach it is notable that $\text{Rb}_3\text{WO}_4\text{H}$ differs the most from the phase prototype for tetragonal structures and also differs the most from an ideal value of 1. Despite the lanthanide contraction, the tungstate ions have a marginal larger ionic radius compared to the molybdate ion. Thus, the tungstate ions demand more space within the cuboctahedra voids. The rubidium ions are too small to compensate this. In sum, the tolerance factor supports the structural distortions observed for $\text{Rb}_3\text{WO}_4\text{H}$.

Table 4.4. Determined Goldschmidt tolerance factors.

Compound	Tolerance factor t
$\text{Rb}_3\text{MoO}_4\text{H}$	1.12
$\text{Cs}_3\text{MoO}_4\text{H}$	1.11
$\text{Rb}_3\text{WO}_4\text{H}$	1.14
$\text{Cs}_3\text{WO}_4\text{H}$	1.12
$\text{K}_3\text{SO}_4\text{F}$	1.09

To supplement the structural models obtained by the diffraction techniques, vibrational spectroscopy was applied. Unfortunately, FT-IR spectroscopy on all samples did not produce interpretable spectra. Diluting the samples in FT-IR-inactive KBr did not improve the experimental outcome of the spectra. Optical effects presumably disturb measurements, rendering this method inapplicable for the analysis of these compounds.

Raman spectroscopy contrarily shows sharp signals. Unfortunately, no modes arising from hydride vibrations are predicted for the tetragonal crystallizing compounds. Accordingly, the experimental spectra of three respective compounds show only the vibrational modes of the complex oxometalate anions $\nu_1 - \nu_4$. Generally, the experimentally obtained Raman spectra are in good agreement with the simulated spectra, conjointly in the predicted intensity, splitting of the modes as well as the expected wavenumber region. The respective Raman experimental and simulated (DFT-PBE0 level of theory) spectra of the tetragonal phases are shown in **Figure**

4.12. Whilst no prove of the hydride abundance is provided, the presence of complex oxometalate anions is clearly perceptible.

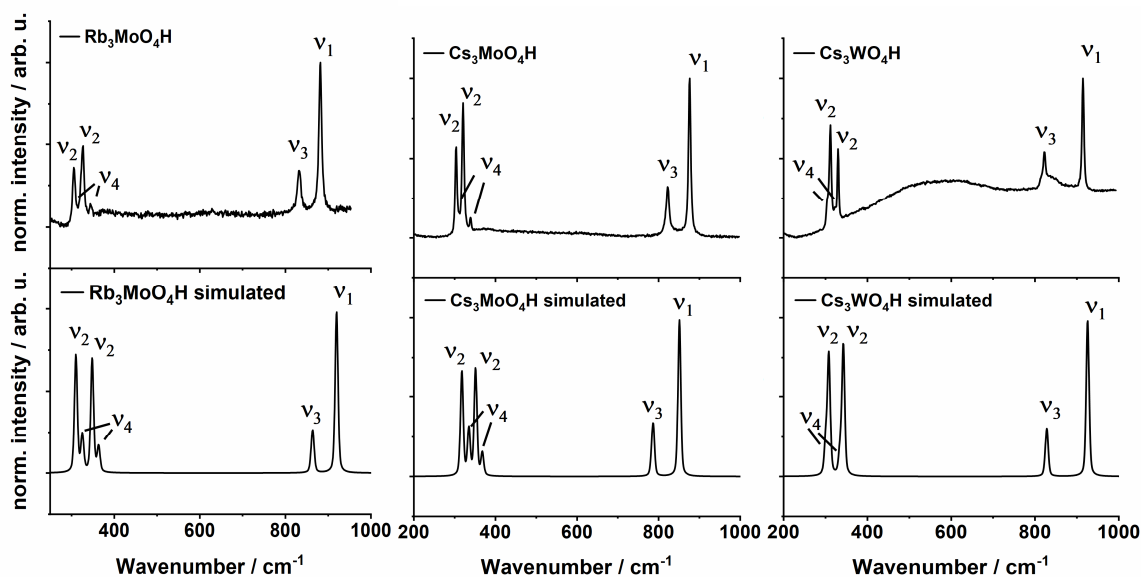


Figure 4.12. Experimental Raman spectra of the tetragonal crystallizing phases with the respective simulated spectra (DFT-PBE0 level of theory) depicted below.

The structure of $\text{Rb}_3\text{WO}_4\text{H}$ differs from the further three compounds. The Raman spectrum consequently shows a similar, yet different topology in comparison with the tetragonal phases (**Figure 4.13**).

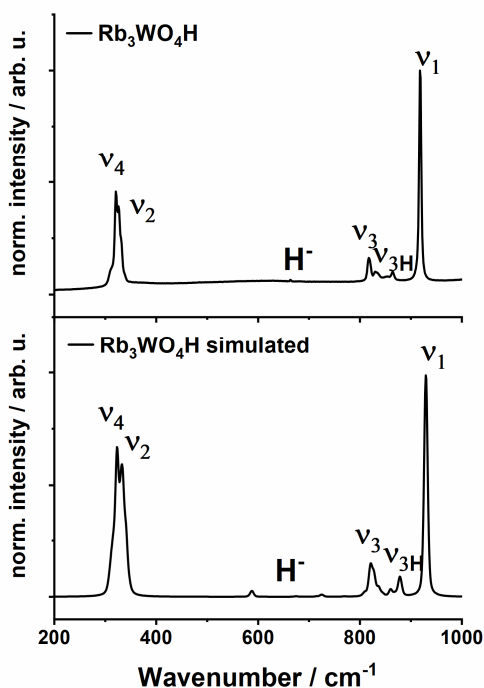


Figure 4.13. Experimental Raman spectrum of $\text{Rb}_3\text{WO}_4\text{H}$ with the simulated spectrum (DFT-PBE0 level of theory) depicted below.

Again, all the Raman active modes $\nu_1 - \nu_4$ arising from the tungstate ions are observed. More interestingly, hydride modes are now additionally observed. This is prominently noticeable as ν_{3H} modes at approx. 870 cm^{-1} . This mode originates from hydride vibrations coupled to asymmetric stretch vibrations of the tungstate ions, a clear evidence of hydride ions. Overall, as shown in **Figure 4.13**, the simulated spectrum matches to the experimental spectrum exceptionally well. This does not only prove the tungstate abundance, but also the simultaneous hydride abundance in $\text{Rb}_3\text{WO}_4\text{H}$. Furthermore, the structural model obtained by the diffraction techniques is supported.

The hydride abundance, especially for the tetragonal phases is yet to be unambiguously proven. As in the present study vibrational spectroscopy does not reliably prove of the hydride abundance, MAS NMR spectroscopy was applied to obtain the hydride proofs through local structure determination. ^1H MAS NMR has shown several impurity peaks and therefore ^2H MAS NMR was selected. External, protonic impurities can be excluded herein. The corresponding ^2H MAS NMR spectra are shown in **Figure 4.14**.

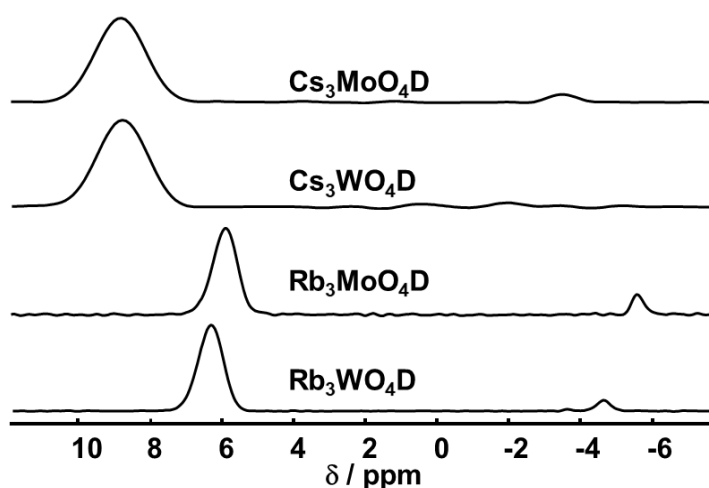


Figure 4.14. Room temperature ^2H MAS NMR spectra of the four phases. The spectra were acquired with spinning frequencies of 5 kHz and a magnetic field strength of $B_0 = 17.6\text{ T}$.

All four compounds show a single signal with a chemical shift in the range typical for salt-like hydride ions. Small impurity peaks are additionally observed for all phases. Due to their very low intensity, their origin was not further investigated. However, these signals are expected to originate from minor amorphous impurities, not visible in the diffraction patterns. The rubidium compounds show signals with a chemical shift of 6.0 ppm or 6.4 ppm for the molybdate and tungstate species respectively, the cesium compounds show a single signal at 9.8 ppm each. This reflects the trend for the $^1\text{H}/^2\text{H}$ chemical shifts to be downfield shifted in the presence of heavier atoms, as observed for the binary alkaline hydrides.^[219] DFT-PBE calculations on the chemical shifts yield 5.5 ppm for the rubidium compounds, 6.4 ppm and 6.2 ppm for $\text{Cs}_3\text{MoO}_4\text{H}$ and $\text{Cs}_3\text{WO}_4\text{H}$ respectively. The predicted chemical shifts of the rubidium compounds fit rather well, whereas for the cesium compounds a large discrepancy can be noticed. The very heavy cesium atoms might have spin coupling effects on lighter atoms and consequently, deshielding

effects on the hydride ions. Such effects are not taken into account for the calculations and thus might be an origin of the discrepancy with the experimental values. Nonetheless, quantum chemical calculations support the experimental findings and again reflect the downfield shift for heavier atomic environments. Together with the long range structure determination by the neutron diffraction, ^2H MAS NMR confirms the hydride abundance and conclusively, the newly formed species are of hydridic character.

Calculations on the electronic band structure reveal direct transitions for all four compounds. The band structures of the tetragonal phases show a very similar topology. The band structures are stacked above in **Figure 4.15** to illustrate the similarity. Yet again, the reoccurring scheme within heteroanionic hydrides where hydride states dominate the valance band is observable. The tetragonal phases are also predicted to be wide range semiconductors with band gaps ranging from 3.2 eV for $\text{Cs}_3\text{MoO}_4\text{H}$ to 3.4 eV for $\text{Rb}_3\text{MoO}_4\text{H}$ and 3.8 eV for $\text{Cs}_3\text{WO}_4\text{H}$. This is also reflected by the colourless appearance of the polycrystalline samples. Interestingly, the direct transition occurs directly from the hydride states to states arising from the complex oxometalate anions. In general, the metalate anions states are split in to the valence and conduction bands and enclose the hydride states energetically above and below. The hydride states with only minor contributions of other elements lastly determine the band gap.

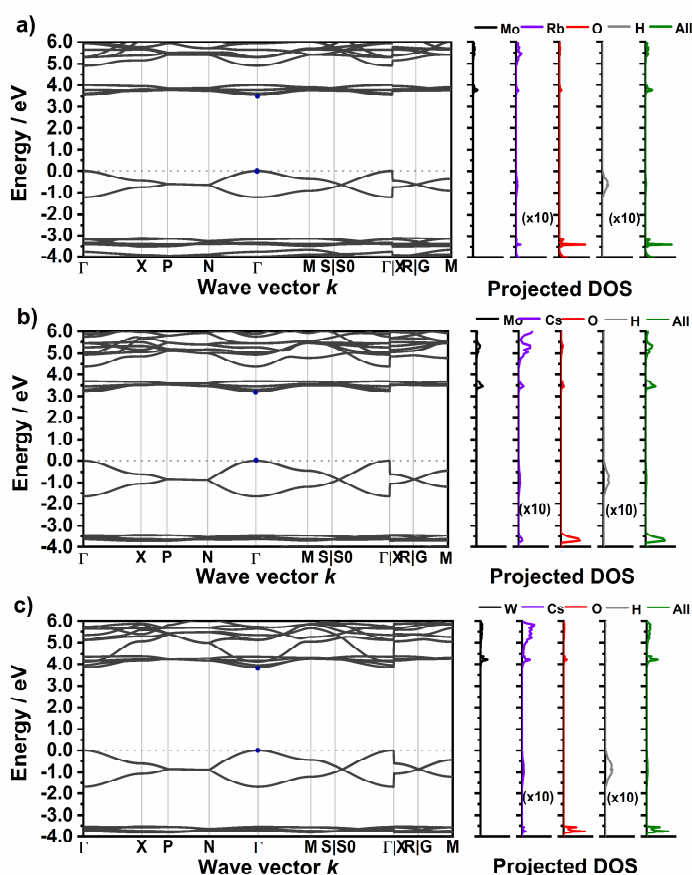


Figure 4.15. Electronic band structure of the tetragonal phases with the respective projected density of states at the DFT-PBE0 level of theory. a) $\text{Rb}_3\text{MoO}_4\text{H}$, b) $\text{Cs}_3\text{MoO}_4\text{H}$ and c) $\text{Cs}_3\text{WO}_4\text{H}$.

To prove that the compounds are direct and wide band gap semiconductors, UV-VIS absorption spectroscopy was applied. With the Tauc-method, the predicted band gaps could be confirmed and the direct transition character was proven. An exemplary Tauc-plot of $\text{Cs}_3\text{WO}_4\text{H}$ is depicted in **Figure 4.16**.

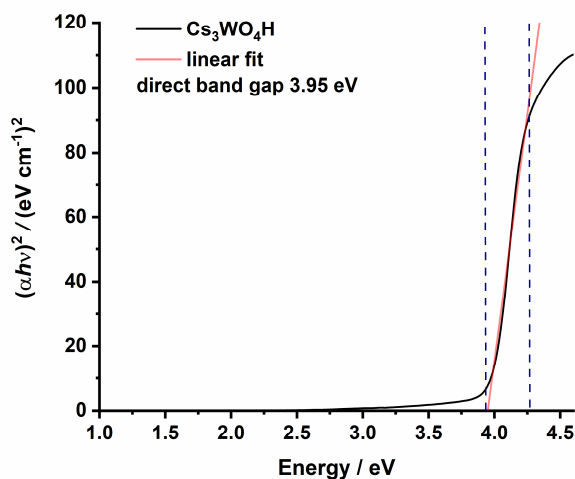


Figure 4.16. Tauc-plot of $\text{Cs}_3\text{WO}_4\text{H}$ determined by UV-VIS absorption spectroscopy. The blue vertical dashed lines indicate the region considered for the linear fit. A direct band gap of 3.66 eV is determined and matches the predicted band gap of 3.56 eV.

The electronic band structure of $\text{Rb}_3\text{WO}_4\text{H}$ (**Figure 4.17**) shows similar characteristics observed for the tetragonal phases. A direct transition is predicted and moreover, hydride states dominate the valence band, with the metalate states situated above and below. However, a very unique, peculiar dispersion for the hydrides states can be observed. The states are degenerate at the R-point and non-degenerate at the origin Γ . This topology arises from the pseudo-cubic arrangement of the hydride ions within the crystal structure which results in slightly dissimilar paths in the reciprocal space.

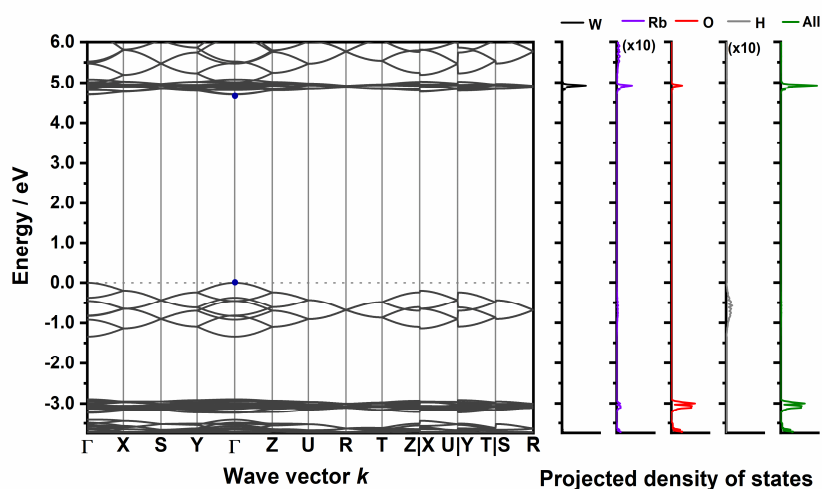


Figure 4.17. Electronic band structure of $\text{Rb}_3\text{WO}_4\text{H}$ with the projected density of states at the DFT-PBE0 level of theory.

The electronic band structure calculations demonstrate yet again the strong polarizability of the hydride ion. For the tetragonal crystallizing phases, the high polarizability even leads to a semiconducting character where the hydride states are directly responsible for.

Doping of the compounds with divalent europium did not result in observable luminescence. Due to the ionic radii, it might be possible that divalent europium can substitute the alkaline metals (Rb^+ , Cs^+). It was shown before in e.g. Eu^{2+} or Yb^{2+} doped NaMgF_3 or KMgF_3 that the divalent activator ions are expected to substitute monovalent alkaline ions, as the Mg^{2+} sites are too narrow.^[30,220–222] However, in the compounds charge compensation is missing. Similar to the sulfate hydride, only monovalent cation lattice sites are available. For the tetragonal phases the band gap might be additionally too small. The $4f^65d^1$ state of the Eu^{2+} ion is eventually situated energetically within the CB, making an excitations of electrons in this state unfeasible.

4.2.2 Low temperature phase transition of $\text{Rb}_3\text{WO}_4\text{H}$

Further investigations regarding the structural modifications of the previously introduced four compounds were conducted. Therefore, to see if phase transitions from one structure type into another occur, temperature dependent X-ray diffraction data in a range from 100 K - 400 K on the four compounds was collected. Surprisingly, the tetragonal phases show no phase transition, whereas $\text{Rb}_3\text{WO}_4\text{H}$ undergoes a low temperature phase transition at approx. -14°C . The stacked p-XRD patterns for each temperature step measured are depicted in **Figure 4.18**.

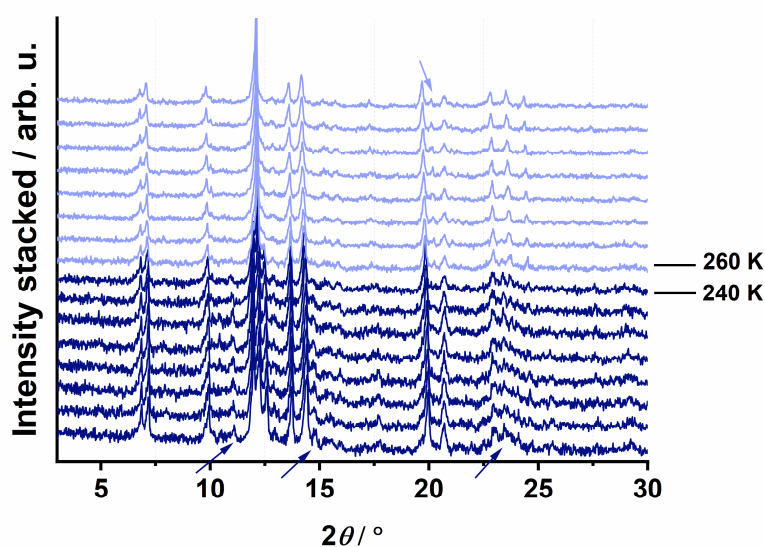


Figure 4.18. Temperature dependent p-XRD patterns of $\text{Rb}_3\text{WO}_4\text{H}$. Individual patterns were measured in 20 K steps. Arrows mark emerging and diminishing differences between the RT and low temperature phase patterns.

However, diffraction pattern obtained at temperatures below do not fit to the structural model of the tetragonal phases. Thus, $\text{Rb}_3\text{WO}_4\text{H}$ undergoes a phase transition to another different, presumably lower symmetric crystal structure. DSC measurements reaffirm the phase transition, proven by an endothermic peak at approx. -14°C as shown in **Figure 4.19**. Further

signals, marked with asterisks, are visible that might arise from sample impurities or beginning dissociation at elevated temperatures. By a direct comparison of the XRD patterns of both polymorphs, a similar topology is notable. Although, several differences are noticeable, indexed with arrows in **Figure 4.18**. By cooling down, small reflections at 11° , 15° 2θ emerge and noisily overlap at 23° 2θ . In turn, a reflection at 21° 2θ diminishes. As the most prominent difference, the 222 (hkl) reflection, intensely visible at 12° 2θ in XRD patterns of the RT phase, is split in patterns of the LT phase. Instead of a single, intense reflection, three distinct reflections are observed for the low temperature polymorph. This is noted as 222^* in **Figure 4.20**. Starting from the orthorhombic structure, such a splitting can be simulated by the alteration of at least two more crystallographic angles. Therefore, a symmetry reduction from an orthorhombic crystal system to a triclinic crystal system is probable.

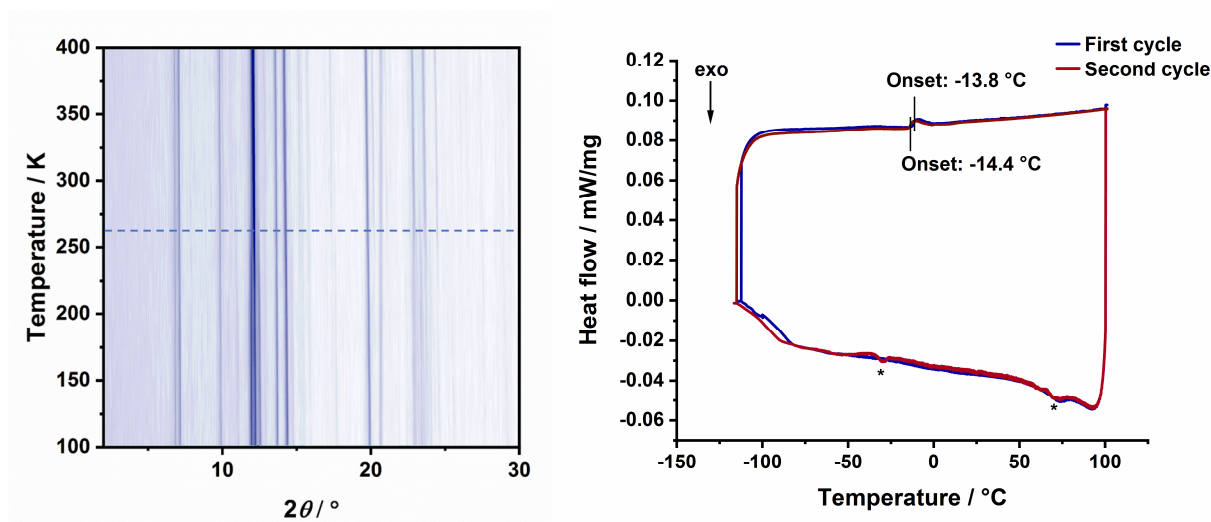


Figure 4.19. Left: contour plot of the temperature dependent X-ray diffraction data of $\text{Rb}_3\text{WO}_4\text{H}$. The approximate phase transition region is marked with a dashed line. Right: DSC curve with the peaks corresponding to the low temperature phase transitions.

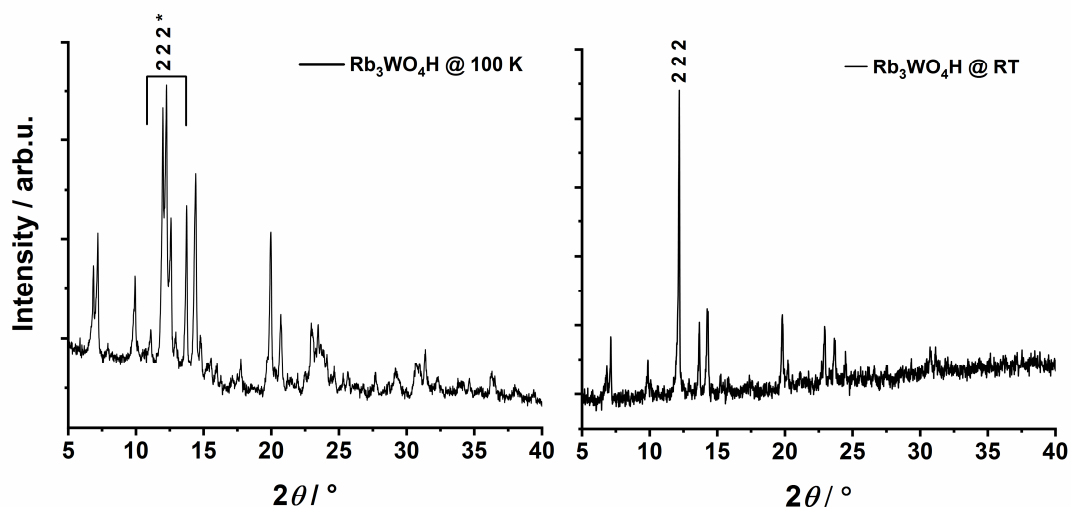


Figure 4.20. Comparison of the low temperature phase p-XRD pattern (left) with the RT p-XRD pattern (right). Due to Rb-fluorescence, a large background is visible.

Neutron diffraction data on all four compounds at 4 K further indicate no phase transition of the tetragonal phases. Rietveld refinement validate the RT structural model, with expected low thermal displacement parameters. The refinement plots and crystallographic data thereof is depicted in the appendix. However, the phase transition of $\text{Rb}_3\text{WO}_4\text{H}$ ($\text{Rb}_3\text{WO}_4\text{D}$) is observed and reaffirmed. A Rietveld refinement of the 4K neutron diffraction data based on the RT structural model does not sufficiently converge. Large discrepancies between the fit and the experimental data is evident as shown in the refinement plot in **Figure 4.21**. Atomic displacement parameters, conflicting the low temperature, are estimated to be very high from refinement. The corresponding crystallographic data is listed in **Table 4.5**.

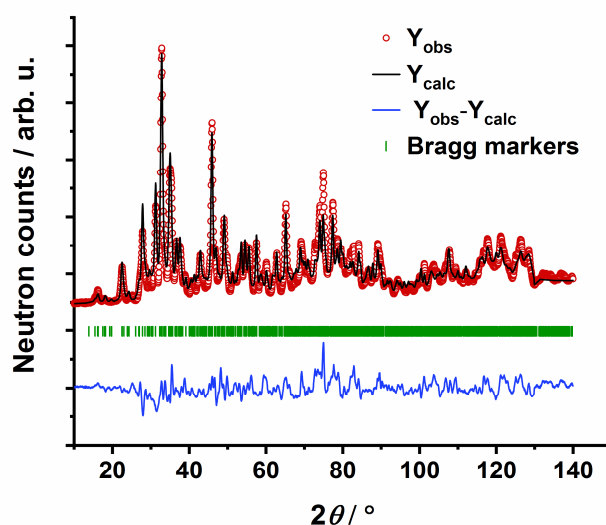


Figure 4.21. Rietveld refinement plot of $\text{Rb}_3\text{WO}_4\text{D}$ based on neutron data collected from the D2B ILL at 4K. $R_p = 8.17\%$, $R_{wp} = 9.98\%$, $R_{exp} = 0.86\%$, $\chi^2 = 136$.

Table 4.5. Crystallographic data obtained by Rietveld refinement of $\text{Rb}_3\text{WO}_4\text{D}$.

Cell parameters						
$a = 11.8441(18) \text{ \AA}$, $b = 11.278(2) \text{ \AA}$, $c = 11.337(2) \text{ \AA}$; $a/b=1.0502$, $b/c=0.9948$, $c/a=0.9572$						
$V = 1556.24(10) \text{ \AA}^3$						
$Pbca$ (61)						
Atom	Wyckoff position	Site	x/a	y/b	z/c	$U_{iso} (\text{Å}^2)$
W1	8c	1	0.747(3)	0.000(3)	-0.016(2)	0.031(4)
Rb1	8c	1	0.747(3)	0.231(3)	0.7223(17)	0.17(3)
Rb2	8c	1	-0.001(2)	0.7797(10)	-0.0182(10)	0.0036(16)
Rb3	8c	1	0.0014(20)	-0.0087(19)	0.7075(13)	0.036(4)
O1	8c	1	0.870(2)	-0.004(3)	0.0722(19)	0.153(6)
O2	8c	1	0.778(3)	-0.007(3)	0.838(3)	0.17(8)
O3	8c	1	0.722(3)	0.185(3)	-0.010(3)	0.083(10)
O4	8c	1	0.632(5)	-0.080(4)	0.052(3)	0.17(2)
D1	8c	1	0.504(4)	0.763(3)	0.262(3)	0.094(6)

Ultimately, no sufficient structural solution could be obtained. Indexing of the reflections, either from X-ray or neutron diffraction data, did not succeed in finding a unit cell. By the similarity

of both patterns, a small distortion to monoclinic or triclinic cell set-up might be the most likely case. Further investigations with X-ray radiations of longer wavelengths might help to attain a structural solution of the low temperature phase. Reflections can be indexed more reliably and the fluorescence of rubidium is pronounced less distinctly, so an ab-initio structural solution may be facilitated.

4.2.3 $\text{K}_3\text{MoO}_4\text{H}$ as a further transition oxometalate hydride

Since in total four oxometalate hydrides with either rubidium or cesium cations were found, synthesis attempts of transition oxometalate hydrides of the lighter alkaline metals were reasonable. Regardless of different synthesis procedures with several temperature variations, the formation of new compounds with lithium or sodium cations did not succeed. Solely the reaction of KH with K_2MoO_4 resulted in the formation of a new phase. Applying the previous established sophisticated autoclave synthesis method and lowering the reaction temperature to 245 °C (345 °C OT*), delivered an XRD pattern with unknown reflections of unassignable phases. Solely reduced molybdenum residues were indexable.

Indexing of several intense reflections of the obtained pattern formed yielded a hexagonal cell with the parameters $a = 8.08 \text{ \AA}$ and $c = 9.37 \text{ \AA}$. Due to the large amount of impurities, an ab-initio structural solution was not possible. An initial structural model could be adapted from the rhombohedral sub cell of $\text{Na}_3\text{SO}_4\text{F}^{[144]}$ with the space group $R3m$ (160) that shows a similar arrangement of reflections in corresponding diffraction patterns as shown in **Figure 4.22**.

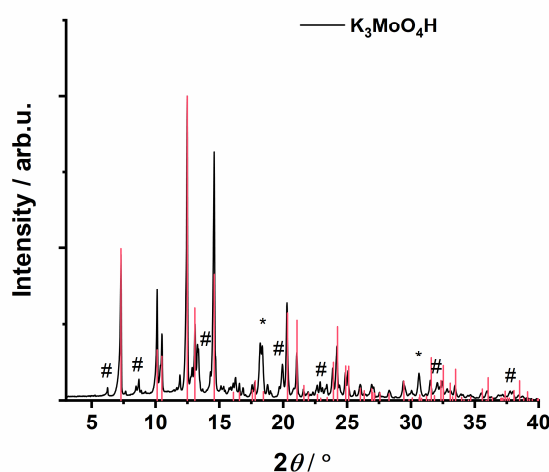


Figure 4.22. P-XRD measurement of the sample obtained by the attempted synthesis of $\text{K}_3\text{MoO}_4\text{H}$. Vertical red bars resemble simulated Bragg reflections of a structure adapted from rhombohedral $\text{Na}_3\text{SO}_4\text{F}$. Asterisks mark molybdenum reflections. Rhombuses mark unknown reflections.

An early attempt of a Rietveld refinement based on the adapted structure of a trigonal $\text{Na}_3\text{SO}_4\text{F}$ converges. However, large discrepancies between the experimental and the simulated pattern are apparent despite the exclusion of tentatively assigned impurity phases during the refinement as noticeable in the refinement plot in **Figure 4.23**. The corresponding crystallographic data determined by Rietveld refinement is listed in **Table 4.6**. Effectively, the obtained atomic

parameters have high standard deviations and the thermal displacement parameters adopt unrealistic negative values. Even though the refinement was unsatisfactory, a crude picture of the structural motive can be drawn.

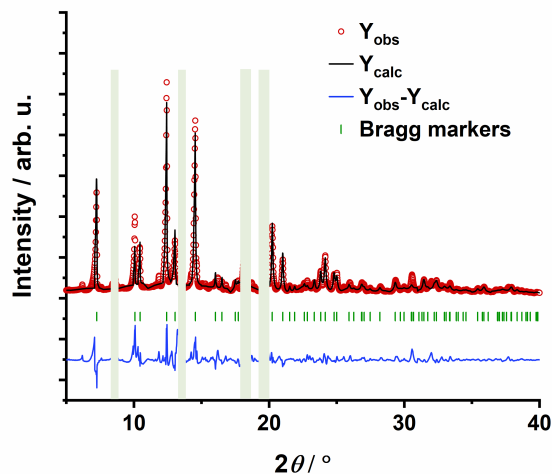


Figure 4.23. Rietveld refinement plot of K_3MoO_4H . Greyed-out areas were cut out during refinement. $R_p = 12.4\%$, $R_{wp} = 16.5\%$, $R_{exp} = 1.24\%$, $\chi^2 = 178$.

Table 4.6. Crystallographic data of K_3MoO_4H obtained from Rietveld refinement.

Cell parameters						
$a=8.0766(5) \text{ \AA}$, $c=9.3688(8) \text{ \AA}$, $V = 529.26(8) \text{ \AA}^3$						
$R3m (160)$						
Atom	Wyckoff position	Site	x/a	y/b	z/c	$U_{iso} (\text{Å}^2)$
K1	9b	m	1/6	1-x	0.297(2)	-0.008(5)
Mo1	3a	$3m$	0	0	0	0.017(7)
O1	9b	m	0.540(2)	1-x	0.412(3)	-0.021(14)
O2	3a	$3m$	0	0	0.78(2)	-0.027(19)
H1	3a	$3m$	0	0	0.4960*	0.0380*

*fixed values used.

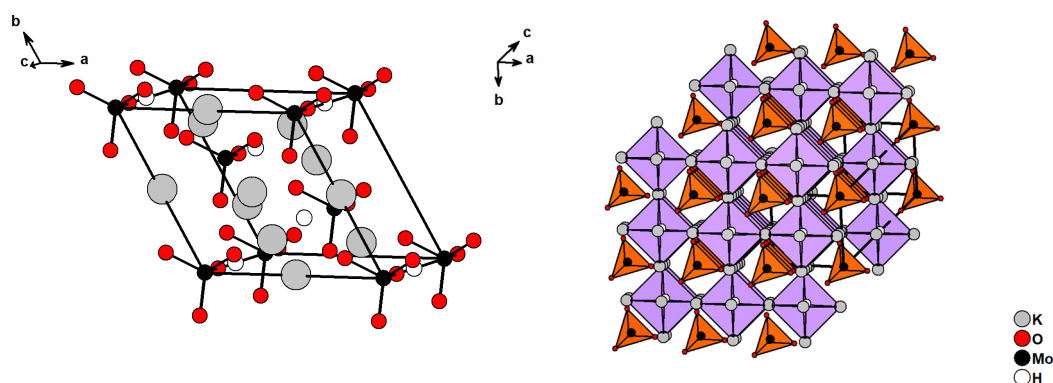


Figure 4.24. Left: proposed crystal structure of K_3MoO_4H . Right: depiction as antiperovskite with HK_6 octahedra in lilac and molybdate ions in orange.

With hydride ions assumed to occupy the sites within the potassium octahedra, an antiperovskite-like build up is resembled once more. In contrast to the previously discussed antiperovskite-like structures, only the HK_6 octahedra are slightly distorted and cause a deviation from the ideal cubic arrangement to a lower symmetric trigonal/rhombohedral cell. Anyhow, this initial structural model is not fully corroborated by this premature refinement. Another space group or a different, larger cell cannot be excluded as some of the tentatively assigned impurity phases are likely reflections corresponding thereto.

Despite the discrepancies of the refinement, a basic, rudimentary model is drawn. However, room for improvement is left. Further exploratory work is required to obtain crystalline phase pure samples and to improve this initial model. Ultimately, neutron diffraction of deuterated samples is necessary to accurately solve this structure.

5 Summary and conclusion

Within the last decade, the research of heteroanionic hydrides has gained a lot of attraction. To date, many widely desired properties are reported repeatedly, demonstrating the potential of such heteroanionic compounds. Still, many simple systems remain unexplored and hide likely further desirable characteristics. Especially hydride fluorides prove to be excellent host materials to study luminescent processes arising in rare earth doped materials.

In this regard, the previously unreported full solid-solution series of $\text{RbCaH}_x\text{F}_{3-x}$ and $\text{CsCaH}_x\text{F}_{3-x}$ were synthesized to supplement the previous studied hydride fluoride solid-solutions. By long range structure determination in combination with vibrational spectroscopy, it could be proven that, despite previous assumptions, the ideal perovskite structure is preserved in both solid solution series. Europium doped $\text{RbCaH}_x\text{F}_{3-x}$ did not exhibit mentionable luminescence. Contrarily, bright and tunable luminescence could be observed for europium doped $\text{CsCaH}_x\text{F}_{3-x}$. A gradual redshift of the luminescence glow is visible which ranges from cyan-green to red with increasing hydride content. Yet again, the sensitivity of Eu^{2+} luminescence to its local environment and the corresponding $4f^65d^1 - 4f^7$ transitions could be shown. However, a completely different kind of redshift is observed, originating from new emerging narrow emission bands at the low energy site rather than from a gradual shift of a single emission band. Besides the possibility to tune the emission colour through the hydride content, also the dopant concentration is strongly influencing the emission colour. This demonstrates the importance of such easily adjustable model systems in order to enhance the understanding of luminescent processes. Especially the latter investigated system does not only provide new methods to tune the emission wavelength but also allows for the design of new narrow band emitting phosphors.

In sum, hydride fluorides are a well-researched class of materials. To date, many desirable materials properties were found in compositions alike. Especially, the possibility to selectively tune emission wavelengths in europium doped systems attracted recent research. Nevertheless, even such established systems still continue to provide unexpected and advantageous properties. In this regard, several hydride-to-anion combinations with likely as much hidden potential are still to be discovered. With this in mind, approaches to accomplish such new hydride-to-anion combinations were made. Such materials may equally be suited as host materials for lanthanide activated luminescence, but also may inherit other highly advantageous properties useful for future applications. The primal focus is placed herein on the synthetic and analytical strategies towards unprecedented anion combinations.

By a sophisticated synthesis method, $\text{Na}_3\text{SO}_4\text{H}$ could be prepared as the first compound to simultaneously contain both hydride and sulfate anions, an unparalleled anion combination. This shows the significance for exploratory synthesis approaches in order to realize new, in particularly hydridic, structures. Only a very narrow reaction temperature window of 10 °C allows for a feasible synthesis of the novel compound. $\text{Na}_3\text{SO}_4\text{H}$ is obtained as a colourless,

moisture sensitive powder and crystallizes in a tetragonal antiperovskite-like structure, differently to its fluoride analogue. A set of manifold analytical methods is given that each independently but also altogether undeniably prove the abundance of hydride ions within this structure. This in turn also provides a well-applied catalogue of analytical methods, useful for the proof and identification of further, new potential hydrides.

With the establishment of the sulfate hydrides, it was shown that seemingly challenging compounds can be synthesized by carefully monitoring the reaction conditions. Consequently, further, still unexplored heteroanionic hydride combinations were investigated using the beforehand attained insights.

The sophisticated synthesis approach that proved to be expedient before, led to the accomplishment of a further heteroanionic composition – the combinations of hydrides with complex transition oxometalate ions. In total, the four compounds A_3MO_4H ($A = Rb, Cs, M = Mo, W$) could be synthesized and introduce this new, potentially large class of materials. Again, only narrow reaction temperature windows allow for the synthesis of the compounds. The air and moisture sensitive samples are obtained as colourless polycrystalline powders. Utilizing the previously established analytical routine, the hydridic character of the newly found phases was proven. Unusual structural modifications lead to two distinct antiperovskite-like structures. Apart from Rb_3WO_4H , all phases crystallize in the tetragonal K_3SO_4F -type. Rb_3WO_4H in turn crystallizes in a unique perovskite-like variant that has not been observed before. This structural peculiarity is expanded by a low temperature phase transition near room temperature. Overall, the compounds also reveal interesting electronic properties. The tetragonal phases are direct and wide band gap semiconductors with band gaps ranging from ca. 3 to 4 eV. Rb_3WO_4H in turn shows a unique, peculiar band structure dominated by hydride states. In all four compounds, hydride states dominate the band structures and are the responsible part for the direct transition character. As the tetragonal phases are isostructural, a band gap tuning might be possible by synthesis of solid solution series. These compounds overall may help with the design of semiconductors and contribute to the highly researched field of (anti)perovskites. Ultimately, combinations of hydrides with other transition oxometalate anions, e.g. chromates or vanadates are likely to be discovered based on these findings.

Finally, the existence of K_3MoO_4H as another oxometalate hydride is reasonably indicated. Yet again, a structure with an antiperovskite motive is discernible, adding up to the third antiperovskite structures within this compound class alone.

This work started with compounds crystallizing in the ideal perovskite structure and concluded with the structural counterpart – the antiperovskites. In total, five different structural motives, all of which can be ascribed to a perovskite building principle are presented in this work. The frequently occurring perovskite structure provides a suitable architecture to stabilize heteroanionic hydrides. The ratio of the ionic radii lastly determines the exact structure.

No noteworthy luminescence of the latter compounds could be detected, although it was attempted to find new heteroanionic hydrides also as host materials for lanthanide activated luminescence causally. Nonetheless, fundamental groundwork was made and crucial insights to new heteroanionic materials were obtained within this work. A clear description of synthetic and analytical methods to new heteroanionic materials with complex oxoanions is given and in

total, two unprecedented anion combinations were realized for the first time in the scope of this work. As a common scheme it can be summarized that all of the new compounds are accessible by a sophisticated thermal synthesis route under rather mild conditions. Only reaction temperatures well below 350 °C with very narrow temperature windows allow for the synthesis of the new compounds. This is particularly pronounced for the formation of the sulfate hydride where only less than 10 °C deviations from the optimal reaction temperature allow for a feasible synthesis. Also, all newly found compounds follow an antiperovskite-like build-up. The hydride ions seem to be sufficiently stabilized and encapsulated within the highly electropositive alkaline metals in order to sustain these heteroanionic structures. In the future, it might be interesting to enhance the understanding why so far no structure with divalent ions was synthetically accessible. Applying the HSAB principle in combination with DFT calculations could be an interesting approach thereto.^[223,224] Whilst the new materials itself might not be suitable as host materials for lanthanide activated luminescence, many application of the new materials are possible. The compounds itself might serve as a chemical template to synthesize further, more complex hydridic structures containing other complex oxoanions. Furthermore, the possibility to introduce strongly polarizable ions, such as the hydride ions is given. In the future, this can be utilized for sulfate or oxometalate based luminescent or ion conducting materials.^[50,225] Lastly, the direct and wide band gap semiconducting tetragonal transition oxometalate hydrides might be interesting for applications as optoelectronics or photodetectors.^[226] Further work may now approach synthesis of structures with different valent cations and other distinct stoichiometries starting from the insights attained hereof and eventually reinvestigate luminescent properties.

6 References

- [1] E. Anders, M. Ebihara, *Geochim. Cosmochim. Acta*, **1982**, 46, 2363–2380.
- [2] K. Lodders, *Astrophys. J.*, **2003**, 591, 1220–1247.
- [3] V. Trimble, *Rev. Mod. Phys.*, **1975**, 47, 877–976.
- [4] R. A. Alpher, H. Bethe, G. Gamow, *Phys. Rev.*, **1948**, 73, 803–804.
- [5] C. Janiak; H.-J. Meyer; D. Gudat; R. Alsfasser; E. Riedel, *Moderne anorganische Chemie*, De Gruyter, **2012**.
- [6] W. M. Mueller, *Metal Hydrides*, Elsevier Science, **2013**.
- [7] A. F. Holleman; N. Wiberg; E. Wiberg, *Lehrbuch der anorganischen Chemie*, De Gruyter, **2007**.
- [8] C. E. Housecroft; A. G. Sharpe, *Inorganic chemistry*, Prentice Hall, **2006**.
- [9] L. Schlapbach, *Hydrogen in Intermetallic Compounds I: Electronic, Thermodynamic, and Crystallographic Properties, Preparation*, Springer, **1988**.
- [10] K. Yvon, G. Renaudin, C. M. Wei, M. Y. Chou, *Phys. Rev. Lett.*, **2005**, 94, 66403.
- [11] R. C. Bowman, B. Fultz, *MRS Bull.*, **2002**, 27, 688–693.
- [12] B. Sukinta, F. Lamari-Darkrim, M. Hirscher, *Int. J. Hydrog. Energy*, **2007**, 32, 1121–1140.
- [13] K. Yvon, G. Renaudin, in *Encyclopedia of inorganic chemistry*, Wiley, **2005**.
- [14] S.-I. Orimo, Y. Nakamori, J. R. Eliseo, A. Züttel, C. M. Jensen, *Chem. Rev.*, **2007**, 107, 4111–4132.
- [15] M. Matsuo, S.-I. Orimo, *Adv. Energy Mater.*, **2011**, 1, 161–172.
- [16] M. B. Ley, L. H. Jepsen, Y.-S. Lee, Y. W. Cho, J. M. Bellosta von Colbe, M. Dornheim, M. Rokni, J. O. Jensen, M. Sloth, Y. Filinchuk, J. E. Jørgensen, F. Besenbacher, T. R. Jensen, *Mater. Today*, **2014**, 17, 122–128.

- [17] K. Yoshida, T. Sato, A. Unemoto, M. Matsuo, T. Ikeshoji, T. J. Udovic, S.-I. Orimo, *Appl. Phys. Lett.*, **2017**, *110*, 103901 (5 pages).
- [18] L. H. Jepsen, M. Paskevicius, T. R. Jensen, in *Nanotechnology for energy sustainability*, Wiley-VCH, **2017**, p. 415.
- [19] K. Møller, D. Sheppard, D. Ravnsbæk, C. Buckley, E. Akiba, H.-W. Li, T. R. Jensen, *Energies*, **2017**, *10*, 1645 (30 pages).
- [20] F. Schüth, B. Bogdanović, M. Felderhoff, *Chem. Commun.*, **2004**, 2249–2258.
- [21] W. Grochala, P. P. Edwards, *Chem. Rev.*, **2004**, *104*, 1283–1316.
- [22] A. L. Allred, *J. Inorg. Nucl. Chem.*, **1961**, *17*, 215–221.
- [23] S. Yamaguchi, *Science*, **2016**, *351*, 1262–1263.
- [24] W. Bronger, *Z. anorg. allg. Chem.*, **1996**, *622*, 9–16.
- [25] Q. Wang, J. Guo, P. Chen, *Joule*, **2020**, *4*, 705–709.
- [26] L. Pauling, *J. Am. Chem. Soc.*, **1927**, *49*, 765–790.
- [27] K. Hayashi, P. V. Sushko, Y. Hashimoto, A. L. Shluger, H. Hosono, *Nat. Commun.*, **2014**, *5*, 3515 (8 pages).
- [28] P. F. Lang, B. C. Smith, *Dalton Trans.*, **2010**, *39*, 7786–7791.
- [29] A. J. Maeland, W. D. Lahar, *Z. Phys. Chem.*, **1993**, *179*, 181–185.
- [30] R. D. Shannon, *Acta Cryst. A*, **1976**, *32*, 751–767.
- [31] C. E. Messer, *J. Solid State Chem.*, **1970**, *2*, 144–155.
- [32] C. N. R. Rao; J. Gopalakrishnan, *New directions in solid state chemistry*, Cambridge University Press, **1997**.
- [33] S. Banerjee; A. Tyagi, *Functional materials: Preparation, processing and applications*, Elsevier, **2012**.
- [34] Y. Kobayashi, Y. Tsujimoto, H. Kageyama, *Annu. Rev. Mater. Res.*, **2018**, *48*, 303–326.
- [35] H. Kageyama, K. Hayashi, K. Maeda, J. P. Attfield, Z. Hiroi, J. M. Rondinelli, K. R. Poeppelmeier, *Nat. Commun.*, **2018**, *9*, 772.
- [36] H. Kageyama, T. Yajima, Y. Tsujimoto, T. Yamamoto, C. Tassel, Y. Kobayashi, *Bull. Chem. Soc. Jpn.*, **2019**, *92*, 1349–1357.

- [37] K. Kobayashi, J.-I. Yamaura, S. Iimura, S. Maki, H. Sagayama, R. Kumai, Y. Murakami, H. Takahashi, S. Matsuishi, H. Hosono, *Sci. Rep.*, **2016**, *6*, 39646 (6 pages).
- [38] H. Hosono, S. Matsuishi, *Curr. Opin. Solid State Mater. Sci.*, **2013**, *17*, 49–58.
- [39] Ø. S. Fjellvåg, J. Armstrong, P. Vajeeston, A. O. Sjøstad, *J. Phys. Chem. Lett.*, **2018**, *9*, 353–358.
- [40] H. Ubukata, T. Broux, F. Takeiri, K. Shitara, H. Yamashita, A. Kuwabara, G. Kobayashi, H. Kageyama, *Chem. Mater.*, **2019**, *31*, 7360–7366.
- [41] H. Ubukata, F. Takeiri, K. Shitara, C. Tassel, T. Saito, T. Kamiyama, T. Broux, A. Kuwabara, G. Kobayashi, H. Kageyama, *Sci. Adv.*, **2021**, *7*, eabf7883 (7 pages).
- [42] F. Takeiri, A. Watanabe, K. Okamoto, D. Bresser, S. Lyonnard, B. Frick, A. Ali, Y. Imai, M. Nishikawa, M. Yonemura, T. Saito, K. Ikeda, T. Otomo, T. Kamiyama, R. Kanno, G. Kobayashi, *Nat. Mater.*, **2022**, *21*, 325–330.
- [43] K. Fukui, S. Iimura, T. Tada, S. Fujitsu, M. Sasase, H. Tamatsukuri, T. Honda, K. Ikeda, T. Otomo, H. Hosono, *Nat. Commun.*, **2019**, *10*, 2578 (8 Pages).
- [44] K. Fukui, S. Iimura, A. Iskandarov, T. Tada, H. Hosono, *J. Am. Chem. Soc.*, **2022**, *144*, 1523–1527.
- [45] T. Wylezich, R. Valois, M. Suta, A. Mutschke, C. Ritter, A. Meijerink, A. J. Karttunen, N. Kunkel, *Chem. Eur. J.*, **2020**, *26*, 11742–11750.
- [46] T. Wylezich, S. Welinski, M. Hoelzel, P. Goldner, N. Kunkel, *J. Mater. Chem. C*, **2018**, *6*, 13006–13012.
- [47] C. Pflug, A. Franz, H. Kohlmann, *J. Solid State Chem.*, **2018**, *258*, 391–396.
- [48] F. Gehlhaar, R. Finger, N. Zapp, M. Bertmer, H. Kohlmann, *Inorg. Chem.*, **2018**, *57*, 11851–11854.
- [49] T. Wu, K. Fujii, T. Murakami, M. Yashima, S. Matsuishi, *Inorg. Chem.*, **2020**, *59*, 15384–15393.
- [50] N. Kunkel, T. Wylezich, *Z. anorg. allg. Chem.*, **2019**, *645*, 137–145.
- [51] C. Pflug, H. Kohlmann, *Z. anorg. allg. Chem.*, **2020**, *646*, 175–179.
- [52] H.-H. Park, J. Senegas, J. M. Reau, M. Pezat, B. Darriet, P. Hagenmuller, *Mater. Res. Bull.*, **1988**, *23*, 1127–1138.
- [53] J.-F. Brice, A. Courtois, J. Aubry, *J. Solid State Chem.*, **1978**, *24*, 381–387.

- [54] N. Kunkel, A. Meijerink, H. Kohlmann, *Inorg. Chem.*, **2014**, *53*, 4800–4802.
- [55] J.-P. Soulié, J.-P. Laval, A. Bouamrane, *Solid State Sci.*, **2003**, *5*, 273–276.
- [56] A. Bouamrane, J.-P. Laval, J. P. Soulie, J. P. Bastide, *Mater. Res. Bull.*, **2000**, *35*, 545–549.
- [57] P. Ehrlich, B. Alt, L. Gentsch, *Z. anorg. allg. Chem.*, **1956**, *283*, 58–73.
- [58] P. Ehrlich, H. Grtz, *Z. anorg. allg. Chem.*, **1956**, *288*, 148–155.
- [59] P. Ehrlich, H. Kulke, *Z. anorg. allg. Chem.*, **1956**, *288*, 156–170.
- [60] N. Kunkel, D. Rudolph, A. Meijerink, S. Rommel, R. Weihrich, H. Kohlmann, T. Schleid, *Z. anorg. allg. Chem.*, **2015**, *641*, 1220–1224.
- [61] D. Rudolph, T. Wylezich, A. D. Sontakke, A. Meijerink, P. Goldner, P. Netzsch, H. A. Höpfe, N. Kunkel, T. Schleid, *J. Lumin.*, **2019**, *209*, 150–155.
- [62] B. Tangu, M. Pezat, C. Fontenit, J. Portier, *C. R. Acad. Sci. C*, **1975**, *280*, 1019–1020.
- [63] Jay C. Molstad, Scott Levy, Francis J. DiSalvo, *Z. Naturforsch. B*, **104**, *62*, 23–27.
- [64] H. P. Beck, A. Limmer, *Z. Naturforsch. B*, **1982**, *37*, 574–578.
- [65] O. Reckeweg, F. J. DiSalvo, *Z. Naturforsch. B*, **2011**, *66*, 1087–1091.
- [66] O. Reckeweg, J. C. Molstad, S. Levy, F. J. DiSalvo, *Z. Naturforsch. B*, **2007**, *62*, 23–27.
- [67] O. Reckeweg, F. J. DiSalvo, *Z. Naturforsch. B*, **2011**, *66*, 21–26.
- [68] O. Reckeweg, F. J. DiSalvo, S. Wolf, T. Schleid, *Z. anorg. allg. Chem.*, **2014**, *640*, 1254–1259.
- [69] F. L. Carter, *Rare Earth Research*, **1962**, *2*, 311.
- [70] M. A. Hayward, E. J. Cussen, J. B. Claridge, M. Bieringer, M. J. Rosseinsky, C. J. Kiely, S. J. Blundell, I. M. Marshall, F. L. Pratt, *Science*, **2002**, *295*, 1882–1884.
- [71] Y. Kobayashi, O. J. Hernandez, C. Tassel, H. Kageyama, *Sci. Technol. Adv. Mater.*, **2017**, *18*, 905–918.
- [72] K. Higashi, M. Ochi, Y. Nambu, T. Yamamoto, T. Murakami, N. Yamashina, C. Tassel, Y. Matsumoto, H. Takatsu, C. M. Brown, H. Kageyama, *Inorg. Chem.*, **2021**, *60*, 11957–11963.

- [73] C. Tassel, Y. Goto, Y. Kuno, J. Hester, M. Green, Y. Kobayashi, H. Kageyama, *Angew. Chem. Int. Ed.*, **2014**, *53*, 10377–10380.
- [74] J. Bang, S. Matsuishi, S. Maki, J.-I. Yamaura, M. Hiraishi, S. Takeshita, I. Yamauchi, K. M. Kojima, H. Hosono, *Phys. Rev. B*, **2015**, *92*, 064414 (7 pages).
- [75] T. Yamamoto, R. Yoshii, G. Bouilly, Y. Kobayashi, K. Fujita, Y. Kususe, Y. Matsushita, K. Tanaka, H. Kageyama, *Inorg. Chem.*, **2015**, *54*, 1501–1507.
- [76] C. A. Bridges, G. R. Darling, M. A. Hayward, M. J. Rosseinsky, *J. Am. Chem. Soc.*, **2005**, *127*, 5996–6011.
- [77] Y. Wei, H. Gui, X. Li, Z. Zhao, Y.-H. Zhao, W. Xie, *J. Phys. Condens. Matter*, **2015**, *27*, 206001 (6 pages).
- [78] T. Uchimura, F. Takeiri, K. Okamoto, T. Saito, T. Kamiyama, G. Kobayashi, *J. Mater. Chem. A*, **2021**, *9*, 20371–20374.
- [79] T. Yajima, A. Kitada, Y. Kobayashi, T. Sakaguchi, G. Bouilly, S. Kasahara, T. Terashima, M. Takano, H. Kageyama, *J. Am. Chem. Soc.*, **2012**, *134*, 8782–8785.
- [80] Y. Kobayashi, O. J. Hernandez, T. Sakaguchi, T. Yajima, T. Roisnel, Y. Tsujimoto, M. Morita, Y. Noda, Y. Mogami, A. Kitada, M. Ohkura, S. Hosokawa, Z. Li, K. Hayashi, Y. Kusano, J. e. Kim, N. Tsuji, A. Fujiwara, Y. Matsushita, K. Yoshimura, K. Takegoshi, M. Inoue, M. Takano, H. Kageyama, *Nat. Mater.*, **2012**, *11*, 507–511.
- [81] J. Matsumoto, K. Hanzawa, M. Sasase, S. Haindl, T. Katase, H. Hiramatsu, H. Hosono, *Phys. Rev. Materials*, **2019**, *3*, 103401 (9 pages).
- [82] N. Zapp, D. Sheptyakov, A. Franz, H. Kohlmann, *Inorg. Chem.*, **2021**, *60*, 3972–3979.
- [83] N. Zapp, H. Auer, H. Kohlmann, *Inorg. Chem.*, **2019**, *58*, 14635–14641.
- [84] Y. Tang, Y. Kobayashi, K. Shitara, A. Konishi, A. Kuwabara, T. Nakashima, C. Tassel, T. Yamamoto, H. Kageyama, *Chem. Mater.*, **2017**, *29*, 8187–8194.
- [85] S. Gao, T. Broux, S. Fujii, C. Tassel, K. Yamamoto, Y. Xiao, I. Oikawa, H. Takamura, H. Ubukata, Y. Watanabe, K. Fujii, M. Yashima, A. Kuwabara, Y. Uchimoto, H. Kageyama, *Nat. Commun.*, **2021**, *12*, 201 (10 pages).
- [86] T. Schleid, M. Folchnandt, *Z. anorg. allg. Chem.*, **1996**, *622*, 455–461.
- [87] T. Schleid, H.-J. Meyer, *J. Alloys Compd.*, **1992**, *189*, 75–82.
- [88] M. Folchnandt, D. Rudolph, J.-L. Hoslauer, T. Schleid, *Z. Naturforsch. B*, **2019**, *74*, 513–518.

- [89] C. Pflug, D. Rudolph, T. Schleid, H. Kohlmann, *Eur. J. Inorg. Chem.*, **2022**, 2022, 1434–1948.
- [90] J.-F. Brice, J.-P. Motte, A. Courtois, J. Protas, J. Aubry, *J. Solid State Chem.*, **1976**, 17, 135–142.
- [91] M. Kitano, K. Yamagata, H. Hosono, *Res. Chem. Intermed.*, **2021**, 47, 235–248.
- [92] R. Marx, *Z. anorg. allg. Chem.*, **1997**, 623, 1912–1916.
- [93] B. Wegner, R. Essmann, J. Bock, H. Jacobs, P. Fischer, *Eur. J. Solid State Inorg. Chem.*, **1992**, 29, 1217–1227.
- [94] B. Blaschkowski, T. Schleid, *Z. anorg. allg. Chem.*, **2007**, 633, 2644–2648.
- [95] D. M. Liu, Q. Q. Liu, T. Z. Si, Q. A. Zhang, *J. Alloys Compd.*, **2010**, 495, 272–274.
- [96] H. Abe, Y. Niwa, M. Kitano, Y. Inoue, M. Sasase, T. Nakao, T. Tada, T. Yokoyama, M. Hara, H. Hosono, *J. Phys. Chem. C*, **2017**, 121, 20900–20904.
- [97] A. J. Rowberg, C. G. van de Walle, *ACS Appl. Energy Mater.*, **2021**, 4, 6348–6355.
- [98] F. Altorfer, W. Buhner, B. Winkler, G. Coddens, R. Essmann, H. Jacobs, *Solid State Ion.*, **1994**, 70-71, 272–277.
- [99] D. A. Lang, J. V. Zaikina, D. D. Lovingood, T. E. Gedris, S. E. Lattner, *J. Am. Chem. Soc.*, **2010**, 132, 17523–17530.
- [100] G. Renaudin, K. Yvon, S. K. Dolukhanyan, N. N. Aghajanyan, V. S. Shekhtman, *J. Alloys Compd.*, **2003**, 356-357, 120–127.
- [101] J. M. Haschke, *Inorg. Chem.*, **1975**, 14, 779–783.
- [102] M. Makovec, Z. Ban, *J. Less-Common Met.*, **1970**, 21, 169–180.
- [103] A. V. Skripov, H. Wu, T. J. Udovic, Q. Huang, R. Hempelmann, A. V. Soloninin, A. A. Rempel, A. I. Gusev, *J. Alloys Compd.*, **2009**, 478, 68–74.
- [104] T. V. Blankenship, M. J. Dickman, L. J. van de Burgt, S. E. Lattner, *Inorg. Chem.*, **2015**, 54, 914–921.
- [105] M. A. Hassen, I. J. McColm, *J. Alloys Compd.*, **2000**, 313, 95–103.
- [106] A. Simon, T. Gulden, *Z. anorg. allg. Chem.*, **2004**, 630, 2191–2198.
- [107] M. Ruck, A. Simon, *Z. anorg. allg. Chem.*, **1992**, 617, 7–18.

- [108] M. Armbruster, M. Wörle, F. Krumeich, R. Nesper, *Z. anorg. allg. Chem.*, **2009**, *635*, 1758–1766.
- [109] M. J. Evans, G. P. Holland, F. J. Garcia-Garcia, U. Häussermann, *J. Am. Chem. Soc.*, **2008**, *130*, 12139–12147.
- [110] U. Häussermann, *Z. Kristallogr. Cryst. Mater.*, **2008**, *223*, 628–635.
- [111] I. A. Ovchenkova, S. A. Nikitin, I. S. Tereshina, A. Y. Karpenkov, Y. A. Ovchenkov, J. Ćwik, Y. S. Koshkid'ko, H. Drulis, *J. Appl. Phys.*, **2020**, *128*, 143903 (8 pages).
- [112] A. Werwein, H. Kohlmann, *Z. anorg. allg. Chem.*, **2020**, *646*, 1227–1230.
- [113] H. Wu, W. Zhou, T. J. Udovic, J. J. Rush, T. Yildirim, *Phys. Rev. B*, **2006**, *74*, 224101 (5 pages).
- [114] M. Jehle, A. Hoffmann, H. Kohlmann, H. Scherer, C. Röhr, *J. Alloys Compd.*, **2015**, *623*, 164–177.
- [115] F. Bernardini, G. Garbarino, A. Sulpice, M. Núñez-Regueiro, E. Gaudin, B. Chevalier, M. A. Méasson, A. Cano, S. Tencé, *Phys. Rev. B*, **2018**, *97*, 100504(R) (5 pages).
- [116] T. F. Fässler, *Zintl Phases: Principles and Recent Developments*, Springer, **2011**.
- [117] D. Rudolph, D. Enseling, T. Jüstel, T. Schleid, *Z. anorg. allg. Chem.*, **2017**, *643*, 1525–1530.
- [118] N. Zapp, H. E. Fischer, H. Kohlmann, *Inorg. Chem.*, **2021**, *60*, 17775–17782.
- [119] K. Wissel, S. Dasgupta, A. Benes, R. Schoch, M. Bauer, R. Witte, A. D. Fortes, E. Erdem, J. Rohrer, O. Clemens, *J. Mater. Chem. A*, **2018**, *6*, 22013–22026.
- [120] F. Takeiri, T. Yajima, T. Yamamoto, Y. Kobayashi, T. Matsui, J. Hester, H. Kageyama, *J. Solid State Chem.*, **2017**, *256*, 33–37.
- [121] Y. Kobayashi, Y. Tang, T. Kageyama, H. Yamashita, N. Masuda, S. Hosokawa, H. Kageyama, *J. Am. Chem. Soc.*, **2017**, *139*, 18240–18246.
- [122] B. Huang, J. D. Corbett, *J. Solid State Chem.*, **1998**, *141*, 570–575.
- [123] K. Hayashi, H. Hosono, *Phys. Chem. Chem. Phys.*, **2016**, *18*, 8186–8195.
- [124] A. Mutschke, T. Wylezich, C. Ritter, A. J. Karttunen, N. Kunkel, *Eur. J. Inorg. Chem.*, **2019**, *2019*, 5073–5076.
- [125] T. L. Wylezich; *Dissertation*, Technische Universität München, **2020**.

- [126] M. Somer, Ö. Yaren, O. Reckeweg, Y. Prots, W. Carrillo-Cabrera, *Z. anorg. allg. Chem.*, **2004**, *630*, 1068–1073.
- [127] M. S. Bailey, M. N. Obrovac, E. Baillet, T. K. Reynolds, D. B. Zax, F. J. DiSalvo, *Inorg. Chem.*, **2003**, *42*, 5572–5578.
- [128] N. W. Falb, J. N. Neu, T. Besara, J. B. Whalen, D. J. Singh, T. Siegrist, *Inorg. Chem.*, **2019**, *58*, 3302–3307.
- [129] Y. Guan, W. Zhang, Q. Wang, C. Weidenthaler, A. Wu, W. Gao, Q. Pei, H. Yan, J. Cui, H. Wu, S. Feng, R. Wang, H. Cao, X. Ju, L. Liu, T. He, J. Guo, P. Chen, *Chem. Catalysis*, **2021**, *1*, 1042–1054.
- [130] C. E. Messer, J. C. Eastman, R. G. Mers, A. J. Maeland, *Inorg. Chem.*, **1964**, *3*, 776–778.
- [131] H. Kohlmann, K. Yvon, *J. Alloys Compd.*, **2000**, *299*, L16-L20.
- [132] C. E. Messer, K. Hardcastle, *Inorg. Chem.*, **1964**, *3*, 1327–1328.
- [133] V. M. Goldschmidt, *Naturwissenschaften*, **1926**, *14*, 477–485.
- [134] U. Müller, *Inorganic structural chemistry*, Wiley, **2007**.
- [135] Y. Wang, H. Zhang, J. Zhu, X. Lü, S. Li, R. Zou, Y. Zhao, *Adv. Mater.*, **2020**, *32*, 201905007 (16 pages).
- [136] J. Zheng, H. Fang, L. Fan, Y. Ren, P. Jena, Y. Wu, *J. Phys. Chem. Lett.*, **2021**, *12*, 7120–7126.
- [137] S. V. Krivovichev, *Z. Kristallogr. Cryst. Mater.*, **2008**, *223*, 109–113.
- [138] W. Li, Z. Wang, F. Deschler, S. Gao, R. H. Friend, A. K. Cheetham, *Nat. Rev. Mater.*, **2017**, *2*, 16099 (18 pages).
- [139] S. Fujii, S. Gao, C. Tassel, T. Zhu, T. Broux, K. Okada, Y. Miyahara, A. Kuwabara, H. Kageyama, *J. Am. Chem. Soc.*, **2021**, *143*, 10668–10675.
- [140] J. M. Skakle, J. G. Fletcher, A. R. West, *J. Chem. Soc., Dalton Trans.*, **1996**, 2497–2501.
- [141] A. Pabst, *Z. Kristallogr. Cryst. Mater.*, **1934**, *89*, 514–517.
- [142] Y. Sun, Y. Wang, X. Liang, Y. Xia, L. Peng, H. Jia, H. Li, L. Bai, J. Feng, H. Jiang, J. Xie, *J. Am. Chem. Soc.*, **2019**, *141*, 5640–5644.
- [143] J. Curda, E. M. Peters, W. Klein, M. Jansen, *Z. Kristallogr. NCS*, **2001**, *216*, 190.

- [144] L. Fanfani, G. Giuseppetti, C. Tadini, P. F. Zanazzi, *Mineral. mag.*, **1980**, *43*, 753–759.
- [145] A. Pabst, W. N. Sharp, *Am. Mineral.*, **1973**, *58*, 116–127.
- [146] J. W. Jeffery, *Acta Cryst.*, **1952**, *5*, 26–35.
- [147] D. DiLaura, *Opt. Photonics News*, **2008**, *19*, 22.
- [148] I. L. Azevedo, M. G. Morgan, F. Morgan, *Proc. IEEE*, **2009**, *97*, 481–510.
- [149] G. Blasse; B. C. Grabmaier, *Luminescent materials*, Springer-Verlag, **1994**.
- [150] U. Noomnarm, R. M. Clegg, *Photosynth. Res.*, **2009**, *101*, 181–194.
- [151] S. C. Gedam, S. J. Dhoble, S. V. Moharil, *Eur. Phys. J. Appl. Phys.*, **2007**, *37*, 73–78.
- [152] B. R. Judd, *Phys. Rev.*, **1962**, *127*, 750–761.
- [153] H. G. Friedman, G. R. Choppin, D. G. Feuerbacher, *J. Chem. Educ.*, **1964**, *41*, 354.
- [154] P. Dorenbos, *J. Phys.: Condens. Matter*, **2003**, *15*, 2645–2665.
- [155] B. Moine, C. Pedrini, B. Courtois, *J. Lumin.*, **1991**, *50*, 31–38.
- [156] J. L. Sommerdijk, A. Bril, *J. Lumin.*, **1975**, *10*, 145–147.
- [157] Uwe Happek, M. Aycibin, A. M. Srivastava, Holly Comanzol, S. Camardello, *ECS Trans.*, **2009**, *25*, 39–43.
- [158] P. Cai, L. Shi, C. Chen, M. Grinberg, H. J. Seo, *J. Lumin.*, **2018**, *195*, 141–152.
- [159] H. Bethe, *Ann. Phys.*, **1929**, *395*, 133–208.
- [160] J. J. Zuckerman, *J. Chem. Educ.*, **1965**, *42*, 315.
- [161] R. Krishnamurthy, W. B. Schaap, *J. Chem. Educ.*, **1969**, *46*, 799.
- [162] C. K. Jørgensen, in *Progress in inorganic chemistry: Volume 4*, Interscience, **1962**, p. 73.
- [163] C. K. Jørgensen, in *Advances in chemical physics: Volume 5*, John Wiley, **1963**, p. 33.
- [164] A. L. Tchougréeff, R. Dronskowski, *Int. J. Quantum Chem.*, **2009**, *109*, 2606–2621.
- [165] N. Kunkel, H. Kohlmann, A. Sayede, M. Springborg, *Inorg. Chem.*, **2011**, *50*, 5873–5875.

- [166] N. Kunkel, A. Meijerink, H. Kohlmann, *Phys. Chem. Chem. Phys.*, **2014**, *16*, 4807–4813.
- [167] *WinXPOW*, Stoe & Cie GmbH, **2011**.
- [168] P. Villars; K. Cenzual, *Pearson's Crystal Data*, ASM International: Materials Park, **2013**.
- [169] O. Madelung, U. Rössler, M. Schulz, **2010**, Springer Materials—The Landolt-Börnstein Database.
- [170] A. Jain, S. P. Ong, G. Hautier, W. Chen, W. D. Richards, S. Dacek, S. Cholia, D. Gunter, D. Skinner, G. Ceder, K. A. Persson, *APL Mater.*, **2013**, *1*, 011002 (11 pages).
- [171] A. W. Hewat, *MSF*, **1986**, *9*, 69–80.
- [172] M. Hoelzel, A. Senyshyn, N. Juenke, H. Boysen, W. Schmahl, H. Fuess, *Nucl. Instrum. Methods Phys. Res. A*, **2012**, *667*, 32–37.
- [173] H. M. Rietveld, *J. Appl. Cryst.*, **1969**, *2*, 65–71.
- [174] J. Rodríguez-Carvajal, *Physica B: Condensed Matter*, **1993**, *192*, 55–69.
- [175] V. Petříček, M. Dušek, L. Palatinus, *Z. Kristallogr. Cryst. Mater.*, **2014**, *229*, 345–352.
- [176] A. A. Coelho, *J. Appl. Cryst.*, **2003**, *36*, 86–95.
- [177] J. Tauc, R. Grigorovici, A. Vancu, *Phys. Stat. Sol. B*, **1966**, *15*, 627–637.
- [178] R. Dovesi, A. Erba, R. Orlando, C. M. Zicovich-Wilson, B. Civalleri, L. Maschio, M. Rérat, S. Casassa, J. Baima, S. Salustro, B. Kirtman, *Wiley Interdiscip. Rev. Comput. Mol. Sci.*, **2018**, *8*, e1360 (36 pages).
- [179] J. Perdew, K. Burke, M. Ernzerhof, *Phys. Rev. Lett.*, **1996**, *77*, 3865–3868.
- [180] C. Adamo, V. Barone, *J. Chem. Phys.*, **1999**, *110*, 6158–6170.
- [181] F. Weigend, R. Ahlrichs, *Phys. Chem. Chem. Phys.*, **2005**, *7*, 3297–3305.
- [182] R. E. Stene, B. Scheibe, A. J. Karttunen, W. Petry, F. Kraus, *Eur. J. Inorg. Chem.*, **2019**, *2019*, 3672–3682.
- [183] R. E. Stene, B. Scheibe, A. J. Karttunen, W. Petry, F. Kraus, *Eur. J. Inorg. Chem.*, **2020**, *2020*, 2260–2269.
- [184] A. J. Karttunen, T. Tynell, M. Karppinen, *J. Phys. Chem. C*, **2015**, *119*, 13105–13114.

- [185] N. Glebko, I. Aleksandrova, G. C. Tewari, T. S. Tripathi, M. Karppinen, A. J. Karttunen, *J. Phys. Chem. C*, **2018**, *122*, 26835–26844.
- [186] H. J. Monkhorst, J. D. Pack, *Phys. Rev. B*, **1976**, *13*, 5188–5192.
- [187] A. Togo, I. Tanaka, *arXiv.org*, **2018**, arXiv:1808.01590.
- [188] Y. Hinuma, G. Pizzi, Y. Kumagai, F. Oba, I. Tanaka, *Comput. Mater. Sci.*, **2017**, *128*, 140–184.
- [189] F. Pascale, C. M. Zicovich-Wilson, F. López Gejo, B. Civalleri, R. Orlando, R. Dovesi, *J. Comput. Chem.*, **2004**, *25*, 888–897.
- [190] C. M. Zicovich-Wilson, F. Pascale, C. Roetti, V. R. Saunders, R. Orlando, R. Dovesi, *J. Comput. Chem.*, **2004**, *25*, 1873–1881.
- [191] L. Maschio, B. Kirtman, M. Rérat, R. Orlando, R. Dovesi, *J. Chem. Phys.*, **2013**, *139*, 164101 (14 pages).
- [192] J. L. Sommerdijk, A. Bril, *J. Lumin.*, **1976**, *11*, 363–367.
- [193] U. Happek, M. Aycibin, A. M. Srivastava, H. Comanzol, S. Camardello, *ECS Trans.*, **2009**, *25*, 39–43.
- [194] F. Gingl, T. Vogt, E. Akiba, K. Yvon, *J. Alloys Compd.*, **1999**, *282*, 125–129.
- [195] W. L. Ludekens, A. J. Welch, *Acta Cryst.*, **1952**, *5*, 841.
- [196] M. Pezat, J. Senegas, G. Villeneuve, H.-H. Park, A. Tressaud, *J. Solid State Chem.*, **1988**, *77*, 389–393.
- [197] W. Bronger, L. Breil, *Z. anorg. allg. Chem.*, **1997**, *623*, 119–121.
- [198] H.-H. Park, M. Pezat, B. Darriet, *Rev. Chim. Min.*, **1986**, *23*, 323–328.
- [199] J. Ueda, S. Matsuishi, T. Tokunaga, S. Tanabe, *J. Mater. Chem. C*, **2018**, *6*, 7541–7548.
- [200] L. Sebastian, J. Gopalakrishnan, Y. Piffard, *J. Mater. Chem.*, **2002**, *12*, 374–377.
- [201] S. Fan, M. Lei, H. Wu, J. Hu, C. Yin, T. Liang, C. Li, *Energy Storage Mater.*, **2020**, *31*, 87–94.
- [202] W. Zhou, Y. Xu, L. Han, D. Zhu, *Dalton Trans.*, **2010**, *39*, 3681–3686.
- [203] S. C. Gedam, S. J. Dhoble, S. V. Moharil, *J. Lumin.*, **2007**, *124*, 120–126.

- [204] F. Yang, L. Wang, Y. Ge, L. Huang, D. Gao, J. Bi, G. Zou, *J. Alloys Compd.*, **2020**, 834, 155154 (7 pages).
- [205] B.-K. Choi, H. J. Labbé, D. J. Lockwood, *Solid State Commun.*, **1990**, 74, 109–113.
- [206] S. E. Rasmussen, J. E. Jørgensen, B. Lundtoft, *J. Appl. Cryst.*, **1996**, 29, 42–47.
- [207] Y. Yu, Z. Wang, G. Shao, *J. Mater. Chem. A*, **2019**, 7, 21985–21996.
- [208] V. F. Sears, *Neutron News*, **1992**, 3, 26–37.
- [209] L. Jin, M. A. Hayward, *Angew. Chem.*, **2020**, 132, 2092–2095.
- [210] N. Matsui, Y. Hinuma, Y. Iwasaki, K. Suzuki, J. Guangzhong, H. Nawaz, Y. Imai, M. Yonemura, M. Hirayama, G. Kobayashi, R. Kanno, *J. Mater. Chem. A*, **2020**, 8, 24685–24694.
- [211] S. Steinsvik, *Solid State Ion.*, **2001**, 143, 103–116.
- [212] X. Liu, T. S. Bjørheim, R. Haugsrud, *J. Mater. Chem. A*, **2017**, 5, 1050–1056.
- [213] G. Kobayashi, Y. Hinuma, S. Matsuoka, A. Watanabe, M. Iqbal, M. Hirayama, M. Yonemura, T. Kamiyama, I. Tanaka, R. Kanno, *Science*, **2016**, 351, 1314–1317.
- [214] F. Takeiri, A. Watanabe, A. Kuwabara, H. Nawaz, N. I. Ayu, M. Yonemura, R. Kanno, G. Kobayashi, *Inorg. Chem.*, **2019**, 58, 4431–4436.
- [215] S. Iimura, H. Hosono, *J. Phys. Soc. Jpn.*, **2020**, 89, 051006 (15 pages).
- [216] O. Schmitz-Dumont, A. Weeg, *Z. anorg. allg. Chem.*, **1951**, 265, 139–155.
- [217] D. Durach, W. Schnick, *Eur. J. Inorg. Chem.*, **2015**, 2015, 4095–4100.
- [218] J. A. Kechele, C. Schmolke, S. Lupart, W. Schnick, *Z. anorg. allg. Chem.*, **2010**, 636, 176–182.
- [219] F. Gehlhaar; *Master's thesis*, Universität Leipzig, **2019**.
- [220] M. Grinberg, S. Mahlik, K. Wisniewski, H. J. Seo, *J. Phys.: Condens. Matter*, **2011**, 23, 35404.
- [221] S. Lizzo, A. Meijerink, G. J. Dirksen, G. Blasse, *J. Phys. Chem. Solids*, **1995**, 56, 959–964.
- [222] A. Ellens, A. Meijerink, G. Blasse, *J. Lumin.*, **1994**, 60-61, 70–73.
- [223] P. K. Chattaraj, H. Lee, R. G. Parr, *J. Am. Chem. Soc.*, **1991**, 113, 1855–1856.

- [224] C. Balarew, R. Duhlev, *J. Solid State Chem.*, **1984**, *55*, 1–6.
- [225] M. A. Kraft, S. P. Culver, M. Calderon, F. Böcher, T. Krauskopf, A. Senyshyn, C. Dietrich, A. Zevalkink, J. Janek, W. G. Zeier, *J. Am. Chem. Soc.*, **2017**, *139*, 10909–10918.
- [226] H. Morkoç, S. Strite, G. B. Gao, M. E. Lin, B. Sverdlov, M. Burns, *J. Appl. Phys.*, **1994**, *76*, 1363–1398.

7 Publications and manuscripts

7.1 $\text{M}\text{CaH}_x\text{F}_{3-x}$ (M = Rb, Cs): Synthesis, Structure, and Bright, Site-Sensitive Tunable Eu^{2+} Luminescence

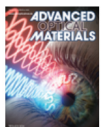
Alexander Mutschke, Thomas Wylezich, Atul D. Sontakke, Andries Meijerink, Markus Hoelzel and Nathalie Kunkel

Published in:

Adv. Optical Mater. **2021**, *9*, 2002052

Reproduced from Alexander Mutschke, Thomas Wylezich, Atul D. Sontakke, Andries Meijerink, Markus Hoelzel, Nathalie Kunkel*, *Adv. Optical Mater.* **2021**, *9*, 2002052 with permission from Wiley-VCH Verlag GmbH & Co. KGaA, Weinheim.

© 2021 Wiley-VCH Verlag GmbH & Co. KGaA, Weinheim.



MCaH_xF_{3-x} (M = Rb, Cs): Synthesis, Structure, and Bright, Site-Sensitive Tunable Eu²⁺ Luminescence

Author: Nathalie Kunkel, Markus Hoelzel, Andries Meijerink, et al

Publication: Advanced Optical Materials

Publisher: John Wiley and Sons

Date: Feb 4, 2021

© 2021 The Authors. Advanced Optical Materials published by Wiley-VCH GmbH

Welcome to RightsLink


John Wiley and Sons has partnered with Copyright Clearance Center's RightsLink service to offer a variety of options for reusing this content.

Note: This article is available under the [Creative Commons CC-BY-NC-ND](#) license and permits non-commercial use of the work as published, without adaptation or alteration provided the work is fully attributed.

For commercial reuse, permission must be requested below.

For an understanding of what is meant by the terms of the Creative Commons License, please refer to [Wiley's Open Access Terms and Conditions](#).

If you wish to adapt, alter, translate or create any other derivative work from this article, permission must be sought from the Publisher. Please email your requirements to RightsLink@wiley.com.

I would like to... 

Figures in chapter 3 were adapted and adjusted with permission from Wiley-VCH Verlag GmbH & Co. KGaA, Weinheim.

Content

This publication concerns the synthesis, structures and optical properties of the two solid-solution series $\text{RbCaH}_x\text{F}_{3-x}$ and $\text{CsCaH}_x\text{F}_{3-x}$. Hydridic samples are accessible by solid-state reactions under hydrogen pressure. The pure fluorides can be synthesized *via* a simple solid-state reaction in Ni-alloy ampoules. The structures are elucidated by powder X-ray and powder neutron diffraction in combination with Raman spectroscopy. Hereby it is shown that both solid-solution series retain the ideal cubic perovskite structure and follow Vegard's law throughout all anionic constitutions. Thus, heteroanionic phases with disordered anions are formed. Upon doping the solid-solution series $\text{CsCaH}_x\text{F}_{3-x}$ with 1 mol% divalent europium, bright luminescence with varying emission colours depending on the hydride content within the mixed phases can be detected. Gradually replacing the fluoride anions by hydrides results in observable redshifted luminescence which is in line with several previous studied europium doped hydride fluorides. In contrast to the earlier reported related systems, a complete new type of redshift is observed. By photoluminescence spectroscopy it can be detected that the redshift is solely due to new narrow emission bands emerging at lower energy regions instead of a gradual shift of a single emission band. Overall, the ratio of the respective emission bands determines the optically discernible redshift. By lifetime measurements of the excited states it is shown that several distinct emissive Eu^{2+} centres are formed that preferably occupy hydridic sites. This introduces a further mechanism to selectively tune the emission colour by varying the dopant concentrations. Higher amounts of Eu^{2+} dopants further redshift the emission colour due to more intense emission bands at the low energy sites.

Contributions

This publication was written in the scope of this thesis. Preparation of the samples was conducted by A.M. Structural characterization, *i.e.* Rietveld refinements of the samples were performed by A.M. Neutron diffraction in this regard was conducted by M.H. Beam time at the SPODI of the FRMII, Garching is gratefully acknowledged. Luminescence emission and excitation spectroscopy were conducted and evaluated by A.M., T.W. and A.D.S. Lifetime measurements were conducted by A.D.S.

The manuscript was written through contribution of all co-authors. Leading author is A.M., corresponding author N.K.



RESEARCH ARTICLE

M₂CaH_xF_{3-x} (M = Rb, Cs): Synthesis, Structure, and Bright, Site-Sensitive Tunable Eu²⁺ Luminescence

Alexander Mutschke, Thomas Wylezich, Atul D. Sontakke, Andries Meijerink, Markus Hoelzel, and Nathalie Kunkel*

Dedicated to Prof. H. P. Beck on the occasion of his 80th birthday

With increasing interest in mixed-anionic hydrides, a number of interesting properties have been reported. Here, the structural and optical properties of (Eu²⁺-doped) M₂CaH_{3-x}CaF₃ (M = Rb, Cs) are investigated. For M = Rb, a complete hydride–fluoride solid solution series is found and for M = Cs, the known solid solution series (0 ≤ x ≤ 1.70) can be extended to x = 3. In case of Cs, a very bright luminescence emission is observed in Eu²⁺-doped samples, whereas the luminescence is fairly weak in Rb based compounds. With increasing hydride content, a shift of the emission color from cyan-green to red can be observed. In contrast to earlier reports for mixed fluoride–hydride host, the redshift is not a gradual shift of a single broad emission band, but the appearance of new narrow emission bands on the low energy side, which are assigned to the occupation of sites with higher hydride content. Consequently, this finding represents the first example in a mixed anionic hydride with a site-sensitive emission for sites with locally varying hydride content in the first coordination sphere and may serve as a general example for emission color tuning taking advantage of mixed-anionic compounds.

is known to allow for a tailoring of the emission properties of the 5d–4f transition of Eu²⁺,^[7–10] in the following, the structural and optical properties of the (Eu²⁺-doped) systems M₂CaH_{3-x}CaF₃ (M = Rb, Cs) are investigated.

In case of M = Rb, so far no solid solution series was reported and the pure hydride and fluoride both crystallize in the ideal cubic perovskite structure type at room temperature.^[11–15] For M = Cs, the partial solid solution series CsCaH_xF_{3-x} (0 ≤ x ≤ 1.70) crystallizing in the cubic perovskite structure type has been reported earlier^[16] as well as the pure hydride CsCaH₃.^[17] However, due to the synthesis route starting from CsF, CaF₂, and CaH₂, the possible composition range of the solid solution was limited to an upper limit of x = 2. In case of the lighter M = K, a solid-solution series with a miscibility gap as well as a change

from a tetragonal structure with partial anion ordering to the GdFeO₃ structure type for fluoride rich samples has been reported.^[18–19] Doped with rare earth ions and codoped with divalent manganese, alkali alkaline earth fluoroperovskites have been of interest for photoluminescence application and radiation dosimetry.^[20–28] For instance, Sommerdijk and Brill reported on weak Eu²⁺ luminescence in RbCaF₃ (475 nm at 300 K) and bright green emission in CsCaF₃. Lately, Eu²⁺ emission has also been studied in such hydride–fluoride solid solution series or hydrides with fluoride structural analogs,

1. Introduction

Due to the increasing interest in alternative energy storage, materials for hydrogen-based energy storage have been studied.^[1–2] As a result of the similar radii of fluoride and hydride ions, structural similarities between metal hydrides and fluorides can be found^[3] and fluoride substitution in metal hydrides is, for instance, proposed to tune the temperature of hydrogen release for thermal energy storage applications and thermally activated anion diffusion was studied.^[4–6] Since tuning the anion chemistry

A. Mutschke, Dr. T. Wylezich, Dr. N. Kunkel
Chair for Inorganic Chemistry with Focus on Novel Materials
Technical University of Munich
Lichtenbergstr. 4, Garching 85748, Germany
E-mail: nathalie.kunkel@uni-goettingen.de

The ORCID identification number(s) for the author(s) of this article can be found under <https://doi.org/10.1002/adom.202002052>.

© 2021 The Authors. Advanced Optical Materials published by Wiley-VCH GmbH. This is an open access article under the terms of the Creative Commons Attribution-NonCommercial-NoDerivs License, which permits use and distribution in any medium, provided the original work is properly cited, the use is non-commercial and no modifications or adaptations are made.

DOI: 10.1002/adom.202002052

Dr. T. Wylezich, Dr. N. Kunkel
Institut für Anorganische Chemie
Georg-August-University Goettingen
Tammannstr. 4, Goettingen 37077, Germany

Dr. T. Wylezich, Dr. N. Kunkel
Woehler Research Institute for Sustainable Chemistry (WISCh)
Georg-August-University Goettingen
Tammannstr. 2, Goettingen 37077, Germany

Dr. A. D. Sontakke, Prof. A. Meijerink
Condensed Matter & Interfaces
Debye Institute for Nanomaterials Science
Utrecht University
Princetonplein 1, Utrecht 3584 CC, The Netherlands

Dr. M. Hoelzel
Heinz Maier-Leibnitz-Zentrum (MLZ)
Technische Universität München
Lichtenbergstr. 1, Garching 85748, Germany

such as $\text{MMgH}_x\text{F}_{3-x}$ ($M = \text{Na, K, Rb}$), K_2MgH_4 , LiMH_3 ($M = \text{Sr, Ba}$), $\text{LiSr}_2\text{SiO}_4\text{H}$ or $\text{Sr}_5(\text{BO}_3)_3\text{H}$,^[29–36] and a correlation between the hydride content and redshift of the emission energies was found, which can be explained by the stronger nephelauxetic effect of hydride compared to fluoride.^[37]

Here, we present the structural and optical properties of Eu^{2+} -doped samples of $\text{MCAH}_3\text{-MCAf}_3$ ($M = \text{Rb, Cs}$). In contrast to earlier reports on mixed hydride–fluorides, where a red shift of a single emission band could be observed with increasing hydride content, in the present case the changes in the emission color are rather caused by additional new emerging emission bands in the orange/red emission range. These new emissions bands exhibit narrow bandwidths and are assigned to a site-sensitive Eu^{2+} 5d–4f emission originating from different local F^-/H^- environments with different hydride content.

2. Results and Discussion

The undoped compounds $\text{MCAH}_x\text{F}_{3-x}$ ($M = \text{Rb, Cs}$) were obtained as colorless powders. On Eu^{2+} doping, the higher hydride content samples of $\text{MCAH}_x\text{F}_{3-x}$ ($M = \text{Rb, Cs}$) showed slightly red coloration. In the CsCaH_3 sample, the side phase Cs_2CaH_4 is always additionally found, which also had earlier been mistaken for CsCaH_3 ^[38] and later it was clarified that both phases coexists.^[17,39] While the Eu^{2+} -doped $\text{RbCaH}_x\text{F}_{3-x}$ did not show any strong emission even at liquid nitrogen temperature, bright cyan-green to red emission could be observed from $\text{CsCaH}_x\text{F}_{3-x}$ (see Figure 1).

2.1. Crystal Structure of $\text{MCAH}_x\text{F}_{3-x}$ ($M = \text{Rb, Cs}$)

Since the pure MCAH_3 ($M = \text{Rb, Cs}$) as well as MCAf_3 ($M = \text{Rb, Cs}$) crystallize in the ideal cubic perovskite structure in space



Figure 1. Photographic images of the solid solution series $\text{CsCaH}_x\text{F}_{3-x}:\text{Eu}^{2+}$ ($x \leq 2.5$) under day light (top) and the corresponding emission glow under 376 nm UV irradiation (bottom). (From left to right: $x = 0, 0.25, 0.5, 0.75, 1.0, 1.5, 2.0,$ and 2.5 .)

group $Pm\bar{3}m$ (221), the solid solution series were found to crystallize isotopic as well. Here, only one distinct anion site (3c) is present which can be occupied by hydride or fluoride. Since no symmetry reduction could be noticed in the diffraction patterns, an ordered anion distribution, which would lead to a splitting of the 3c site, is ruled out. Additionally, Raman spectra were recorded (see Figures S1 and S2 in the Supporting Information) and no signals could be observed. This is consistent with the expectation that due to the Raman-inactive space group symmetry (O_h) of the ideal cubic perovskite structure no Raman signals are supposed to be visible. For example, however, for the tetragonal low temperature phase ($I4/mcm, D_{4h}^{18}$) of RbCaF_3 Raman signals are observed.^[14]

X-ray powder diffraction patterns were recorded and analyzed by the means of Rietveld refinement. Here, the total occupancy of the anion site (3c) by hydride and fluoride was set to 1, as it can be expected for an ionic compound. The fluoride content was refined and the remaining anion content assumed to be hydride. This was double-checked for several samples by analyzing the hydride content via elemental analysis (see the Experimental Section). Furthermore, for $\text{CsCaD}_{1.5}\text{F}_{1.5}$ also a neutron powder diffraction pattern was recorded and simultaneously refined together with the X-ray data. In contrast to X-ray data, where hydrogen is nearly invisible, ^2H has a bound coherent scattering length of 6.671(4) fm,^[40] so that its position and occupation numbers can be reliably determined from neutron diffraction. Bound coherent scattering lengths for ^{19}F , $^{\text{nat}}\text{Ca}$, and ^{133}Cs are 5.654(10), 4.70(2), and 5.42(2) fm, respectively.

The X-ray powder diffraction patterns obtained for the solid solution series $\text{MCAH}_x\text{F}_{3-x}$ ($M = \text{Rb, Cs}$) as well as the refined lattice parameters (a) as function of the hydrogen content x for both solid solution series are shown in Figure 2.

For both systems it can be clearly seen that with increasing hydride content, the Bragg reflections are gradually shifted toward smaller 2θ angles. This is in agreement with previous reports of hydride–fluoride solid solution series,^[30] where the crystal lattice gradually expands with incorporation of hydride and can be explained by the higher thermal vibration of hydride due to its lower mass and the less polarizable character of fluoride. Furthermore, some reflections lose scattering intensity by the hydride–fluoride exchange. This is most noticeable on the Bragg reflection at $\approx 35^\circ$ 2θ (111). While this reflection is strongly visible for the pure fluorides RbCaF_3 and CsCaF_3 , its intensity gradually diminishes by increasing the hydride content, being barely visible for the pure hydrides RbCaH_3 and CsCaH_3 . This is in good agreement with hydride incorporation, since as more fluoride ions are exchanged by hydrides, the scattering power of some lattice planes is reduced since hydride is a much weaker X-ray scatterer than fluoride. The cell parameters were refined using the program package FullProf. An exemplary refinement plot is depicted in the Figure 3a. Refined lattice parameters as well as interatomic distances and H-content of $\text{RbCaH}_x\text{F}_{3-x}$ are listed in Table S1 (Supporting Information), additional structural information in Tables S2 and S3 (Supporting Information).

As seen in Figure 2c a linear increase of the lattice parameter can be assumed, hence the following relation for the cell parameters and cell volume in dependency of the hydride

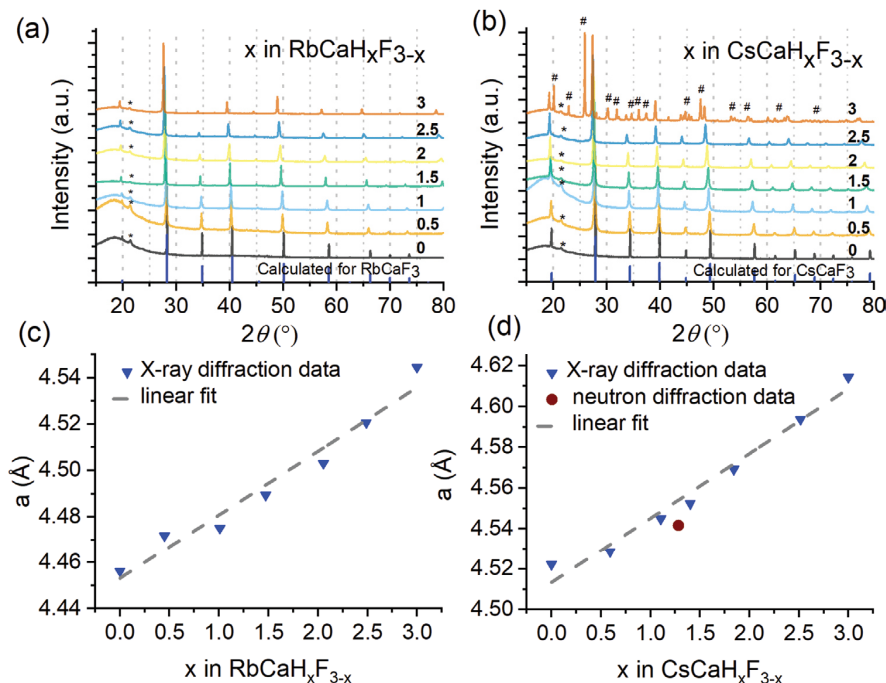


Figure 2. X-ray diffraction patterns of the solid solution series a) $\text{RbCaH}_x\text{F}_{3-x}$ and b) $\text{CsCaH}_x\text{F}_{3-x}$. The vertical dotted lines are meant to guide the eye. The asterisks mark a background reflection caused by the grease used to fixate the sample between the kapton foil. # marks reflection belonging to the side phase Cs_2CaH_4 . Refined cell parameters (a) plotted in dependency of the hydride (x) content in the mixed phase c) $\text{RbCaH}_x\text{F}_{3-x}$ and d) $\text{CsCaH}_x\text{F}_{3-x}$.

content x can be formulated for the solid solution series $\text{RbCaH}_x\text{F}_{3-x}$

$$a = 0.028(3)x\text{\AA} + 4.453(5)\text{\AA} \quad (1)$$

$$V = 1.7(1)x\text{\AA}^3 + 88.2(2)\text{\AA}^3 \quad (2)$$

In case of the heavier homologues CsCaH_3 and CsCaF_3 a solid solution series $\text{CsCaH}_x\text{F}_{3-x}$ with an upper limit $x = 1.7$ had already been known.^[16] Since only CsF and no elemental Cs or CsH had been used in the reported synthesis route, an upper limit of $x = 2.0$ was set due to the starting materials. To test if high hydride contents can be obtained, we used elemental cesium metal, which was hydrogenated during the reaction, and were able to synthesize the complete solution series $\text{CsCaH}_x\text{F}_{3-x}$.

However, the side phase Cs_2CaH_4 is clearly visible (marked with #) and unavoidable with the accessible synthesis methods. A Rietveld refinement plot thereof is depicted in Figure 3b.

To check for hydrogen positions and anion distribution, an additional neutron powder pattern was recorded for phase $\text{CsCaD}_{1.5}\text{F}_{1.5}$. The Rietveld refinement of the structure using the neutron data is depicted in Figure 3c. Refinement with a lower space group symmetry that allows for ordering of the anions (instead of a random distribution of F^- and H^- over the anion sites) was tested, but resulted in a strong deviation of the calculated refinement from the measured pattern. Hence, a statistical distribution of the anions in the ideal perovskite structure is assumed. As expected, the lattice parameter of the deuteride

is slightly smaller than for the corresponding hydride, which is typical due to the higher mass and therefore lower thermal vibration of ^2H compared to ^1H .^[41]

Refined lattice parameters as well as interatomic distances and H-content of the solid solution series $\text{CsCaH}_x\text{F}_{3-x}$ are listed in Table S4 (Supporting Information), additional information on the refinement can be found in Tables S5 and S6 (Supporting Information).

As can be seen in Figure 2d the lattice parameter a shows a nearly linear increase with increasing hydride content and the relation of a and cell volume V as a function of hydride content obtained from X-ray data can be formulated as follows

$$a = 0.032(2)x\text{\AA} + 4.513(4)\text{\AA} \quad (3)$$

$$V = 2.0(2)x\text{\AA}^3 + 91.9(3)\text{\AA}^3 \quad (4)$$

To further substantiate the incorporation of hydrogen within the crystal lattice and to confirm the values obtained from Rietveld refinement, elemental analysis of the hydrogen content of three mixed phases ($x = 0.5, 1.5, 2.5$) of both solid solution series has been carried out. The determined hydrogen content compared to the determined values obtained by Rietveld refinement is shown in Tables S7 and S8 (Supporting Information). All obtained values of the elemental analysis reports are depicted in Figures S4–S6 (Supporting Information).

The determined weight percentages by Rietveld refinement are very close to the values of the mixed phases with ideal

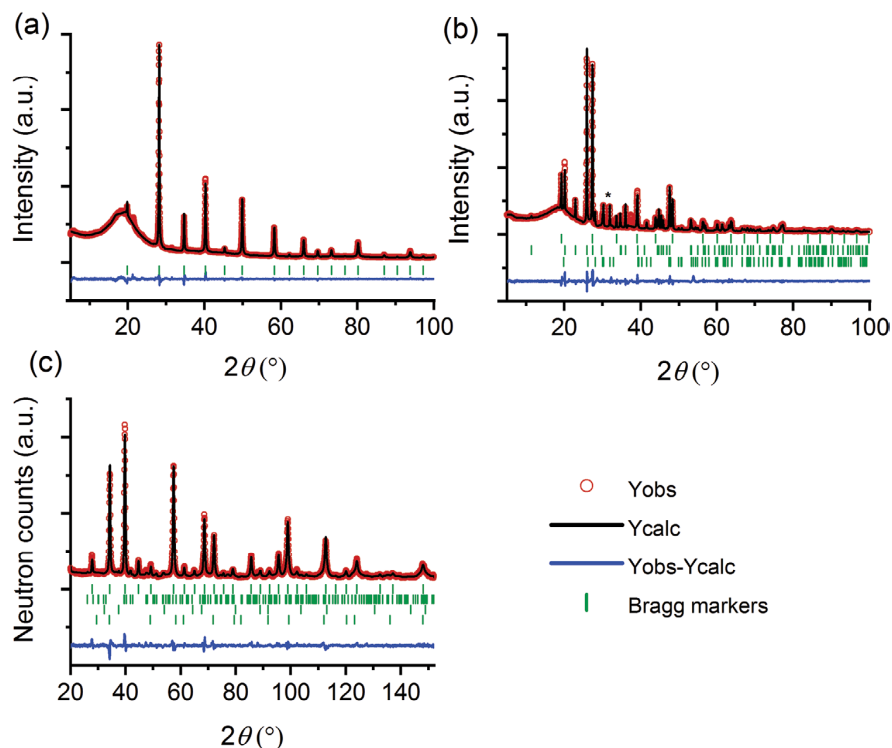


Figure 3. X-ray powder diffraction Rietveld refinement plots of a) the crystal structure of RbCaHF_2 , and of b) the crystal structure of CsCaH_3 . Bragg markers from top to bottom: CsCaH_3 (31.6(4) wt%), Cs_2CaH_4 (45.6(5) wt%), and CaH_2 (22.8(4) wt%). $R_p = 4.0\%$, $R_{wp} = 5.94$, $R_{exp} = 3.91$, $\chi^2 = 2.31$. The asterisk (*) marks a Bragg reflection of an unidentified sidephase. It was excluded from Rietveld refinement. c) Rietveld refinement plot of the neutron diffraction pattern. Bragg markers from top to bottom: $\text{CsCaD}_{1.5}\text{F}_{1.5}$ (97.04 wt%), CaD_2 (2.15 wt%), CaO (0.43 wt%), CaF_2 (0.39 wt%). $R_p = 5.10\%$, $R_{wp} = 6.53\%$, $R_{Bragg} = 3.15\%$, $\chi^2 = 4.97$.

stoichiometric compositions. This finding could also be confirmed by elemental analysis, which shows a good agreement with the targeted compositions with only small deviations.

2.2. Luminescence Properties of Eu^{2+} -Doped $\text{CsCaH}_x\text{F}_{3-x}$

As shown in Figure 1, the solid solution series of $\text{CsCaH}_x\text{F}_{3-x}$ exhibit bright Eu^{2+} emission under UV excitation causing intense cyan-green to deep red emission glow. Figure 4a presents the corresponding luminescence spectra at room temperature. The bright cyan-green emission found in the fluoride $\text{CsCaF}_3:\text{Eu}^{2+}$ was first described by Sommerdijk and Bril in 1975.^[24] In a following publication, the authors also described a large redshift of the luminescence of 100 nm when decreasing the temperature from 300 to 77 K, which they explain by the existence of two distinct Eu^{2+} centers.^[23] However, compared to other fluorides the Stokes shift is rather large; for instance, in LiBaF_3 or KMgF_3 , Eu^{2+} 4f–4f emission could be observed due to the high-lying 5d states for Eu^{2+} on the large 12-coordinated lattice site in these fluoride perovskites.^[42,43] The observation of longer wavelength emission in CsCaF_3 reflects that here Eu^{2+} substitutes on the six-coordinated Ca^{2+} site (see Figure S7 in the Supporting Information). Dorenbos ascribed the large Stokes shift and the comparatively wide emission band in $\text{CsCaF}_3:\text{Eu}^{2+}$ to an anomalous

Eu^{2+} luminescence.^[28] Another explanation by Happek et al. assumed a Jahn–Teller distortion in the excited $5d^1$ state.^[27]

As clearly seen in Figure 4a, the emission red shift with increasing hydride content as perceived with the naked eye is not solely caused by a red shift of a single emission band, but it involves a rather interesting phenomenon demonstrating appearance of narrowband emissions at lower energies and their subsequent intensity tuning. The emission of CsCaF_3 found here has an emission maximum of 510 nm and is same as the value found in earlier reports.^[23,27–28] As the hydride content within the mixed phase increases, a small shift of the emission band of about 30 nm can be observed unto the phase $\text{CsCaH}_{0.5}\text{F}_{2.5}$, showing its emission maximum at ≈ 540 nm. The red shift agrees with earlier observations of other mixed hydride–fluorides and pure hydrides that all show a red shift caused by the nephelauxetic effect induced by the more polarizable and covalent hydride ions compared to fluoride.^[29–37] However, emission spectra of the $\text{CsCaH}_x\text{F}_{3-x}$ solid solutions appear to exhibit several rather narrower emission bands, which become more prominent in samples with a hydride content above $x \geq 0.5$. The emission spectra show the emergence of emission bands at roughly 540, 575, 635 nm, etc. The emission band at 540 nm gradually loses intensity with further increasing hydride content in the solid solutions and shifts the emission maxima to newly emerged emission band at about 575 nm.

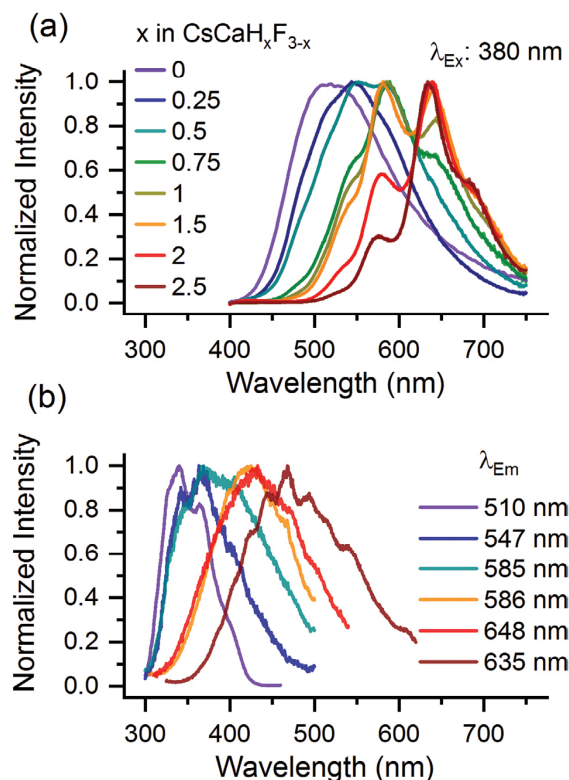


Figure 4. a) Room temperature PL spectra of the Eu^{2+} (1 mol% regarding Ca^{2+} via addition of EuF_2) doped solid solution series of $\text{CsCaH}_x\text{F}_{3-x}$; and b) the PLE spectra monitoring peak emission in different samples. The samples are identified with line colors as indicated in (a). $\lambda_{\text{exc}} = 380$ nm for PL in (a), whereas the PLE spectra were monitored at different wavelengths as indicated in (b).

The 575 nm emission band also loses intensity for solid solutions with a hydride content $x > 1.5$, while the emission band at ≈ 635 nm reaches its intensity maximum with a hydride content of $x = 2$. Figure 4b presents the PLE spectra of different samples monitoring the respective peak emission wavelengths. The PLE spectra reveal structureless profiles, but consistently shifts toward longer wavelength following the emission wavelength shift and hydride contents. This suggests that the different emission bands are arising from different sites in $\text{CsCaH}_x\text{F}_{3-x}$ solid solution. A careful observation reveals that the excitation band monitoring same emission wavelength in different samples also differ. The higher hydride content composition exhibits relatively larger red shifted PLE.

The appearance of narrowband PL with hydride contents is rather unusual and may be caused by several effects. As in case of the pure fluoride, an excitonic emission might also be discussed. In rocksalt-type alkali metal halides as well as in alkaline-earth metal fluoride halides, different types of defects have been modeled and experimentally observed, such as self-trapped holes, electrons trapped at halide-vacancies or Schottky type lattice defects in BaFCl .^[44–46] Given the hydride–fluoride analogy^[5] and recent observations of defect formation in mixed anionic hydrides,^[47] defect formation could be a

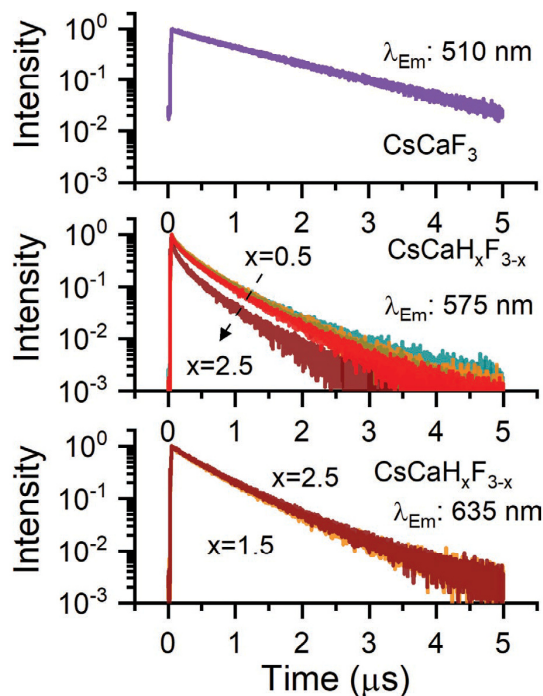


Figure 5. Eu^{2+} PL decay curves in $\text{CsCaH}_x\text{F}_{3-x}$ compounds monitored at different peak emission wavelengths. The excitation wavelength is 375 nm. Doping with Eu^{2+} via addition of EuF_2 during synthesis.

possible explanation. However, this does not explain the narrower nature of emission bands. Furthermore, since Eu^{2+} -emission in pure CaH_2 was reported to be at 764 nm and exhibits significantly broadband profile (full width at half maximum, FWHM, ≈ 200 nm),^[48] the possibility of a possible luminescent $\text{CaH}_2:\text{Eu}^{2+}$ side phase can be ruled out. A more likely explanation might be the occupation of sites with different hydride content. For a statistical distribution, locally, different sites with different F:H ratio may appear, where such sites can exhibit relatively stronger site rigidity brought about by mixed anions offering a more compact packing of coordination sphere, and thus leading narrower emissions. With increasing overall hydride content, the weight fractions of the different arrangements will follow the relative F/H ratio, leading to an increase in lower energy emission sites with hydrogen rich arrangement over the fluorine rich arrangements. Analysis of low temperature emission spectra (vide infra) support this explanation.

Figure 5 presents the Eu^{2+} PL decay curves for different emission peaks in $\text{CsCaH}_x\text{F}_{3-x}$ solid solutions. The $\text{CsCaF}_3:\text{Eu}^{2+}$ sample reveals single exponential decay profile, agreeing well with single Eu^{2+} site in this compound.^[49] With hydride inclusion, the prominent narrowband emissions appear at around 575 and 635 nm. The decay curves monitoring at 575 nm reveals nonexponential feature, and exhibits faster relaxation for higher hydride contents, whereas the 635 nm decay curves did not show significant variation with hydride contents. This suggests that for the 575 nm emission an additional decay path opens which increases as hydride contents increase. The results are consistent with PL observations. Accordingly, with increasing

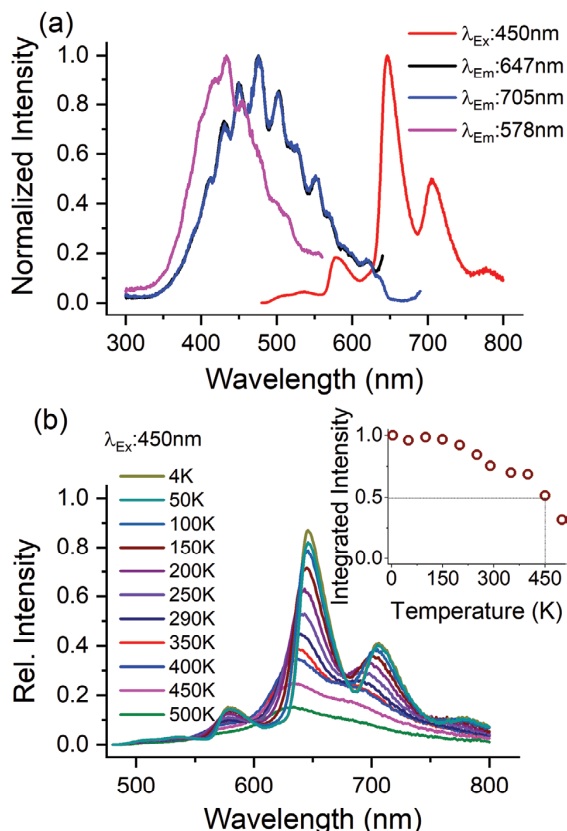


Figure 6. a) 4.2 K PL-PLE spectra of CsCaH₂F:Eu²⁺ sample; and b) temperature dependence of PL. The inset shows a plot of integrated intensity versus temperature. The sample was doped with Eu²⁺ by the addition of EuF₂ during synthesis.

hydride contents in CsCaH_xF_{3-x}, the fraction of longer wavelength emitting sites increases which additionally quenches the 575 nm emission following resonant energy transfer from the 575 nm sites to the red emitting sites.^[50]

To get further insight on Eu²⁺ luminescence in CsCaH_xF_{3-x} solid solution, the luminescence properties were investigated at 4.2 K. **Figure 6a** presents the PL and PLE of CsCaH₂F:Eu²⁺ (1%) sample at 4.2 K. The PL bands are better resolved and can be distinctively identified. Accordingly, there are four prominent emissions peaking at 578, 647, 705, and 780 nm. In addition, few weak emission bands could be identified at around 510 and 540 nm. The PLE monitored for 578 nm emission peaks at 427 nm, whereas for 647 and 705 nm, the PLE is almost identical with peak maximum at about 470 nm. This indicates that the 705 nm emission is primarily fed through sensitization from 647 nm emitting Eu²⁺ ions. This suggests that the 705 nm emitting sites are less abundant than the 647 and 578 nm emitting sites. Also, a clear evidence of multiple sites is evident from the differences in PLE of 578 nm emission and the PLE of the 647 and 705 nm emission.

A tentative assignment can be made to the different narrow emission peaks to Eu²⁺ with 0 to 6 H⁻ (and thus 6–0 F⁻) in the first octahedral coordination shell. Based on the observed peak intensities and the relative intensities expected based on

a statistical occurrence of a specific 6-coordination in CsCaH₂F (66.6% H⁻, 33.3%F⁻), the weak 510 nm emission feature is assigned to Eu²⁺ with 0 or 1 H⁻ (expected abundances 0.1% and 1.6%). The 540 nm peak to Eu²⁺ with a 2 H⁻/4F⁻ coordination (8.2%), 578 nm to Eu²⁺ with 3H⁻/3F⁻ (21.9%), 647 nm to 4H⁻/2F⁻ (32.9%, most abundant coordination), 705 nm to 5H⁻/1F⁻ (26.3%), and 780 nm to Eu²⁺ with full octahedral H⁻ coordination (8.8%). There is a good agreement with the observed relative intensities and expected intensities based on a statistical distribution of F⁻ and H⁻ in the first coordination shell. For CsCaH₂F indeed the 4H⁻/2F⁻ coordination is the most abundant in line with the observation of the strongest emission line at 647 nm. Energy transfer between the different Eu²⁺ sites can explain some of the observed differences such as the somewhat lower than expected relative intensity of the 578 nm emission line due to energy transfer to Eu²⁺ ions emitting at 647 nm, in line with the faster decay observed for the 575 nm emission (see Figure 5). It is interesting to see that with every additional H⁻ replacing F⁻ the emission band shifts to ≈1500 cm⁻¹ lower energies, although there some variation in the energy shifts. It will be interesting to use recently developed model for energy level calculations for the 4f⁶5d state of Eu²⁺ to verify the observed energy shifts upon gradually changing the coordination from [EuF₆]⁴⁻ to [EuH₆]⁴⁻.^[51] Possibly, the observation of multiple site emission instead of a broad band might be caused by the occupation of the octahedral Ca²⁺-site, which might, with its smaller ionic radius lead to a rather rigid environment. In previously studied perovskite hydride, Eu²⁺ luminescence was never reported for a Ca²⁺-containing perovskite. The emission spectra as a function of temperature are presented in Figure 6b. The spectra show a small peak blueshift and band broadening with temperature. A blueshift in the emission of Eu²⁺ or Ce³⁺ with increasing temperature may have several reasons, among others the increase of the activator–ligand distance and the consequent decrease of the crystal field strength and covalency of the ligand-activator bond.^[27,52] The observed blueshift of the main emission maximum from Figure 6b (see Figure S8 in the Supporting Information) is ≈370 cm⁻¹, larger than thermochromic blueshifts of the 4f⁶5d¹–4f⁷ emission of Eu²⁺ in other halide hosts, but still significantly smaller than the blueshifts reported for pure borohydride systems.^[52,53]

The FWHM for the most prominent emission at 647 nm is about 28 nm at 4.2 K and increases till 35 nm at 300 K with the peak position shifting from 647 to 635 nm. This is due to temperature-induced effects, such as site expansion, which leads to a reduced crystal field strength, and an increase in bond length variations. The integrated PL intensity is constant till 150 K and then slowly reduces. The T_{50%} is at about 450 K, suggesting good PL stability of studied mixed halide-fluorides. It is difficult to evaluate individual thermal stability of different bands due to their intermixed nature, both in PL and PLE features as well as thermally induced spectral changes and temperature dependent energy transfer between different Eu²⁺ sites. Nevertheless, it is evident that the emission is fairly stable till room temperature and all emission bands are present even at room temperature spectrum.

Figure 7a shows the Eu²⁺ PL in CsCaH₂F compounds having different doping concentrations. Interestingly, the low

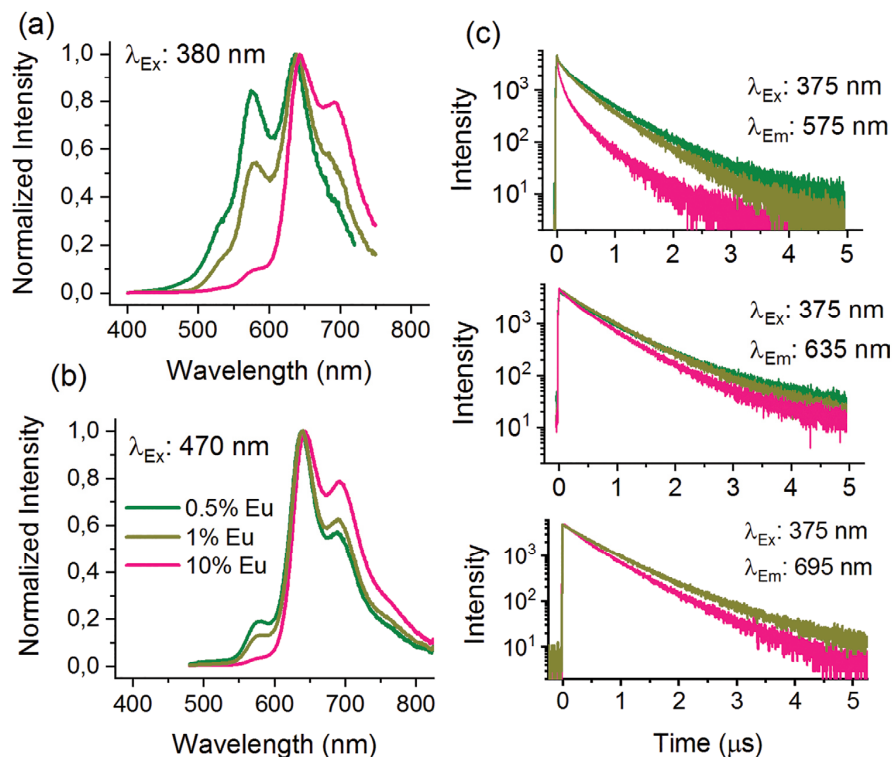


Figure 7. PL spectra of CsCaH₂F doped with different Eu contents under a) 380 nm excitation and b) 470 nm excitation. The PL decay curves monitoring different emission peaks are presented in (c). The samples were doped with Eu²⁺ by adding the appropriate amounts of EuF₂ during synthesis.

Eu²⁺ concentration sample exhibits more prominent higher energy emission bands, which systematically decrease in intensity as the doping concentration increases. This is consistent with the energy transfer-based quenching. Similar effects are observed under 470 nm excitation (Figure 7b). The decay curves (Figure 7c) further confirm the energy transfer quenching as the 575 nm emission is quenched faster with increase in Eu²⁺ contents as demonstrated by the faster decay in the higher doped materials.

The observed redshift upon substitution of F⁻ by H⁻ is very interesting and offers great emission tunability. Both composition and doping concentration in CsCaH_xF_{3-x} solid solution can easily be exploited to tune the emission color. In former case, the composition modification avails new sites with longer wavelength emissions, whereas in latter case, the higher doping increases population of emitting ions, thus increasing interionic interactions and promoting energy transfer to Eu²⁺ sites emitting at longer wavelength. The combined control over site distribution and energy transfer leads to unique capabilities to tune the emission color from green to deep red. It is also anticipated that the doping precursor may affect the dopant site distribution. To see the effect of dopant precursor, we prepared CsCaH₂F:Eu²⁺ (1 mol%) sample using CaH₂:Eu²⁺ as doping precursors (CaH₂:Eu²⁺ where calcium and europium had been melted and the resulting alloy hydrogenated). Figure 8a presents the PL spectrum of CsCaH₂F compounds doped using

CaH₂:Eu²⁺ and compared with the PL spectra of CsCaH₂F compounds doped with 1% and 10% Eu using EuF₂ based precursor. Accordingly, the 575 nm emission band is totally quenched in 1% Eu²⁺ doped sample using CaH₂:Eu²⁺ compared to the fluoride precursor sample. The spectrum matches more with 10% Eu²⁺ fluoride precursor doped sample at higher energy side but exhibits relatively brighter red emission and narrower emission profile. This is explained by the fact that the CaH₂:Eu²⁺ based doping allows more Eu²⁺ ions in hydride rich sites, but as the overall Eu²⁺ concentration is less, the energy transfer is limited. The PLE spectrum reveals that the CaH₂:Eu²⁺ doping offers Eu²⁺ in more covalent sites and energy transfer-based feeding is limited. A further confirmation of restricted energy transfer is witnessed from the PL decay curves (Figure 8b). Here, the 575 nm emission decay is relatively slower in CaH₂:Eu²⁺ doped sample compared to similar spectral shape 10% EuF₂ doped sample. Moreover, the red emission at 635 nm PL decay is also less quenched in sample using CaH₂:Eu²⁺ as precursor.

It is evident that the use of the CaH₂:Eu²⁺ europium source leads to a higher probability of finding Eu²⁺ in a hydrogen rich arrangement. In contrast, the redshift of the emission with increasing europium concentration is assigned to energy transfer related quenching of higher energy emission bands which will lead to a preferential emission from the hydride-rich lower energy emission sites. The results are highly advantageous in spectral tuning and achieving narrowband emission

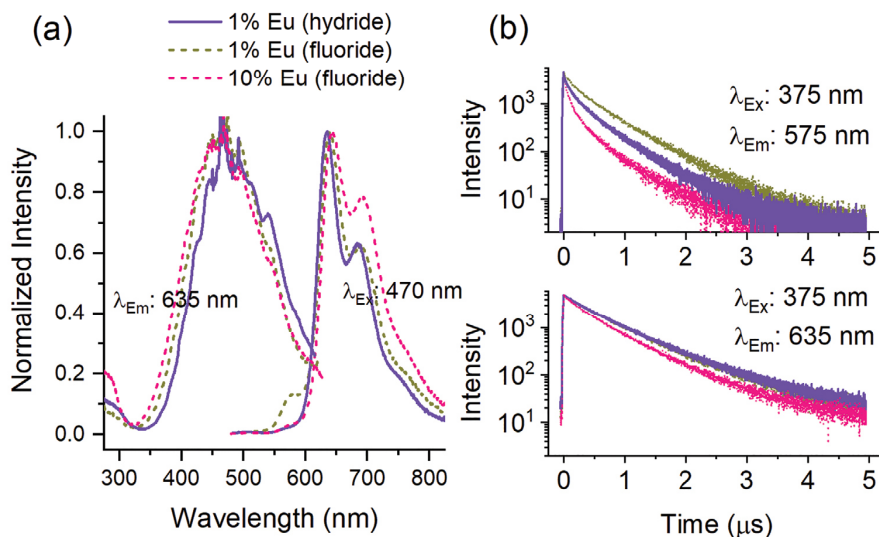


Figure 8. a) PL-PLE spectra of $\text{CsCaH}_2\text{F}:\text{Eu}^{2+}$ using $\text{CaH}_2:\text{Eu}^{2+}$ and EuF_2 as doping precursors; and b) respective decay curves monitoring different emission wavelengths.

in such mixed anionic hosts. The emission bandwidth of individual bands is as low as 30–40 nm at room temperature, which is relatively narrow and comparable to the emission bandwidth found in the green narrow-band emitter $\text{RbLi}(\text{Li}_3\text{SiO}_4)_2:\text{Eu}^{2+}$ ($\text{RLSO}:\text{Eu}^{2+}$)^[54] and the recently developed narrowband red emitting oxide nitride $\text{Sr}[\text{Li}_2\text{Al}_2\text{O}_2\text{N}_2]:\text{Eu}^{2+}$ ($\text{SALON}:\text{Eu}^{2+}$) phosphors.^[55]

3. Conclusion

In the present work, we report the successful synthesis of the complete solid solution series $\text{RbCaH}_x\text{F}_{3-x}$ and $\text{CsCaH}_x\text{F}_{3-x}$ and find a bright Eu^{2+} -luminescence for $M = \text{Cs}$. In contrast to earlier reports on doped hydride materials, we did not observe a gradual redshift of a single broad band with increasing hydride content, but instead a step-wise color shift from cyan-green to red is observed. Replacing F^- by H^- reveals the appearance of several new relatively narrow emission bands on the lower energy side, which are explained by the change in F^-/H^- coordination for Eu^{2+} on the octahedral site in $\text{CsCaH}_x\text{F}_{3-x}$ from $[\text{EuF}_6]^{4-}$ to $[\text{EuH}_6]^{4-}$ with all possible intermediates and follows the overall F/H ratio in the samples. With regard to the increasing importance of mixed-anionic hydrides, these results are of interest for the design of phosphors using more stable mixed-anionic hydrides, for instance among the oxide, silicate or borate hydrides and can also deliver useful information about effects of varying hydride contents in a local environment.

4. Experimental Section

Synthesis: As the hydrides are sensitive to air and moisture and the fluorides are hygroscopic, all manipulations were carried out in an argon-filled glove box. To remove any traces of moisture, the binary

fluorides were dried under dynamic vacuum at 200 °C for 2 h before use. The perovskites $\text{MCAH}_x\text{F}_{3-x}$ ($M = \text{Rb}, \text{Cs}$) can be synthesized from stoichiometric amounts of the alkaline metals with binary hydrides or fluorides. Therefore rubidium metal (Rb, 99.8%, Alfa Aesar) or cesium metal (Cs, 99.9%, Chempur) is grinded thoroughly in an agate mortar with the required amounts of rubidium fluoride (RbF, 99.9%, abcr) or cesium fluoride (99.99%, Chempur) and calcium hydride (CaH_2 , prepared by hydrogenation of calcium ingots, Alfa Aesar, 99.5%) or calcium fluoride (99.95%, Alfa Aesar). These mixtures were heated in an autoclave made of a hydrogen-resistant alloy (Inconel Böhler 718) at 550 °C under 50 bars of hydrogen pressure (H_2 , 99.9%, Westfalen AG) for ≈ 2 days. For $\text{CsCaH}_x\text{F}_{3-x}$ and $x \geq 2$ the reaction mixture was heated at 600 °C for 2 days to avoid the formation of Cs_2CaH_4 as a side product. The pure fluorides MCAF_3 ($M = \text{Rb}, \text{Cs}$) were synthesized from the solid-state reaction of the binary fluorides in arc welded Ni alloy ampules (Alloy 400, Eugen-Geyer GmbH). The ampules were enclosed in evacuated ($\approx 10^{-2}$ mbar) quartz glass to avoid oxidation and decomposition of the ampule material. The reaction mixture was subsequently heated to 800 °C for 12 h. Doping with europium was achieved by adding either 1 mol% europium hydride (EuH_2 , prepared by hydrogenation of europium metal, Eu, Alfa Aesar, 99.9%), 1 mol% europium fluoride (EuF_2 , 99.9% Alfa Aesar) or $\text{CaH}_2:\text{Eu}^{2+}$ (prepared from the hydrogenation of $\text{Ca}:\text{Eu}$ alloy) to the reaction mixtures. For neutron powder diffraction ≈ 4 g of $\text{CsCaD}_{1.5}\text{F}_{1.5}$ was synthesized as described above, using deuterium gas (D_2 , 99.9%, AirLiquide) instead of hydrogen gas and CaD_2 .

Characterization—X-Ray and Neutron Powder Diffraction: X-ray powder diffraction data were recorded on a Stoe STADI-P in transmission geometry with $\text{Cu-K}\alpha_1$ radiation ($\lambda = 1.54056$ Å), a curved Ge-monochromator (111) and a Dectris Mythen DCS 1K solid-state detector. In order to avoid decomposition of the samples during measurements, the powders were mixed with grease (glisseal HV, Borer Chemie) and placed between two kapton foils in a flat sample holder. Scattering angle corrections were determined by an external silicon standard (NIST SRM 640c). Neutron powder diffraction data of $\text{CsCaD}_{1.5}\text{F}_{1.5}$ were recorded at the high-resolution neutron powder diffractometer SPODI at the research reactor FRM II.^[56] The sample was placed in a thin-walled 13 mm diameter vanadium cylinder sealed with an indium wire and a filling height of ≈ 4 cm. For the measurement the cylinder was placed inside a sample changer with a rotary engine. The diffractometer was operated in standard high-resolution mode in Debye–Scherrer geometry. As the monochromator, germanium (551) was used with a resulting wavelength of 1.548 Å and

a take-off angle of 155°. Data was collected with a multidetector system consisting of 80 ³He detector tubes. By stepwise positioning of the detector array $\Delta 2\theta = 0.05^\circ$, corresponding in 40 individual steps, the powder diffraction pattern in the range $0^\circ \leq 2\theta \leq 160^\circ$ was obtained after 4 h. LaB₆ was measured for ≈ 30 min as an external standard for angle correction. Crystal structure refinement was carried out using the program package FullProf with the Rietveld method.^[57–57] Wavelength corrections were determined using the externally measured silicon standard (NIST SRM 640c). For profile fitting pseudo-Voigt functions were used. Zero shift, cell parameters, form factors, 4 asymmetry parameters, atomic parameters deuterium/hydrogen and fluorine content and thermal displacement parameters were refined. The background correction was carried out with linear interpolations of background points. In the case of CsCaD_{1.5}F_{1.5} a joint Rietveld refinement of both X-ray and neutron data was carried out. Cell parameters were allowed to differ, while atomic parameters and occupations were coupled.

Characterization—Luminescence Spectroscopy: Luminescence emission and excitation spectra were recorded both on a Horiba Jobin Yvon Fluorolog 3 as well as a FLS920 spectrofluorometer from Edinburgh Instruments. In both cases, as excitation source, a 450 W Xe-lamp was used and for detection a R928 Hamamatsu photomultiplier tube was used. For the excitation beam, a double monochromator according to Czerny–Turner with 300 nm blaze (FLS920) or 330 nm blaze (Fluorolog) was used. For emission, a double monochromator (500 nm blaze) was used on the Fluorolog 3 and a single monochromator (500 nm blaze) on the FLS920. All spectra were corrected for lamp intensity and detector response. Decay measurements were recorded on the FLS920 spectrofluorometer with a pulsed diode laser (376.8 nm, Edinburgh Instruments) as excitation source and a Hamamatsu H74220 60 photomultiplier tube for detection. For cryogenic (4.2 K) measurements, the samples were cooled down using an Oxford Instruments liquid He flow cryostat. For temperature dependence study, liquid He flow cryostat attached with an Oxford instruments temperature controller was employed at 4.2–500 K temperature range.

Characterization—Elemental Analysis: Elemental analysis was conducted on a Vario El microanalyzer. Due to the samples being sensitive to air and moisture, ≈ 3 mg of the sample was packed within a small tin boat and folded several times to be sealed airtight before being analyzed. Then, they were heated under oxygen and the evolving hydride was analyzed quantitatively using a thermal conductivity detector. The measurements were each repeated twice.

Characterization—Raman Spectroscopy: Raman spectra were recorded on powders sealed in glass capillaries (0.3 mm diameter) on a Renishaw inVia Reflex Raman System equipped with a CCD detector and a $\lambda = 532$ nm laser in the range of 100–1000 cm^{-1} .

Further details of the crystal structure investigation(s) may be obtained from the Fachinformationszentrum Karlsruhe, 76344 Eggenstein-Leopoldshafen (Germany), on quoting the depository number CSD 2040237, CSD 2040629, CSD 2040630, CSD 2040682, CSD 2040714, CSD 2040715, CSD 2040716.

Supporting Information

Supporting Information is available from the Wiley Online Library or from the author.

Acknowledgements

The authors would like to thank the Research Neutron Source Heinz Maier-Leibnitz (FRM II) for beamline time. N.K. and T.W. thank the Fonds der Chemischen Industrie for a Liebig and a doctoral fellowship (Li 197/02) and Prof. Thomas Fässler for support. The authors thank Johanna Haimerl for help with synthetic work. The research leading to these results had received funding from the DFG (KU 3427/4-1, INST 186/1328-1, INST 186/1346-1) and the ATUMS Alberta/Technical

University of Munich International Graduate School “Functional Hybrid Materials” (IRTG 2022; 245845833).

Open access funding enabled and organized by Projekt DEAL.

Conflict of Interest

The authors declare no conflict of interest.

Data Availability Statement

Research data are not shared.

Keywords

Eu²⁺ luminescence, hydride fluoride, perovskites, site-sensitivity

Received: November 30, 2020

Revised: January 4, 2021

Published online: February 4, 2021

- [1] M. Hirscher, V. A. Yartys, M. Baricco, J. Bellosta von Colbe, D. Blanchard, R. C. Bowman, D. P. Broom, C. E. Buckley, F. Chang, P. Chen, Y. W. Cho, J.-C. Crivello, F. Cuevas, W. I. F. David, P. E. de Jongh, R. V. Denys, M. Dornheim, M. Felderhoff, Y. Filinchuk, G. E. Froudakis, D. M. Grant, E. M. Gray, B. C. Hauback, T. He, T. D. Humphries, T. R. Jensen, S. Kim, Y. Kojima, M. Latroche, H.-W. Li, M. V. Lototsky, J. W. Makepeace, K. T. Möller, L. Naheed, P. Ngene, D. Noréus, M. M. Nygård, S.-i. Orimo, M. Paskevicius, L. Pasquini, D. B. Ravnsbæk, M. Veronica Sofianos, T. J. Udovic, T. Vegge, G. S. Walker, C. J. Webb, C. Weidenthaler, C. Zlotea, J. *Alloys Compd.* **2020**, 827, 153548.
- [2] M. Paskevicius, L. H. Jepsen, P. Schouwink, R. Černý, D. B. Ravnsbæk, Y. Filinchuk, M. Dornheim, F. Besenbacher, T. R. Jensen, *Chem. Soc. Rev.* **2017**, 46, 1565.
- [3] A. J. Maeland, W. D. Lahar, *Z. Phys. Chem.* **1993**, 179, 181.
- [4] T. D. Humphries, D. A. Sheppard, M. R. Rowles, M. V. Sofianos, C. E. Buckley, *J. Mater. Chem. A* **2016**, 4, 12170.
- [5] M. Heere, M. H. Sørby, C. Pistidda, M. Dornheim, B. C. Hauback, *Int. J. Hydrogen Energy* **2016**, 41, 13101.
- [6] D. Wiedemann, E. M. Heppke, A. Franz, *Eur. J. Inorg. Chem.* **2015**, 5085.
- [7] M. Zeuner, S. Pagano, W. Schnick, *Angew. Chem., Int. Ed.* **2011**, 50, 7754.
- [8] P. Pust, V. Weiler, C. Hecht, A. Tücks, A. S. Wochnik, A.-K. Henß, D. Wiechert, C. Scheu, P. J. Schmidt, W. Schnick, *Nat. Mater.* **2014**, 13, 891.
- [9] G. J. Hoerder, S. Peschke, K. Wurst, M. Seibald, D. Baumann, I. Stoll, H. Huppertz, *Inorg. Chem.* **2019**, 58, 12146.
- [10] K. Horky, W. Schnick, *Chem. Mater.* **2017**, 29, 4590.
- [11] H. Wu, W. Zhou, T. J. Volovic, J. J. Rush, T. Yildirim, *Phys. Chem. C* **2009**, 113, 15091.
- [12] P. Vajeeston, P. Ravindran, H. Fjellvåg, *J. Chem. Phys.* **2010**, 132, 114504.
- [13] F. A. Modine, E. Sonde, W. P. Unruh, *Phys. Rev. B* **1974**, 10, 1623.
- [14] P. Daniel, M. Rousseau, J. Toulouse, *Phys. Rev. B* **1997**, 55, 6222.
- [15] K. S. Knight, *J. Solid State Chem.* **2018**, 263, 172.
- [16] H.-H. Park, J. Senegas, J. M. Reau, M. Pezat, B. Darriet, P. Hagenmüller, *Mater. Res. Bull.* **1988**, 23, 1127.
- [17] F. Gingl, T. Vogt, E. Akiba, K. Yvon, *J. Alloys Compd.* **1999**, 282, 125.

- [18] J.-P. Soulié, J.-P. Laval, A. Bouamrane, *Solid State Sci.* **2003**, *5*, 273.
- [19] C. Pflug, H. Kohlmann, *Z. Anorg. Allg. Chem.* **2020**, *646*, 175.
- [20] D. J. Daniel, A. Raja, V. Madhussodanan, O. Annalakshmi, P. Ramasamy, *Opt. Mater.* **2016**, *58*, 497.
- [21] A. Raja, G. Annadurai, D. J. Daniel, P. Ramasamy, *J. Alloys Compd.* **2016**, *683*, 654.
- [22] A. Raja, R. Nagaraj, K. Ramacandran, V. Sivasubramani, G. Amadurai, D. J. Daniel, P. Ramasamy, *Adv. Powder Technol.* **2020**, *31*, 2597.
- [23] J. L. Sommerdijk, A. Bril, *J. Lumin.* **1976**, *11*, 363.
- [24] J. L. Sommerdijk, A. Bril, *J. Lumin.* **1975**, *10*, 145.
- [25] C. Gaedtke, G. V. Williams, S. Janssens, S. Raymond, D. Clark, *Radiat. Meas.* **2013**, *56*, 187.
- [26] J. Garcia, M. W. A. Sibley, *J. Lumin.* **1988**, *42*, 109.
- [27] U. Happek, M. Aycibin, A. M. Srivastava, H. A. Comanzo, S. Camardello, *ECS Trans.* **2009**, *25*, 39.
- [28] P. Dorenbos, *J. Phys.: Condens. Matter* **2003**, *15*, 2245.
- [29] C. Pflug, A. Franz, H. Kohlmann, *J. Solid State Chem.* **2018**, *258*, 391.
- [30] T. Wylezich, S. Welinski, M. Hölzel, P. Goldner, N. Kunkel, *J. Mater. Chem. C* **2018**, *6*, 13006.
- [31] J. Ueda, T. Wylezich, N. Kunkel, S. Tanabe, *J. Mater. Chem. C* **2020**, *8*, 5124.
- [32] N. Kunkel, A. Meijerink, H. Kohlmann, *Phys. Chem. Chem. Phys.* **2014**, *16*, 4807.
- [33] F. Gehlhaar, R. Finger, N. Zapp, M. Bertmer, H. Kohlmann, *Inorg. Chem.* **2018**, *57*, 11851.
- [34] T. Wu, A. Ishikawa, T. Honda, H. Tamatsukuri, K. Ikeda, T. Otomo, S. Matsuishi, *RSC Adv.* **2019**, *9*, 5282.
- [35] T. Wylezich, R. Valois, M. Suta, A. Mutschke, C. Ritter, A. Meijerink, A. J. Karttunen, N. Kunkel, *Chem. - Eur. J.* **2020**, *26*, 11742.
- [36] N. Kunkel, T. Wylezich, *Z. Anorg. Allg. Chem.* **2019**, *645*, 137.
- [37] H. Daicho, Y. Shinomiya, K. Enamoto, A. Nakano, H. Sawa, S. Matsuishi, H. Hosono, *Chem. Commun.* **2018**, *54*, 884.
- [38] H. H. Park, M. Pezat, B. Darriet, *Rev. Chim. Miner.* **1986**, *23*, 323.
- [39] W. Bronger, L. Breil, *Z. Anorg. Allg. Chem.* **1997**, *623*, 119.
- [40] V. F. Sears, *Neutron News* **1992**, *3*, 26.
- [41] V. P. Ting, P. F. Henry, H. Kohlmann, C. C. Wilson, M. T. Weller, *Phys. Chem. Chem. Phys.* **2010**, *12*, 2083.
- [42] A. Meijerink, *J. Lumin.* **1993**, *55*, 125.
- [43] N. S. Altsuler, L.-D. Livanova, A. L. Stolov, *Opt. Spectrosc.* **1974**, *36*, 72.
- [44] K. Somaiah, H. Hari Babu, *Phys. Status Solidi B* **1983**, *117*, 75.
- [45] R. C. Baetzold, *Phys. Rev. B* **1987**, *36*, 9182.
- [46] R. C. Baetzold, K. S. Song, *Phys. Rev. B* **1993**, *48*, 14907.
- [47] K. Hayashi, H. Hosono, *Phys. Chem. Chem. Phys.* **2016**, *18*, 8186.
- [48] N. Kunkel, H. Kohlmann, A. Sayede, M. Springborg, *Inorg. Chem.* **2011**, *50*, 5873.
- [49] S. M. Poort, A. Meyerink, G. Blasse, *J. Phys. Chem. Solids* **1997**, *58*, 1451.
- [50] A. D. Sontakke, J.-M. Mouesc, V. Castaing, A. Ferrier, M. Salaün, I. Gautier-Luneau, V. Maurel, A. Ibanez, B. Viana, *Phys. Chem. Chem. Phys.* **2018**, *20*, 23294.
- [51] J. Joos, P. F. Smet, L. Seijo, Z. Barandiaran, *Inorg. Chem. Front.* **2020**, *7*, 871.
- [52] T. Wylezich, A. D. Sontakke, V. Castaing, M. Suta, B. Viana, A. Meijerink, N. Kunkel, *Chem. Mater.* **2019**, *31*, 8957.
- [53] M. Suta, C. Wickleder, *J. Mater. Chem. C* **2015**, *3*, 5233.
- [54] M. Zhao, H. Liao, L. Ning, Q. Zhang, Q. Liu, Z. Xia, *Adv. Mater.* **2018**, *30*, 1802489.
- [55] J. Hoerder, M. Seibald, D. Baumann, T. Schröder, S. Peschke, P. C. Schmid, T. Tyborski, P. Pust, I. Stoll, M. Bergler, C. Patzig, S. Reißaus, M. Krause, L. Berthold, T. Höche, D. Johrendt, H. Huppertz, *Nat. Commun.* **2019**, *10*, 1824.
- [56] M. Hoelzel, A. Senyshyn, N. Juenke, H. Boysen, W. Schmahl, H. Fuess, *Nucl. Instrum. Methods Phys. Res., Sect. A* **2012**, *667*, 32.
- [57] J. Rodríguez-Carvajal, *Phys. Rev. B: Condens. Matter Mater. Phys.* **1993**, *192*, 55.
- [58] H. M. Rietveld, *J. Appl. Crystallogr.* **1969**, *2*, 65.

© 2021 Wiley-VCH GmbH

**ADVANCED
OPTICAL
MATERIALS**

Supporting Information

for *Adv. Optical Mater.*, DOI: 10.1002/adom.202002052

**MCaH_xF_{3#x} (M = Rb, Cs): Synthesis, Structure, and Bright,
Site-Sensitive Tunable Eu²⁺ Luminescence**

*Alexander Mutschke, Thomas Wylezich, Atul D. Sontakke,
Andries Meijerink, Markus Hoelzel, and Nathalie Kunkel**

WILEY-VCH

© Copyright 2021. WILEY-VCH GmbH.

Supporting Information

 $A\text{CaH}_x\text{F}_{3-x}$ ($A=\text{Rb}, \text{Cs}$): Synthesis, structure and bright, site-sensitive tunable Eu^{2+} luminescence

Alexander Mutschke, Thomas Wylezich, Atul D. Sontakke, Andries Meijerink, Markus Hoelzel, Nathalie Kunkel*

Raman spectroscopy

Obtained Raman spectra of the solid solution series $\text{RbCaH}_x\text{F}_{3-x}$ do not show any sharp signals. A rise of Raman intensity towards higher wavenumbers is assigned to the self-fluorescence of the measured samples.

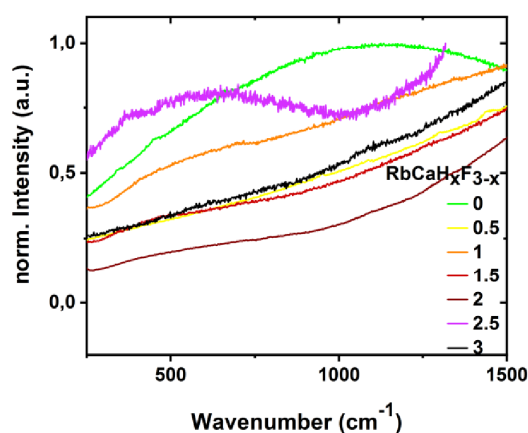


Figure S1. Raman spectra of the solid solution series $\text{RbCaH}_x\text{F}_{3-x}$ in the range between 250 cm^{-1} and 1500 cm^{-1} .

Also in the case of $\text{CsCaH}_x\text{F}_{3-x}$ Raman spectra do not show any sharp signals. A rise of Raman intensity towards higher wavenumbers is assigned to the self-fluorescence of the measured samples.

WILEY-VCH

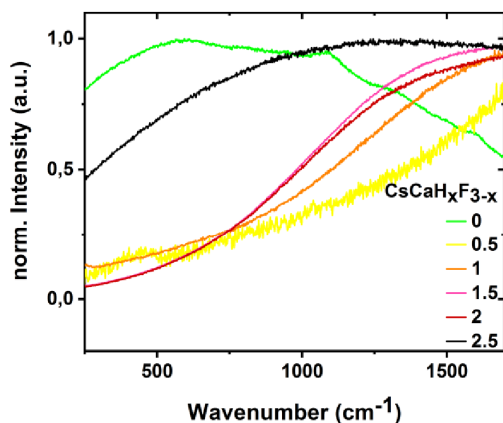


Figure S2. Raman spectra of the solid solution series $\text{CsCaH}_x\text{F}_{3-x}$ in the range between 250 cm^{-1} and 1750 cm^{-1} .

Structural analysis

Table S1. Refined lattice parameters, volume, interatomic distances and H-occupation on the $3c$ site as well as overall hydride content x (in brackets $[x]$) for $\text{RbCaH}_x\text{F}_{3-x}$, space group $Pm\bar{3}m$ (221) based on XRPD.

$\text{RbCaH}_x\text{F}_{3-x}$ (X-ray data)					
x_{target}	a [Å]	V [Å ³]	d (Rb-H/F)	d (Ca-H/F)	S.O.F.: H [x_{refined}]
0	4.4562(0)	88.49	3.151(0)	2.2281(0)	0 [0]
0.5	4.4718(1)	89.42	3.1620(1)	2.2359(1)	0.150(4) [0.45]
1	4.4751(1)	89.62	3.1644(1)	2.2376(1)	0.337(3) [1.01]
1.5	4.4894(1)	90.48	3.1745(0)	2.2447(0)	0.491(3) [1.473]
2	4.5031(1)	91.31	3.1842(0)	2.2516(0)	0.685(4) [2.055]
2.5	4.5206(1)	92.38	3.1966(0)	2.2603(0)	0.834(3) [2.487]
3	4.5445(0)	93.86	3.2134(0)	2.2722(0)	1 [3]

Table S2. Wyckoff sites and thermal displacement parameters obtained for the refined crystal structures of $\text{RbCaH}_x\text{F}_{3-x}$ based on XRPD.

$\text{RbCaH}_x\text{F}_{3-x}$							
Atom	Site			x	y	z	
Rb	1a			0	0	0	
Ca	1b			$\frac{1}{2}$	$\frac{1}{2}$	$\frac{1}{2}$	
H/F	3c			0	$\frac{1}{2}$	$\frac{1}{2}$	
Atom	RbCaF_3 B_{iso} (Å ²)	$\text{RbCaH}_{0.5}\text{F}_{2.5}$ B_{iso} (Å ²)	RbCaHF_2 B_{iso} (Å ²)	$\text{RbCaH}_{1.5}\text{F}_{1.5}$ B_{iso} (Å ²)	RbCaH_2F B_{iso} (Å ²)	$\text{RbCaH}_{2.5}\text{F}_{0.5}$ B_{iso} (Å ²)	RbCaH_3 B_{iso} (Å ²)
Rb	0.63(4)	1.83(5)	1.81(4)	1.94(3)	2.27(5)	1.96(4)	2.38(4)
Ca	0.03(5)	0.16(6)	0.34(4)	0.58(3)	0.20(6)	0.53(4)	0.47(5)
H/F	1.94(7)	1.80(11)	2.40(12)	2.42(14)	1.48(31)	3.63(48)	6.75(100)

WILEY-VCH

Table S3. R-values obtained for Rietveld refinement of the structure of $\text{RbCaH}_x\text{F}_{3-x}$ shown in Table 1 and Table S1.

x_{ideal}	$\text{RbCaH}_x\text{F}_{3-x}$ (X-ray data)				
	R_p (%)	R_{wp} (%)	R_{Bragg} (%)	R_{exp} (%)	χ^2
0	2.29	3.55	4.40	2.44	2.12
0.5	1.83	2.49	2.62	2.98	0.802
1	2.00	3.04	1.68	2.38	1.63
1.5	2.66	3.93	1.15	2.70	2.12
2	2.58	3.77	1.16	2.68	2.68
2.5	2.12	3.02	1.14	2.26	1.79
3	3.07	4.96	2.45	2.64	3.54

Table S4. Refined lattice parameters, volume, interatomic distances and H-occupation on the 3c site as well as overall hydride content x (in brackets [x]) for $\text{CsCaH}_x\text{F}_{3-x}$, space group $\text{Pm}\bar{3}\text{m}$ (221) based on XRPD as well as CsCaD1.5F1.5 (italic) based on neutron powder data.

x_{targeted}	$\text{CsCaH}_x\text{F}_{3-x}$ (X-ray and neutron data)				
	a [Å]	V [Å ³]	d (Cs-II/F)	d (Ca-II/F)	S.O.F.: II [xrefined]
0	4.5222(0)	92.48	3.1977(0)	2.2611(0)	0 [0]
0.5	4.5286(1)	92.88	3.2022(0)	2.2643(0)	0.197(6) [0.591]
1	4.5449(2)	93.88(1)	3.2137(1)	2.2724(1)	0.368(6) [1.104]
1.5	4.5524(1)	94.35	3.2190(0)	2.2762(0)	0.467(6) [1.401]
<i>D1.5</i>	<i>4.5416(3)</i>	<i>93.68(1)</i>	<i>3.2114(2)</i>	<i>2.2708(2)</i>	<i>0.428(12) [1.284]</i>
2	4.5693(2)	95.40(1)	3.2310(1)	2.2846(1)	0.614(6) [1.842]
2.5	4.5937(2)	96.93(1)	3.2482(1)	2.2968(1)	0.838(7) [2.514]
3	4.6144(1)	98.25	3.2629(1)	2.3027(1)	1 [3]

Table S5. Wyckoff sites and thermal displacement parameters obtained for the refined crystal structures of $\text{CsCaH}_x\text{F}_{3-x}$ based on XRPD.

Atom	$\text{CsCaH}_x\text{F}_{3-x}$							
	Site	X	y	z				
Cs	1a	0	0	0				
Ca	1b	½	½	½				
H/D/F	3c	0	½	½				
	CsCaF_3 B_{iso} (Å ²)	$\text{CsCaH}_{0.5}\text{F}_{2.5}$ B_{iso} (Å ²)	CsCaHF_2 B_{iso} (Å ²)	$\text{CsCaH}_{1.5}\text{F}_{1.5}$ B_{iso} (Å ²)	$\text{CsCaD}_{1.5}\text{F}_{1.5}$	CsCaH_2F B_{iso} (Å ²)	$\text{CsCaH}_{2.5}\text{F}_{0.5}$ B_{iso} (Å ²)	CsCaH_3 B_{iso} (Å ²)
Cs	1.17(3)	1.76(4)	1.35(4)	1.47(4)	0.94(3)	1.75(4)	2.43(4)	2.71(7)
Ca	0.66(5)	0.77(6)	0.91(7)	0.86(6)	0.49(4)	1.13(6)	1.71(7)	1.74(13)
H/D/F	1.33(7)	0.74(17)	0.65(24)	0.86(27)	2.02(4)	1.84(38)	0.26(80)	-7.75(78)

Table S6. R-values obtained for Rietveld refinement of the structure of $\text{CsCaH}_x\text{F}_{3-x}$ shown in Table 3 and Table S3.

x_{ideal}	$\text{CsCaH}_x\text{F}_{3-x}$ (X-ray refinement)				
	R_p (%)	R_{wp} (%)	R_{Bragg} (%)	R_{exp} (%)	χ^2
0	2.61	4.03	2.52	3.05	1.75
0.5	3.32	4.72	1.74	3.72	1.61
1	2.61	3.52	2.88	2.59	1.84
1.5	3.29	4.76	1.50	3.54	1.80
D1.5	5.10	6.53	3.15	1.47	4.97
2	4.10	6.13	1.72	3.75	2.67
2.5	4.55	6.39	2.40	5.11	1.57
3	4.05	5.94	3.70	3.91	2.31

WILEY-VCH

Elemental analysis**Table S7.** Weight percentages (wt.-%) of hydrogen in the solid solution $\text{RbCaH}_x\text{F}_{3-x}$ obtained by Rietveld refinement and elemental analysis in comparison to the weight percentage of hydrogen of mixed phases with ideal compositions.

x_{target}	$\text{RbCaH}_x\text{F}_{3-x}$		
	wt.-% (XRD)	wt.-% (elemental analysis)	wt.-% ideal composition
0.5	0.26	0.31 0.31	0.288
1.5	0.95	0.93 0.91	0.964
2.5	1.81	1.92 1.86	1.817

The values determined by the Rietveld refinement elemental analysis each match the weight percentages of hydrogen of the ideal composition with only small deviations.

Table S8. Weight percentages (wt.-%) of hydrogen in the solid solution $\text{CsCaH}_x\text{F}_{3-x}$ obtained by Rietveld refinement and elemental analysis in comparison to the weight percentage of hydrogen of mixed phases with ideal compositions.

x_{target}	$\text{CsCaH}_x\text{F}_{3-x}$		
	wt.-% (XRD/neutron diffraction)	wt.-% (elemental analysis)	wt.-% ideal composition
0.5	0.27	0.22 0.18	0.226
1.5	0.68	0.74 0.73	0.738
$D_{1.5}$	0.61	0.98 0.75	0.738
2.5	1.36	1.37 1.42	1.351

Again, the values determined by Rietveld refinement as well as elemental analysis each match the weight percentages of hydrogen of the ideal composition with only small deviations. However, the hydrogen content determined by neutron diffraction seems to be slightly underestimated as the hydrogen content according to elemental analysis rather matches the value of the ideal stoichiometry rather than the obtained value of the Rietveld refinement.

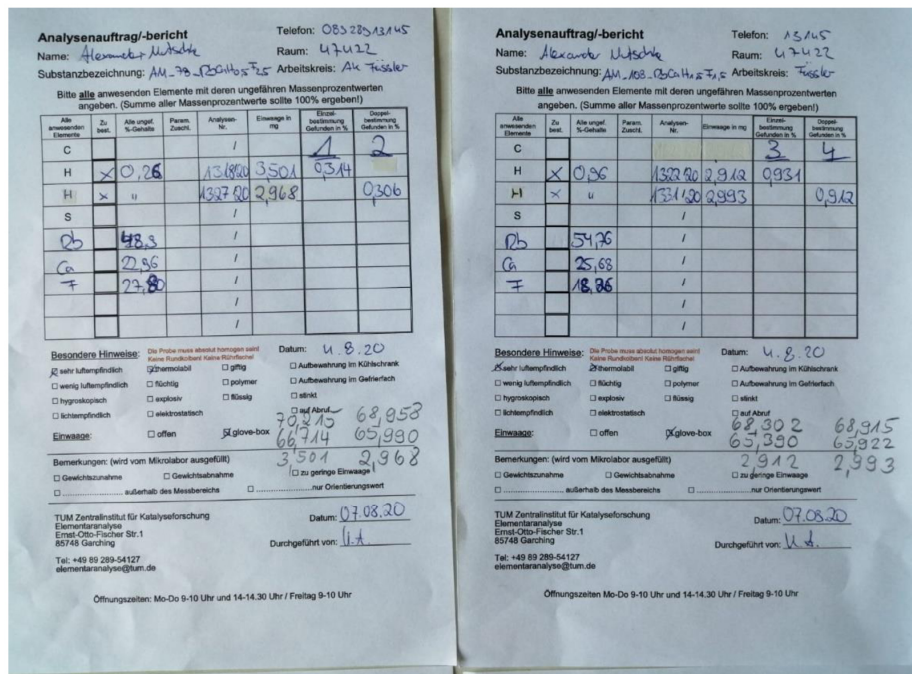


Figure S3. Pictures of the obtained elemental analysis reports of RbCaH_{0.5}F_{1.5}

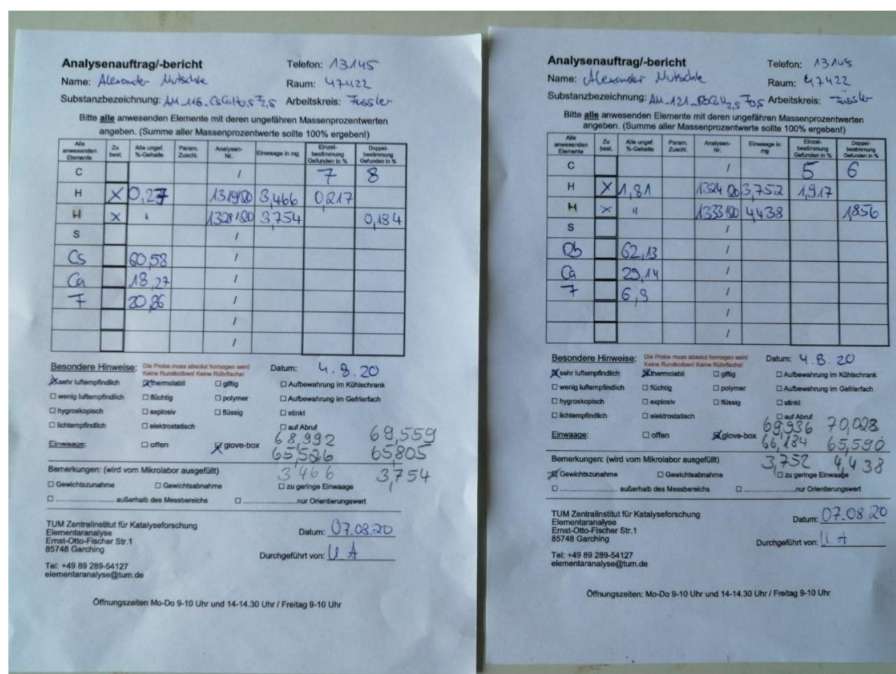


Figure S4. Pictures of the obtained elemental analysis reports of RbCaH_{2.5}F_{0.5} and CsCaH_{0.5}F_{1.5}

WILEY-VCH

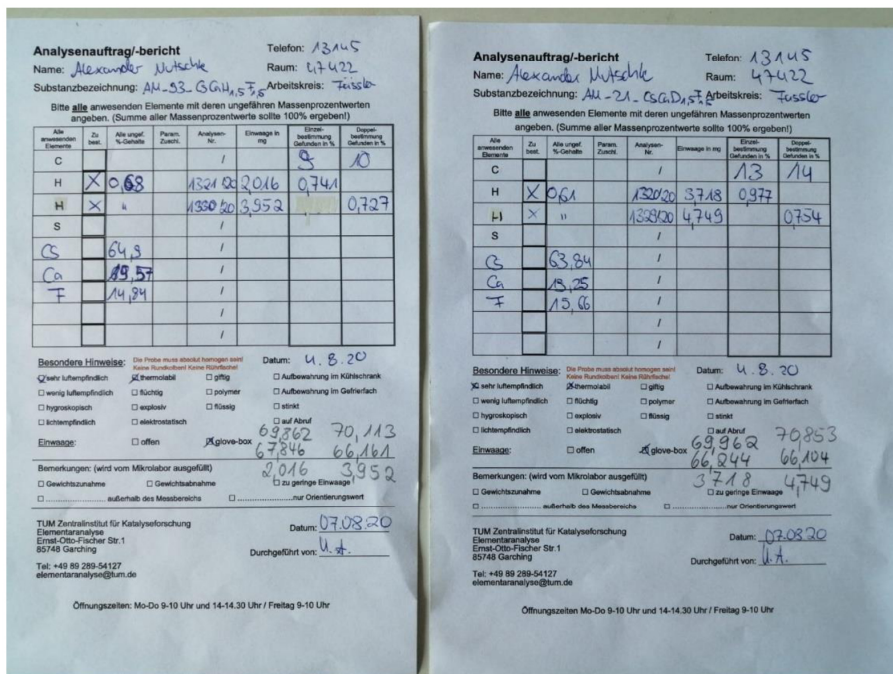


Figure S5. Pictures of the obtained elemental analysis reports of CsCaH_{1.5}F_{1.5} and CsCaD_{1.5}F_{1.5}

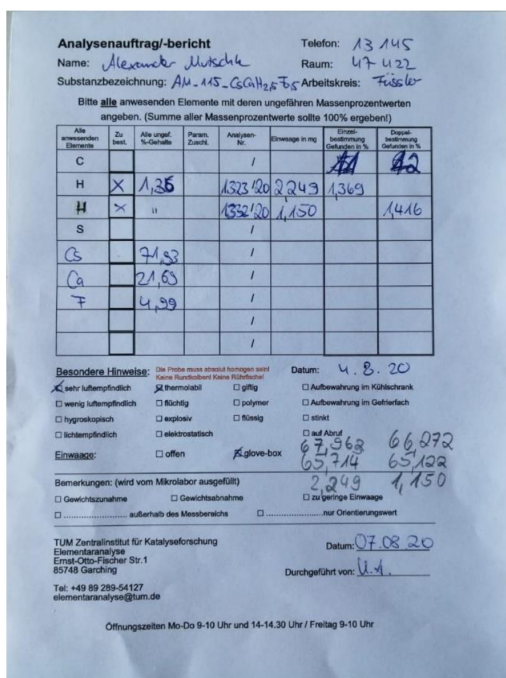


Figure S6. Picture of the obtained elemental analysis reports of CsCaH_{2.5}F_{0.5}

WILEY-VCH

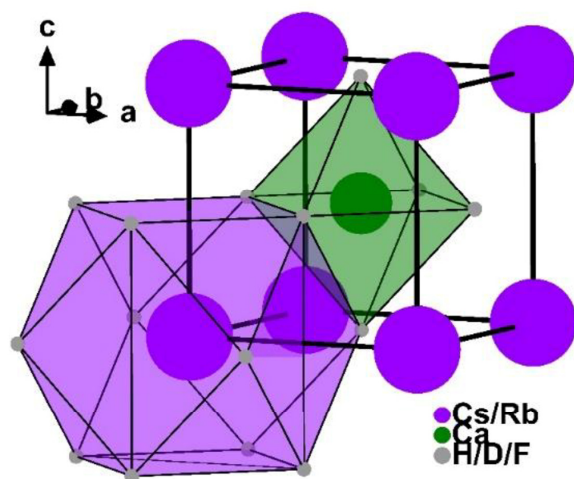


Figure S7. Crystal structure of the ideal cubic perovskite structure. The alkaline metal (Cs/ Rb) is cubeoctahedrally coordinated by the anions (H/D/F) while the smaller earth alkaline metal (Ca) is octahedrally coordinated by the anions (H/D/F).

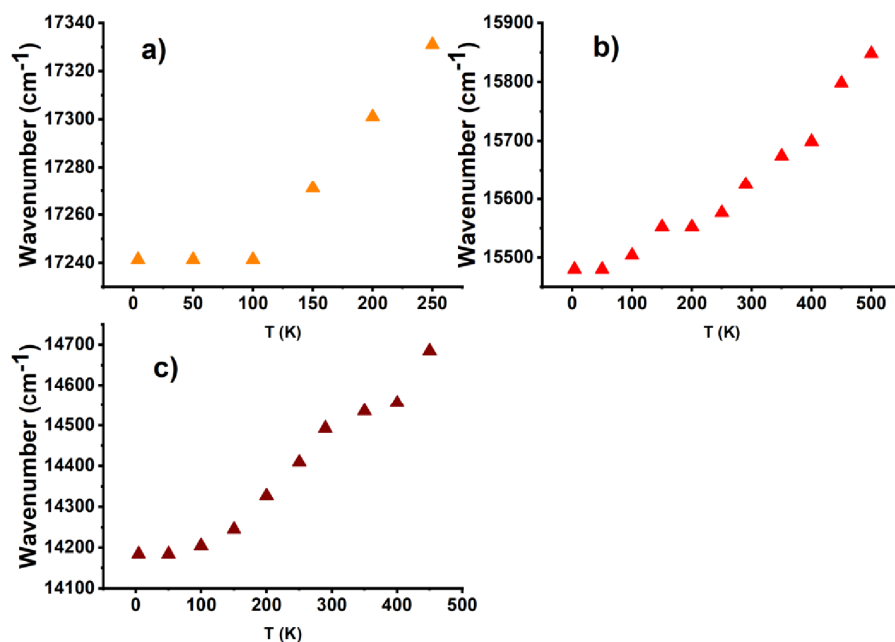


Figure S7. Emission maximum of the peaks at a) 578, b) 647 and c) 705 nm as a function of temperature for the sample shown in Fig 6b, CsCaH₂F:Eu²⁺. For a) and c) thermal quenching of the emission bands was observed, thus, not all peak positions were determinable.

7.2 Na₃SO₄H—The First Representative of the Material Class of Sulfate Hydrides


Alexander Mutschke, Guy M. Bernard, Marko Bertmer, Antti J. Karttunen, Clemens Ritter, Vladimir K. Michaelis and Nathalie Kunkel

Published in:

Angew. Chem. Int. Ed. **2021**, *60*, 5683-5687 and as German version in *Angew. Chem.* **2021**, *133*, 5747-5741.

Reproduced from Alexander Mutschke, Guy M. Bernard, Marko Bertmer, Antti J. Karttunen, Clemens Ritter, Vladimir K. Michaelis, Nathalie Kunkel*, *Angew. Chem. Int. Ed.* **2021**, *60*, 5683-5687 with permission from Wiley-VCH Verlag GmbH & Co. KGaA, Weinheim.

© 2021 Wiley-VCH Verlag GmbH & Co. KGaA, Weinheim.



Na₃SO₄H—The First Representative of the Material Class of Sulfate Hydrides

Author: Nathalie Kunkel, Vladimir K. Michaelis, Clemens Ritter, et al

Publication: Angewandte Chemie International Edition

Publisher: John Wiley and Sons

Date: Feb 1, 2021

© 2021 The Authors. Angewandte Chemie International Edition published by Wiley-VCH GmbH

Welcome to RightsLink


John Wiley and Sons has partnered with Copyright Clearance Center's RightsLink service to offer a variety of options for reusing this content.

Note: This article is available under the [Creative Commons CC-BY-NC-ND](#) license and permits non-commercial use of the work as published, without adaptation or alteration provided the work is fully attributed.

For commercial reuse, permission must be requested below.

For an understanding of what is meant by the terms of the Creative Commons License, please refer to [Wiley's Open Access Terms and Conditions](#).

If you wish to adapt, alter, translate or create any other derivative work from this article, permission must be sought from the Publisher. Please email your requirements to RightsLink@wiley.com.

I would like to... 

Figures in chapter 4 were adapted and adjusted with permission from Wiley-VCH Verlag GmbH & Co. KGaA, Weinheim.

Content

By this publication $\text{Na}_3\text{SO}_4\text{H}$ is presented as the first the sulfate hydride to introduce a new class of heteroanionic materials. The synthesis and structure is carefully analysed and discussed. $\text{Na}_3\text{SO}_4\text{H}$ can be synthesized by a solid-state reaction of NaH with dry Na_2SO_4 under precisely controlled conditions. Only an exact reaction temperature of 330 °C allows for a synthesis of the novel compound. To avoid an early thermal decomposition of NaH, hydrogen pressure is additionally required for the synthesis. The structure is solved from powder X-ray diffraction and corroborated by powder neutron diffraction. $\text{Na}_3\text{SO}_4\text{D}$ is determined to crystallize in the tetragonal space group $P4/nmm$ (129, O2) with the cell parameters $a = 7.0034(2)$ and $b = 4.8569(2)$ Å. With a manifold set of analytical methods, the unprecedented simultaneous abundance of sulfate ions next to hydride ions within a single material is proven. Here, both FT-IR and Raman spectroscopy prove to be ideal tools for the analytical evidence of hydride ions but also deuteride ions in the case of $\text{Na}_3\text{SO}_4\text{D}$. Simulated spectra obtained by quantum chemical calculations at the DFT-PBE0 level of theory allow for an assignment of the hydride and deuteride modes. Overall, the simulated spectra show very good agreement with experimental spectra. Also, a remarkable isotopic shift from hydride to deuteride modes by a factor of $\sqrt{2}$ to lower wavenumbers is clearly perceived, equally as predicted by the simulated spectra. Local structure determination is obtained by solid-state NMR spectroscopy. ^1H MAS NMR shows a single peak with a chemical shift typical for ionic hydrides. ^{23}Na MAS NMR shows two signals also in accordance with the two distinct sodium sites in the crystal structure. Quantum chemical calculations on the chemical shifts are within the same region of the experimental values and additionally support the experimental findings. Electronic band structure calculations reveal an insulating character of $\text{Na}_3\text{SO}_4\text{H}$ with an indirect band gap of 7.4 eV. Due to its high polarizability, hydride states are predicted to dominate the topmost valence band.

Contributions

The syntheses of the samples were performed by A.M. Structural characterization, *i.e.* structure solutions and Rietveld refinements were conducted by A.M. Neutron diffraction data in respect thereof was collected by C.R. Beam time allocated at the D2B at the ILL, Grenoble is gratefully acknowledged. FT-IR spectra were recorded and evaluated by A.M. MAS NMR spectroscopy was performed G.M.B, V.K.M and M.B. Quantum chemical calculations were conjointly performed by A.M and A.J.K.

The manuscript was written through contribution of all co-authors. Leading author is A.M., corresponding author N.K.



Sulfate Hydrides

Na₃SO₄H—The First Representative of the Material Class of Sulfate Hydrides

Alexander Mutschke, Guy M. Bernard, Marko Bertmer, Antti J. Karttunen, Clemens Ritter, Vladimir K. Michaelis, and Nathalie Kunkel*

Dedicated to Professor H. P. Beck on the occasion of his 80th birthday

Abstract: The first representative of a novel class of mixed-anionic compounds, the sulfate hydride Na₃SO₄H, and the corresponding deuteride Na₃SO₄D were obtained from the solid-state reaction of NaH or NaD with dry Na₂SO₄. Precise reaction control is required, because too harsh conditions lead to the reduction of sulfate to sulfide. A combined X-ray and neutron diffraction study revealed that the compound crystallizes in the tetragonal space group *P4/nmm* with the lattice parameters *a* = 7.0034(2) Å and *c* = 4.8569(2) Å. The sole presence of hydride and absence of hydroxide ions is proven by vibrational spectroscopy and comparison with spectra predicted from quantum chemical calculations. ¹H and ²³Na MAS NMR spectra are consistent with the structure of Na₃SO₄H: a single ¹H peak at 2.9 ppm is observed, while two peaks at 15.0 and 6.2 ppm for the inequivalent ²³Na sites are observed. Elemental analysis and quantum chemical calculations further support these results.

Whereas controlling the cation chemistry has been a tool to tune materials for many years, tailoring of the anion chemistry has recently become more and more important.^[1–5] Materials with desired physical and chemical properties can be obtained by taking advantage of the different anion radii, electronegativities or polarizabilities. Mainly during the last decade, this concept has become important due to the discovery of new mixed anionic hydrides. For instance, fast conductivity in a pure hydride anion conductor, La_{2–x–y}Sr_{x+y}LiH_{1–x+y}O_{3–y}^[6–10]

How to cite: *Angew. Chem. Int. Ed.* **2021**, *60*, 5683–5687
International Edition: doi.org/10.1002/anie.202016582
German Edition: doi.org/10.1002/ange.202016582

electronic conductivity in oxide hydride perovskite-type titanates^[11–13] and even superconductivity^[14] were found in oxide hydrides. Tuning of the anion chemistry, for instance, allows for a tailoring of the bonding situations from more ionic to more covalent or varying the polarizabilities from rather hard to soft anions, tailoring crystal fields, or electronic properties.^[1] Very recently the novel material classes of phosphate hydrides,^[15,16] silicate hydrides,^[17,18] and borate hydrides^[19] were also discovered. Some mixed anionic hydrides, such as silicate hydrides, borate hydrides, oxide hydrides, and halide hydrides, also allowed for tuning of bright rare earth ion luminescence.^[17–25] Encouraged by these recent breakthroughs in an emerging field, we aimed to broaden our search for yet-to-be-discovered anion combinations with possibly unique chemical and physical properties. A possible candidate seemed to be the combination of sulfate and hydride anions, which, however, appeared to represent a synthetic challenge, since too reductive reaction conditions may be expected to reduce the sulfate anion instead of yielding the mixed anionic compound. Besides their importance in biological systems,^[26–28] sulfate anions also play an important role in inorganic materials, for instance exhibiting interesting optical properties, e.g., the non-linear optical compound K₄Sb(SO₄)₃Cl,^[29] materials for lanthanide-activated luminescence LnFSO₄·H₂O (Ln = Tb, Nd)^[30] or as candidates for solid state ion conduction.^[31,32]

*] A. Mutschke, Prof. Dr. N. Kunkel
Institut für Anorganische Chemie
Georg-August-University Goettingen
Tammannstrasse 4, 37077 Goettingen (Germany)
E-mail: nathalie.kunkel@uni-goettingen.de

A. Mutschke, Prof. Dr. N. Kunkel
Chair for Inorganic Chemistry with Focus on Novel Materials
Technical University of Munich
Lichtenbergstrasse 4, 85748 Garching (Germany)

Dr. G. M. Bernard, Prof. Dr. V. K. Michaelis
Department of Chemistry, University of Alberta
Edmonton, Alberta, T6G 2G2 (Canada)

Dr. M. Bertmer
Felix Bloch Institute for Solid State Physics
Leipzig University
Linnéstrasse 5, 04103 Leipzig (Germany)

Prof. Dr. A. J. Karttunen
Department of Chemistry and Materials Science
Aalto University
P.O. Box 16100, FI-00076 Aalto (Finland)

Dr. C. Ritter
Institut Laue-Langevin
71 avenue des Martyrs, 38042 Grenoble Cedex 9 (France)

Prof. Dr. N. Kunkel
Woehler Research Institute for Sustainable Chemistry (WISCh)
Georg-August-University, Goettingen (Germany)

Supporting information and the ORCID identification number(s) for the author(s) of this article can be found under:
https://doi.org/10.1002/anie.202016582.

© 2021 The Authors. Angewandte Chemie International Edition published by Wiley-VCH GmbH. This is an open access article under the terms of the Creative Commons Attribution Non-Commercial NoDerivs License, which permits use and distribution in any medium, provided the original work is properly cited, the use is non-commercial and no modifications or adaptations are made.

Herein, we report on the first representative of a novel anion combination, sulfate and hydride, $\text{Na}_3\text{SO}_4\text{H}$, synthetically accessible via a solid-state reaction of NaH with Na_2SO_4 under controlled conditions. For detailed experimental details see SI. A first structural model was obtained from powder X-ray diffraction using the program Jana2006.^[33] Due to the weak X-ray scattering ability of hydrides, it is necessary to additionally apply neutron diffraction in order to obtain a reliable structural model with hydride positions and occupation numbers.

Here, the bound coherent scattering cross section of ^2H (5.6 barn) is significant and also differs significantly from that of ^{23}Na (1.66 barn), ^{16}O (4.232 barn), and ^{32}S (1.0186 barn).^[34] The Rietveld refinement of the structure of deuterium-enriched $\text{Na}_3\text{SO}_4\text{D}$ using neutron powder data and X-ray diffraction data are depicted in Figures S1 and S2 in the SI.

$\text{Na}_3\text{SO}_4\text{D}$ was found to crystallize in the $\text{Ag}_3\text{CrO}_4\text{Cl}$ structure type^[35] in the tetragonal space group $P4/mmm$ (129)⁺ with the cell parameters $a = 7.0034(2)$ Å and $c = 4.8569(2)$ Å and is isotypic to the tungstate and molybdate chlorides $\text{Na}_3\text{MO}_4\text{Cl}$ ($M = \text{Mo}, \text{W}$;^[36] for detailed structural data see SI). Surprisingly, the structure does not show any similarity to the known fluoride analogues, as could be expected from the fluoride hydride analogy.^[37,38] In case of the fluorides, two phases of $\text{Na}_3\text{SO}_4\text{F}$ are known, a monoclinic ($P2_1/m$) low-temperature phase (α) and a trigonal ($R\bar{3}m$) high-temperature phase (β).^[32,39,40]

In the $\text{Na}_3\text{SO}_4\text{D}$ structure, two distinct sodium sites Na1 ($4e$) and Na2 ($2c$) exist with both sodium atoms being octahedrally surrounded by four oxygen and two deuterium/hydrogen atoms (see Figure 1 and Figure S4) resulting in two distinct $\text{D}_2\text{O}_4\text{Na}$ units.

While the octahedra around the Na1 position are interconnected via edge sharing, the octahedra surrounding the Na2 position are interconnected along the a and b axes via sulfate ions and corner sharing along the c axis. The deuteride ions are located within the octahedral voids built up by the sodium atoms forming DNa_6 subunits. In summary, the structure may also be described as a checkerboard pattern formed by a two-dimensional plane built up by the Na1 atoms. The planar-square fields of the Na1 atoms are then occupied

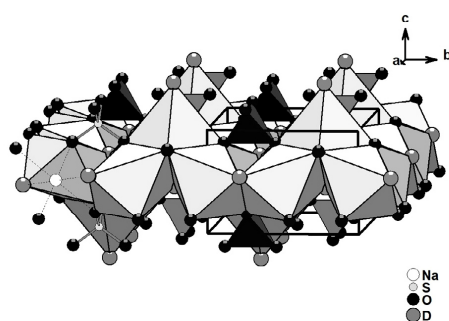


Figure 1. Crystal structure of $\text{Na}_3\text{SO}_4\text{D}$ along the a/b plane with coordination spheres of the cations.

either by sulfate tetrahedra or sodium Na2 ($2c$) and deuteride in an alternating order comparable to a checkerboard (Figures 1 and S3–S6).

Alternatively, the structure can also be described as an anti-perovskite-like structure. Here, the sulfate tetrahedra are located at the Ca sites and the hydride ions at the Ti sites, while the sodium atoms occupy the O sites (Figure 2). Anti-perovskite-like structures with tetrahedral building units are not uncommon, for example, $\text{K}_3\text{SO}_4\text{F}$ crystallizes in a similar anti-perovskite-like structure.^[41,42] Also minerals like the related anti-elpasolite-like sulfosalite $\text{Na}_6(\text{SO}_4)_2\text{ClF}$ are known to crystallize in such a manner.^[43]

In $\text{Na}_3\text{SO}_4\text{H}$, interatomic distances between deuteride/hydride and sodium ions are found to be between 2.25 and 2.61 Å, which is in the range of typical inorganic metal hydrides^[44] (e.g., NaH 2.4 Å^[45,46]). The S–O distance of 1.47 Å matches the typical interatomic S–O distance and covalent bond lengths of covalent sulfur–oxygen bonds of sulfate tetrahedra. The tetrahedral angles of 108.85–109.78° show only minor deviations compared to the ideal tetrahedron angle of 109.47°.^[47,48] The compound is susceptible to moisture. Contact with water shows visible formation of gas bubbles, which are tentatively assigned to the formation of H_2 or HD gas. However, it is possible to briefly expose the compound to dry air without decomposition or formation of hydrogen gas. Longer exposure to air and reaction with water result in a dissociation into Na_2SO_4 and $\text{Na}_4[\text{SO}_4]_{1.5}[\text{CO}_3]_{0.5}$, an indication that a likely hydroxide species $\text{Na}_3\text{SO}_4\text{OH}$ is not stable and indeed an air sensitive hydride is formed.

To support experimental findings, quantum chemical calculations using a hybrid density functional method have been performed. The crystal structure of $\text{Na}_3\text{SO}_4\text{H}$ was first optimized at the DFT-PBE0/TZVP level of theory (see Supporting Information for computational details). The optimized lattice parameters a and c differed from the experimental parameters by +0.1% and –0.5%, respectively. The optimized structure of $\text{Na}_3\text{SO}_4\text{H}$ was confirmed to be a true local minimum with no imaginary frequencies.

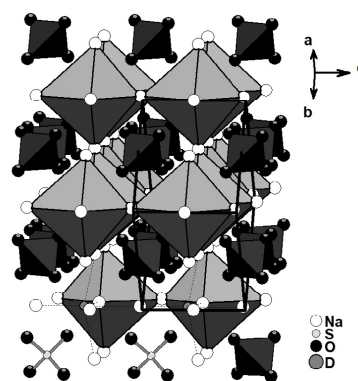


Figure 2. Alternative depiction of the crystal structure as an anti-perovskite-like structure. Here, the sulfate tetrahedra occupy the voids between the DNa_6 octahedra.

Electronic band structure and density of states (DOS) calculations suggest an insulating compound with an indirect band gap of 7.4 eV. The topmost valence bands are dominated by hydride anions, with minor contributions from the other atoms, which agrees with previous studies on mixed anionic hydrides.^[19] See Figure S13 for a detailed depiction of the electronic band structure and DOS. The reaction $\text{NaH} + \text{Na}_2\text{SO}_4 \rightarrow \text{Na}_3\text{SO}_4\text{H}$ is exoenergetic by 17 kJ mol^{-1} , showing that the formation of $\text{Na}_3\text{SO}_4\text{H}$ is energetically favorable (based on total energies at 0 K).

Because of its sensitivity to the local atomic-level structure, ^1H and ^{23}Na magic angle spinning nuclear magnetic resonance (MAS NMR) spectra of $\text{Na}_3\text{SO}_4\text{H}$ were acquired to complement the average long-range structure determined from diffraction data discussed above. The ^1H MAS NMR spectrum (Figure 3a) is dominated by a single symmetric peak at $\delta_{\text{iso}} = 2.9 \text{ ppm}$. The source of this peak is attributed to the hydride proton of the target compound, a similar value to the 4.3 ppm calculated at the DFT-PBE/USPP level of theory (see SI for computational details). The full width half maximum (fwhm) of 400 Hz for this peak is attributed primarily to incomplete decoupling of the heteronuclear ^1H - ^{23}Na dipolar (through space) coupling from neighbouring ^{23}Na nuclei ($I = 3/2$, 100% natural abundance). A smaller peak (< 10% of the total intensity) at -4 ppm is thought to be due to hydride impurities from the starting materials, small amounts of amorphous hydridic or proton-containing side phases, such as, for example, hydrogen sulfate anions not

visible in the diffraction patterns; however, shielded ^1H nuclei for hydrides are also not uncommon.^[49] Figure 3b illustrates the experimental ^{23}Na MAS NMR spectrum for $\text{Na}_3\text{SO}_4\text{H}$ and the corresponding spectral simulation.

The sharp peak at 15.0 ppm is attributed to Na2, since the more symmetric environment (4 mm) about this nucleus is expected to yield a negligible quadrupolar coupling interaction (C_Q), as observed from the simulation (dotted trace). The broad asymmetric peak at $\delta = 6.2 \text{ ppm}$ (note that the signal position is affected by the second-order quadrupolar shift in Figure 3b) is attributed to Na1, which has a less symmetric octahedral environment (2/m). Here C_Q is determined to be 1.5 MHz, which is close to the DFT-PBE value of 1.85 MHz. The difference in the experimentally determined ^{23}Na isotropic chemical shifts between Na1 and Na2 (ppm) is found to be 8.8 ppm which is accurately predicted from theoretical ^{23}Na NMR calculation results, 9.9 ppm (Na1: $\delta_{\text{iso}} = -2.5$, Na2: $\delta_{\text{iso}} = 7.7 \text{ ppm}$ in reference to solid NaCl).

NMR spectra are consistent with the structure proposed via X-ray and neutron diffraction: a single hydrogen position is attributed to the hydride of $\text{Na}_3\text{SO}_4\text{H}$, and two ^{23}Na NMR sites are observed, with line shapes reflecting the local chemical environments about these nuclei.

To further confirm the hydridic character of the compound, as well as exclude the possibility of a hydroxide species, Raman and FT-IR spectroscopy were carried on both the hydride and deuteride-enriched samples. The experimental spectra were compared to spectra obtained with quantum chemical methods. Figure S10 shows the FT-IR spectrum in the region between 4000 and 450 cm^{-1} with an enlarged inset of the typical OH-stretching vibration energies (3800–2250 cm^{-1}). No signal can be observed for such OH vibrations, indicating that the compound is indeed a hydroxide-free hydride.

As recently applied in the case of a novel borate hydride/deuteride, vibrational spectroscopy may also be a suitable tool to prove the presence of a mixed anionic hydride by hydride or deuteride modes and by comparison with calculated spectra.^[19] Replacing the hydride with a deuteride will usually lead to a shift of the energies to lower wavenumbers by a factor of $\sqrt{2}$ caused by the higher deuterium mass.

An enlarged view of the FT-IR spectrum (Figure 4) in the range from 1200 to 400 cm^{-1} does indeed show a hydride out-of-plane mode (H_{op}^-) visible at 831 cm^{-1} , which is in good agreement with the band at 837 cm^{-1} in the theoretical spectrum. The plane is defined by the square plane set up by the Na1 sodium atoms in the 4e site as depicted in Figure S12. Apart from this, hydride in-plane modes are clearly visible at 653 cm^{-1} and 570 cm^{-1} (H_{ip}^-), which fit to the theoretical values of 640 cm^{-1} and 579 cm^{-1} , respectively. The H_{ip}^-* mode describes hydride vibration coupled with sulfate bending modes.

Furthermore, besides hydride vibrations, vibrational bands corresponding to the sulfate ions are clearly visible and perfectly match the calculated bands. A detailed assignment of these bands can be found in the SI.

For the deuteride modes, a shift of nearly $\sqrt{2}$ can be observed, leading to the out-of-plane mode D_{op}^- appearing at 581 cm^{-1} and the in-plane mode D_{ip}^- of the deuteride at

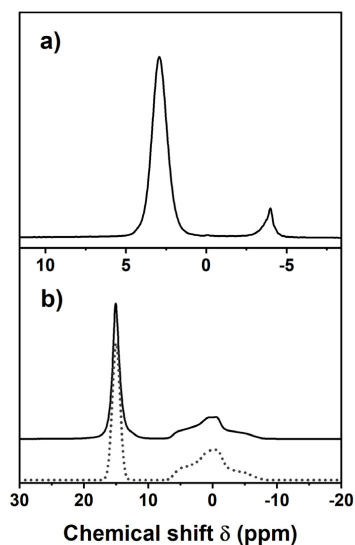


Figure 3. a) ^1H NMR spectrum of $\text{Na}_3\text{SO}_4\text{H}$, acquired at room temperature with a spinning frequency of 10.0 kHz, $B_0 = 9.4 \text{ T}$, ^1H NMR chemical shifts at $\delta_{\text{H}} = 2.9 \text{ ppm}$ and $\delta = -3.9 \text{ ppm}$. b) Simulation (dotted trace) and experimental (solid trace) ^{23}Na NMR spectra. Na1: $C_Q = 1.5 \text{ MHz}$ and $\eta = 0.74$, Na2: $C_Q = 0 \text{ MHz}$, chemical shifts at $\delta_{\text{Na2}} = 15.0 \text{ ppm}$ and $\delta_{\text{Na1}} = 6.2 \text{ ppm}$.

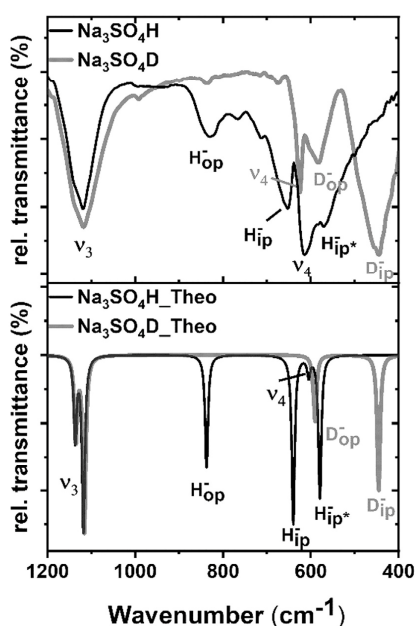


Figure 4. FT-IR spectra of $\text{Na}_3\text{SO}_4\text{H}$ and $\text{Na}_3\text{SO}_4\text{D}$ between 1200 cm^{-1} and 400 cm^{-1} (upper traces) in comparison to the theoretical FT-IR spectra of $\text{Na}_3\text{SO}_4\text{H}$ and $\text{Na}_3\text{SO}_4\text{D}$ (lower traces).

450 cm^{-1} . An additional signal at 600 cm^{-1} is tentatively assigned to the asymmetric bending mode of the sulfate that is predicted to be very weak in the theoretical spectrum. Raman spectra are depicted in Figure S11 and the assignment of the vibrational modes can be found in detail in the SI. The good agreement with calculated spectra reaffirms the presence of a novel sulfate hydride compound.

To further confirm the existence of hydrogen within the crystal lattice, elemental analysis has been conducted using a Vario El microanalyzer and the hot-gas extraction method. Here, the experimentally determined value of 0.61 wt% hydrogen matches almost perfectly to the theoretical value of 0.60 wt%.

In summary, the novel sulfate hydride $\text{Na}_3\text{SO}_4\text{H}$ was obtained by a simple solid-state reaction under controlled conditions. It crystallizes in the anti-perovskite-like $\text{Ag}_3\text{CrO}_4\text{Cl}$ structure type. The successful incorporation of hydride and the absence of hydroxide was proven by several independent methods, including X-ray and neutron powder diffraction, vibrational spectroscopy, solid-state NMR spectroscopy, elemental analysis, and quantum chemical calculations. To the best of our knowledge, such a combination of sulfate and hydride has not been realized so far, opening the door to a new class of mixed anionic hydrides, which may, in the future, be useful in different applications. For instance, especially if sulfate hydrides with di- or tri-valent cations can be found, such materials may be of interest for lanthanide-

activated optical materials. Furthermore, perovskite-like structures with the formulation of $\text{Na}_3\text{AO}_4\text{X}$ ($\text{A} = \text{S}, \text{Se}$; $\text{X} = \text{Cl}, \text{F}$) have been discussed as potential high-performance solid sodium ion electrolytes. Since it is known that in such solid-state electrolytes, the incorporation of polarizable anions may lead to better conduction properties,^[50,51] tuning of such materials using mixed-anionic hydrides may lead to promising materials for solid-state ion conduction in the future.

Acknowledgements

The authors thank Christoph Wallach for Raman and Jan Berger for FT-IR measurements. Beam time at the D2B (Institut Laue-Langevin) under the project number EASY-648 (<https://doi.org/10.5291/ILL-DATA.EASY-648>) is also gratefully acknowledged. N.K. would like to thank the Fonds der Chemischen Industrie for a Liebig fellowship (Li 197/02). The work received funding from the DFG (project number 245845833) within International Research Training Group IRTG 2022—Alberta Technical University of Munich School for Functional Hybrid Materials (ATUMS), the DAAD and the Academy of Finland (324973) as a part of the PPP Finland 2019 funding Scheme. A.J.K. thanks CSC, the Finnish IT Center for Science for computational resources. V.K.M. is supported by NSERC (DG & CREATE), CFI and the Gov. of Alberta. Open access funding enabled and organized by Projekt DEAL.

Conflict of interest

The authors declare no conflict of interest.

Keywords: anions · density functional calculations · hydrides · NMR spectroscopy

- [1] H. Kageyama, K. Hayashi, K. Maeda, J. P. Attfield, Z. Hiroi, J. M. Rondinelli, K. R. Poeppelmeier, *Nat. Commun.* **2018**, *9*, 772.
- [2] M. Zeuner, S. Pagano, W. Schnick, *Angew. Chem. Int. Ed.* **2011**, *50*, 7754–7775; *Angew. Chem.* **2011**, *123*, 7898–7920.
- [3] H. Kageyama, T. Yajima, Y. Tsujimoto, T. Yamamoto, C. Tassel, Y. Kobayashi, *Bull. Chem. Soc. Jpn.* **2019**, *92*, 1349–1357.
- [4] Y. Kobayashi, Y. Tsujimoto, H. Kageyama, *Annu. Rev. Mater. Res.* **2018**, *48*, 303–326.
- [5] S. G. Jantz, R. Erdmann, S. Hariyani, J. Brgoch, H. A. Höpfe, *Chem. Mater.* **2020**, *32*, 8587–8594.
- [6] G. Kobayashi, Y. Hinuma, S. Matsuoka, A. Watanabe, M. Iqbal, M. Hirayama, M. Yonemura, T. Kamiyama, I. Tanaka, R. Kanno, *Science* **2016**, *351*, 1314–1317.
- [7] Ø. S. Fjellvåg, J. Armstrong, P. Vajeeston, A. O. Sjøstad, *J. Phys. Chem. Lett.* **2018**, *9*, 353–358.
- [8] Y. Kobayashi, O. J. Hernandez, T. Sakaguchi, T. Yajima, T. Roisnel, Y. Tsujimoto, M. Morita, Y. Noda, Y. Mogami, A. Kitada, *Nat. Mater.* **2012**, *11*, 507–511.
- [9] H. Ubukata, T. Broux, F. Takeiri, K. Shitara, H. Yamashita, A. Kuwabara, G. Kobayashi, H. Kageyama, *Chem. Mater.* **2019**, *31*, 7360–7366.



- [10] G. Bouilly, T. Yajima, T. Terashima, W. Yoshimune, K. Nakano, C. Tassel, Y. Kususe, K. Fujita, K. Tanaka, T. Yamamoto, Y. Kobayashi, H. Kageyama, *Chem. Mater.* **2015**, *27*, 6354–6359.
- [11] C. Eklöf-Osterberg, R. Nedumkandathil, U. Häussermann, A. Jaworski, A. J. Pell, M. Tyagi, N. H. Jalarvo, B. Frick, A. Faraone, M. Karlsson, *J. Phys. Chem. C* **2019**, *123*, 2019–2030.
- [12] T. Yajima, A. Kitada, Y. Kobayashi, T. Sakguchi, G. Bouilly, S. Kasahara, T. Terashima, M. Takano, H. Kageyama, *J. Am. Chem. Soc.* **2012**, *134*, 8782–8785.
- [13] H. Nawaz, F. Takeiri, A. Kuwabara, M. Yonemura, G. Kobayashi, *Chem. Commun.* **2020**, *56*, 10373.
- [14] K. Kobayashi, J. Yamaura, S. Iimura, S. Maki, H. Sagayama, R. Kumai, Y. Murakami, H. Takahashi, S. Matsuishi, H. Hosono, *Sci. Rep.* **2016**, *6*, 39646.
- [15] A. Mutschke, T. Wylezich, C. Ritter, A. J. Karttunen, N. Kunkel, *Eur. J. Inorg. Chem.* **2019**, 5073–5076.
- [16] K. Hayashi, H. Hosono, *Phys. Chem. Chem. Phys.* **2016**, *18*, 8186–8195.
- [17] F. Gehlhaar, R. Finger, N. Zapp, M. Bertmer, H. Kohlmann, *Inorg. Chem.* **2018**, *57*, 11851–11854.
- [18] T. Wu, A. Ishikawa, T. Honda, H. Tamatsukuri, K. Ikeda, T. Otomo, S. Matsuishi, *RSC Adv.* **2019**, *9*, 5282.
- [19] T. Wylezich, R. Valois, M. Suta, A. Mutschke, C. Ritter, A. Meijerink, A. J. Karttunen, N. Kunkel, *Chem. Eur. J.* **2020**, *26*, 11742–11750.
- [20] N. Kunkel, T. Wylezich, *Z. Anorg. Allg. Chem.* **2019**, *645*, 137–145.
- [21] C. Pflug, A. Franz, H. Kohlmann, *J. Solid State Chem.* **2018**, *258*, 391–396.
- [22] D. Rudolph, D. Ensling, T. Jüstel, T. Schleid, *Z. Anorg. Allg. Chem.* **2017**, *643*, 1525–1530.
- [23] T. Wylezich, S. Welinski, M. Hoelzel, P. Goldner, N. Kunkel, *J. Mater. Chem. C* **2018**, *6*, 13006–13012.
- [24] J. Ueda, S. Matsuishi, T. Tokunaga, S. Tanabe, *J. Mater. Chem. C* **2018**, *6*, 7541–7548.
- [25] T. Wu, K. Fujii, T. Murakami, M. Yashima, S. Matsuishi, *Inorg. Chem.* **2020**, *59*, 15384–15393.
- [26] M. Bernfield, M. Götte, P. W. Park, O. Reizes, M. L. Fitzgerald, J. Lincecum, M. Zako, *Annu. Rev. Biochem.* **1999**, *68*, 729–777.
- [27] S. Sarrazin, W. C. Lamanna, J. D. Esko, *Cold Spring Harbor Perspect. Biol.* **2011**, *3*, a004952.
- [28] F. Lipmann, *Science* **1958**, *128*, 575–580.
- [29] F. Yang, L. Wang, Y. Ge, L. Huang, D. Gao, J. Bi, G. Zou, *J. Alloys Compd.* **2020**, *834*, 155154.
- [30] W. Zhou, Y. Xu, L. Han, D. Zhu, *Dalton Trans.* **2010**, *39*, 3681–3686.
- [31] Y. Yu, Z. Wang, G. Shao, *J. Mater. Chem. A* **2019**, *7*, 21985–21996.
- [32] S. Fan, M. Lei, H. Wu, J. Hu, C. Yin, T. Liang, C. Li, *Energy Storage Mater.* **2020**, *31*, 87–94.
- [33] V. Petříček, M. Dušek, L. Palatinus, *Z. Kristallogr. - Cryst. Mater.* **2014**, *229*, 345–352.
- [34] V. F. Sears, *Neutron News* **1992**, *3*, 26.
- [35] J. Curda, E.-M. Peters, W. Klein, M. Jansen, *Z. Kristallogr.* **2001**, *216*, 190.
- [36] S. Han, C. Bai, B. Zhang, Z. Yang, S. Pan, *J. Solid State Chem.* **2016**, *237*, 14–18.
- [37] A. J. Maeland, W. D. Lahar, *Z. Phys. Chem.* **1993**, *179*, 181–185.
- [38] C. E. Messer, *J. Solid State Chem.* **1970**, *2*, 144–155.
- [39] L. Fanfani, G. Giuseppetti, C. Tadini, P. F. Zanazzi, *Mineral. Mag.* **1980**, *43*, 753–759.
- [40] M. S. Avdontceva, A. A. Zolotarev, S. V. Krivovichev, *J. Solid State Chem.* **2015**, *231*, 42–46.
- [41] S. Fan, M. Lei, H. Wu, J. Hu, C. Yin, T. Liang, C. Li, *Energy Storage Mater.* **2020**, *31*, 87–94.
- [42] J. M. S. Skakle, J. G. Fletcher, A. R. West, *Dalton Trans.* **1996**, 2497–2501.
- [43] A. Pabst, *Z. Kristallogr.* **1934**, *89*, 514–517.
- [44] “Hydrides: Solid State Transition Metal Complexes”: K. Yvon, G. Renaudin, *Encyclopedia of Inorganic and Bioinorganic Chemistry*, **2011**, John Wiley & Sons, Hoboken.
- [45] E. Zintl, A. Harder, *Z. Phys. Chem. Abt. B* **1931**, 14–265.
- [46] C. G. Shull, E. O. Wollan, G. A. Morton, W. L. Davidson, *Phys. Rev.* **1948**, *73*, 842.
- [47] F. C. Hawthorne, S. V. Krivovichev, P. C. Burns, *Rev. Mineral. Geochem.* **2000**, *40*, 1–112.
- [48] S. J. Louisnathan, R. J. Hill, G. V. Gibbs, *Phys. Chem. Miner.* **1977**, *1*, 53–69.
- [49] C. J. Jameson, J. Mason, *Multinuclear NMR*, Plenum Press, New York, **1987**, p. 51.
- [50] M. A. Kraft, S. P. Culver, M. Calderon, F. Böcher, T. Krauskopf, A. Senyshyn, C. Dietrich, A. Zevalkink, J. Janek, W. G. Zeier, *J. Am. Chem. Soc.* **2017**, *139*, 10909–10918.
- [51] Y. Wang, W. D. Richards, S. P. Ong, L. J. Miara, J. C. Kim, Y. Mo, G. Ceder, *Nat. Mater.* **2015**, *14*, 1026–1031.

Manuscript received: December 14, 2020
Accepted manuscript online: January 13, 2021
Version of record online: February 1, 2021



Supporting Information

Na₃SO₄H—The First Representative of the Material Class of Sulfate Hydrides

*Alexander Mutschke, Guy M. Bernard, Marko Bertmer, Antti J. Karttunen, Clemens Ritter, Vladimir K. Michaelis, and Nathalie Kunkel**

anie_202016582_sm_miscellaneous_information.pdf

WILEY-VCH

SUPPORTING INFORMATION

Table of Contents

1 Experimental Procedures	2
1.1 Synthesis	2
1.2 X-ray and neutron powder diffraction.....	2
1.3 Raman spectroscopy.....	2
1.4 FTIR spectroscopy	2
1.5 Solid-state nuclear magnetic resonance spectroscopy	2
1.6 Elemental analysis	2
1.7 Density functional calculations	3
2 Results and Discussion.....	4
2.1 Structural analysis.....	4
2.1.1 Neutron diffraction data	4
2.1.2 X-ray diffraction data	5
2.1.3 Crystal structure depictions	6
2.1.4 Difference Fourier map.....	8
2.1.5 Elemental analysis and air sensitivity	9
2.2 Vibrational spectroscopy	11
2.2.1 Detailed discussion of the FTIR and Raman spectra	15
2.3 Electronic structure	16
2.3.1 Optimized crystal structures as CIF (DFT-PBE0/TZVP level of theory).....	16
3 References.....	18
4 Author Contributions	18

SUPPORTING INFORMATION

1 Experimental Procedures

1.1 Synthesis

Since hydrides are sensitive to air and moisture and sulphates tend to bind water which hinder the reactions, all manipulations were handled in an argon-filled glovebox, with O₂ and H₂O concentrations kept below 0.5 ppm respectively. Na₃SO₄H can be obtained by the solid-state reaction of water-free Na₂SO₄ (anhydrous, Alfa Aesar, 99%) with NaH (Sigma Aldrich, 90%). Therefore, Na₂SO₄ (dried under dynamic vacuum at 200 °C for 48h) and NaH (10% excess) were ground thoroughly in an agate mortar and subsequently ball-milled in a Fritsch Pulverisette 7 premium line high energy ball-mill in a zirconia beaker with an overpressure valve and 10 mm zirconia balls at 250 rpm (2 min milling time, 3 min pause, 3 cycles) to ensure a complete homogenous mixture of the reactants. The mixture was then heated in a self-made autoclave made of a hydrogen-resistant alloy (Inconel Böhler 718) at 328 °C and 20 bars of hydrogen (H₂, 99.9%, Westfalen AG) pressure for 48 h. For neutron powder diffraction, large amounts of the deuterium enriched sample Na₃SO₄D (~5 g) were synthesized. The synthesis follows the same route as for Na₃SO₄H but with NaD and applied deuterium (D₂, 99.9%, AirLiquide) pressure. NaD is synthesized from NaH via an isotopic hydrogen-deuterium exchange. Thereto NaH is heated at 355 °C for 48 h under 80 bars of D₂ pressure. This is repeated for 5 times to reach a high isotope exchange. From neutron powder diffraction, only small traces (ca. 5%) of ¹H were determined. For simplification, the deuterium enriched sample Na₃SO₄D_{0.95}H_{0.05} is subsequently indicated as Na₃SO₄D. For a detailed structural analysis see below and manuscript.

1.2 X-ray and neutron powder diffraction

X-ray powder diffraction data were recorded on a Stoe STADI-P in transmission geometry with Cu-Kα1 radiation (λ = 1.54056 Å), a curved Ge-monochromator (111) and a Dectris Mythen DCS 1K solid state detector. In order to avoid decomposition of the samples during measurements, the powders were placed in sealed glass capillaries (Ø 0.3 mm, 0.1 mm wall thickness). Angle corrections were determined by an external silicon standard (NIST SRM 640c).

Neutron powder diffraction data of Na₃SO₄D were recorded at the two-axis high-resolution powder neutron diffractometer D2B at the Institute Laue-Langevin (ILL), Grenoble, with a wavelength of 1.594 Å over the course of 5h. For the measurement ~4 g of the sample were enclosed in an 8 mm vanadium cylinder and sealed airtight with an indium wire.

Crystal structure refinement of the X-ray diffraction and neutron diffraction data was done using the program package FullProf with the Rietveld method and the fundamental parameter approach^[1]. Profiles were fitted via pseudo-Voigt functions. The zero shift, cell parameters, three form factors (caglioti parameters U, V, W), four asymmetry parameters, atomic parameters and anisotropic thermal displacement parameters were refined. The background correction was done with linear interpolations of background points.

Further details on the crystal structure investigations may be obtained from the Fachinformationszentrum Karlsruhe, 76344 Eggenstein-Leopoldshafen, Germany (fax: (+49)7247-808-666; e-mail: crysdata@fiz-karlsruhe.de), on quoting the depository number CSD 2049318.

1.3 Raman spectroscopy

Raman spectra were recorded on powders sealed in glass capillaries (Ø 0.3 mm, 0.1 mm wall thickness) on a Renishaw inVia Reflex Raman System equipped with a CCD detector and a λ = 532 nm laser in the range of 100-1200 cm⁻¹.

1.4 FTIR spectroscopy

FTIR spectra were recorded on a Bruker Alpha-P FT-IR spectrometer with an ATR unit. To avoid water and air contamination, the spectrometer was operated within an argon filled glovebox. Measurements were taken in the range of 450-4000 cm⁻¹ and a spectral resolution of 1 cm⁻¹.

1.5 Solid-state nuclear magnetic resonance spectroscopy

Samples were stored under argon until ready for NMR analysis, then packed in a 4.0 mm outer-diameter zirconia NMR rotor within an Ar-filled glove box. Solid-state ¹H NMR spectra of Na₃SO₄H were acquired at room temperature on a Bruker Avance III 400 HD NMR spectrometer, operating at 400.3 MHz, with a 4.0 μs 90° pulse (ν_{rf} = 62.5 kHz) and a recycle delay of 180 s and with a magic-angle spinning (MAS) frequency of 10.0 kHz; 4 transients were co-added and the spectra were referenced with respect to TMS (δ = 0 ppm) by setting the isotropic peak of an MAS sample of adamantane to 1.85 ppm. Solid-state ²³Na NMR spectra of this sample were also acquired on a Bruker Avance III 400 HD NMR spectrometer, operating at 106.9 MHz. Each spectrum was acquired using a 4.0 μs solid 90° excitation pulse, 5 s recycle delay, 64 co-added transients and an MAS frequency of 10 kHz. Spectra were referenced by setting the isotropic peak of NaNO₃ to -7.1 ppm under MAS.^[2] The ²³Na NMR spectra were simulated using the WSOLIDS program.^[3]

1.6 Elemental analysis

SUPPORTING INFORMATION

Elemental analysis has been conducted on a Vario EL microanalyzer with the Na₃SO₄H via the hot gas extraction method in air-tight tin crucibles. To avoid water and air contamination, ~5 mg of the samples were packed in an argon filled glovebox and folded several times within the tin crucible.

1.7 Density functional calculations

The structure, electronic properties, and vibrational spectra of Na₃SO₄H were investigated with the CRYSTAL17 program package.^[4] PBE0 hybrid density functional method and Gaussian-type basis sets were used.^[5,6] The basis sets for Na, S, O, and H have been previously derived from the molecular Karlsruhe def2 basis sets.^[7] Polarized triple-zeta-valence (TZVP) basis sets were used for S, O, and H, polarized split-valence basis set for Na.^[8] The reciprocal space was sampled using a 4×4×6 Monkhorst-Pack-type *k*-mesh.^[9] NaH and Na₂SO₄ were also studied at the same level of theory to evaluate the energetics of the formation of Na₃SO₄H. 6×6×4 and 10×10×10 *k*-meshes were applied for NaH (*Fm-3m*) and Na₂SO₄ (*Cmcm*), respectively. For the evaluation of the Coulomb and exchange integrals (TOLINTEG), tight tolerance factors of 8, 8, 8, 8, and 16 were used. Both the atomic positions and lattice constants were fully optimized within the constraints imposed by the space group symmetry. The optimized lattice parameters *a* and *c* differed from the experimental parameters by +0.1% and -0.5%, respectively. The harmonic vibrational frequencies, IR intensities, and Raman intensities were obtained by using the computational schemes implemented in CRYSTAL.^[10] The optimized structure of Na₃SO₄H was confirmed to be a true local minimum with no imaginary frequencies. The final IR spectra were obtained by using Lorentzian peak profile with FWHM of 8 cm⁻¹. The Raman intensities have been calculated for a polycrystalline powder sample (total isotropic intensity in arbitrary units). When simulating the Raman spectrum, the temperature and laser wavelength were set to values corresponding to the experimental setup (*T* = 298.15 K, *λ* = 532 nm). The final spectrum was obtained by using pseudo-Voigt peak profile (50:50 Lorentzian: Gaussian) and FWHM of 8 cm⁻¹.

The solid-state NMR magnetic shielding (¹H and ²³Na) and electric field gradient (²³Na) tensors of Na₃SO₄H were calculated with the DFT-PBE method^[5] using the CASTEP program package and the GIPAW formalism as implemented in CASTEP-NMR.^[11,12] Ultrasoft pseudopotentials generated with the on-the-fly scheme and a plane-wave basis set cut-off of 660 eV were applied.^[13] The reciprocal space was sampled using a 4×4×6 Monkhorst-Pack-type *k*-mesh.^[9] The NMR shielding tensor of Na₃SO₄H was calculated both at the experimental geometry and DFT-PBE optimized geometry. In the geometry optimization, both the lattice parameters and atomic positions were fully optimized with a total energy convergence criterion of 0.5 × 10⁻⁶ eV/atom. The optimized lattice parameters *a* and *c* differed from the experimental parameters by +1.2% and +1.1%, respectively. Molecular SiMe₄ and solid NaCl were used as references to convert the computed shieldings to ¹H NMR and ²³Na chemical shifts. The calculations on SiMe₄ were carried out in a primitive cubic cell (*a* = 15 Å) using a plane-wave basis set cut-off of 700 eV and Γ -point for reciprocal space sampling. The structure of the SiMe₄ molecule was relaxed within the *T_d* point group. The isotropic ¹H shielding of SiMe₄ is 31.01 ppm. The isotropic ¹H shielding of the hydride in Na₃SO₄H is 26.70 ppm at the experimental geometry and 26.67 ppm at the optimized geometry, corresponding to a ¹H chemical shift of 4.3 ppm in both cases. The calculations on NaCl (*Fm-3m*) were carried out using a plane-wave basis set cut-off of 660 eV and 8×8×8 *k*-mesh. The optimized lattice constant *a* differs from the experimental value by +0.9%. The isotropic ²³Na shielding of NaCl is 544.91 ppm at the optimized geometry. The isotropic ²³Na shieldings in Na₃SO₄H are 547.38 ppm for Na1 and 537.25 for Na2.

WILEY-VCH

SUPPORTING INFORMATION

2 Results and Discussion

2.1 Structural analysis

2.1.1 Neutron diffraction data

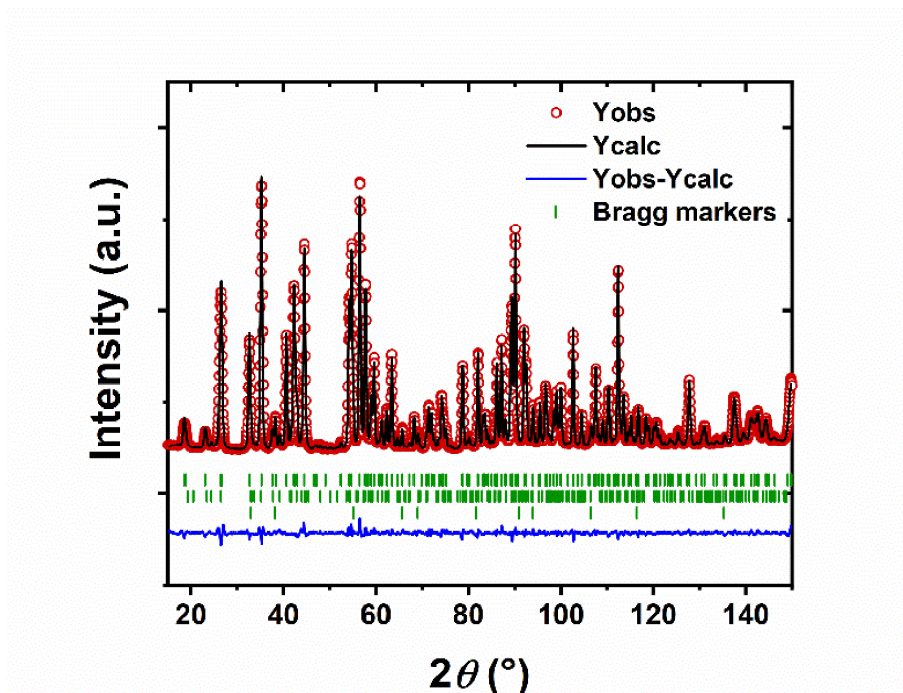


Figure S1 Rietveld refinement plot of $\text{Na}_3\text{SO}_4\text{D}$. Bragg markers from top to bottom: $\text{Na}_3\text{SO}_4\text{D}$ (92.2(9) wt.%), Na_2SO_4 ($Cmcm$) (6.3(7) wt.%), NaD (1.5(2) wt.%). R-factors not corrected for background intensity: $R_p = 1.70\%$ $R_{wp} = 3.63\%$ $R_{exp} = 3.63\%$. Conventional Rietveld R-factors: $R_p = 5.48\%$ $R_{wp} = 9.11\%$ $R_{exp} = 9.10$, $\chi^2 = 1.00$.

Table S1. Crystallographic data on $\text{Na}_3\text{SO}_4\text{D}$ ($P4/nmm$) determined by Rietveld refinement of neutron diffraction data

Cell parameters					
$a = 7.0034(2) \text{ \AA}$ $c = 4.8569(2) \text{ \AA}$, $V = 238.22(2) \text{ \AA}^3$					
Atom	Wyckoff position	Site	x/a	y/b	z/c
D1	2c	4mm	1/4	1/4	0.5991(4)
Na1	4e	.2/m	0	0	1/2
Na2	2c	4mm	1/4	1/4	0.0621(7)
S1	2a	-4m2	3/4	1/4	0
O1	8i	.m.	1/4	0.9212(1)	0.1766(2)

Table S2. Anisotropic displacement parameters of $\text{Na}_3\text{SO}_4\text{D}$ determined by neutron diffraction data

Anisotropic displacement parameters, in \AA^2						
Atom	U_{11}	U_{22}	U_{33}	U_{12}	U_{13}	U_{23}
D1	0.0281(8)	0.0281(8)	0.0201(14)	0.00000	0.00000	0.00000
H1	0.0281(8)	0.0281(8)	0.0201(14)	0.00000	0.00000	0.00000
Na1	0.0172(8)	0.0172(8)	0.0231(14)	0.0031(12)	0.0046(7)	0.0046(7)
Na2	0.0145(11)	0.0145(11)	0.0175(16)	0.00000	0.00000	0.00000
S1	0.0058(10)	0.0058(10)	0.0102(18)	0.00000	0.00000	0.00000
O1	0.0175(5)	0.0089(5)	0.0177(5)	0.00000	0.00000	-0.0041(5)

Table S3. Selected interatomic distances of $\text{Na}_3\text{SO}_4\text{D}$

WILEY-VCH

SUPPORTING INFORMATION

Atom 1	Atom 2	Distance (Å)
Na1	O1(1)	2.4160(9)
Na1	O1(2)	2.4160(7)
Na1	D1/H1	2.5224(4)
Na2	O1	2.3687(12)
Na2	D1/H1	2.2488(39)
Na2	D1/H1	2.6082(39)
S1	O1(1)	1.4744(9)
S1	O1(2)	1.4744(9)

2.1.2 X-ray diffraction data

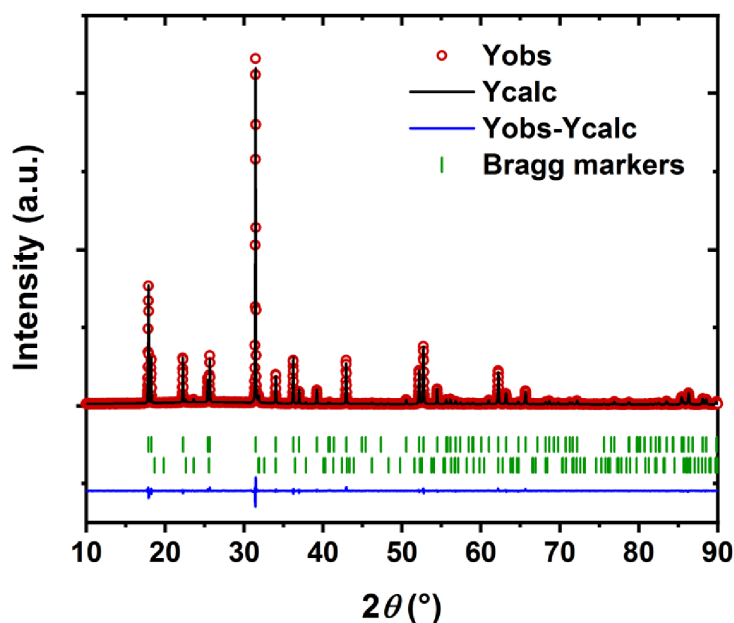


Figure S2. Rietveld refinement plot of $\text{Na}_3\text{SO}_4\text{H}$. Bragg markers from top to bottom: $\text{Na}_3\text{SO}_4\text{H}$ (93.9(7) wt.%), Na_2SO_4 ($Cmcm$) (6.1(4) wt.%), R-factors not corrected for background intensity: $R_p = 4.32\%$ $R_{wp} = 5.48\%$ $R_{exp} = 4.72\%$. Conventional Rietveld R-factors: $R'_p = 11.90\%$ $R'_{wp} = 10.20\%$ $R'_{exp} = 8.76$, $X^2 = 1.35$.

Table S4. Crystallographic data on $\text{Na}_3\text{SO}_4\text{H}$ ($P4/nmm$) determined by Rietveld refinement of X-ray diffraction data. *the thermal displacement parameter of hydride has been set to a positive value. Due to the very weak scattering power of hydrides in X-ray diffraction, no realistic value was obtainable during refinement.

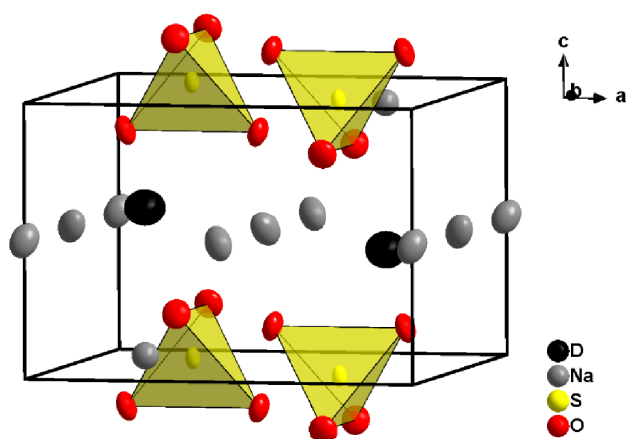
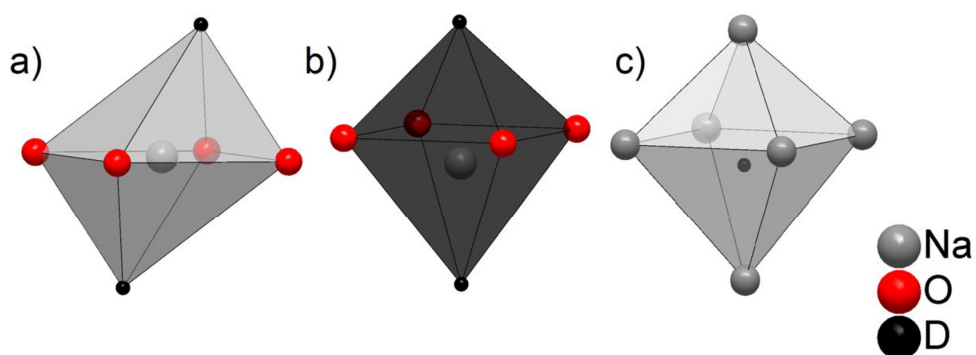
Cell parameters						
$a = 7.00530(5) \text{ \AA}$, $c = 4.85822(4) \text{ \AA}$, $V = 238.414(3) \text{ \AA}^3$						
Atom	Wyckoff position	Site	x/a	y/b	z/c	U [\AA^2]
H1	2c	4mm	1/4	1/4	0.6080(50)	0.0063*
Na1	4e	2/m	0	0	1/2	0.0122(6)
Na2	2c	4mm	1/4	1/4	0.0644(4)	0.0092(7)
S1	2a	-4m2	3/4	1/4	0	0.0046(6)
O1	8i	m	1/4	0.9208(2)	0.1774(3)	0.0052(5)

SUPPORTING INFORMATION

Table S5. Selected interatomic distances of Na₃SO₄H

Atom 1	Atom 2	Distance (Å)
Na1	O1(1)	2.4149(13)
Na1	O1(2)	2.4149(10)
Na1	H1	2.5317(60)
Na2	O1(1)	2.3709(13)
Na2	O1(2)	2.3924(18)
Na2	H1	2.6409(292)
Na2	H1	2.2173(292)
S1	O1(1)	1.4744(13)
S1	O1(2)	1.4744(9)

2.1.3 Crystal structure depictions

**Figure S3.** Simplified Crystal structure of Na₃SO₄D determined from neutron powder diffraction. Ellipsoids are depicted with a probability of 75%.**Figure S4.** Coordination polyhedra of the sodium atoms Na1 (a) and Na2 (b) and deuteride (c).

WILEY-VCH

SUPPORTING INFORMATION

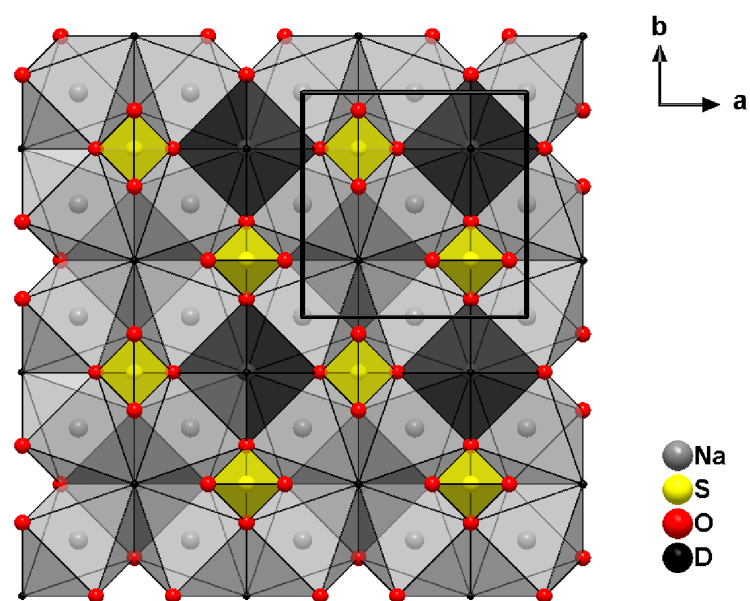


Figure S5. Alternative view of the crystal structure of $\text{Na}_3\text{SO}_4\text{D}$ along the c-axis showing a checkerboard pattern

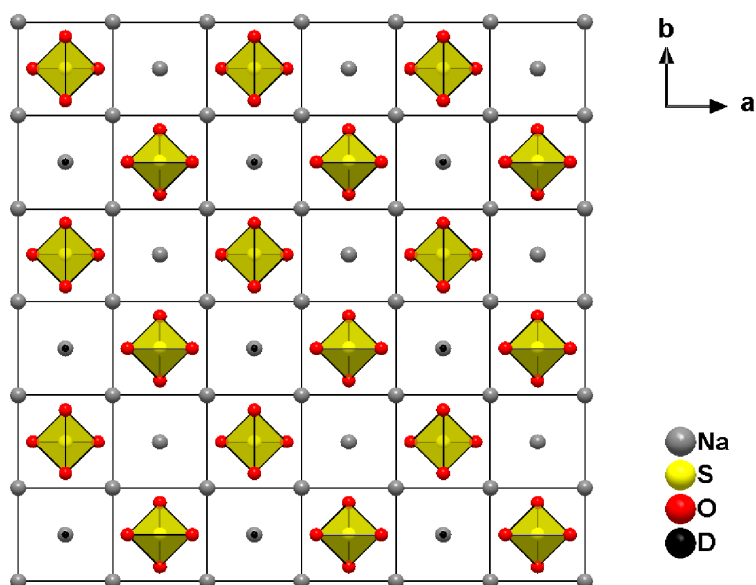


Figure S6. Crystal structure of $\text{Na}_3\text{SO}_4\text{D}$ with checkerboard-like occupied voids of the sodium square lattice.

WILEY-VCH

SUPPORTING INFORMATION

2.1.4 Difference Fourier map

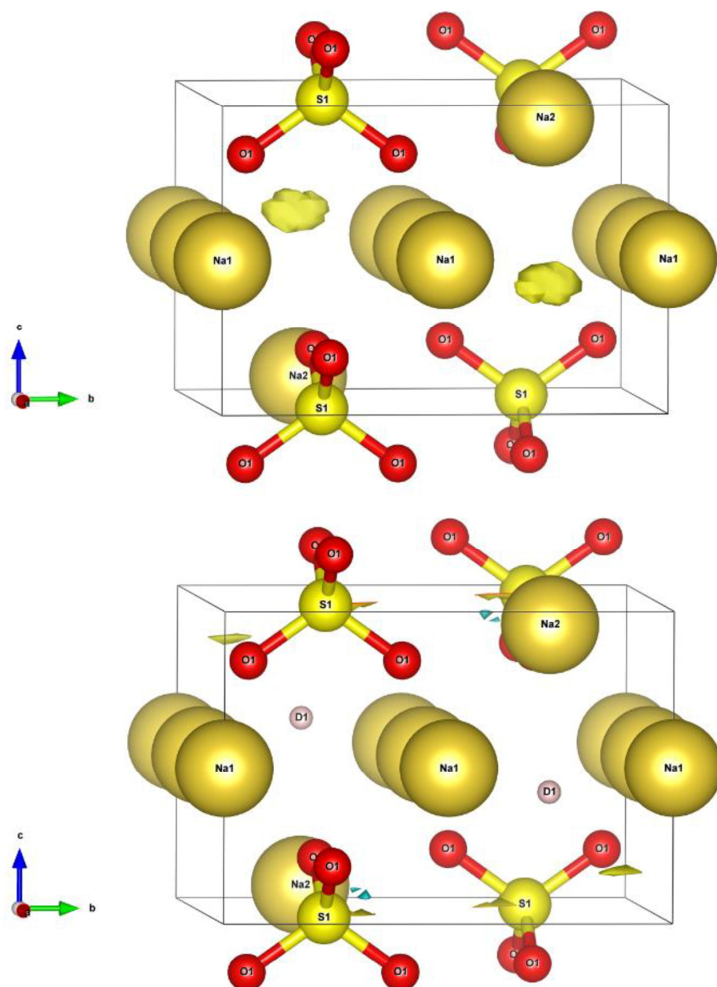


Figure S7. Difference Fourier map of the refinement Na_3SO_4 (top), in which the deuterium position was kept unoccupied (symbol \square , in FullProf Occ and B_{iso} were set to 0). Na is shown in gold, sulfur in yellow and oxygen in red. The positive, oval-shaped residual density (yellow isosurface, projected at an isosurface level of 0.11) is in good agreement with the deuterium position in $\text{Na}_3\text{SO}_4\text{D}$. For comparison: difference Fourier map of the refinement $\text{Na}_3\text{SO}_4\text{D}$ (bot). Almost no residual density is found at a very low isosurface level of 0.0035. Also, no residual density is found next to the deuteride position. This further excludes a likely hydroxide/deuterioxide species. Graphic representation is shown in VESTA.^[14]

SUPPORTING INFORMATION

2.1.5 Elemental analysis and air sensitivity

Analysenauftrag-bericht Telefon: 89 289 13115
 Name: Alexander Nutschler Raum: 47422
 Substanzbezeichnung: AM-183-Na₂SO₄H Arbeitskreis: Füssler

Bitte **alle** anwesenden Elemente mit deren ungefähren Massenprozentwerten angeben. (Summe aller Massenprozentwerte sollte 100% ergeben!)

Alle anwesenden Elemente	Zu best.	Als ungef. %-Gehalte	Param. Zuechl.	Analysen-Nr.	Einwaage in mg	Elementarbestimmung Gehalten in %	Doppelbestimmung Gehalten in %
C	<input checked="" type="checkbox"/>			282/19	4,894	0,05	
H	<input checked="" type="checkbox"/>	0,00		/		0,61	
N	<input checked="" type="checkbox"/>			/		0,01	
S	<input checked="" type="checkbox"/>	19,31		/		> 13,5	
O	<input checked="" type="checkbox"/>	39,54		/			
Na	<input checked="" type="checkbox"/>	41,53		/			
				/			
				/			

Besondere Hinweise: Die Probe muss absolut homogen sein!
 Keine Rundkolben Keine Rührscheitel
 sehr luftempfindlich thermolabil giftig Aufbewahrung im Kühlschrank
 wenig luftempfindlich flüchtig polymer Aufbewahrung im Gefrierfach
 hygroskopisch explosiv flüssig atink
 lichtempfindlich elektrostatisch auf Abnd. auf glove-box
 Einwaage: offen glove-box

Bemerkungen: (wird vom Mikrolabor ausgefüllt)
 Gewichtszunahme Gewichtsabnahme zu geringe Einwaage
 außerhalb des Messbereichs nur Orientierungswert

TUM Zentralinstitut für Katalysatorforschung
 Elementaranalyse
 Ernst-Otto-Fischer Str. 1
 85748 Garching
 Tel: +49 89 289-54127
 elementaranalyse@tum.de

Datum: 06.12.19
 Durchgeführt von: U.A.

Öffnungszeiten Mo-Do 9-10 Uhr und 14-14.30 Uhr / Freitag 9-10 Uhr

Figure S8. Picture of the elemental analysis report of Na₂SO₄H. The experimental determined value of 0.61 wt.% matches almost identically to the theoretical value of 0.60 wt.%. The determined mass percentage of sulfur is lower due to the formation of NaS during the elemental analysis, disturbing the determination of the sulfur content.

WILEY-VCH

SUPPORTING INFORMATION

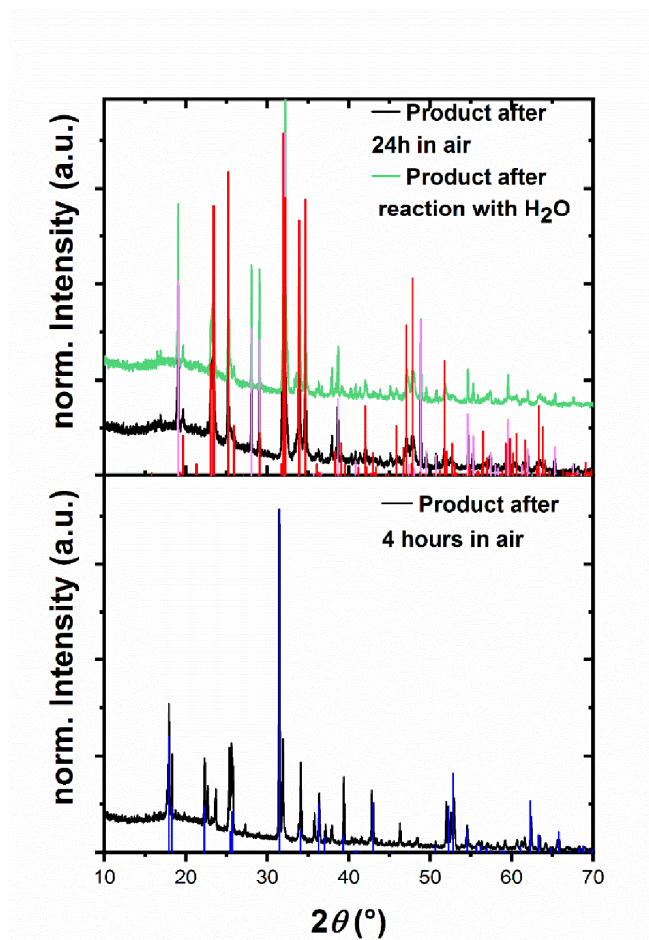


Figure S9. Short-scan X-ray diffraction patterns of the decomposition products after reaction of Na₂SO₄H with air after 4h (bottom) and with air after 24h and water (top). Simulated pattern of Na₂SO₄H blue, Na₄[SO₄]_{1.5}[CO₃]_{0.5} (Burkeite) red and Na₂SO₄ (Thenardite, *Fdd*), purple.

WILEY-VCH

SUPPORTING INFORMATION

2.2 Vibrational spectroscopy

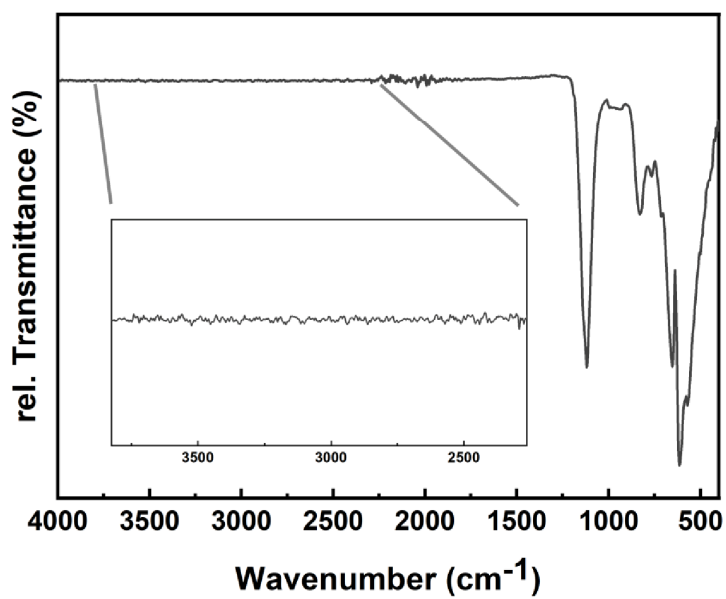


Figure S10. Full FT-IR spectrum of Na₃SO₄H between 4000 cm⁻¹ and 450 cm⁻¹ with an enlarged area between 3800 cm⁻¹ and 2250 cm⁻¹. The enlarged area does not show a visible signal; thus, a hypothetical hydroxide species can be further excluded.

WILEY-VCH

SUPPORTING INFORMATION

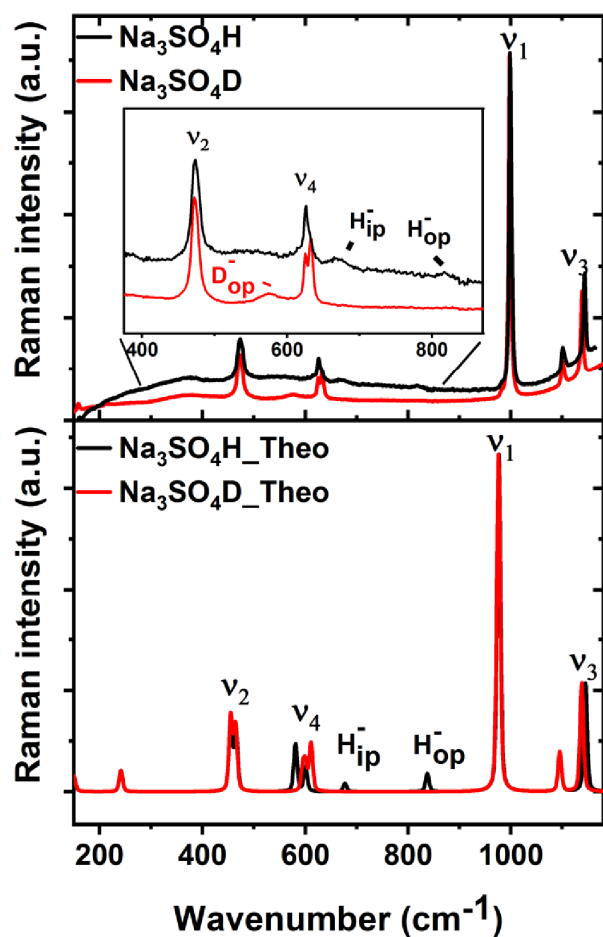


Figure S11. Raman spectra of $\text{Na}_3\text{SO}_4\text{H}$ and $\text{Na}_3\text{SO}_4\text{D}$ between 1200 cm^{-1} and 150 cm^{-1} (upper traces) compared to the corresponding theoretical spectra (lower traces). The area from $400\text{--}850\text{ cm}^{-1}$ is enlarged for a better depiction of hydride/deuteride modes. Raman intensities are in arbitrary units.

WILEY-VCH

SUPPORTING INFORMATION

Table S6. Vibrational Raman data obtained by quantum chemical calculations. The frequency, irreducible representation, intensity and assignment to vibrations are given within this table for Na₃SO₄H and Na₃SO₄D. The plane is described as the plane build by the sodium atoms in the 4e position as depicted in Figure S10.

Na ₃ SO ₄ H				Na ₃ SO ₄ D			
Frequency (cm ⁻¹)	Γ _{irrep}	Intensity (arbitrary units)	Assignment	Frequency (cm ⁻¹)	Γ _{irrep}	Intensity (arbitrary units)	Assignment
112	E _g	4	SO ₄ ²⁻ in-plane mode coupled with Na ⁺ and H ⁺	112	E _g	3	SO ₄ ²⁻ in-plane mode coupled with Na ⁺ and D ⁺
121	B _{1g}	20	SO ₄ ²⁻ out-of-plane mode	121	B _{1g}	19.91	SO ₄ ²⁻ out-of-plane mode
145	A _{1g}	49	Na ⁺ out-of-plane mode	145	A _{1g}	50.16	Na ⁺ out-of-plane mode
150	E _g	31	SO ₄ ²⁻ wagging	150	E _g	31.81	SO ₄ ²⁻ wagging
241	E _g	62	Na ⁺ in-plane mode	241	E _g	62.80	Na ⁺ in-plane mode
455	B _{2g}	214	SO ₄ ²⁻ symmetrical bending (ν ₂)	455	B _{2g}	218.18	SO ₄ ²⁻ symmetrical bending (ν ₂)
466	A _{1g}	177	SO ₄ ²⁻ symmetrical bending (ν ₂)	462	E _g	26.07	Deuteride in-plane mode
581	E _g	140	Hydride in-plane mode coupled with SO ₄ ²⁻ bending	465	A _{1g}	171.65	SO ₄ ²⁻ symmetrical bending (ν ₂)
600	B _{1g}	71	SO ₄ ²⁻ antisymmetrical bending (ν ₄)	595	A _{1g}	67.15	Deuteride out-of-plane mode
677	E _g	24	Hydride in-plane mode	600	B _{1g}	72.89	SO ₄ ²⁻ antisymmetrical bending (ν ₄)
837	A _{1g}	53	Hydride out-of-plane mode	611	E _g	141.11	SO ₄ ²⁻ wagging coupled with deuteride in-plane mode
975	A _{1g}	1000	SO ₄ ²⁻ symmetrical stretching (ν ₁)	976	A _{1g}	1000.00	SO ₄ ²⁻ symmetrical stretching (ν ₁)
1095	B _{1g}	116	SO ₄ ²⁻ antisymmetrical stretching (ν ₃)	1095	B _{1g}	118.19	SO ₄ ²⁻ antisymmetrical stretching (ν ₃)
1145	E _g	319	SO ₄ ²⁻ antisymmetrical stretching (ν ₃)	1138	E _g	322.43	SO ₄ ²⁻ antisymmetrical stretching (ν ₃)

WILEY-VCH

SUPPORTING INFORMATION

Table S7. Vibrational Infrared data obtained by quantum chemical calculations. The frequency, irreducible representation, intensity and assignment to vibrations are given within this table for Na₃SO₄H and Na₃SO₄D. The plane is described as the plane build by the sodium atoms in the 4e position as depicted in Figure S10.

Na ₃ SO ₄ H				Na ₃ SO ₄ D			
Frequency (cm ⁻¹)	Γ _{irrep}	Intensity (km/mol)	Assignment	Frequency (cm ⁻¹)	Γ _{irrep}	Intensity (km/mol)	Assignment
0	E _u	0	Isotropic lattice vibration	0	E _u	0	Isotropic lattice vibration
0	A _{2u}	0	Isotropic lattice vibration	0	A _{2u}	0	Isotropic lattice vibration
108	E _u	312	lattice low frequency vibration	107	E _u	315	lattice low frequency vibration
135	E _u	3	lattice low frequency vibration	135	E _u	3	lattice low frequency vibration
147	A _{2u}	135	Na ⁺ out-of-plane mode	147	A _{2u}	134	Na ⁺ out-of-plane mode
180	A _{2u}	85	Na ⁺ -plane vibration	180	A _{2u}	85	Na ⁺ -plane vibration
216	E _u	123	Na ⁺ -plane vibration	216	E _u	123	Na ⁺ -plane vibration
223	E _u	67	Na ⁺ -plane vibration	223	E _u	65	Na ⁺ -plane vibration
242	E _u	311	Na ⁺ in-plane mode	242	E _u	290	Na ⁺ in-plane mode
249	A _{2u}	188	Na ⁺ -plane vibration	249	A _{2u}	188	Na ⁺ -plane vibration
579	E _u	1922	Hydride in-plane mode coupled with SO ₄ ²⁻ bending	445	E _u	2097	Deuteride in-plane mode
605	A _{2u}	254	antisymmetrical bending	590	A _{2u}	956	Deuteride out-of-plane mode
640	E _u	2250	Hydride in-plane mode	595	E _u	135	Deuteride in-plane mode coupled with SO ₄ ²⁻ bending
838	A _{2u}	1512	Hydride out-of-plane mode	610	A _{2u}	1	SO ₄ ²⁻ antisymmetrical bending
1118	E _u	2334	SO ₄ ²⁻ antisymmetrical stretching (ν ₃)	1116	E _u	2684	SO ₄ ²⁻ antisymmetrical stretching (ν ₃)
1137	A _{2u}	1099	SO ₄ ²⁻ antisymmetrical stretching (ν ₃)	1135	A _{2u}	1257	SO ₄ ²⁻ antisymmetrical stretching (ν ₃)

SUPPORTING INFORMATION

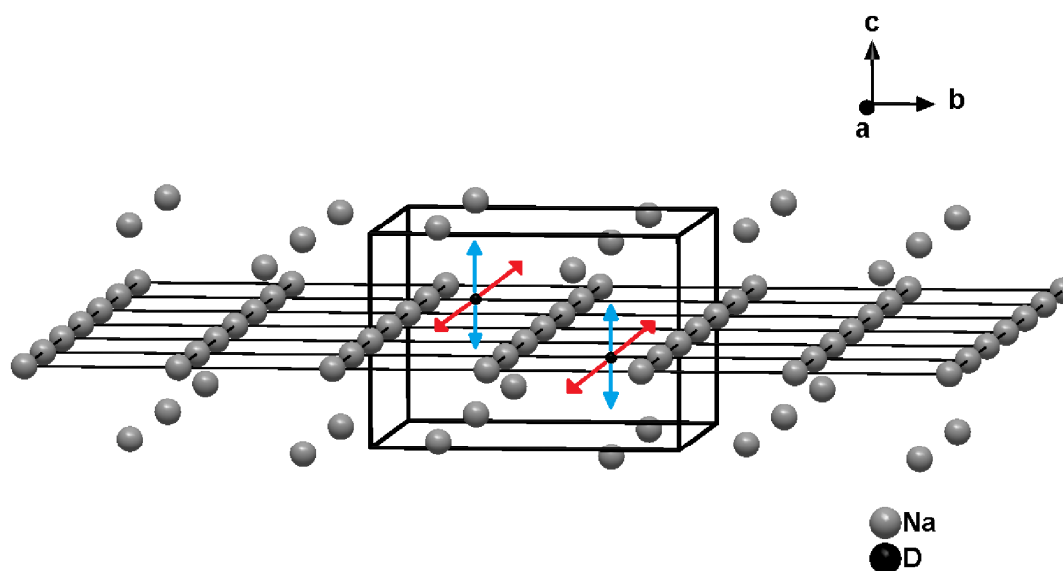


Figure S12. Only the sodium atoms and deuteride ions depicted to visualize the hydride/deuteride vibrational modes along the square plane build by the sodium atoms in the 4e position necessary to understand the vibrational spectra. Red arrows depict the in-plane modes, blue arrows out-of-plane modes.

2.2.1 Detailed discussion of the FTIR and Raman spectra

FT-IR

Besides bands caused by the hydride vibrations, vibrational bands corresponding to the sulphate ions are clearly visible (Fig 3). The antisymmetric S-O stretch (ν_3) vibrations are visible as a doublet at around 1119 cm^{-1} and 1135 cm^{-1} , both fitting almost exactly to the simulated spectrum. Symmetrical stretch vibrations are not seen as this mode is IR-inactive according to the group symmetry. The asymmetric S-O bending vibration (ν_4) can be observed at around 600 cm^{-1} according to the theoretical spectrum but is underestimated in intensity in the theoretical spectrum. The symmetric bending mode ν_2 is not visible and in agreement with the rules of the group symmetry.

Raman

The hydride out of plane and in plane modes yield small signals at 820 cm^{-1} (H_{op}) and 673 cm^{-1} (H_{ip}) respectively, both being close to the corresponding calculated values of 837 cm^{-1} and 677 cm^{-1} . The Raman spectrum of the $\text{Na}_3\text{SO}_4\text{D}$ shows a deuteride out of plane mode (D_{op}) as a bulky signal at 577 cm^{-1} being shifted almost exactly by a factor of $\sqrt{2}$ from the hydride out of plane mode at 820 cm^{-1} . Additionally, the Raman spectrum, similar to the FT-IR-spectrum, shows the typical S-O stretch and bending vibrations with the Raman-active symmetric S-O stretching (ν_1) mode being the most intense signal at 999 cm^{-1} . The signal is shifted 23 cm^{-1} towards higher energies compared to the simulated spectrum. The antisymmetric S-O stretching modes (ν_3) can be seen at about 1101 cm^{-1} and 1145 cm^{-1} alongside the ν_1 mode. The ν_3 modes both fit the simulated spectra rather well with the calculated values of 1095 cm^{-1} and 1145 cm^{-1} respectively. The symmetrical bending modes (ν_2) of the sulphate ions appear as a doublet at 471 cm^{-1} and 477 cm^{-1} and as doublet at 625 cm^{-1} for the antisymmetric bending modes (ν_4) which is in good agreement with the theoretical spectrum albeit being shifted slightly towards higher wavenumbers. Due to the resolution of the Raman spectrometer, the doublets cannot be resolved properly and appear as a bulky single signal.

WILEY-VCH

SUPPORTING INFORMATION

2.3 Electronic structure

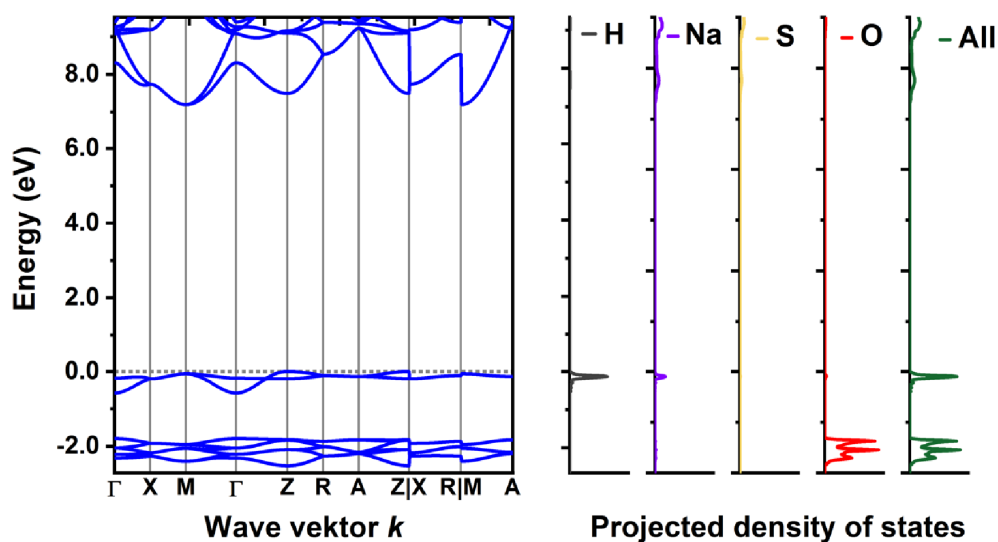


Figure S13. Electronic band structure and atom-projected density of states of $\text{Na}_3\text{SO}_4\text{H}$ at the DFT-PBE0/TZVP level of theory. The band gap is 7.4 eV. The topmost valence bands are dominated by hydride anions, with minor contributions from the other atoms. The band paths in the reciprocal space were obtained from the Seek-path web service.^[15]

2.3.1 Optimized crystal structures as CIF (DFT-PBE0/TZVP level of theory)

```

data_Na3SO4H
_audit_creation_method FINDSYM

_cell_length_a 7.0094425500
_cell_length_b 7.0094425500
_cell_length_c 4.8334431900
_cell_angle_alpha 90.0000000000
_cell_angle_beta 90.0000000000
_cell_angle_gamma 90.0000000000

_symmetry_space_group_name_H-M "P 4/n 21/m 2/m (origin choice 2)"
_symmetry_Int_Tables_number 129
_space_group.reference_setting '129: -P 4a 2a'
_space_group.transform_Pp_abc a,b,c;0,0,0

loop_
_space_group_symop_id
_space_group_symop_operation_xyz
1 x,y,z
2 x+1/2,-y,-z
3 -x,y+1/2,-z
4 -x+1/2,-y+1/2,z
5 -y,-x,-z
6 -y+1/2,x,z
7 y,-x+1/2,z
8 y+1/2,x+1/2,-z
9 -x,-y,-z
10 -x+1/2,y,z

```

WILEY-VCH

SUPPORTING INFORMATION

```
11 x, -y+1/2, z
12 x+1/2, y+1/2, -z
13 y, x, z
14 y+1/2, -x, -z
15 -y, x+1/2, -z
16 -y+1/2, -x+1/2, z

loop_
_atom_site_label
_atom_site_type_symbol
_atom_site_symmetry_multiplicity
_atom_site_Wyckoff_label
_atom_site_fract_x
_atom_site_fract_y
_atom_site_fract_z
_atom_site_occupancy
Na1 Na 4 e 0.00000 0.00000 0.50000 1.00000
Na2 Na 2 c 0.25000 0.25000 0.06638 1.00000
S1 S 2 a 0.75000 0.25000 0.00000 1.00000
O1 O 8 i 0.25000 -0.07544 0.18168 1.00000
H1 H 2 c 0.25000 0.25000 0.60403 1.00000

-----
data_Na2S04
_audit_creation_method FINDSYM

_cell_length_a 5.6758931020
_cell_length_b 8.9561781623
_cell_length_c 6.9242946300
_cell_angle_alpha 90.0000000000
_cell_angle_beta 90.0000000000
_cell_angle_gamma 90.0000000000

_symmetry_space_group_name_H-M "C 2/m 2/c 21/m"
_symmetry_Int_Tables_number 63
_space_group.reference_setting '063: -C 2c 2'
_space_group.transform_Pp_abc a,b,c;0,0,0

loop_
_space_group_symop_id
_space_group_symop_operation_xyz
1 x,y,z
2 x,-y,-z
3 -x,y,-z+1/2
4 -x,-y,z+1/2
5 -x,-y,-z
6 -x,y,z
7 x,-y,z+1/2
8 x,y,-z+1/2
9 x+1/2,y+1/2,z
10 x+1/2,-y+1/2,-z
11 -x+1/2,y+1/2,-z+1/2
12 -x+1/2,-y+1/2,z+1/2
13 -x+1/2,-y+1/2,-z
14 -x+1/2,y+1/2,z
15 x+1/2,-y+1/2,z+1/2
16 x+1/2,y+1/2,-z+1/2

loop_
_atom_site_label
_atom_site_type_symbol
_atom_site_symmetry_multiplicity
_atom_site_Wyckoff_label
_atom_site_fract_x
_atom_site_fract_y
_atom_site_fract_z
_atom_site_occupancy
Na1 Na 4 a 0.00000 0.00000 0.00000 1.00000
Na2 Na 4 c 0.00000 0.31267 0.25000 1.00000
```

WILEY-VCH

SUPPORTING INFORMATION

51	S	4	c	0.00000	0.65045	0.25000	1.00000
01	O	8	g	0.28378	0.05106	0.25000	1.00000
02	O	8	f	0.00000	0.74713	0.07390	1.00000

NaH

NaCl structure type (*Fm-3m*), lattice constant $a = 4.8241 \text{ \AA}$.

3 References

- [1] J. Rodriguez-Carvajal, *Physica B*, 1993, **192**, 55.
[2] R. Tabeta; M. Aida, H. Saito, *Bull. Chem. Soc. Jpn.*, **1986**, 59, 1957-1966
[3] WSolids NMR simulation package, V. 1.15.1; K. Eichele, *Universität Tübingen*; 2015.
[4] R. Dovesi, A. Erba, R. Orlando, C. M. Zicovich-Wilson, B. Civalleri, L. Maschio, M. Rérat, S. Casassa, J. Baima, S. Salustro, B. Kirtman, *Wiley Interdiscip. Rev. Comput Mol. Sci.* **2018**, 8, 1-36.
[5] J. Perdew, K. Burke, M. Ernzerhof, *Phys. Rev. Lett.* **1996**, 77, 3865-3868.
[6] C. Adamo, V. Barone, *Chem. Phys.* **1999**, 110, 6158-6170.
[7] F. Weigend, R. Ahlrichs, *Phys. Chem. Chem. Phys.* **2005**, 7, 3297-3305.
[8] a) A. J. Karttunen, T. Tynell, M. Karppinen, *J. Phys. Chem. C* **2015**, 119, 13105-13114; b) R. E. Stene, B. Scheibe, A. J. Karttunen, W. Petry, and F. Kraus, *Eur. J. Inorg. Chem.* **2019**, 3672. c) N. Glebko, I. Aleksandrova; G. C. Tewari, T. S. Tripathi, M. Karppinen, A. J. Karttunen, *J. Phys. Chem. C*, **2018**, 122, 26835–26844.
[9] H. J. Monkhorst, J. D. Pack, *Phys. Rev. B* **1976**, 13, 5188-5192.
[10] a) F. Pascale, C. M. Zicovich-Wilson, F. Lopez Gejo, B. Civalleri, R. Orlando, R. Dovesi, *Comput Chem.* **2004**, 25, 888-897; b) C. Zicovich-Wilson, F. Pascale, C. Roetti, V. Saunders, R. Orlando, R. Dovesi, *Comput. Chem.* **2004**, 25, 1873-1881; c) L. Maschio, B. Kirtman, R. Orlando, M. Rérat, *J. Chem. Phys.* **2012**, 137, 204113. d) L. Maschio, B. Kirtman, M. Rérat, R. Orlando, R. Dovesi, *J. Chem. Phys.* **2013**, 139, 164101.
[11] S. J. Clark, M. D. Segall, C. J. Pickard, P. J. Hasnip, M. I. Probert, K. Refson, M. C. Payne, *Z. Kristallogr.* **2005**, 220, 567-570;
[12] a) C. J. Pickard, F. Mauri, *Phys. Rev. B* **2001**, 63, 245101; b) J. R. Yates, C. J. Pickard, F. Mauri, *Phys. Rev. B* **2007**, 76, 024401.
[13] D. Vanderbilt, *Phys. Rev. B* **1990**, 41, 7892-7895.
[14] K. Momma, F. Izumi, *J. Appl. Crystallogr.*, 2011, **44**, 1272-1276.
[15] a) Y. Hinuma, G. Pizzi, Y. Kumagai, F. Oba, I. Tanaka, *Comp. Mat. Sci.* **2017**, 128, 140. b) A. Togo, I. Tanaka, "Spglib: a software library for crystal symmetry search", arXiv:1808.01590, **2018**.

4 Author Contributions

A. M. and N. K. coordinated the research and wrote the main parts of the manuscript, A. M. performed the syntheses, G. M. B., M. B. and V. K. M. performed the NMR experiments, A. M. and A. J. K. performed DFT calculations, C. R. collected the neutron diffraction data, N. K. acquired funding and administrated the project. All authors commented on the paper.

7.3 Expanding the hydride chemistry: antiperovskites A_3MO_4H (A = Rb, Cs; M = Mo, W) introducing the transition oxometalate hydrides

Alexander Mutschke, Annika Schulz, Marko Bertmer, Clemens Ritter, Antti J. Karttunen, Gregor Kieslich and Nathalie Kunkel

Published in:

Chem.Sci. **2022**, 13, 7773-7779

Reproduced from Alexander Mutschke*, Annika Schulz, Marko Bertmer, Clemens Ritter, Antti J. Karttunen, Gregor Kieslich, Nathalie Kunkel*, *Chem.Sci.* **2022**, 13, 7773-7779 with permission from the Royal Society of Chemistry.

© Royal Society of Chemistry 2022

Expanding the hydride chemistry: antiperovskites A_3MO_4H (A = Rb, Cs; M = Mo, W) introducing the transition oxometalate hydrides

A. Mutschke, A. Schulz, M. Bertmer, C. Ritter, A. J. Karttunen, G. Kieslich and N. Kunkel, *Chem. Sci.*, 2022, **13**, 7773 DOI: 10.1039/D2SC01861F 

This article is licensed under a [Creative Commons Attribution 3.0 Unported Licence](#). You can use material from this article in other publications without requesting further permissions from the RSC, provided that the correct acknowledgement is given.

Read more about [how to correctly acknowledge RSC content](#).

Content

This publication presents the new heteroanionic combination of hydrides with complex transition oxometalate anions. The synthesis, structure and properties of in total four new compounds that establish this new class of materials are discussed. The phases with the stoichiometry A_3MO_4H ($A = \text{Rb, Cs}$; $M = \text{Mo, W}$) can be synthesized by solid-state reactions of alkaline metal with quasi-binary oxometalate salts under hydrogen pressure. Only a small reaction temperature window allows for the synthesis of the compounds. Slightly too high reaction temperatures facilitate the reductions of the metalate ions towards the elemental transition metals. The structures of the newly formed phases were solved from powder X-ray diffraction. Neutron diffraction on the deuterated homologues altogether corroborate the initial structural models and allow for the location of the hydride ions. Three phases were found to crystallize in the tetragonal K_3SO_4F -structure type. Solely the compound $\text{Rb}_3\text{WO}_4\text{H}$ adopts a different, orthorhombic structure with a new perovskite-like building principle. To understand the structural modifications of the compounds, the Goldschmidt-tolerance factors of the compounds are determined and compared with similar structures. The hydridic character of the compounds is proven by ^2H MAS NMR spectroscopy. All compounds show single peaks with chemical shifts typical for salt-like hydrides. In combination with quantum chemical calculations, the peaks can be assigned and the hydridic character is eventually confirmed. Raman spectroscopy in combination with simulated spectra at the DFT-PBE0 level of theory matches well and supports the abundance of the metalate ions. In the case of $\text{Rb}_3\text{WO}_4\text{H}$, the simulated spectrum matches exceptionally well with the experimental spectrum, supporting the herein presented new structural motive. Also, hydride modes can be assigned therefrom and provide a further prove of the presence thereof. Electronic band structure calculations predict direct transitions for all four compounds. In the case of the tetragonal crystallizing compounds, band gaps ranging from approx. 3 - 4 eV are estimated, classifying the compounds as wide band gap semiconductors. $\text{Rb}_3\text{WO}_4\text{H}$ shows a unique, very peculiar band structure solely dominated by hydride states. Overall, for all compounds the transition is predicted to occur from hydride to oxometalate states.

Contributions

The syntheses of the samples were conducted by A.M with the help of A.S. Structure solutions and Rietveld refinements were done by A.M. Neutron diffraction data in respect thereof was collected by C.R. at the ILL, Grenoble. Beam time allocated at the D2B at the ILL is gratefully acknowledged. Raman spectra were evaluated by A.M. MAS NMR spectroscopy was performed by M.B. Quantum chemical calculations were performed by A.M and A.J.K. Perovskite related discussions were guided by G.K.

The manuscript was written by contributions of all co-authors. Leading author is A.M. Corresponding authors are A.M. and N.K.



Cite this: DOI: 10.1039/d2sc01861f

All publication charges for this article have been paid for by the Royal Society of Chemistry

Received 31st March 2022
Accepted 24th May 2022

DOI: 10.1039/d2sc01861f
rsc.li/chemical-science

Expanding the hydride chemistry: antiperovskites A_3MO_4H ($A = Rb, Cs$; $M = Mo, W$) introducing the transition oxometalate hydrides†

Alexander Mutschke,^a Annika Schulz,^a Marko Bertmer,^b Clemens Ritter,^c Antti J. Karttunen,^d Gregor Kieslich^e and Nathalie Kunkel^{*a}

The four compounds A_3MO_4H ($A = Rb, Cs$; $M = Mo, W$) are introduced as the first members of the new material class of the transition oxometalate hydrides. The compounds are accessible *via* a thermal synthesis route with carefully controlled conditions. Their crystal structures were solved by neutron diffraction of the deuterated analogues. Rb_3MoO_4D , Cs_3MoO_4D and Cs_3WO_4D crystallize in the antiperovskite-like K_2SO_4F -structure type, while Rb_3WO_4D adopts a different orthorhombic structure. 2H MAS NMR, Raman spectroscopy and elemental analysis prove the abundance of hydride ions next to oxometalate ions and experimental findings are supported by quantum chemical calculations. The tetragonal phases are direct and wide band gap semiconductors arising from hydride states, whereas Rb_3WO_4H shows a unique, peculiar valence band structure dominated by hydride states.

Introduction

Mixed anionic hydrides as a subclass of mixed anionic compounds¹ have recently raised a lot of attention due to a variety of academically interesting and technological relevant properties such as fast hydride ion conduction,² tunable optical properties³ and superconductivity⁴ amongst others. In addition, the number of mixed anionic hydrides with acceptable air and moisture stability is steadily increasing which facilitates their application in the future.^{5–8} To date, oxy hydrides with isolated oxide ions represent the largest group of this materials class which includes a variety of transition metal based oxy hydrides.^{9–11} The latter are typically synthesized by high pressure synthesis or reductive topotactic reaction which often leads to materials with disordered anions such as $AECrO_2H$ ($A = Sr, Ba$)^{10,11} or $BaTiO_{3-x}H_x$ ^{12,13} as archetypical examples. Undoubtedly, transition metal-based oxy hydrides show fascinating characteristics on their own such as magnetic ordering at elevated temperatures^{10,11,14} diffusional dynamics,¹⁵ good

electronic^{13,16} or ionic¹⁷ conductivities. However, yet no single hydridic compound containing complex transition orthooxometalate anions such as tetrahedral MoO_4^{2-} or WO_4^{2-} anions has been reported. The reductive nature of hydrogenation reactions often requires carefully designed synthetic routes to keep the complex anions intact. In turn, only a handful mixed anionic hydrides with complex (oxo-)anions, such as aluminate hydrides^{18,19} or borate hydrides⁷ are reported to date. The combination of complex oxoanions of transition metals with hydrides has not yet been realized to date. Expanding the field of mixed anionic hydrides to complex transition metalate anions, by binding the oxygen covalently to the metal center, is expected to uncover different and potentially unforeseen and desirable material properties.

Here we report the direct synthesis, structure and electronic properties of the compounds A_3MO_4H ($A = Rb, Cs$; $M = Mo, W$) which are the first four representatives of the transition oxometalate hydrides. These are also the first oxide-based hydrides containing molybdenum and tungsten as transition metal. Reduction of the transition metal is avoided by an exploratory optimized synthesis route which allows to keep the transition metal with high oxidation number and the complex metalate ions intact. Moreover, covalent or coordinative interactions between the hydride and the transition metal center can be excluded in the presented compounds.

Results and discussion

The transition oxometalate hydrides are synthetically accessible by a solid-state reaction under hydrogen pressure with controlled conditions. As inspired by a recent study about

^aChair of Inorganic Chemistry with Focus on Novel Materials, Technical University of Munich, Lichtenbergstrasse 4, 85748 Garching, Germany. E-mail: Alex.Mutschke@tum.de; ga74lud@mytum.de

^bFelix Bloch Institute for Solid State Physics Leipzig University, Linnéstrasse 5, 04103 Leipzig, Germany

^cInstitut Laue-Langevin, 71 Avenue des Martyrs, 38042 Grenoble Cedex 9, France

^dDepartment of Chemistry and Materials Science, Aalto University, P.O. Box 16100, FI-00076 Aalto, Finland

^eChair of Inorganic and Metal-Organic Chemistry, Technical University of Munich, Lichtenbergstrasse 4, 85748 Garching, Germany

† Electronic supplementary information (ESI) available. See <https://doi.org/10.1039/d2sc01861f>.



a novel sulfate hydride,²⁰ a thermal synthesis route is applied to synthesize the herein presented compounds. In a typical synthesis, the alkaline metal A (A = Rb, Cs) is reacted with the quasi-binary oxometalate salts (A_2MoO_4 , A_2WO_4) at 528 K for the molybdate hydrides and 600 K for the tungstate hydrides under an applied hydrogen pressure of 10 bar. The hydrogen pressure is required to hydrogenate the alkaline metal to form the alkaline hydride which readily reacts with the quasi-binary molybdate or tungstate salts to form the respective transition oxometalate hydrides. Mild conditions are required to avoid reduction of the transition metalate ion to the elemental transition metal or different bronzes thereof; however, too mild conditions drastically prolong the reaction time and impede phase pure synthesis or prevent the reaction as a whole. The molybdate hydrides are only accessible in a temperature window of approximately 15 K as the reduction of the molybdate ions is beginning above 535 K. The formation of the tungstate analogues occurs over a range of up to 60 K. A mechanochemical activation route as demonstrated in previous studies about new mixed anionic hydrides²¹ resulted in the reduction of the oxometalate ions into several different valent transition metal oxides. Short scan powder X-ray diffraction measurements of the obtained polycrystalline powders revealed diffraction patterns of new, unknown phases. Indexing of reflections from the X-ray diffraction patterns return tetragonal structures for Rb_3MoO_4H , Cs_3MoO_4H and Cs_3WO_4H and an orthorhombic structure for Rb_3WO_4H . Initial structural models were obtained by using superflip²² as implemented in Jana2006.²³ Due to the very weak X-ray scattering power of hydrogen and the abundance of heavy metal atoms, we applied powder neutron diffraction of the deuterated analogues to obtain complete structural models of the newly formed phases. Due to the large bound coherent scattering length (6.671 barn) of deuterium (2H),²⁴ the deuteride and the corresponding equal hydride positions were determined reliably, completing and enhancing the initial structural models obtained by X-ray diffraction. Subsequently, structure solution has been carried out by Rietveld-refinement of neutron diffraction data at room temperature with Fullprof.²⁵ An exemplary neutron refinement plot of Cs_3MoO_4D is shown in Fig. 1. Structural data and all further Rietveld refinement plots obtained from X-ray and neutron diffraction data can be found in the ESI.†

The compounds Rb_3MoO_4D , Cs_3MoO_4D and Cs_3WO_4D crystallize isostructural in the tetragonal K_3SO_4F -structure type with the space group $I4/mcm$ (140),²⁶ while Rb_3WO_4D presumably adopts a different structure-type. The corresponding cell parameters are listed in Table 1. The building principle of all compounds is related to an A_3BX antiperovskite-like structure. The hydride (X) occupies the octahedral site and is octahedrally coordinated by the alkaline metal (A). The larger complex anions (B) occupy the cuboctahedral voids within the $[A_3B]^+$ ReO_3 -type network. The tetragonal phases belong to the K_3SO_4F -structure type and show activated octahedral tilts along the c -direction when compared to the ideal cubic perovskite structure in $Pm\bar{3}m$. The assigned glazer tilt notation is $a^0a^0c^-$.²⁷ In addition to the prototype K_3SO_4F ,²⁶ several compounds with tetrahedral complex anions are known to crystallize in this structure-

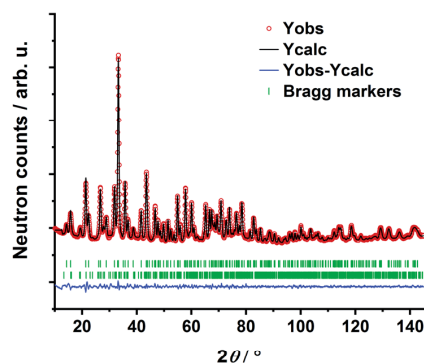


Fig. 1 Rietveld refinement of Cs_3MoO_4D based on powder neutron diffraction. Bragg markers: Cs_3MoO_4D (top) (90.3(10) wt%); CsD (bottom) (9.7(1) wt%). $R_p = 1.18\%$, $R_{wp} = 1.57\%$, $R_{exp} = 0.83\%$, $R_{Bragg} = 1.60\%$, $\chi^2 = 3.59$.

type such as the selenate fluoride K_3SeO_4F ,²⁸ the oxonitrosilicates $Ln_3[SiN_3O]O$ ($Ln = La, Ce, Pr$),²⁹ or the aluminate hydride Sr_3AlO_4H .¹⁹ A schematic of the crystal structure of the tetragonal phases can be found in the ESI in Fig. S9.†

The Mo–O bond lengths are found to be in average 1.766 Å, while the W–O bond lengths are found to be 1.775 Å. Both agree with typical Mo–O bond lengths within the orthomolybdate ion (1.70 Å)³⁰ and W–O bond lengths (1.79 Å) of orthotungstate ions.³¹ The tetrahedron angles within the complex orthometalate ions are found to have mean values in the range of 109.17–109.32° which fit closely to the ideal tetrahedron angle of 109.47°.

Solely Rb_3WO_4H could not be solved in $I4/mcm$. Careful structural analysis based on neutron and X-ray diffraction data, delivers a new orthorhombic structure type with the space group $Pbca$ (61). In this presented structure model, the Rb-built octahedrons surrounding the hydrides are distorted and tilted towards each other, most notably in the c -direction (Fig. 2). Also, the tungstate ions located in the cuboctahedral voids between the corner-sharing Rb_6D octahedrons are tilted slightly towards each other in all three crystallographic directions. Overall, these slight distortions result in an antiperovskite-like structure with a pseudo tetragonal setup ($a/b = 1.0464$, $b/c = 0.9955$, $c/a = 0.9600$). Notably, such a distorted (anti)perovskite-like variant has not been observed this far and differs from other orthorhombic perovskite variants in the $GdFeO_3$ -structure type and derivatives thereof. As the Rb_6D octahedra are unusual with Rb-positions close to special positions, several different structure solutions with varying space-groups were tested; however, no other obtained solution sufficiently converged or enhanced the herein presented model. We thus conclude the reported structural model to be the most fitting hitherto. In average the W–O bond lengths are found to be 1.77 Å, again fitting the typical W–O bond length of orthotungstate ions of 1.79 Å.³¹ The tetrahedron angles are found to be in average 109.42° which fits very closely to the ideal tetrahedron angle of 109.47°. The Rb–D distances are found to be between 2.8529 Å and 3.0040 Å corresponding to the typical bond lengths found in ionic metal



Table 1 Crystallographic data of the four new compounds $A_3MO_4D(H)$ ($A = Rb, Cs$; $M = Mo, W$)

	Rb_3MoO_4D	Cs_3MoO_4D	Cs_3WO_4D	Rb_3WO_4D
Space group	$I4/mcm$ (140)	$I4/mcm$ (140)	$I4/mcm$ (140)	$Pbca$ (61)
Phase prototype	K_3SO_4F	K_3SO_4F	K_3SO_4F	Own structure type
Lattice parameter (Å)	$a = 7.8620(3)$ $c = 12.2998(5)$	$a = 8.2113(2)$ $c = 12.7893(4)$	$a = 8.2331(2)$ $c = 12.8289(3)$	$a = 11.9262(3)$ $b = 11.3972(5)$ $c = 11.4492(5)$
Formular units (Z)	4	4	4	8
M–O dist. (Å)	1.766(1)	1.767(1)	1.775(1)	1.735(10)–1.784(7)
\angle (θ): O–M–O, (M = Mo, W)	109.32°	109.17°	109.17°	109.42°
Glazer tilt notation	$a^0a^0c^-$	$a^0a^0c^-$	$a^0a^0c^-$	a

^a Due to distortions of the octahedra, the application of the Glazer-notation is not straightforwardly applicable; however, when neglecting these distortions, the same tilt-system as for the other compounds is obtained.

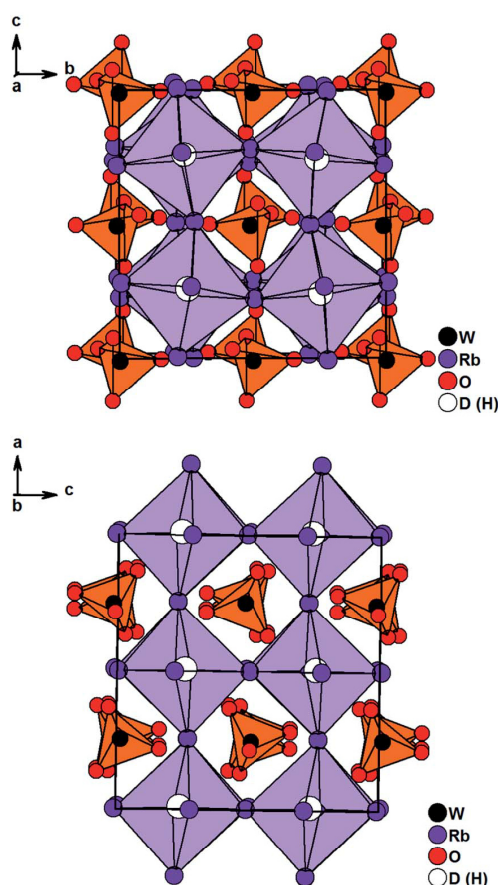


Fig. 2 Crystal structure of Rb_3WO_4D along the c -axis (top) and the a -axis (bottom). Tungstate anions are depicted as orange tetrahedrons, Rb_6D octahedrons are lilac.

hydrides.^{7,20,21,32} Further details on the crystal structure investigations are given in the ESI,[†] on quoting the depository numbers CSD 2127403 (Rb_3MoO_4D), CSD 2127400 (Cs_3MoO_4D), CSD 2127401 (Cs_3WO_4D), CSD 2127405 (Rb_3WO_4D). As already stated, the cesium compounds Cs_3MoO_4H and Cs_3WO_4H are

isostructural and rather unexpectedly, the structures of the rubidium based phases Rb_3MoO_4H and Rb_3WO_4H differ from one another. Due to the lanthanide contraction, molybdenum and tungsten have equal ionic radii, therefore it is expected for both compounds to be isostructural; however, when considering M–O bond lengths, the Mo–O bond length is in average about 0.01 Å shorter than the W–O bond length and thus, the molybdate ions overall have a marginal smaller total ionic radius compared to the tungstate ions. This results in slightly different packing factors which might cause the formation of different structural distortions. Interestingly, Schmitz-Dumont and Weeg observed an identical trend of the corresponding fluoride molybdates and fluoride tungstates. Even though they did not report any structural data, laboratory powder diffraction data revealed two different crystallographic set-ups for Rb_3MoO_4F and Rb_3WO_4F .³³

To further understand the structural modifications of the antiperovskite-like structures, we calculated the Goldschmidt-tolerance factor of all four compounds. According to Goldschmidt, a compound with the general formula ABX_3 forms the ideal cubic (anti)perovskite structure when the ionic radii have a certain ratio or simply when $t \approx 1$.³⁴ Such compounds usually adopt distorted variants if t differs too far from the ideal value of 1, often if $t < 0.9$ or $t > 1.1$.^{34–36} While many deviations from this trend are known, the tolerance factor is a powerful approach for rationalizing the crystal chemistry especially when applied to material series. For the here investigated systems, the tolerance factors can be calculated by considering the molybdates and tungstates as complex ions, applying the formula below:^{35–37}

$$t = \frac{r_{MO_4^{2-}} + r_{A^+}}{\sqrt{2} (r_{H^-} + r_{A^+})}$$

For details on the determination of ionic radii of MO_4^{2-} and H^- see ESI.[†]

As seen in Table 2, the determined tolerance factors all deviate from the ideal value of $t \approx 1$; however, they fit closely to the determined value of the phase prototype K_3SO_4F , with Cs_3MoO_4H having the best fitting value of 1.11. By a further look at the tolerance factors, it is recognizable that Rb_3WO_4H deviates the most from the phase prototype and the related tetragonal



Table 2 Determined Goldschmidt-tolerance factors

Compound	Tolerance factor t
Rb ₃ MoO ₄ H	1.12
Cs ₃ MoO ₄ H	1.11
Rb ₃ WO ₄ H	1.14
Cs ₃ WO ₄ H	1.12
K ₃ SO ₄ F	1.09
Na ₃ SO ₄ H	1.15

phases, with a calculated tolerance factor of 1.14. As suggested by the Goldschmidt-factor, the Rb⁺ ion in this structure might be just too small in relation to the large complex WO₄²⁻ anion to stabilize Rb₃WO₄H in a less distorted structure when compared to the other compounds reported in this work. The tolerance factor deviates even more from 1 in Na₃SO₄H which represents a further antiperovskite-like hydride (*P4/nmm*, Ag₃-CrO₄Cl-type).²⁰ Compared to the structure types presented in this work, the assembly is different in Na₃SO₄H as the alkaline (Na⁺) ions are now considerably smaller than the hydride ions. In turn, the sulfate anions demand less space within the cuboctahedral voids in relation to the larger oxometalate anions. This overall results in another tetragonal structure with only distorted but not tilted (Na₆D) octahedra.

MAS NMR spectroscopy

Structure analysis based on X-ray and neutron diffraction is complemented by magic angle spinning nuclear magnetic resonance (MAS NMR) to obtain information on the atomic level. Especially ¹H and ²H MAS NMR have proven to be a powerful tool to confirm the presence of hydride ions.^{7,8,20,21,38}

¹H is the most receptive nuclear spin, however, the ²H spin is superior as the spectra are not affected by any other present hydrogen containing material like impurities from the probe background or from synthesis.

The ²H MAS spectra of the four samples are summarized in Fig. 3. Corresponding ¹H spectra show the same signals with

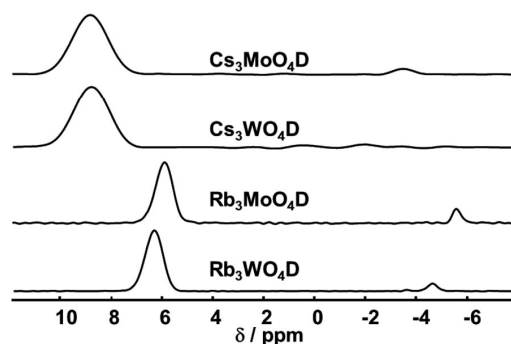


Fig. 3 ²H MAS NMR spectra of the four compounds (isotropic region only). The spectra were acquired at room temperature with a spinning frequency of 5 kHz and a magnetic field $B_0 = 17.6$ T.

quasi identical shifts, yet contain additionally other signals originating from the rotor cap or other external impurities. All obtained ²H MAS NMR spectra contain one dominant signal that is assigned to the parent material. Additionally, in all samples a minor signal with a small linewidth at negative chemical shift is present. This signal originates from hydrides covalently bound to transition elements, typically showing negative shifts.³⁹ In the case of Rb₃WO₄D and Cs₃MoO₄D a quadrupolar pattern indicative of a covalent bond is seen. Since these signals contribute only to a minor amount besides the main signal, a more detailed analysis was not done.

Both rubidium and both cesium containing samples show each very similar shifts, about 6.0–6.4 ppm for rubidium and 9.8 ppm for cesium. The higher shift for cesium is expected following the trend of the size of alkali metal hydrides and corresponding shifts in the simple hydrides (LiH: 2.9 ppm, NaH: 3.6 ppm, KH: 4.7 ppm).⁴⁰ DFT-PBE calculations of the chemical shift of the ¹H nucleus support the experimental findings. The shifts were calculated to be 6.4 ppm for Cs₃MoO₄H, 6.2 ppm for Cs₃WO₄H and 5.5 ppm for both rubidium compounds in reference to SiMe₄. While the calculated shifts of the cesium compounds differ compared to the experimental findings, the trend of the higher homologues to be downfield shifted is reproduced. In the case of cesium, the mismatching downfield shift might be due to the spin-orbit heavy-atom effect on the light-atom, where the heavy cesium atom has a deshielding effect of on the neighbouring H atom.⁴¹ Spin-orbit coupling effects have not been taken into account in the present calculations.

Overall, the chemical shifts were found to be in the region typical for inorganic salt-like hydrides.^{7,8,20,21,38,40} In combination with DFT calculations, ²H MAS NMR proves the abundance of hydrides within the crystal lattice.

Further evidence of the hydride abundance is provided by simple elemental analysis. Here, the experimental determined weight percentage of hydrogen is determined to be close to the theoretical values in all four compounds. The simultaneous abundance of either tungsten or molybdenum is additionally determined and underlines the abundance of both hydride anions next to tungstate and molybdate ions. The elemental analysis reports can be seen in the ESI†

Raman spectroscopy is used to verify the abundance of complex tetrahedral (*ortho*)anions through the presence of their typical stretching and bending modes. The experimental spectra were additionally compared to simulated spectra obtained by density functional theory (DFT-PBE0) calculations of the hydridic species (see ESI† for the computational details). As can be seen in Fig. 4 and S25–S27† the obtained Raman spectra are in good agreement with the simulated spectra. All Raman-active vibrational modes, ν_1 to ν_4 , are observed in the expected wavenumber regions with the predicted intensity, confirming the abundance of the complex orthometalate anions and supporting in overall the structural models. The Raman spectra also differ from the corresponding Raman spectra of the binary oxometalate salts. The respective spectra, due to the lower orthorhombic symmetry of the starting materials, show a splitting of the ν_3 mode and overlapping ν_2 and ν_4 modes. This



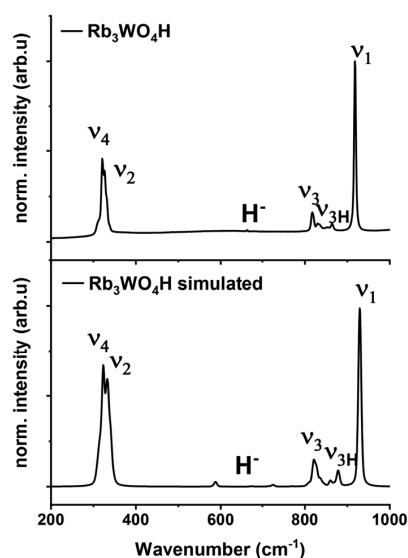


Fig. 4 Experimental Raman spectrum of $\text{Rb}_3\text{WO}_4\text{H}$ (top) and simulated Raman spectrum of $\text{Rb}_3\text{WO}_4\text{H}$ (bottom, DFT-PBE0 method).

deviates from the spectra of the newly formed phases where the ν_2 and ν_4 modes appear noticeable distant to each other and the ν_3 mode does not show splitting.⁴² As the structure of $\text{Rb}_3\text{WO}_4\text{H}$ differs from the structure of the tetragonal phases, its Raman spectrum shows a slightly different Raman spectrum (Fig. 4). In addition to the vibrational modes of the tungstate anions, vibrational modes of the tungstate anions coupled to hydride modes ($\nu_{3\text{H}}$) are seen at about $850\text{--}900\text{ cm}^{-1}$ as predicted in the simulated spectrum. This again confirms the abundance of hydride ions and supports the structural model obtained by neutron diffraction. By comparison with the Raman spectrum of Rb_2WO_4 , it is apparent that in this case the ν_3 modes are more distinctly split and the $\nu_{3\text{H}}$ modes are missing. Similarly for the ν_2 and ν_4 modes that show more recognizable and pronounced bending modes, not seen in the Raman spectrum of

$\text{Rb}_3\text{WO}_4\text{H}$.⁴³ This overall affirms the successful formation of a new phase.

Figs. S19, S21 and S23† show the calculated electronic band structures and density of states of the tetragonal phases crystallizing in the $\text{K}_3\text{SO}_4\text{F}$ -structure. All three compounds can be classified as wide band gap semiconductors with direct band gaps of approximately 3.2 eV ($\text{Cs}_3\text{MoO}_4\text{H}$), 3.4 eV ($\text{Rb}_3\text{MoO}_4\text{H}$) and 3.8 eV ($\text{Cs}_3\text{WO}_4\text{H}$). All three calculated band structures show similar features where hydride is dominating the topmost valence band with only minor contributions from rubidium or cesium. Due to the polarizability of hydride and the strong covalent character of the hydride ion, the topology of the band structure is directly influenced by the hydride ion and is directly responsible for the direct band gap and thus the semiconducting character of the tetragonal compounds. These findings reflect and are in line with previous studies of inorganic salt like hydrides where hydride is always predicted to dominate the topmost valence band.^{6–8,20,44} UV/Vis absorption spectroscopy and the resulting Tauc-plots confirm the direct band gaps and are close to the estimated band gap value which underlines the direct influence of the hydride ion regarding the direct band gap. As the compounds are isostructural, a band gap tuning might be possible by the synthesis of mixed cationic or mixed tungstate/molybdate solid-solutions.

The calculated band structure of $\text{Rb}_3\text{WO}_4\text{H}$ (Fig. 5) is very peculiar and the valence bands are dominated by the hydride states. At the Γ -point, all eight hydride bands are non-degenerate, while at the R -point all states are degenerate. In this crystal structure, the hydrides form a quasi-cubic arrangement, resulting in slightly unequal paths within the reciprocal space. Even though a relatively large band gap of approx. 4.6 eV is estimated, again a direct transition is predicted.

Interestingly, in all four calculated band structures the states arising from the hydride ions are located between states arising from the complex transition metalate ion. An initial approach for the design of direct semiconductors might target a modification of this band structure.

Conclusions

In summary, we hereby provide the groundwork for a potentially broad class of materials: the transition oxometalate hydrides. The four compounds $\text{A}_3\text{MO}_4\text{H}$ ($\text{A} = \text{Rb}, \text{Cs}; \text{M} = \text{Mo}, \text{W}$) are accessible *via* a sophisticated thermal synthesis route and are introduced as the first representatives of this new class. To the best of our knowledge, such a combination of transition metal anions with hydride ions has not been realized this far. The unprecedented abundance of hydrides next to complex oxoanions within single structures is proven by several analytical methods including neutron diffraction, Raman spectroscopy, MAS NMR spectroscopy, elemental analysis and beyond that supported by quantum chemical calculations. The four compounds show interesting electronic and structural features. While the compounds of the tetrahedral class are direct and wide band gap semiconductors, $\text{Rb}_3\text{WO}_4\text{H}$ shows a very dispersive, peculiar valence band structure dominated by hydride states arising from the pseudo cubic arrangement of

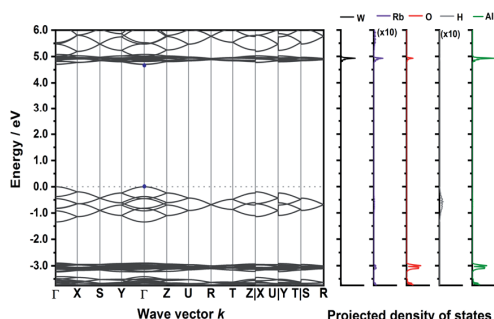


Fig. 5 Electronic band structure of $\text{Rb}_3\text{WO}_4\text{H}$ and projected density of states (DFT-PBE0). The band paths in the reciprocal space have been determined by the Seek-path webservice.⁴⁵ The DOS of Rb and H are enhanced by a factor of ten for better visibility.



the hydride ions within the orthorhombic crystal structure. Overall, these findings demonstrate a pathway to hitherto unexplored anion combinations and open the door for further anion combinations containing other complex transition metalate ions like *e.g.* (di)chromates or orthovanadates. Likewise, these compounds may act as chemical templates for new, more complex structures such as combinations of hydrides with polymetalate ions.

Data availability

Full experimental details and further data supporting the research are provided in the ESI.†

Author contributions

A. M., G. K. and N. K. coordinated the research and wrote the main parts of the manuscript, A. M. and A. S. performed the syntheses, M. B. performed the NMR experiments, A. M. and A. J. K. performed DFT calculations, C. R. collected the neutron diffraction data, N. K. acquired funding and administrated the project. All authors commented on the paper.

Conflicts of interest

The authors declare no conflict of interest.

Acknowledgements

The authors thank Christoph Wallach for Raman measurements and Sabine Zeitz for UV/Vis absorption spectroscopy. A. M. and M. B. thank Leonhard Dorsch for packing of the MAS rotors. Bircan Dilki is thanked gratefully for conducting the elemental analysis. We would like to thank the Institut Laue-Langevin for beam time allocated on D2B; <https://doi.org/10.5291/ILL-DATA.5-21-1170> and <https://doi.org/10.5291/ILL-DATA.EASY-725>. A. M. and N. K. thank the DFG for funding (project number 245845833) within International Research Training Group IRTG 2022—Alberta Technical University of Munich School for Functional Hybrid Materials (ATUMS). A. M. thanks the International Graduate School for Science and Engineering (IGSSE) for support. A. J. K. thanks Academy of Finland for funding (grant 324973) and CSC, the Finnish IT Center for Science for computational resources.

References

- (a) H. Kageyama, K. Hayashi, K. Maeda, J. P. Attfield, Z. Hiroi, J. M. Rondinelli and K. R. Poeppelmeier, *Nat. Commun.*, 2018, **9**, 772; (b) T. Yajima, F. Takeiri, K. Aidzu, H. Akamatsu, K. Fujita, W. Yoshimune, M. Ohkura, S. Lei, V. Gopalan, K. Tanaka, C. M. Brown, M. A. Green, T. Yamamoto, Y. Kobayashi and H. Kageyama, *Nat. Chem.*, 2015, **7**, 1017.
- (a) H. Ubukata, F. Takeiri, K. Shitara, C. Tassel, T. Saito, T. Kamiyama, T. Broux, A. Kuwabara, G. Kobayashi and H. Kageyama, *Sci. Adv.*, 2021, **7**, eabf7883; (b) G. Kobayashi, Y. Hinuma, S. Matsuoka, A. Watanabe, M. Iqbal, M. Hirayama, M. Yonemura, T. Kamiyama, I. Tanaka and R. Kanno, *Science*, 2016, **351**, 1314.
- (a) A. Mutschke, T. Wylezich, A. D. Sontakke, A. Meijerink, M. Hoelzel and N. Kunkel, *Adv. Opt. Mater.*, 2021, **9**, 2002052; (b) T. Wylezich, S. Welinski, M. Hoelzel, P. Goldner and N. Kunkel, *J. Mater. Chem. C*, 2018, **6**, 13006.
- K. Kobayashi, J.-i. Yamaura, S. Iimura, S. Maki, H. Sagayama, R. Kumai, Y. Murakami, H. Takahashi, S. Matsuishi and H. Hosono, *Sci. Rep.*, 2016, **6**, 39646.
- N. Zapp, D. Sheptyakov, A. Franz and H. Kohlmann, *Inorg. Chem.*, 2021, **60**, 3972.
- N. Zapp, H. Auer and H. Kohlmann, *Inorg. Chem.*, 2019, **58**, 14635.
- T. Wylezich, R. Valois, M. Suta, A. Mutschke, C. Ritter, A. Meijerink, A. J. Karttunen and N. Kunkel, *Chem.–Eur. J.*, 2020, **26**, 11742.
- F. Gehlhaar, R. Finger, N. Zapp, M. Bertmer and H. Kohlmann, *Inorg. Chem.*, 2018, **57**, 11851.
- (a) J. Bang, S. Matsuishi, H. Hiraka, F. Fujisaki, T. Otomo, S. Maki, J.-i. Yamaura, R. Kumai, Y. Murakami and H. Hosono, *J. Am. Chem. Soc.*, 2014, **136**, 7221; (b) F. Denis Romero, A. Leach, J. S. Möller, F. Foronda, S. J. Blundell and M. A. Hayward, *Angew. Chem., Int. Ed.*, 2014, **53**, 7556; (c) Y. Goto, C. Tassel, Y. Noda, O. Hernandez, C. J. Pickard, M. A. Green, H. Sakaebe, N. Taguchi, Y. Uchimoto, Y. Kobayashi and H. Kageyama, *Inorg. Chem.*, 2017, **56**, 4840; (d) L. Jin, M. Lane, D. Zeng, F. K. K. Kirschner, F. Lang, P. Manuel, S. J. Blundell, J. E. McGrady and M. A. Hayward, *Angew. Chem., Int. Ed.*, 2018, **130**, 5119; (e) C. Tassel, Y. Goto, D. Watabe, Y. Tang, H. Lu, Y. Kuno, F. Takeiri, T. Yamamoto, C. M. Brown, J. Hester, Y. Kobayashi and H. Kageyama, *Angew. Chem., Int. Ed.*, 2016, **55**, 9667; (f) M. A. Hayward, E. J. Cussen, J. B. Claridge, M. Bieringer, M. J. Rosseinsky, C. J. Kiely, S. J. Blundell, I. M. Marshall and F. L. Pratt, *Science*, 2002, **295**, 1882.
- K. Higashi, M. Ochi, Y. Nambu, T. Yamamoto, T. Murakami, N. Yamashina, C. Tassel, Y. Matsumoto, H. Takatsu, C. M. Brown and H. Kageyama, *Inorg. Chem.*, 2021, **60**, 11957.
- C. Tassel, Y. Goto, Y. Kuno, J. Hester, M. Green, Y. Kobayashi and H. Kageyama, *Angew. Chem., Int. Ed.*, 2014, **53**, 10377.
- X. Liu, T. S. Bjørheim and R. Haugrud, *J. Mater. Chem. A*, 2017, **5**, 1050.
- T. Uchimura, F. Takeiri, K. Okamoto, T. Saito, T. Kamiyama and G. Kobayashi, *J. Mater. Chem. A*, 2021, **9**, 20371–20374.
- (a) J. Bang, S. Matsuishi, S. Maki, J.-i. Yamaura, M. Hiraishi, S. Takeshita, I. Yamauchi, K. M. Kojima and H. Hosono, *Phys. Rev. B: Condens. Matter Mater. Phys.*, 2015, **92**, 064414; (b) T. Yamamoto, R. Yoshii, G. Bouilly, Y. Kobayashi, K. Fujita, Y. Kususe, Y. Matsushita, K. Tanaka and H. Kageyama, *Inorg. Chem.*, 2015, **54**, 1501; (c) L. Jin and M. A. Hayward, *Angew. Chem., Int. Ed.*, 2020, **59**, 2076; (d) Y. Wei, H. Gui, X. Li, Z. Zhao, Y.-H. Zhao and W. Xie, *J. Phys.: Condens. Matter*, 2015, **27**, 206001; (e)



- C. A. Bridges, G. R. Darling, M. A. Hayward and M. J. Rosseinsky, *J. Am. Chem. Soc.*, 2005, **127**, 5996.
- 15 R. Lavén, U. Häussermann, A. Perrichon, M. S. Andersson, M. S. Targama, F. Demmel and M. Karlsson, *Chem. Mater.*, 2021, **33**, 2967.
- 16 T. Yajima, A. Kitada, Y. Kobayashi, T. Sakaguchi, G. Bouilly, S. Kasahara, T. Terashima, M. Takano and H. Kageyama, *J. Am. Chem. Soc.*, 2012, **134**, 8782.
- 17 K. Fukui, S. Iimura, A. Iskandarov, T. Tada and H. Hosono, *J. Am. Chem. Soc.*, 2022, **144**, 1523.
- 18 B. Huang and J. D. Corbett, *J. Solid State Chem.*, 1998, **141**, 570.
- 19 T. Wu, K. Fujii, T. Murakami, M. Yashima and S. Matsuishi, *Inorg. Chem.*, 2020, **59**, 15384.
- 20 A. Mutschke, G. M. Bernard, M. Bertmer, A. J. Karttunen, C. Ritter, V. K. Michaelis and N. Kunkel, *Angew. Chem., Int. Ed.*, 2021, **60**, 5683.
- 21 A. Mutschke, T. Wylezich, C. Ritter, A. J. Karttunen and N. Kunkel, *Eur. J. Inorg. Chem.*, 2019, **2019**, 5073.
- 22 L. Palatinus and G. Chapuis, *J. Appl. Crystallogr.*, 2007, **40**, 786.
- 23 V. Petříček, M. Dušek and L. Palatinus, *Z. Kristallogr. - Cryst. Mater.*, 2014, **229**, 345.
- 24 V. F. Sears, *Neutron News*, 1992, **3**, 26.
- 25 J. Rodríguez-Carvajal, *Phys. B*, 1993, **192**, 55.
- 26 J. M. S. Skakle, J. G. Fletcher and A. R. West, *J. Chem. Soc., Dalton Trans.*, 1996, 2497.
- 27 A. M. Glazer, *Acta Crystallogr., Sect. A: Cryst. Phys., Diffraction, Theor. Gen. Crystallogr.*, 1975, **31**, 756.
- 28 J. M. S. Skakle, J. G. Fletcher and A. R. West, *An. Chim. Univ. Al. I. Cuza Iași*, 1996, **92**, 358.
- 29 (a) D. Durach and W. Schnick, *Eur. J. Inorg. Chem.*, 2015, **2015**, 4095; (b) J. A. Kechele, C. Schmolke, S. Lupart and W. Schnick, *Z. Anorg. Allg. Chem.*, 2010, **636**, 176.
- 30 P. A. Williams, in *Encyclopedia of Geology*, Elsevier, 2005, pp. 551–552.
- 31 F. D. Hardcastle and I. E. Wachs, *J. Raman Spectrosc.*, 1995, **26**, 397.
- 32 N. Zapp, D. Sheptyakov and H. Kohlmann, *Crystals*, 2021, **11**, 750.
- 33 O. Schmitz-Dumont and A. Weeg, *Z. Anorg. Allg. Chem.*, 1951, **265**, 139.
- 34 V. M. Goldschmidt, *Naturwissenschaften*, 1926, **14**, 477.
- 35 H. Fang and P. Jena, *Proc. Natl. Acad. Sci. U. S. A.*, 2017, **114**, 11046.
- 36 W. Li, Z. Wang, F. Deschler, S. Gao, R. H. Friend and A. K. Cheetham, *Nat. Rev. Mater.*, 2017, **2**, 16099.
- 37 S. Fujii, S. Gao, C. Tassel, T. Zhu, T. Broux, K. Okada, Y. Miyahara, A. Kuwabara and H. Kageyama, *J. Am. Chem. Soc.*, 2021, **143**, 10668.
- 38 K. Hayashi, P. V. Sushko, Y. Hashimoto, A. L. Shluger and H. Hosono, *Nat. Commun.*, 2014, **5**, 3515.
- 39 (a) P. Hrobárik, V. Hrobáriková, F. Meier, M. Repický, S. Komorovský and M. Kaupp, *J. Mater. Chem. A*, 2011, **115**, 5654; (b) Y. Ruiz-Morales, G. Schreckenbach and T. Ziegler, *Organometallics*, 1996, **15**, 3920.
- 40 F. Gehlhhar, Master's thesis, Universität Leipzig, 2019.
- 41 (a) J. Vicha, S. Komorovsky, M. Repisky, R. Marek and M. Straka, *J. Chem. Theory Comput.*, 2018, **14**, 3025; (b) J. V1 Cha, J. Novotný, S. Komorovsky, M. Straka, M. Kaupp and R. Marek, *Chem. Rev.*, 2020, **120**, 7065.
- 42 (a) A. Erdöhelyi, K. Fodor, R. Németh, A. Hancz and A. Oszkó, *J. Catal.*, 2001, **199**, 328; (b) M. Naji, F. Di Lemma, A. Kovács, O. Beneš, D. Manara, J.-Y. Colle, G. Pagliosa, P. Raison and R. J. M. Konings, *J. Raman Spectrosc.*, 2015, **46**, 661.
- 43 A. Jorio, P. Saint-Grégoire and M. A. Pimenta, *J. Phys.: Condens. Matter*, 2000, **12**, 9307.
- 44 T. Wu, A. Ishikawa, T. Honda, H. Tamatsukuri, K. Ikeda, T. Otomo and S. Matsuishi, *RSC Adv.*, 2019, **9**, 5282.
- 45 (a) Y. Hinuma, G. Pizzi, Y. Kumagai, F. Oba and I. Tanaka, *Band Structure Diagram Paths Based on Crystallography*, 2016; (b) A. Togo and I. Tanaka, 2018, arXiv:1808.01590v1; (c) Y. Hinuma, G. Pizzi, Y. Kumagai, F. Oba and I. Tanaka, *Comput. Mater. Sci.*, 2017, **128**, 140.



Electronic Supplementary Material (ESI) for Chemical Science.
This journal is © The Royal Society of Chemistry 2022

Expanding the hydride chemistry: Antiperovskites A_3MO_4H ($A = Rb, Cs$; $M = Mo, W$) introducing the transition oxometalate hydrides

Alexander Mutschke, Annika Schulz, Dr. Marko Bertmer, Dr. Clemens Ritter, Prof. Dr. Antti J. Karttunen, Dr. Gregor Kieslich, Dr. Nathalie Kunke

Table of Content

1	Experimental section	3
1.1	Synthesis.....	3
1.2	Powder X-ray diffraction.....	3
1.3	Neutron diffraction.....	3
1.4	Rietveld Refinement	3
1.5	Raman spectroscopy	3
1.6	UV/VIS absorption spectroscopy	3
1.7	Elemental analysis	4
1.8	Solid-state NMR.....	4
1.9	Quantum chemical calculations	4
2	Results and discission	5
2.1	Structural analysis	5
2.1.1	Neutron diffraction.....	5
2.1.2	Supplementary X-ray diffraction data (Hydridic samples).....	13
2.2	Ionic radii for determination of the Goldschmidt tolerance factors	17
2.3	Crystal structure of the K_3SO_4F -structure type	18
2.4	Difference Fourier maps.....	19
2.5	2H MAS NMR Spectroscopy	23
2.6	Calculated electronic band structures and UV/Vis Tauc plots.....	25
2.7	Vibrational Spectroscopy (experimental and DFT-PBE0).....	28
2.8	Elemental Analysis.....	32
2.9	Optimized crystal structures as CIF (DFT-PBE0).....	33
3	Literature	36

1 Experimental section

1.1 Synthesis

Due to the air and moisture sensitivity of the reactants and the resulting products, all preparative and analytical operations were carried out in argon-filled gloveboxes. The O₂ and H₂O concentrations were kept below 0.5 ppm respectively.

The transition oxometalate hydrides A₃MO₄H (A = Rb, Cs; M = Mo, W) can be synthesized by the solid-state reaction of in-situ formed alkaline hydride with the quasi-binary oxometalate salts A₂MO₄. (A = Rb, Cs; M = Mo, W)

The binary molybdate salts were synthesized by a solid-state reaction of MoO₃ (*Alfa Aesar*, 99.5%) with A₂CO₃. (Rb₂CO₃: *Chempur*, 99.9%; Cs₂CO₃: *Alfa Aesar*, ≥ 99%) in stoichiometric ratios. Thereto, the two powders were grinded thoroughly in an agate mortar, transferred in a corundum crucible and heated at 620 °C for 15h. If residual reactants were observed in short scan X-ray diffraction patterns, the product was reground and annealed again with the same temperature program.

The tungstate salts Rb₂WO₄ (*Chempur*, 99.9%), Cs₂WO₄, (*Alfa Aesar*, 99%), were purchased commercially. Before use, the binary oxometalate salts were dried under dynamic vacuum at 200 °C for 24 h, twice, to remove any traces of moisture.

To synthesize the transition oxometalate hydrides, the alkaline metal (Rb: *Alfa Aesar*, 99.75%, Cs: *Alfa Aesar*, 99.8%) is mixed thoroughly in an agate mortar with the dry binary transition metalate salt for several minutes. The reactive mixture is then heated in a self-made autoclave made of a hydrogen-resistant alloy (*Inconel Böhler 718*) at 255 °C (if M = Mo) or at 330 °C (if M = W) and applied hydrogen (*Westfalen AG*, 99.9%)/deuterium (*AirLiquide*, 99.9%) pressure of 10 bars. During the reaction, the alkaline metal is hydrogenated/deuterated to form the alkaline hydride/deuteride (RbH/D or CsH/D) which readily reacts with the binary transition metalate salt to form the products A₃MO₄H/D.

1.2 Powder X-ray diffraction

Powder X-ray diffraction data were recorded on a Stoe STADI-P in transmission geometry with either Cu-K_{α1} (λ = 1.54059 Å) or with Mo-K_{α1} (λ = 0.70930 Å) radiation. Both setups are equipped with a curved Ge-monochromator (111) and a Dectris Mythen DCS 1K solid-state detector. To avoid decomposition of the samples during measurements, the powders were placed in sealed in glass capillaries (Ø 0.3mm, 0.01mm wall thickness). Due to severe X-ray absorption at Cu-K_{α1} radiation and fluorescence at Mo-K_{α1} radiation, Rb₃WO₄H/D was sealed within Ø 0.1 mm glass capillaries to minimize these effects.

1.3 Neutron diffraction

Neutron powder diffraction data of all four deuterium analogue compounds were recorded at room temperature at the two-axis high-resolution powder neutron diffractometer D2B at the Institut Laue-Langevin (ILL), Grenoble using a wavelength of 1.594 Å. Each powder diffraction pattern was recorded over the course of 5h. For the measurement ~4 g of the sample were enclosed in 9 mm vanadium cylinders and sealed airtight with indium wires

1.4 Rietveld Refinement

Crystal structure refinement of X-ray diffraction and neutron diffraction data was done using the program package FullProf¹ with the Rietveld method and the fundamental parameter approach. Profiles were fitted using pseudo-Voigt functions. The zero shift, cell parameters, three form factors (Caglioti parameters U, V, W), either two (neutron diffraction data) or four (X-ray diffraction data) asymmetry parameters, atomic positions, isotropic and if applicable, anisotropic thermal displacement parameters were refined. The background correction was done with linear interpolations between refinable background points.

1.5 Raman spectroscopy

Raman spectra were recorded on the polycrystalline samples sealed in glass capillaries (Ø 0.3mm, 0.1mm wall thickness) on a Renishaw inVia Reflex Raman System equipped with a CCD detector. The wavelength of the laser was λ = 532 nm and the resulting spectra were recorded in the range of 100-1200 cm⁻¹.

1.6 UV/VIS absorption spectroscopy

UV-Vis absorption spectra were recorded on a *Shimadzu* UV-3600 Plus UV-Vis-NIR spectrophotometer. Thin films of the polycrystalline samples were placed within two quartz glass slides under Argon atmosphere. The glass slides were sealed airtight with vacuum grease for measurement. Direct and possible indirect bandgaps were determined from the materials absorption α obtained by the acquired solid-state UV-Vis absorption spectra.

Applied formula:

$$E \text{ (eV)} = \frac{1240}{\lambda \text{ (nm)}} (\alpha h\nu)^r$$

r is set to $\frac{1}{2}$ for an allowed, direct transition (direct bandgap).^[2]

1.7 Elemental analysis

Elemental analysis to determine and prove the hydrogen abundance of the hydridic samples has been conducted by CHNS analysis on a Vario El microanalyzer. Thereto, roughly 3 mg of the analyzed substance was packed within tin crucibles and folded within further tin crucibles to keep the samples air-tight until measurement.

Elemental analysis to determine the tungsten and molybdenum content has been conducted via alkaline pulping of the samples and consecutive photometric analysis. Thereto, 5 mg (molybdenum determination) or 12 mg (tungsten determination) of the respective samples were packed within aluminium boats beforehand and sealed airtight until measurement. The tungsten determination has slight deviations ($\sim 1\%$) due to strong hygroscopic properties of the tungstate salts.

1.8 Solid-state NMR

Measurements were taken at a magnetic field strength of 17.6 T at frequencies of 748.43 MHz and 114.88 MHz for ^1H and ^2H , respectively. Magic angle spinning (MAS) was done at rotation frequencies of 12 and 5 kHz. Single pulse excitation with recycle delays of 60 s and 2000 s for ^1H and ^2H were used, respectively. Recycle delays were chosen to be long enough for full relaxation; exact spin-lattice relaxation measurements (T_1) were not done. In case of ^2H full relaxation might not have been reached for the parent components. The transition metal hydrides with negative shifts relax much faster. Spectra are referenced indirectly to TMS or d-TMS via the ^1H shift of a sample of PDMS (0.07 ppm to TMS).

1.9 Quantum chemical calculations

The geometries, electronic properties, and vibrational properties of the four compounds A_3MO_4H ($A = \text{Rb}, \text{Cs}; M = \text{Mo}, \text{W}$) were studied with the CRYSTAL17 program package^[3]. PBE0 hybrid density functional method and Gaussian-type basis sets were used.^[4,5] The basis sets for Rb, Cs, Mo, W, O, and H have been previously derived from the molecular Karlsruhe def2 basis sets.^[6] Polarized triple-zeta-valence (TZVP) basis sets were used for Mo, W, O, and H polarized split-valence basis set for Rb and Cs (SVP)^[7]. The reciprocal space was sampled using a $4 \times 4 \times 4$ Monkhorst-Pack-type k -mesh for the tetragonal structures and $3 \times 3 \times 3$ Monkhorst-Pack-type k -mesh for the orthorhombic structure of $\text{Rb}_3\text{WO}_4\text{H}$ ^[8]. Tightened tolerance factors (TOLINTEG) of 8, 8, 8, 8 and 16 were used for the evaluation of the Coulomb and exchange integrals. Both the atomic positions and lattice constants were fully optimized within the constraints imposed by the space group symmetry. The optimized lattice parameters a and c for the tetragonal phases differed from the experimental parameters by -0.1% and $+1.2\%$ for $\text{Rb}_3\text{MoO}_4\text{H}$, $+0.1\%$ and $+1.1\%$ for $\text{Cs}_3\text{MoO}_4\text{H}$, $+0.1\%$ and $+0.1\%$ for $\text{Cs}_3\text{WO}_4\text{H}$ respectively. The optimized and experimental lattice parameters a , b and c for the orthorhombic phase $\text{Rb}_3\text{WO}_4\text{H}$ differed $+0.4\%$, $+0.7\%$, and $+0.5\%$, respectively. Raman intensities and corresponding spectra were obtained using the computational schemes implemented in CRYSTAL.^[9] The optimized structures of the tetragonal structures were confirmed to be true local minima with no imaginary frequencies. The optimized structure of $\text{Rb}_3\text{WO}_4\text{H}$ showed a very small imaginary frequency of -16.4 cm^{-1} , which did not disappear when the structure was distorted along the mode (tungstate deformation vibration, B_{1u}). We thus expect this mode to arise for example from small numerical inaccuracies in the numerical integration of the exchange-correlation functional. The Raman intensities have been calculated for a polycrystalline powder sample (total isotropic intensity in arbitrary units). For the simulation of the Raman spectra the temperature and laser wavelength were set to values corresponding to the experimental setup ($T = 298.15 \text{ K}$, $\lambda = 532 \text{ nm}$). The peak profile of the final spectra were simulated using pseudo-Voigt peak profile (50:50, Lorentzian: Gaussian) and FWHM of 8 cm^{-1} .

The solid-state NMR shielding tensors were calculated with the DFT-PBE method^[4], using the CASTEP program package and the GIPAW formalism as implemented in CASTEP-NMR^[10]. Ultrasoft pseudopotentials generated with the on-the-fly scheme and a plane-wave basis were applied^[11]. The kinetic energy cutoff was set to 630 eV for A_3MO_4H ($A = \text{Rb}, \text{Cs}; M = \text{Mo}, \text{W}$), while a cutoff of 450 eV was used for RbH and CsH. The reciprocal space was sampled using the following Monkhorst-Pack-type k -meshes: $4 \times 4 \times 4$ for tetragonal A_3MO_4H structures, $2 \times 2 \times 2$ for $\text{Rb}_3\text{WO}_4\text{H}$, and $8 \times 8 \times 8$ for RbH, CsH. The NMR shielding tensors of A_3MO_4H were calculated at both the experimental geometry and DFT-PBE optimized geometry, but the resulting ^1H NMR shifts are practically similar at both geometries. In the geometry optimization, both the lattice parameters and atomic positions were fully optimized with a total energy convergence criterion of $0.5 \times 10^{-6} \text{ eV/atom}$. Molecular SiMe_4 was used as a reference system for calculating the ^1H NMR shifts. The calculations on SiMe_4 were carried out in a primitive cubic cell ($a = 15 \text{ \AA}$) using a plane-wave basis set cut-off of 700 eV and Γ -point for reciprocal space sampling. The structure of the SiMe_4 molecule was relaxed within the T_d point group. The isotropic ^1H shielding of SiMe_4 is 31.01 ppm.

2 Results and discussion

2.1 Structural analysis

2.1.1 Neutron diffraction

Rb₃MoO₄D (RT)

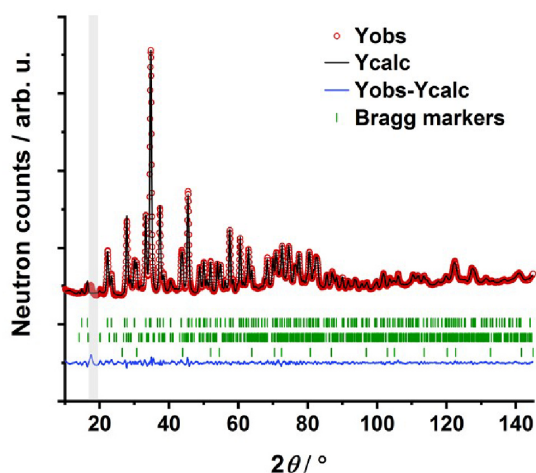


Figure S1 Rietveld refinement plot of Rb₃MoO₄D (*I4/mcm*, 140) at room temperature based on neutron diffraction data. The grey area was cut out during refinement as this reflection was not assignable. Bragg markers from top to bottom: Rb₃MoO₄D (89.3(7) wt.%), Rb₂MoO₄ (*Pnam*) (6.2(3) wt.%), RbD (*Fm $\bar{3}$ m*) (4.6(1) wt.%)

Table S1. Rietveld refinement parameters of Rb₃MoO₄D determined from neutron diffraction data at room temperature with the program Fullprof¹⁾

Rb ₃ MoO ₄ D	
Space group	<i>I4/mcm</i> (140)
Calculated density [g/cm ³]	3.655
Step scan increment	0.05
2θ range (°)	10 - 158
Wavelength (Å)	1.594
Number of profile points	2960
Temperature (K)	298
Program	Fullprof
Shape parameter η	0.539 (10)
Caglioti parameters (<i>U</i> , <i>V</i> , <i>W</i>)	<i>U</i> = 0.484(17) <i>V</i> = -0.510(19) <i>W</i> = 0.395(1)
Number of reflections	230
Number of refined parameters	112
<i>R</i> _{Bragg}	2.84%
<i>R</i> _p	1.49%
<i>R</i> _{wp}	2.03%
<i>R</i> _{exp}	0.65%
Goodness of fit (<i>X</i> ²)	9.60

Table S2. Crystallographic data on $\text{Rb}_3\text{MoO}_4\text{D}$ determined from neutron diffraction data at room temperature

Cell parameters					
a = 7.8620(3) Å, c = 12.2998(5) Å; a/b=1.00, b/c= 0.6392					
V = 760.26(5) Å ³					
Atom	Wyckoff position	Site	x/a	y/b	z/c
Mo	4b	-42m	0	½	¼
Rb1	8h	m2m	0.19049(13)	x+½	0
Rb2	4a	422	0	0	¼
O1	16l	m	0.12924(13)	x+½	0.66646(17)
D1	4c	4/m	0	0	0

Table S3. Anisotropic displacement parameters of $\text{Rb}_3\text{MoO}_4\text{D}$ determined from neutron diffraction data

Anisotropic displacement parameters [Å²]						
Atom	U ₁₁	U ₂₂	U ₃₃	U ₁₂	U ₁₃	U ₂₃
Mo1	0.0227(9)	0.0227(9)	0.0095(14)	0.00000	0.00000	0.00000
Rb1	0.0298(7)	0.0298(7)	0.0267(11)	-0.0054(9)	0.00000	0.00000
Rb2	0.0357(11)	0.0357(11)	0.0399(18)	0.00000	0.00000	0.00000
O1	0.0581(10)	0.0581(10)	0.0450(11)	-0.0184(10)	0.0222(6)	0.0222(6)
D1	0.0363(10)	0.0363(10)	0.0565(20)	0.00000	0.00000	0.00000

Table S4. Selected interatomic distances and tetrahedron angles in $\text{Rb}_3\text{MoO}_4\text{D}$ determined from neutron diffraction data

Atom 1	Atom 2	Distance (Å)	
Mo1	O1	1.7665(15)	
Rb1	D1	2.8573(10)	
Rb2		3.0749(12)	
Tetrahedron angle			
Atom 1	Atom 2	Atom 3	Angle
Mo1	O1	O1	108.865(49)
	O1	O1	109.775(58)
		∅ tetrahedron angle	109.32

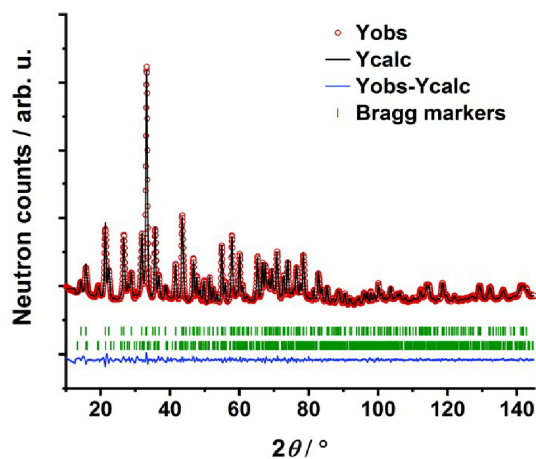
Cs₃MoO₄D (RT)

Figure S2 Rietveld refinement plot of Cs₃MoO₄D (*I4/mcm*, 140) at room temperature based on neutron diffraction data. Bragg markers from top to bottom: Cs₃MoO₄D (90.3 (10) wt.%), Cs₂MoO₄ (*Pnma*) (9.7(1) wt.%)

Table S5. Rietveld refinement parameters of Cs₃MoO₄D determined from neutron diffraction data at room temperature with the program Fullprof¹¹

Cs ₃ MoO ₄ D	
Space group	<i>I4/mcm</i> (140)
Calculated density [g/cm ⁻³]	4.319
Step scan increment	0.05
2θ range (°)	10 - 158
Wavelength (Å)	1.594
Number of profile points	2960
Temperature (K)	298
Program	Fullprof
Shape parameter η	0.541(12)
Caglioti parameters (<i>U</i> , <i>V</i> , <i>W</i>)	<i>U</i> = 0.352(10) <i>V</i> = -0.497(13) <i>W</i> = 0.393(5)
Number of reflections	258
Number of refined parameters	98
<i>R</i> _{Bragg}	1.60%
<i>R</i> _p	1.18%
<i>R</i> _{wp}	1.57%
<i>R</i> _{exp}	0.83%
Goodness of fit (χ ²)	3.59

Table S6. Crystallographic data on Cs₃MoO₄D determined from neutron diffraction data at room temperature

Cell parameters					
a = 8.2113(2) Å, c = 12.7893(4) Å; a/b=1.00, b/c= 0.6420					
V = 833.70(4) Å ³					
Atom	Wyckoff position	Site	x/a	y/b	z/c
Mo	4b	-42 <i>m</i>	0	½	¼
Cs1	8h	<i>m2m</i>	0.18705(16)	x+½	0
Cs2	4a	422	0	0	¼
O1	16l	<i>m</i>	0.12348(11)	x+½	0.66890(11)
D1	4c	4/ <i>m</i>	0	0	0

Table S7. Anisotropic displacement parameters of Cs₃MoO₄D determined from neutron diffraction data

Anisotropic displacement parameters [Å²]						
Atom	U₁₁	U₂₂	U₃₃	U₁₂	U₁₃	U₂₃
Mo1	0.0209(8)	0.0209(8)	0.0154(12)	0.00000	0.00000	0.00000
Cs1	0.0275(7)	0.0275(7)	0.0272(13)	-0.0032(9)	0.00000	0.00000
Cs2	0.0308(10)	0.0308(10)	0.0304(18)	0.00000	0.00000	0.00000
O1	0.0421(7)	0.0421(7)	0.0376(9)	-0.0162(9)	0.0100(5)	0.0100(5)
D1	0.0487(11)	0.0487(11)	0.063(2)	0.00000	0.00000	0.00000

Table S8. Selected interatomic distances and tetrahedron angles in Cs₃MoO₄D determined from neutron diffraction data

Atom 1	Atom 2	Distance (Å)	
Mo1	O1	1.7697(11)	
Cs1	D1	2.9938(13)	
Cs2		3.1973(1)	
Tetrahedron angle			
Atom 1	Atom 2	Atom 3	Angle
Mo1	O1	O1	110.090(48)
	O1	O1	108.240(43)
∅ tetrahedron angle			109.165

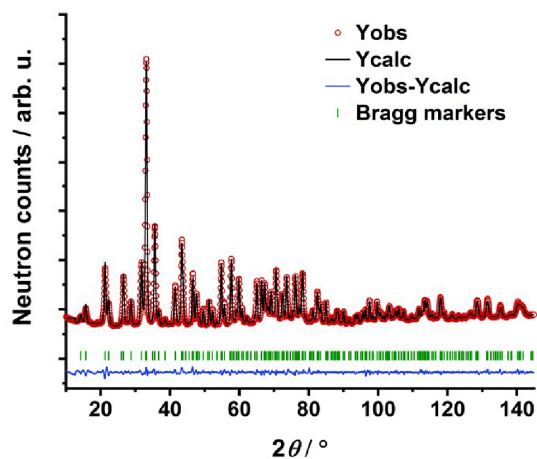
Cs₃WO₄D (RT)

Figure S3 Rietveld refinement plot of Cs₃WO₄D (*I4/mcm*, 140) at room temperature based on neutron diffraction data. Bragg markers Cs₃WO₄D.

Table S9. Rietveld refinement parameters of Cs₃WO₄D determined from neutron diffraction data at room temperature with the program Fullprof¹¹

Cs ₃ WO ₄ D	
Space group	<i>I4/mcm</i> (140)
Calculated density [g/cm ³]	4.954
Step scan increment	0.05
2θ range (°)	10 - 158
Wavelength (Å)	1.594
Number of profile points	2960
Temperature (K)	298
Program	Fullprof
Shape parameter η	0.478(10)
Caglioti parameters (<i>U</i> , <i>V</i> , <i>W</i>)	<i>U</i> = 0.263(6) <i>V</i> = -0.474(10) <i>W</i> = 0.386(4)
Number of reflections	260
Number of refined parameters	73
<i>R</i> _{Bragg}	2.03%
<i>R</i> _p	1.53%
<i>R</i> _{wp}	2.04%
<i>R</i> _{exp}	0.87%
Goodness of fit (χ ²)	5.46

Table S10. Crystallographic data on Cs₃WO₄D determined from neutron diffraction data at room temperature

Cell parameters					
a = 8.2331(2) Å, c = 12.8289(3) Å; a/b=1.00, b/c= 0.6418					
V = 869.58(4) Å ³					
Atom	Wyckoff position	Site	x/a	y/b	z/c
W	4b	-42 <i>m</i>	0	½	¼
Cs1	8h	<i>m2m</i>	0.18917(12)	x+½	0
Cs2	4a	422	0	0	¼
O1	16l	<i>m</i>	0.12355(9)	x+½	0.66889(9)
D1	4c	4/ <i>m</i>	0	0	0

Table S11. Anisotropic displacement parameters of Cs₃WO₄D determined from neutron diffraction data

Anisotropic displacement parameters [Å²]						
Atom	U₁₁	U₂₂	U₃₃	U₁₂	U₁₃	U₂₃
W1	0.0249(8)	0.0249(8)	0.0143(12)	0.00000	0.00000	0.00000
Cs1	0.0279(6)	0.0279(6)	0.0299(10)	0.0023(7)	0.00000	0.00000
Cs2	0.0320(9)	0.0320(9)	0.0322(14)	0.00000	0.00000	0.00000
O1	0.0484(6)	0.0484(6)	0.0417(7)	-0.0184(7)	0.0132(4)	0.0132(4)
D1	0.0405(8)	0.0405(8)	0.0562(15)	0.00000	0.00000	0.00000

Table S12. Selected interatomic distances and tetrahedron angles in Cs₃WO₄D determined from neutron diffraction data

Atom 1	Atom 2	Distance (Å)	
W1	O1	1.7754(9)	
Cs1	D1	2.9958(10)	
Cs2		3.2072(1)	
Tetrahedron angle			
Atom 1	Atom 2	Atom 3	Angle
W1	O1	O1	110.09(4)
	O1	O1	108.240(35)
		∅ tetrahedron angle	109.17

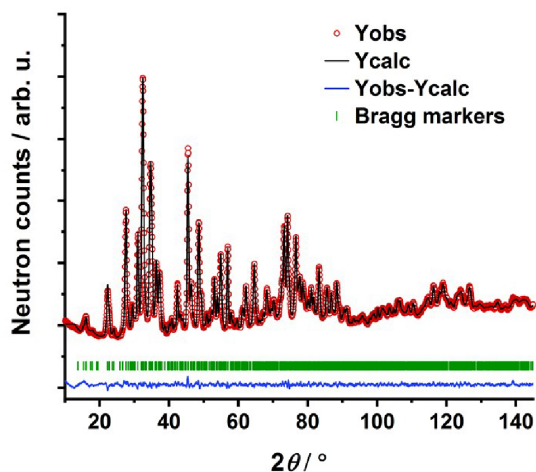
Rb₃WO₄D (RT)

Figure S4 Rietveld refinement plot of Rb₃WO₄D (*Pbca*, 61) at room temperature based on neutron diffraction data. Bragg markers Rb₃WO₄D.

Table S13. Rietveld refinement parameters of Rb₃WO₄D determined from neutron diffraction data at room temperature with the program Fullprof¹¹

Rb ₃ WO ₄ D	
Space group	<i>Pbca</i> (61)
Calculated density [g/cm ⁻³]	4.322
Step scan increment	0.05
2θ range (°)	10 - 158
Wavelength (Å)	1.594
Number of profile points	2960
Temperature (K)	298 K
Program	Fullprof
Shape parameter η	0.540(10)
Caglioti parameters (<i>U</i> , <i>V</i> , <i>W</i>)	<i>U</i> = 0.348(11) <i>V</i> = -0.527(14) <i>W</i> = 0.405(5)
Number of reflections	1610
Number of refined parameters	140
<i>R</i> _{Bragg}	1.60%
<i>R</i> _p	1.08%
<i>R</i> _{wp}	1.44%
<i>R</i> _{exp}	0.86%
Goodness of fit (<i>χ</i> ²)	2.77

Table S14. Crystallographic data on Rb₃WO₄D determined from neutron diffraction data at room temperature

Cell parameters					
a = 11.9262(3) Å, b = 11.3972(5) Å, c = 11.4492(5) Å; a/b=1.0464 b/c=0.9955 c/a=0.9600					
V= 1556.24(10)Å ³					
Atom	Wyckoff position	Site	x/a	y/b	z/c
W1	8c	1	0.7464(7)	0.0054(4)	-0.0149(4)
Rb1	8c	1	0.7464(4)	0.2334(4)	0.7289(3)
Rb2	8c	1	-0.0009(4)	0.7822(4)	-0.0062(5)
Rb3	8c	1	0.0003(4)	-0.0078(4)	0.7188(3)
O1	8c	1	0.8660(5)	-0.0224(5)	0.0730(5)
O2	8c	1	0.7823(5)	-0.0226(5)	0.8365(4)
O3	8c	1	0.7173(5)	0.1588(4)	-0.0086(5)
O4	8c	1	0.6318(6)	-0.0766(5)	0.0303(4)
D1	8c	1	0.5068(6)	0.7562(5)	0.2585(9)

Table S15. Anisotropic displacement parameters on $\text{Rb}_3\text{WO}_4\text{D}$ determined from neutron diffraction data at room temperature

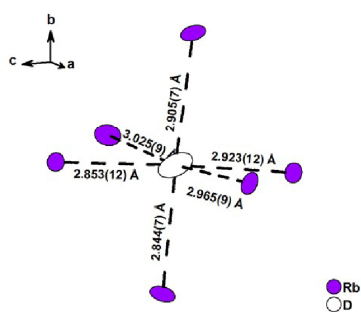
Anisotropic displacement parameters [\AA^2]						
Atom	U_{11}	U_{22}	U_{33}	U_{12}	U_{13}	U_{23}
W1	0.0181(20)	0.016(2)	0.030(3)	-0.008(3)	-0.011(3)	-0.004(3)
Rb1	0.0243(18)	0.035(3)	0.037(3)	0.003(2)	-0.018(3)	0.0047(19)
Rb2	0.029(4)	0.027(2)	0.028(2)	0.003(2)	-0.0096(20)	-0.002(2)
Rb3	0.032(4)	0.017(2)	0.041(3)	0.004(3)	0.007(2)	0.008(2)
O1	0.016(4)	0.064(4)	0.055(4)	0.008(3)	-0.021(3)	0.006(3)
O2	0.065(5)	0.053(4)	0.015(3)	-0.022(3)	0.013(3)	-0.013(2)
O3	0.071(5)	0.032(3)	0.044(3)	0.026(3)	-0.024(3)	0.004(3)
O4	0.047(4)	0.051(4)	0.038(4)	-0.021(4)	0.022(3)	-0.012(3)
D1	0.0542(19)	0.042(3)	0.077(4)	0.023(3)	0.007(3)	-0.008(4)

Table S16. Selected interatomic distances in $\text{Rb}_3\text{WO}_4\text{D}$ determined from neutron diffraction data

Atom 1	Atom 2	Distance (\AA)
W1	O4	1.7347(97)
	O1	1.7742(93)
	O2	1.7832(68)
	O3	1.7839(66)
	\emptyset bond length	1.769 \AA
Rb1	D1	2.9652(86)
		3.0025(86)
Rb2	D1	2.8529(117)
		2.9230(117)
Rb3	D1	2.8440(73)
		2.9046(74)

Table S17. Tetrahedron angles of the tungstate ions in $\text{Rb}_3\text{WO}_4\text{D}$ determined from neutron diffraction data

Atom 1	Atom 2	Atom 3	Angle 2-1-3 ($^\circ$)
W1	O4	O1	111.59(50)
	O4	O2	112.17(37)
	O4	O3	111.26(35)
	O1	O2	108.43(35)
	O1	O3	107.96(37)
	O2	O3	105.11(35)
		\emptyset tetrahedron angle	109.42 $^\circ$

**Figure S5** Bond lengths and depiction of the distorted Rb_6D -octahedron

2.1.2 Supplementary X-ray diffraction data (Hydric samples)

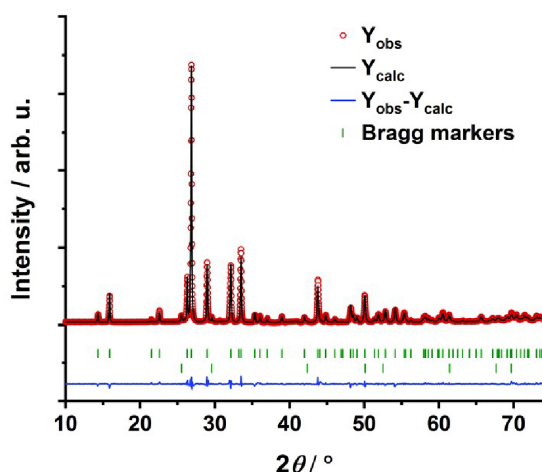
Rb₃MoO₄H

Figure S6. Rietveld refinement plot of Rb₃MoO₄H obtained from X-ray diffraction data at room temperature with the program Fullprof¹¹. Bragg markers: Rb₃MoO₄H (top) (97.9(10) wt.%); RbH (bottom) 2.02(2) wt.%. $R_p = 5.90\%$, $R_{wp} = 8.49\%$, $R_{exp} = 3.63\%$, $R_{bragg} = 4.01\%$, $\chi^2 = 5.90$

Table S18. Crystallographic data on Rb₃MoO₄H determined from X-ray diffraction data at room temperature

Cell parameters						
a = 7.8741(4) Å, c = 12.3172(7) Å;						
a/b=1.00, b/c= 0.6393, V = 760.68(7) Å ³						
Atom	Wyckoff position	Site	x/a	y/b	z/c	B _{iso} (Å ²)
Mo	4b	-42m	0	½	¼	0.0013(13)
Rb1	8h	m2m	0.18962(15)	x+½	0	0.0036(12)
Rb2	4a	422	0	0	¼	0.0129(15)
O1	16l	m	0.1232(6)	x+½	0.6698(6)	0.005(3)
H1	4c	4/m	0	0	0	0.0507*

*The isotropic displacement factor of hydrogen has been set to a realistic value, as no refinement thereof with X-ray diffraction data was possible.

Table S19. Selected interatomic distances and tetrahedron angles in Rb₃MoO₄H determined from X-ray diffraction data

Atom 1	Atom 2	Distance (Å)	
Mo1	O1	1.6906(58)	
Rb1	H1	2.8639(12)	
Rb2		3.0793(2)	
Tetrahedron angle			
Atom 1	Atom 2	Atom 3	Angle 2-1-3 (°)
Mo1	O1	O1	108.489(235)
	O1	O1	109.965(265)
∅ tetrahedron angle			109.227

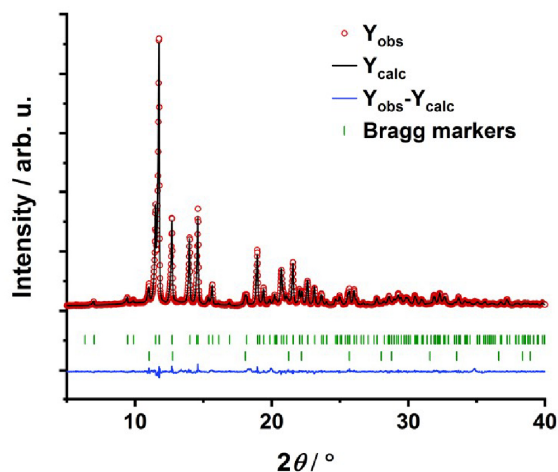
Cs₃MoO₄H

Figure S7. Rietveld refinement plot of Cs₃MoO₄H obtained from X-ray diffraction data at room temperature with the program Fullprof¹¹. Bragg markers: Cs₃MoO₄H (top) (94.3(10) wt.%); CsH (bottom) 5.7(2) wt.%. $R_p = 3.88\%$, $R_{wp} = 5.40\%$, $R_{exp} = 3.32\%$, $R_{bragg} = 2.93\%$, $\chi^2 = 2.65$

Table S20. Crystallographic data on Cs₃MoO₄H determined from X-ray diffraction data at room temperature

Cell parameters

$a = 8.2232(2)\text{\AA}$, $c = 12.8149(3)\text{\AA}$;
 $a/b=1.00$, $b/c= 0.6417$, $V = 866.55(3)\text{\AA}^3$

Atom	Wyckoff position	Site	x/a	y/b	z/c	B_{iso} (\AA^2)
Mo	4b	-42m	0	½	¼	0.0156(11)
Cs1	8h	<i>m2m</i>	0.18685(13)	$x+\frac{1}{2}$	0	0.0203(8)
Cs2	4a	422	0	0	¼	0.0284(10)
O1	16l	<i>m</i>	0.1246(9)	$x+\frac{1}{2}$	0.6736(8)	0.034(4)
H1	4c	4/m	0	0	0	0.0507*

*The isotropic displacement factor of hydrogen has been set to a realistic value, as no refinement thereof with X-ray diffraction data was possible.

Table S21. Selected interatomic distances and tetrahedron angles in Rb₃MoO₄H determined from X-ray diffraction data

Atom 1	Atom 2	Distance (\AA)	
Mo1	O1	1.7488(84)	
Cs1	H1	2.9986(11)	
Cs2		3.1236(90)	
Tetrahedron angle			
Atom 1	Atom 2	Atom 3	Angle 2-1-3 ($^\circ$)
Mo1	O1	O1	111.908(350)
	O1	O1	108.267(383)
∅ tetrahedron angle			110.088

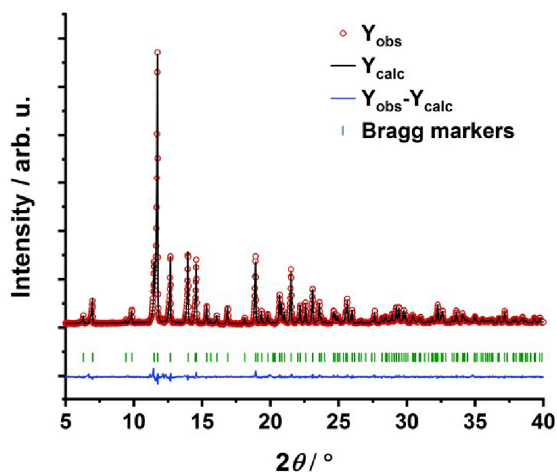
Cs₃WO₄H

Figure S8. Rietveld refinement plot of Cs₃WO₄H obtained from X-ray diffraction data at room temperature with the program Fullprof¹¹. Bragg markers: Cs₃WO₄H. $R_p = 4.83\%$, $R_{wp} = 6.65\%$, $R_{exp} = 5.38\%$, $R_{bragg} = 3.83\%$, $\chi^2 = 1.53$

Table S22. Crystallographic data on Cs₃WO₄H determined from X-ray diffraction data at room temperature

Cell parameters						
a = 8.2391(2) Å, c = 12.8405(3) Å;						
a/b=1.00, b/c= 0.6417, V = 871.66(3) Å ³						
Atom	Wyckoff position	Site	x/a	y/b	z/c	B _{iso} (Å ²)
W	4b	-42m	0	½	¼	0.0049(8)
Cs1	8h	m2m	0.18890(14)	x+½	0	0.0115(8)
Cs2	4a	422	0	0	¼	0.0177(10)
O1	16l	m	0.1251(10)	x+½	0.6668(9)	0.029(5)
H1	4c	4/m	0	0	0	0.0507*

*The isotropic displacement factor of hydrogen has been set to a realistic value, as no refinement thereof with X-ray diffraction data was possible.

Table S23. Selected interatomic distances and tetrahedron angles in Cs₃WO₄H determined from X-ray diffraction data

Atom 1	Atom 2	Distance (Å)	
W1	O1	1.8072(95)	
Cs1	H1	2.9987(12)	
Cs2		3.2101(1)	
Tetrahedron angle			
Atom 1	Atom 2	Atom 3	Angle 2-1-3 (°)
W1	O1	O1	110.454(421)
	O1	O1	107.524(382)
		∅ tetrahedron angle	108.989

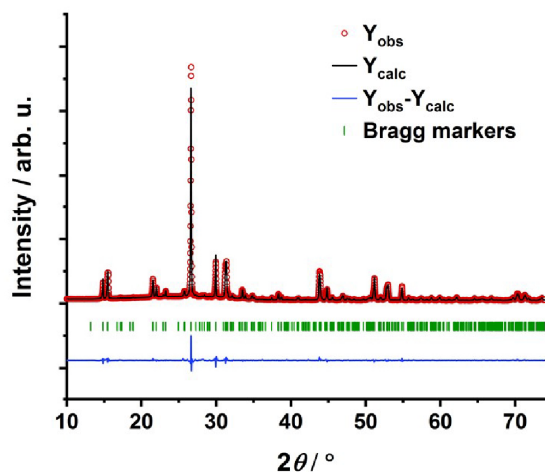
Rb₃WO₄H

Figure S9 Rietveld refinement plot of Rb₃WO₄H at room temperature based on X-ray diffraction data. Bragg markers Rb₃WO₄H. $R_p = 2.91\%$, $R_{wp} = 4.38\%$, $R_{exp} = 1.03\%$, $R_{bragg} = 2.78\%$, $\chi^2 = 17.9$. Due to very high scattering intensity, necessary to properly resolve the splitting of the reflections, the data quality is very high. R_{exp} is therefore estimated to be very low, resulting in a rather high goodness of fit as $\chi^2 = R_{wp}^2 / R_{exp}^2$.

Table S24. Crystallographic data on Rb₃WO₄H determined from neutron diffraction data at room temperature

Cell parameters						
a = 11.9295(3) Å, b = 11.4019(3) Å, c = 11.4516(3) Å; a/b=1.0463 b/c=0.9957 c/a=0.9599						
V = 1557.63(7) Å ³						
Atom	Wyckoff position	Site	x/a	y/b	z/c	B _{iso} (Å ²)
W1	8c	1	0.7502(4)	0.0065(4)	-0.0164(2)	0.0042(8)
Rb1	8c	1	0.7452(13)	0.2331(6)	0.7296(4)	0.0178(17)
Rb2	8c	1	-0.0008(10)	0.7819(3)	0.0057(11)	0.0172(20)
Rb3	8c	1	0.0007(8)	-0.0078(6)	0.7199(3)	0.0110(19)
O1	8c	1	0.858(2)	-0.022(3)	0.0919(20)	0.036(10)
O2	8c	1	0.787(3)	-0.013(3)	0.840(2)	0.007(10)
O3	8c	1	0.710(3)	0.152(2)	-0.011(3)	0.043(14)
O4	8c	1	0.631(3)	-0.068(2)	0.047(2)	0.026(10)
H1	8c	1	0.50680*	0.75620*	0.25850*	0.0507*

*The atomic position of hydrogen was not determinable via X-ray diffraction and assumed to be the position determined by neutron diffraction. The isotropic displacement factor of hydrogen has been set to a realistic value, as no refinement thereof with X-ray diffraction data was possible.

Table S25. Selected interatomic distances in Rb₃WO₄D determined from neutron diffraction data

Atom 1	Atom 2	Distance (Å)
W1	O4	1.8085(318)
	O1	1.8159(241)
	O2	1.7165(243)
	O3	1.7280(245)
	∅ bond length	1.7672 Å
Rb1	H1	2.9795(154)
		3.00118(155)
Rb2	H1	2.7177(125)
		3.0579(125)
Rb3	H1	2.8439(68)
		2.9040(68)

Table S26. Tetrahedron angles of the tungstate ions in Rb₃WO₄D determined from neutron diffraction data

Atom 1	Atom 2	Atom 3	Angle 2-1-3 (°)
W1	O4	O1	101.44(124)
	O4	O2	121.66(123)
	O4	O3	102.61(120)
	O1	O2	116.74(110)
	O1	O3	110.12(143)
	O2	O3	103.28(155)
∅ tetrahedron angle			109.31°

2.2 Ionic radii for determination of the Goldschmidt tolerance factors

The ionic radii of the complex oxoanions are taken from the determined bond lengths of the *M*-O bond (as depicted above) plus the ionic radius of oxygen in sixfold coordination sphere. Ionic radii are taken from Shannon in respect of the coordination spheres of the ions.^[12]

The hydride ion is known to have high polarizability and therefore shows different ionic radii, depending on the chemical environment. We have set the ionic radius of the hydride anion to be 1.399 Å as suggested from Shannon and also from Lang and Smith^[12,13]. This approach is expected to return consistent set of tolerance factors that enable a discussion of chemical packing as a factor for differences in their crystal chemistries.

Table S27. Ionic radii for determination of the Goldschmidt tolerance factors

Ionic species	Ionic radius	Coordination
Na ⁺	1.02	Sixfold
K ⁺	1.38	Eightfold/tenfold
Rb ⁺	1.52	Sixfold (Rb ₃ WO ₄ H)
Rb ⁺	1.63	Eightfold/tenfold
Cs ⁺	1.67	Eightfold/tenfold
MoO ₄ ²⁻	3.170	-
WO ₄ ²⁻	3.180	-
SO ₄ ²⁻	2.87	-
H ⁻	1.399	Sixfold
F ⁻	1.33	Sixfold
O ²⁻	1.40	Sixfold

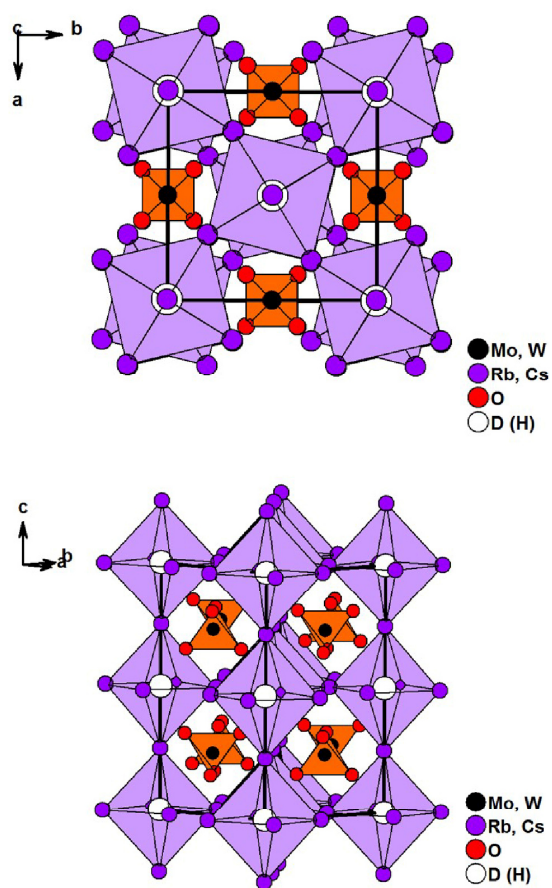
2.3 Crystal structure of the K_3SO_4F -structure type

Figure S10. Crystal structure of the tetragonal phases along the c-axis (top) and along the a/b plane (bottom). The Rb₆D /Cs₆D octahedrons are depicted lilac, the tungstate ions are depicted as orange tetrahedrons.

2.4 Difference Fourier maps

$\text{Rb}_3\text{MoO}_4\text{D}$

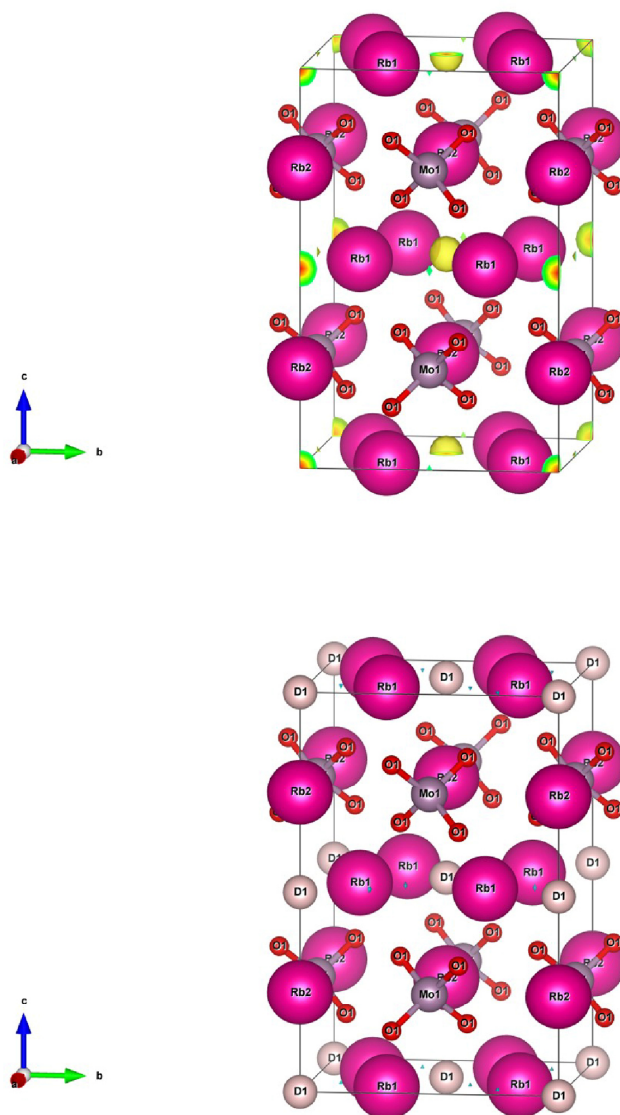


Figure S11. Difference Fourier map of the refinement $\text{Rb}_3\text{MoO}_4\square$ (top) with an unoccupied deuterium position (symbol \square , in FullProf the occupation and B_{iso} were set to 0). Rubidium is shown in pink, tungsten in grey and oxygen in red. The positive, residual density (yellow isosurface, projected at an isosurface level of 0.090) agrees with the experimentally determined deuterium position in $\text{Rb}_3\text{MoO}_4\text{D}$. For comparison: difference Fourier map of the refinement $\text{Rb}_3\text{MoO}_4\text{D}$ (bot). Here, no residual density is found at a ca. twenty times lower isosurface level of 0.0058. The lower the isosurface level is set, the more sensitively residual neutron density is shown.

In addition, no residual neutron density is found next to the now occupied deuteride position. This excludes a likely hydroxide/deuterioxide species as no neutron density of a closely bound atom is observable. Graphic representation is shown in VESTA^[14].

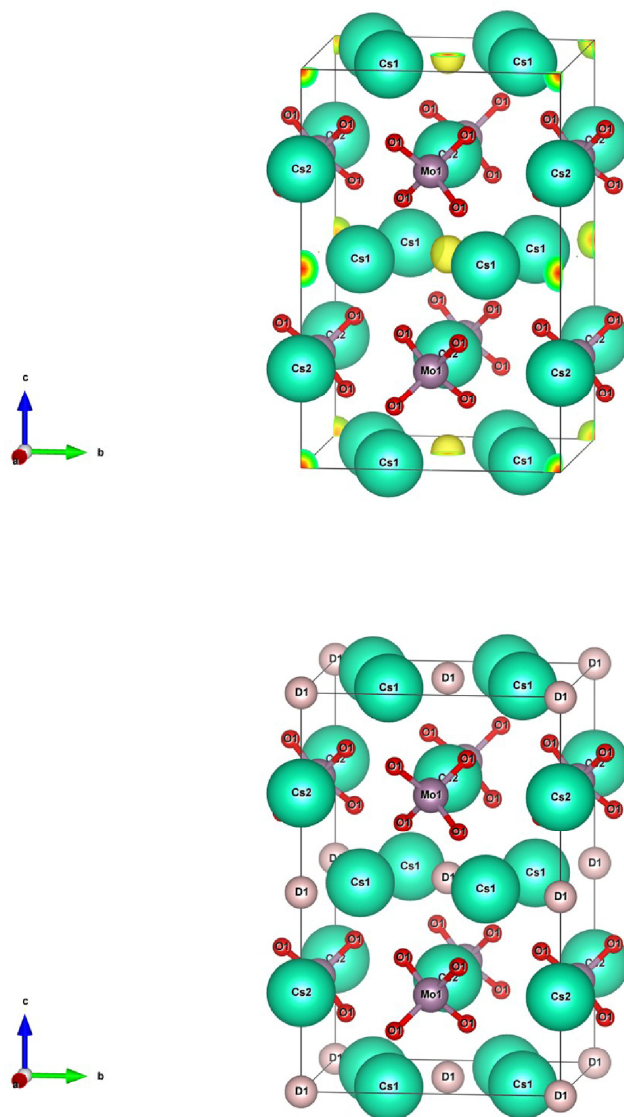


Figure S12. Difference Fourier map of the refinement $\text{Cs}_3\text{MoO}_4\text{D}$ (top) with an unoccupied deuterium position (symbol \square , in FullProf the occupation and B_{iso} were set to 0). Rubidium is shown in pink, tungsten in grey and oxygen in red. The positive, residual density (yellow isosurface, projected at an isosurface level of 0.074) agrees with the experimentally determined deuterium position in $\text{Cs}_3\text{MoO}_4\text{D}$. For comparison: difference Fourier map of the refinement $\text{Cs}_3\text{MoO}_4\text{D}$ (bot). Here, no residual density is found at a ten times lower isosurface level of 0.0075. The lower the isosurface level is set, the more sensitively residual neutron density is shown. Again, no residual neutron density is found next to the here occupied deuteride position. This excludes a likely hydroxide/deuterioxide species as no neutron density of a closely bound atom is observable. Graphic representation is shown in VESTA^[14].

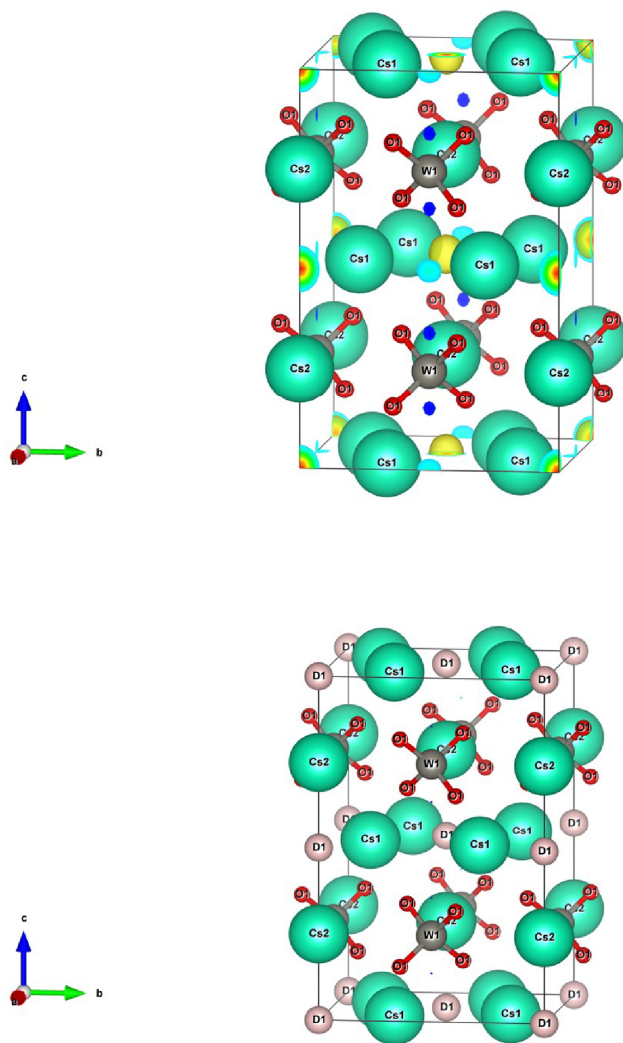
$\text{Cs}_3\text{WO}_4\text{D}$ 

Figure S13. Difference Fourier map of the refinement $\text{Cs}_3\text{WO}_4\text{□}$ (top) with an unoccupied deuterium position (symbol \square , in FullProf the occupation and B_{res} were set to 0). Rubidium is shown in pink, tungsten in grey and oxygen in red. The positive, residual density (yellow isosurface, projected at an isosurface level of 0.043) agrees with the experimentally determined deuterium position in $\text{Cs}_3\text{WO}_4\text{D}$. For comparison: difference Fourier map of the refinement $\text{Cs}_3\text{WO}_4\text{D}$ (bot). Here, no residual density is found at a five times lower isosurface level of 0.009. The lower the isosurface level is set, the more sensitively residual neutron density is shown. No residual neutron density is found next to the now occupied deuteride position. This excludes a likely hydroxide/deuterioxide or any other different species as no neutron density of a closely bound atom is observable. Graphic representation is shown in VESTA^[14].

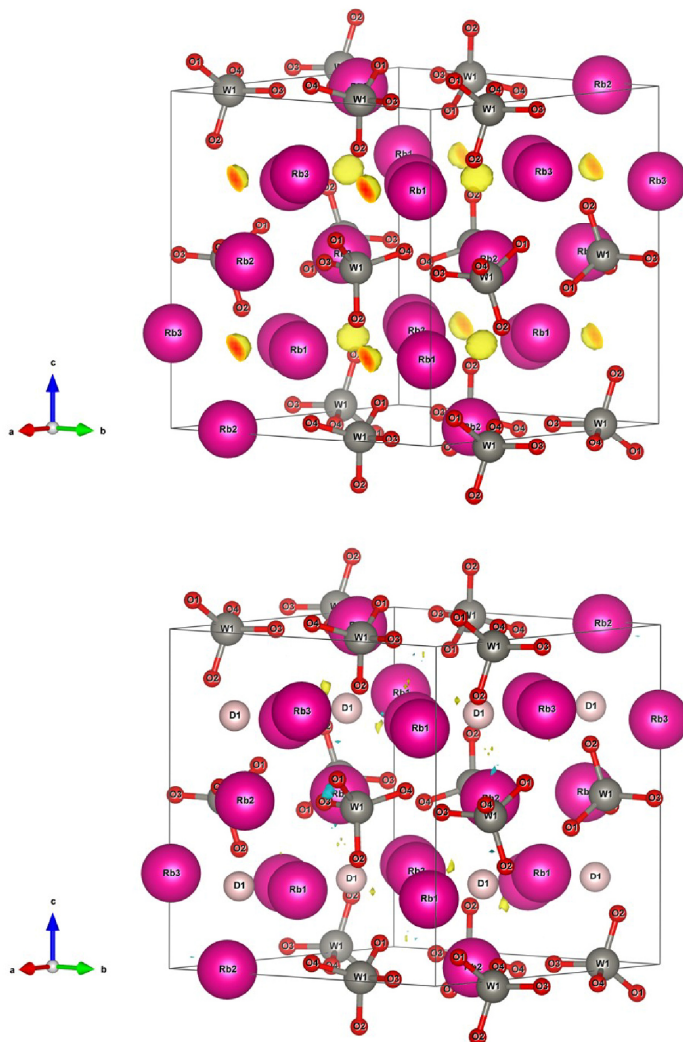
$\text{Rb}_3\text{WO}_4\text{D}$ 

Figure S14. Difference Fourier map of the refinement $\text{Rb}_3\text{WO}_4\text{□}$ (top) with an unoccupied deuterium position (symbol \square , in FullProf the occupation and B_{iso} were set to 0). Rubidium is shown in pink, tungsten in grey and oxygen in red. The positive, residual density (yellow isosurface, projected at an isosurface level of 0.055) agrees with the experimentally determined deuterium position in $\text{Rb}_3\text{WO}_4\text{D}$. For comparison: difference Fourier map of the refinement $\text{Rb}_3\text{WO}_4\text{D}$ (bot). Here, no residual density is found at a ten times lower isosurface level of 0.0055. Once again, no residual neutron density is found next to the now occupied deuterium position. This excludes a likely hydroxide/deuterioxide species as no neutron density of a closely bound atom is observable. Graphic representation is shown in VESTA⁽¹⁴⁾.

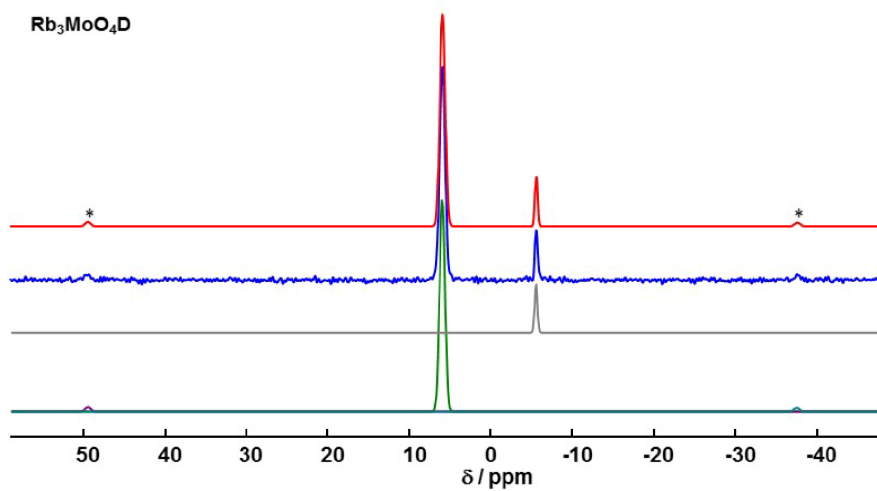
2.5 ^2H MAS NMR Spectroscopy

Figure S15. Full ^2H MAS spectrum of $\text{Rb}_3\text{MoO}_4\text{D}$. Rotational sidebands of the target compound signal are masked with asterisks. Red line full fit, blue line experimental spectrum. Lines below depict the fits of the individual signals.

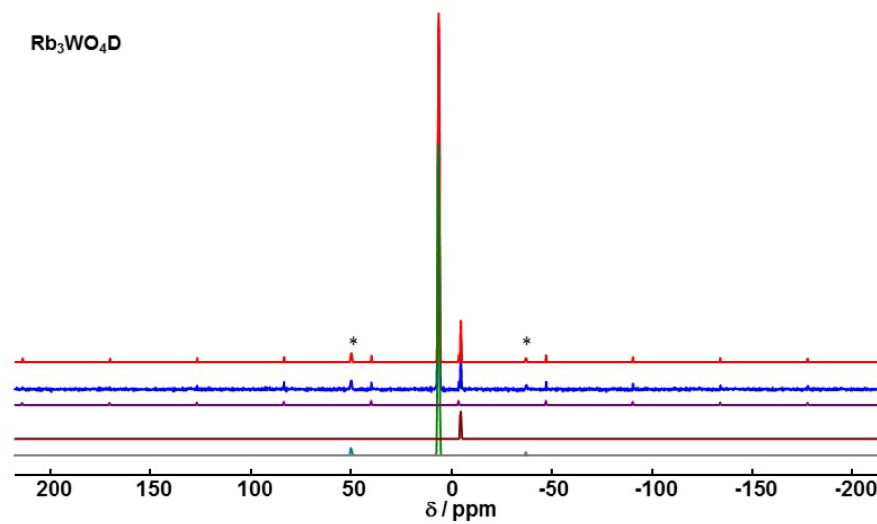


Figure S16. Full ^2H MAS spectrum of $\text{Rb}_3\text{WO}_4\text{D}$. Rotational sidebands of the target compound signal are masked with asterisks. Red line full fit, blue line experimental spectrum. Lines below depict the fits of the individual signals.

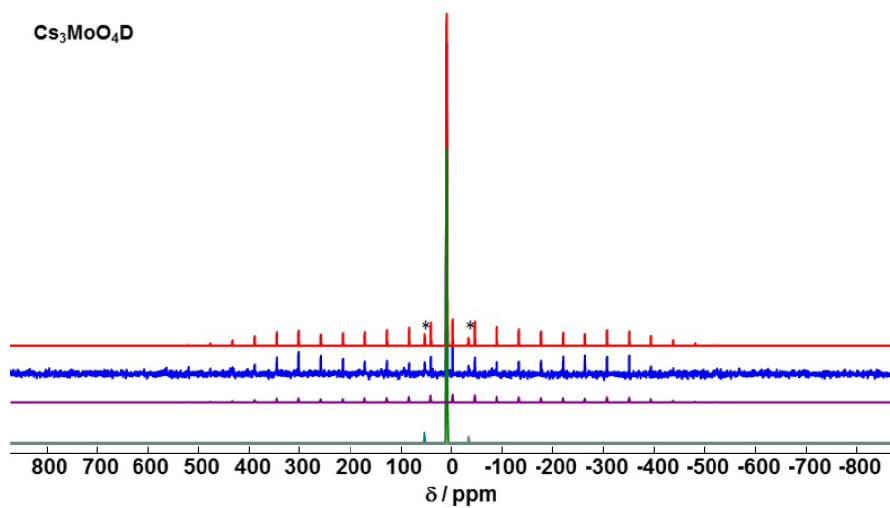


Figure S17. Full ^2H MAS spectrum of $\text{Cs}_3\text{MoO}_4\text{D}$. Rotational sidebands of the target compound signal are masked with asterisks. Red line full fit, blue line experimental spectrum. Lines below depict the fits of the individual signals.

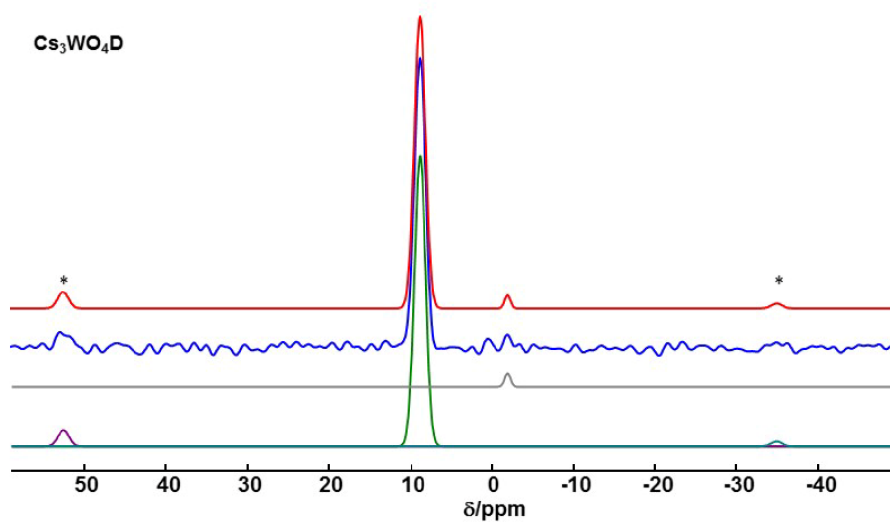


Figure S18. Full ^2H MAS spectrum of $\text{Cs}_3\text{WO}_4\text{D}$. Rotational sidebands of the target compound signal are masked with asterisks. Red line full fit, blue line experimental spectrum. Lines below depict the fits of the individual signals.

2.6 Calculated electronic band structures and UV/Vis Tauc plots

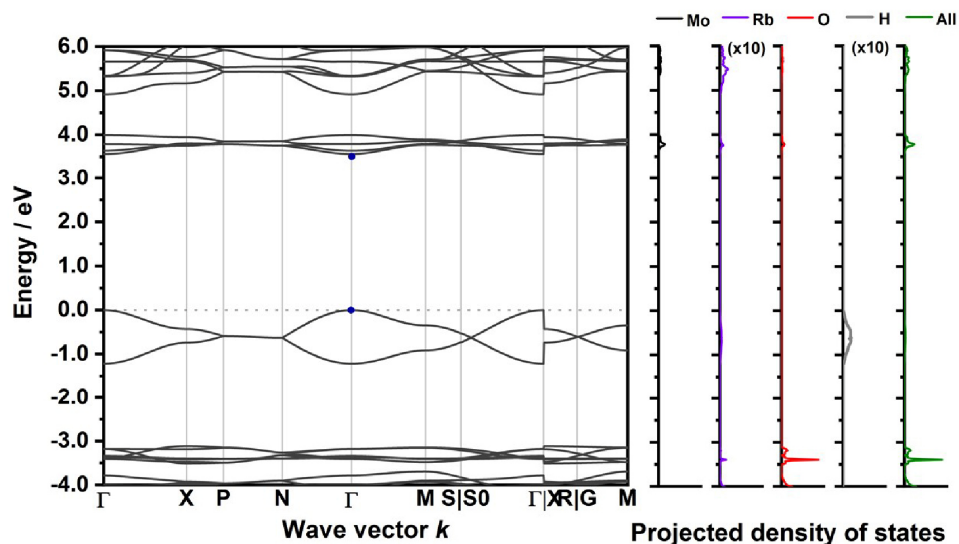
Rb₃MoO₄H

Figure S19. Calculated electronic band structure of Rb₃MoO₄H and projected density of states (DFT-PBE0). The blue dots indicate the direct band gap character. The DOS of Rubidium and Hydrogen are enhanced for better visibility. The band paths in the reciprocal space have been determined by the Seek-path webservice^[15–17].

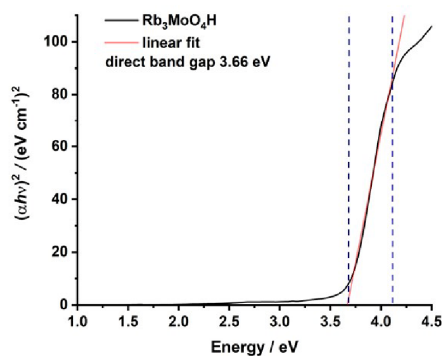


Figure S20. Tauc-plots of Rb₃MoO₄H determined from UV/VIS absorption spectroscopy. For the determination of a direct transition character, the coefficient r (see experimental details) has been set to $r = \frac{1}{2}$, direct transition (left side). The blue vertical dashed lines indicate the area for the linear fit. The resulting determined direct band gap of 3.66 eV is matching the predicted band gap of 3.56 eV.

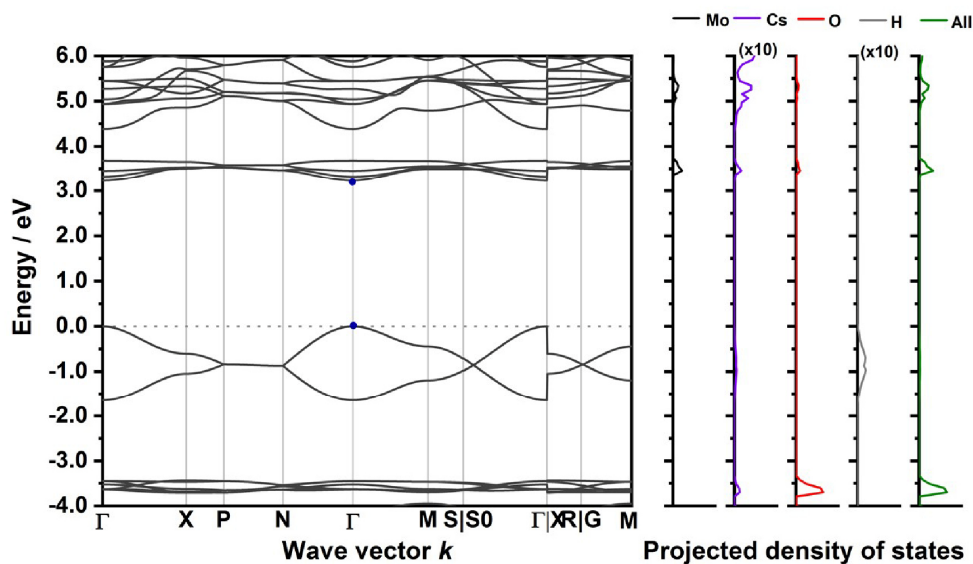
Cs₃MoO₄H

Figure S21. Calculated electronic band structure of Cs₃MoO₄H and projected density of states (DFT-PBE0). The blue dots indicate the direct band gap character. The DOS of Cesium and Hydrogen are enhanced for better visibility. The band paths in the reciprocal space have been determined by the Seek-path webservice^[15–17].

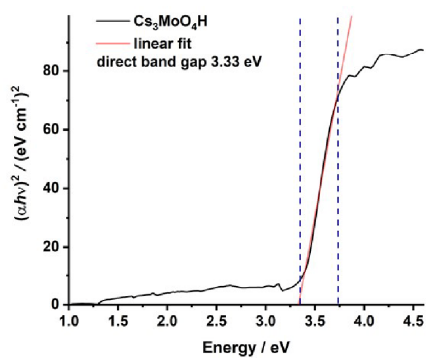


Figure S22. Tauc-plots of Cs₃MoO₄H determined from UV/VIS absorption spectroscopy. For the determination of a direct or indirect transition character, the coefficient r (see experimental details) has been set to $r = \frac{1}{2}$. The blue vertical dashed lines indicate the area for the linear fit. The resulting determined direct band gap of 3.33 eV is matching the predicted band gap of 3.23 eV.

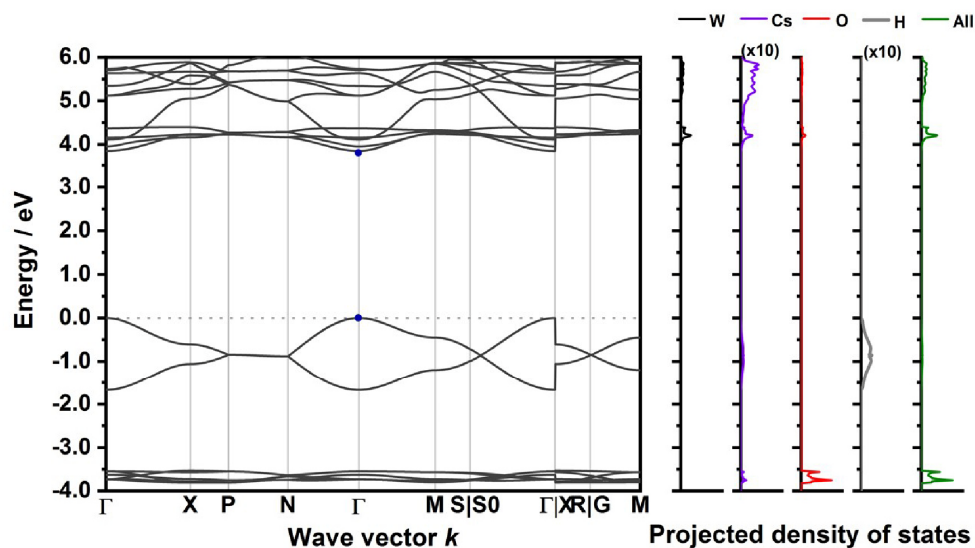
Cs₃WO₄H

Figure S23. Calculated electronic band structure of Cs₃WO₄H and projected density of states (DFT-PBE0). The blue dots indicate the direct band gap character. The DOS of Rubidium and Hydrogen are enhanced for better visibility. The band paths in the reciprocal space have been determined by the Seek-path webservice^[15–17].

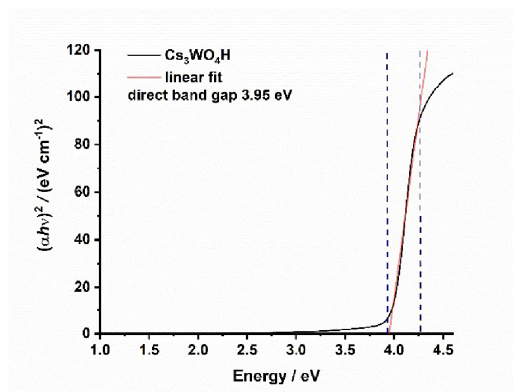


Figure S24. Tauc-plots of Cs₃WO₄H determined from UV/VIS absorption spectroscopy. For the determination of a direct or indirect transition character, the coefficient r (see experimental details) has been set to $r = \frac{1}{2}$. The blue vertical dashed lines indicate the area for the linear fit. The resulting determined direct band gap of 3.95 eV is matching the predicted band gap of 3.85 eV.

2.7 Vibrational Spectroscopy (experimental and DFT-PBE0)

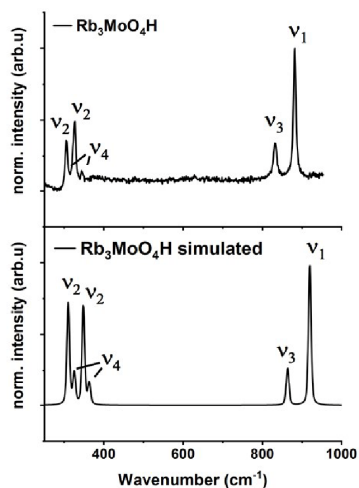
Rb₃MoO₄H

Figure S25. Experimental Raman spectrum of Rb₃MoO₄H (top) and simulated Raman spectrum of Rb₃MoO₄H (bottom).

Table S28. Vibrational Raman data of Rb₃MoO₄H obtained by quantum chemical calculations.

Simulated Raman data on Rb ₃ MoO ₄ H			
Frequency (cm ⁻¹)	Γ_{irrep}	Intensity (arbitrary units)	Assignment
46	E _g	33	Lattice vibrations
56	E _g	31	Lattice vibrations
69	A _{1g}	56	Lattice vibrations
72	B _{1g}	34	Lattice vibrations
76	B _{2g}	2	Lattice vibrations
95	E _g	188	MoO ₄ ²⁻ antisymmetric bending coupled with lattice vibrations
97	E _g	1	Lattice vibrations
114	B _{2g}	49	Lattice vibrations
310	B _{1g}	726	MoO ₄ ²⁻ symmetric bending (v ₂)
325	E _g	225	MoO ₄ ²⁻ antisymmetric bending (v ₄)
348	A _{1g}	705	MoO ₄ ²⁻ symmetric bending (v ₂)
363	B _{2g}	154	MoO ₄ ²⁻ antisymmetric bending (v ₄)
861	B _{2g}	69	MoO ₄ ²⁻ antisymmetric stretching (v ₃)
864	E _g	212	MoO ₄ ²⁻ antisymmetric stretching (v ₃)
919	A _{1g}	1000	MoO ₄ ²⁻ symmetric stretching (v ₁)

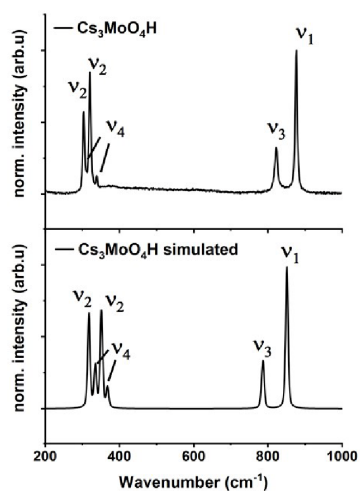
Cs₃MoO₄H

Figure S26. Experimental Raman spectrum of Cs₃MoO₄H (top) and simulated Raman spectrum of Cs₃MoO₄H (bottom).

Table S29. Vibrational Raman data of Cs₃MoO₄H obtained by quantum chemical calculations.

Simulated Raman data on Cs ₃ MoO ₄ H			
Frequency (cm ⁻¹)	Γ_{irrep}	Intensity (arbitrary units)	Assignment
32	E _g	1	Lattice vibrations
39	E _g	83	Lattice vibrations
50	A _{1g}	137	Lattice vibrations
56	B _{2g}	10	Lattice vibrations
56	B _{1g}	168	Lattice vibrations
80	E _g	39	Lattice vibrations
101	B _{2g}	46	Lattice vibrations
141	E _g	102	MoO ₄ ²⁻ antisymmetric bending coupled with lattice vibrations
318	B _{1g}	670	MoO ₄ ²⁻ symmetric bending (v ₂)
334	E _g	289	MoO ₄ ²⁻ antisymmetric bending (v ₄)
351	A _{1g}	685	MoO ₄ ²⁻ symmetric bending (v ₂)
367	B _{2g}	142	MoO ₄ ²⁻ antisymmetric bending (v ₄)
783	B _{2g}	58	MoO ₄ ²⁻ antisymmetric stretching (v ₃)
786	E _g	306	MoO ₄ ²⁻ antisymmetric stretching (v ₃)
850	A _{1g}	1000	MoO ₄ ²⁻ symmetric stretching (v ₁)

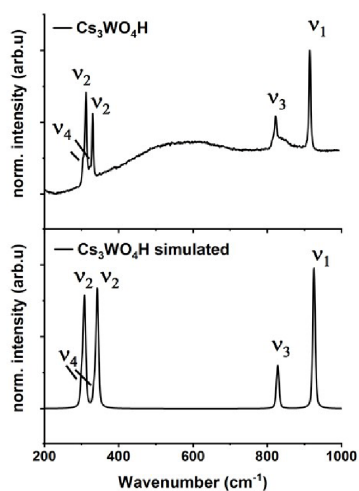
Cs₃WO₄H

Figure S27. Experimental Raman spectrum of Cs₃WO₄H (top) and simulated Raman spectrum of Cs₃WO₄H (bottom).

Table S30. Vibrational Raman data of Cs₃MoO₄H obtained by quantum chemical calculations.

Simulated Raman data on Cs ₃ WO ₄ H			
Frequency (cm ⁻¹)	Γ _{Irrep}	Intensity (arbitrary units)	Assignment
25	E _g	0	Lattice vibrations
36	E _g	55	Lattice vibrations
47	A _{1g}	214	Lattice vibrations
50	B _{2g}	5	Lattice vibrations
55	B _{1g}	288	Lattice vibrations
70	E _g	60	Lattice vibrations
84	B _{2g}	76	Lattice vibrations
86	E _g	277	WO ₄ ²⁻ antisymmetric bending coupled with lattice vibrations
300	E _g	210	WO ₄ ²⁻ antisymmetric bending (v ₄)
308	B _{1g}	766	WO ₄ ²⁻ symmetric bending (v ₂)
335	B _{2g}	147	WO ₄ ²⁻ antisymmetric bending (v ₄)
343	A _{1g}	833	WO ₄ ²⁻ symmetric bending (v ₂)
826	B _{2g}	47	WO ₄ ²⁻ antisymmetric stretching (v ₃)
828	E _g	266	WO ₄ ²⁻ antisymmetric stretching (v ₃)
926	A _{1g}	1000	WO ₄ ²⁻ symmetric stretching (v ₁)

The Raman spectrum of Cs₃WO₄H shows a broad background within the spectrum due to self-fluorescence of the sample.

Rb₃WO₄H**Table S31.** Vibrational Raman data of Rb₃WO₄H obtained by quantum chemical calculations.

Simulated Raman data on Rb ₃ WO ₄ H			
Frequency (cm ⁻¹)	Γ_{irrep}	Intensity (arbitrary units)	Assignment
26 - 146	-	> 20	Lattice vibrations
307	B _{3g}	14	WO ₄ ²⁻ antisymmetric bending (ν_4)
309	B _{1g}	31	WO ₄ ²⁻ antisymmetric bending (ν_4)
311	A _g	15	WO ₄ ²⁻ antisymmetric bending (ν_4)
313	B _{2g}	30	WO ₄ ²⁻ antisymmetric bending (ν_4)
314	B _{3g}	25	WO ₄ ²⁻ antisymmetric bending (ν_4)
315	B _{1g}	101	WO ₄ ²⁻ antisymmetric bending (ν_4)
316	A _g	11	WO ₄ ²⁻ antisymmetric bending (ν_4)
317	B _{2g}	7	WO ₄ ²⁻ antisymmetric bending (ν_4)
320	B _{2g}	28	WO ₄ ²⁻ antisymmetric bending (ν_4)
323	B _{2g}	485	WO ₄ ²⁻ symmetric bending (ν_2)
323	B _{3g}	5	WO ₄ ²⁻ symmetric bending (ν_2)
324	A _g	67	WO ₄ ²⁻ symmetric bending (ν_2)
324	B _{3g}	22	WO ₄ ²⁻ symmetric bending (ν_2)
325	B _{1g}	9	WO ₄ ²⁻ antisymmetric bending (ν_4)
330	B _{3g}	212	WO ₄ ²⁻ symmetric bending (ν_2)
333	B _{1g}	188	WO ₄ ²⁻ symmetric bending (ν_2)
334	A _g	198	WO ₄ ²⁻ symmetric bending (ν_2)
338	B _{2g}	23	WO ₄ ²⁻ symmetric bending (ν_2)
340	A _g	210	WO ₄ ²⁻ symmetric bending (ν_2)
347	B _{1g}	25	WO ₄ ²⁻ symmetric bending (ν_2)
585	A _g	4	Parallel vertical hydride vibrations
588	B _{1g}	24	Parallel vertical hydride vibrations
660	B _{3g}	0	Diagonal hydride vibrations
675	B _{2g}	2	Parallel vertical hydride vibrations
715	A _g	2	Parallel horizontal hydride vibrations
724	B _{3g}	0	Diagonal horizontal hydride vibrations
725	A _g	9	Parallel horizontal hydride vibrations
727	B _{3g}	1	Diagonal horizontal hydride vibrations
770	B _{1g}	1	Antiparallel vertical hydride vibrations
779	B _{2g}	0	Antiparallel horizontal hydride vibrations
804	B _{2g}	1	Hydride symmetric vibrations
810	B _{1g}	15	Hydride symmetric vibrations
821	A _g	121	WO ₄ ²⁻ antisymmetric stretching (ν_3)
822	B _{2g}	9	WO ₄ ²⁻ antisymmetric stretching coupled with symmetric hydride vibrations (ν_{3H})
825	B _{1g}	7	WO ₄ ²⁻ antisymmetric stretching coupled with symmetric hydride vibrations (ν_{3H})
827	A _g	84	WO ₄ ²⁻ antisymmetric stretching (ν_3)
837	B _{3g}	34	WO ₄ ²⁻ antisymmetric stretching (ν_3)
844	A _g	10	WO ₄ ²⁻ antisymmetric stretching (ν_3)
853	B _{3g}	0	WO ₄ ²⁻ antisymmetric stretching coupled with parallel vertical hydride vibrations (ν_{3H})
861	B _{1g}	29	WO ₄ ²⁻ antisymmetric stretching coupled with parallel vertical hydride vibrations (ν_{3H})
869	B _{2g}	9	WO ₄ ²⁻ antisymmetric stretching coupled with diagonal vertical hydride vibrations (ν_{3H})
877	B _{1g}	24	WO ₄ ²⁻ antisymmetric stretching coupled with diagonal vertical hydride vibrations (ν_{3H})
879	B _{3g}	61	WO ₄ ²⁻ antisymmetric stretching (ν_3)
882	B _{2g}	10	WO ₄ ²⁻ antisymmetric stretching coupled with diagonal vertical hydride vibrations (ν_{3H})
930	A _g	1000	WO ₄ ²⁻ symmetric stretching (ν_1)
931	B _{2g}	0	WO ₄ ²⁻ symmetric stretching (ν_1)
931	B _{1g}	1	WO ₄ ²⁻ symmetric stretching (ν_1)
932	B _{3g}	0	WO ₄ ²⁻ symmetric stretching (ν_1)

Hydride vibrations along the crystallographic a/b-plane are defined as vertical hydride vibrations whereas vibrations along the a/c-axis are defined as horizontal vibrations.

2.8 Elemental Analysis

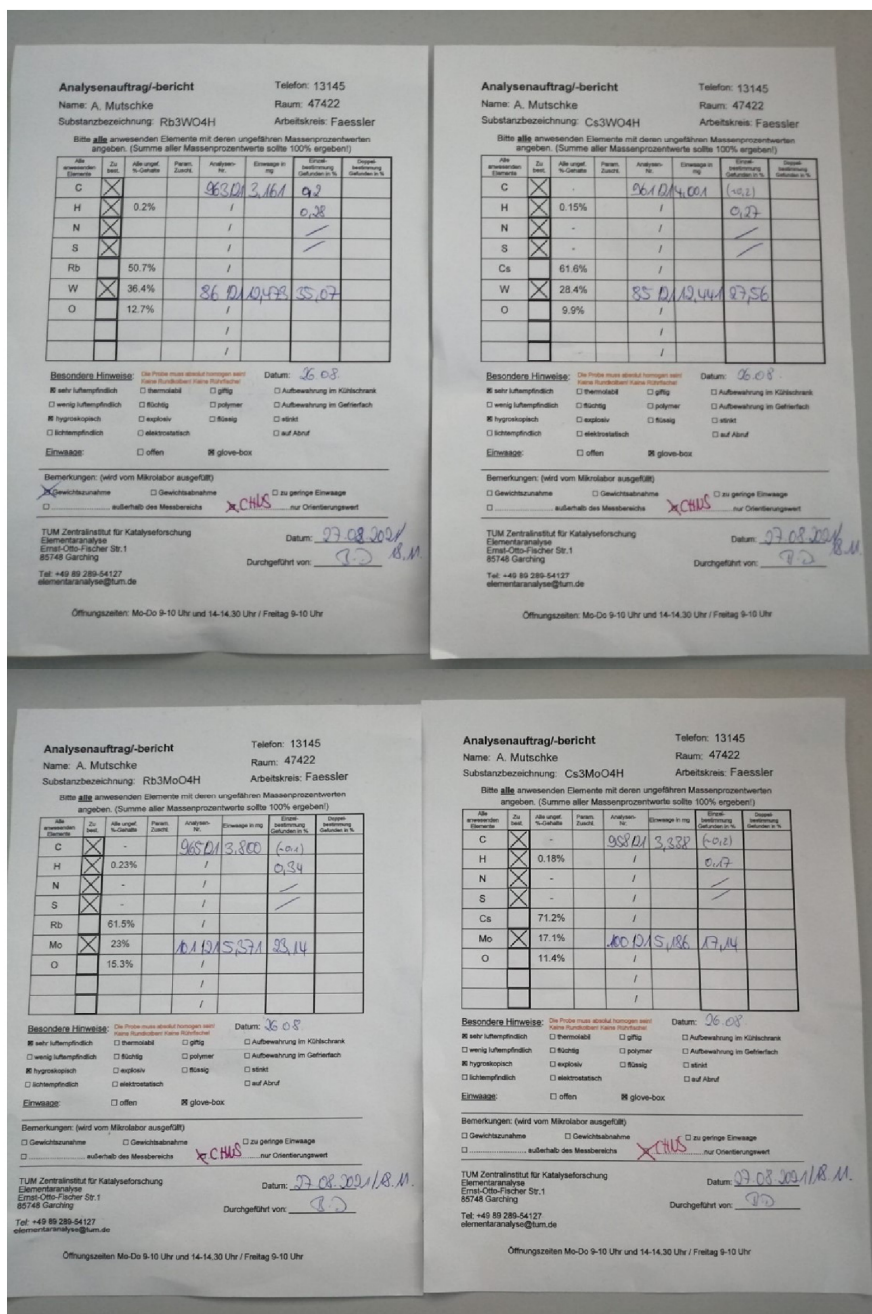


Figure S28. Elemental analysis reports of the four hydric compounds.

2.9 Optimized crystal structures as CIF (DFT-PBE0)

```

data_Rb3MoO4H
_audit_creation_method FINDSYM

_cell_length_a 7.8499197535
_cell_length_b 7.8499197535
_cell_length_c 12.4512660437
_cell_angle_alpha 90.0000000000
_cell_angle_beta 90.0000000000
_cell_angle_gamma 90.0000000000

_symmetry_space_group_name_H-M "T 4/m 2/c 2/m"
_symmetry_Int_Tables_number 140
_space_group.reference_setting '140:-I 4 2c'
_space_group.transform_Pp_abc a,b,c;0,0,0

loop_
_space_group_symop_id
_space_group_symop_operation_xyz
1 x,y,z
2 x,-y,-z+1/2
3 -x,y,-z+1/2
4 -x,-y,z
5 -y,-x,-z+1/2
6 -y,x,z
7 y,-x,z
8 y,x,-z+1/2
9 -x,-y,-z
10 -x,y,z+1/2
11 x,-y,z+1/2
12 x,y,-z
13 y,x,z+1/2
14 y,-x,-z
15 -y,x,-z
16 -y,-x,z+1/2
17 x+1/2,y+1/2,z+1/2
18 x+1/2,-y+1/2,-z
19 -x+1/2,y+1/2,-z
20 -x+1/2,-y+1/2,z+1/2
21 -y+1/2,-x+1/2,-z
22 -y+1/2,x+1/2,z+1/2
23 y+1/2,-x+1/2,z+1/2
24 y+1/2,x+1/2,-z
25 -x+1/2,-y+1/2,-z+1/2
26 -x+1/2,y+1/2,z
27 x+1/2,-y+1/2,z
28 x+1/2,y+1/2,-z+1/2
29 y+1/2,x+1/2,z
30 y+1/2,-x+1/2,-z+1/2
31 -y+1/2,x+1/2,-z+1/2
32 -y+1/2,-x+1/2,z

loop_
_atom_site_label
_atom_site_type_symbol
_atom_site_symmetry_multiplicity
_atom_site_Wyckoff_label
_atom_site_fract_x
_atom_site_fract_y
_atom_site_fract_z
_atom_site_occupancy
Mo1 Mo 4 b 0.00000 0.50000 0.25000 1.00000
Rb1 Rb 8 h 0.18599 0.68599 0.00000 1.00000
Rb2 Rb 4 a 0.00000 0.00000 0.25000 1.00000
O1 O 16 l 0.62870 0.12870 0.16569 1.00000
H1 H 4 c 0.00000 0.00000 0.00000 1.00000

# end of cif

data_Cs3MoO4H
_audit_creation_method FINDSYM

_cell_length_a 8.2190168880
_cell_length_b 8.2190168880

```



```
_cell_length_c 12.9251378714
_cell_angle_alpha 90.0000000000
_cell_angle_beta 90.0000000000
_cell_angle_gamma 90.0000000000

_symmetry_space_group_name_H-M "I 4/m 2/c 2/m"
_symmetry_Int_Tables_number 140
_space_group.reference_setting '140:-I 4 2c'
_space_group.transform_Pp_abc a,b,c;0,0,0

loop_
_space_group_symop_id
_space_group_symop_operation_xyz
1 x,y,z
2 x,-y,-z+1/2
3 -x,y,-z+1/2
4 -x,-y,z
5 -y,-x,-z+1/2
6 -y,x,z
7 y,-x,z
8 y,x,-z+1/2
9 -x,-y,-z
10 -x,y,z+1/2
11 x,-y,z+1/2
12 x,y,-z
13 y,x,z+1/2
14 y,-x,-z
15 -y,x,-z
16 -y,-x,z+1/2
17 x+1/2,y+1/2,z+1/2
18 x+1/2,-y+1/2,-z
19 -x+1/2,y+1/2,-z
20 -x+1/2,-y+1/2,z+1/2
21 -y+1/2,-x+1/2,-z
22 -y+1/2,x+1/2,z+1/2
23 y+1/2,-x+1/2,z+1/2
24 y+1/2,x+1/2,-z
25 -x+1/2,-y+1/2,-z+1/2
26 -x+1/2,y+1/2,z
27 x+1/2,-y+1/2,z
28 x+1/2,y+1/2,-z+1/2
29 y+1/2,x+1/2,z
30 y+1/2,-x+1/2,-z+1/2
31 -y+1/2,x+1/2,-z+1/2
32 -y+1/2,-x+1/2,z

loop_
_atom_site_label
_atom_site_type_symbol
_atom_site_symmetry_multiplicity
_atom_site_Wyckoff_label
_atom_site_fract_x
_atom_site_fract_y
_atom_site_fract_z
_atom_site_occupancy
Mo1 Mo 4 b 0.00000 0.50000 1.00000
Cs1 Cs 8 h 0.18530 0.68530 0.00000 1.00000
Cs2 Cs 4 a 0.00000 0.00000 0.25000 1.00000
O1 O 16 l 0.62336 0.12336 0.16911 1.00000
H1 H 4 c 0.00000 0.00000 0.00000 1.00000

# end of cif

data_Cs3WO4H
_audit_creation_method FINDSYM

_cell_length_a 8.2391299711
_cell_length_b 8.2391299711
_cell_length_c 12.8404999808
_cell_angle_alpha 90.0000000000
_cell_angle_beta 90.0000000000
_cell_angle_gamma 90.0000000000

_symmetry_space_group_name_H-M "I 4/m 2/c 2/m"
_symmetry_Int_Tables_number 140
```

```

_space_group.reference_setting '140:-I 4 2c'
_space_group.transform_Pp_abc a,b,c;0,0,0

loop_
_space_group_symop_id
_space_group_symop_operation_xyz
1 x,y,z
2 x,-y,-z+1/2
3 -x,y,-z+1/2
4 -x,-y,z
5 -y,-x,-z+1/2
6 -y,x,z
7 y,-x,z
8 y,x,-z+1/2
9 -x,-y,-z
10 -x,y,z+1/2
11 x,-y,z+1/2
12 x,y,-z
13 y,x,z+1/2
14 y,-x,-z
15 -y,x,-z
16 -y,-x,z+1/2
17 x+1/2,y+1/2,z+1/2
18 x+1/2,-y+1/2,-z
19 -x+1/2,y+1/2,-z
20 -x+1/2,-y+1/2,z+1/2
21 -y+1/2,-x+1/2,-z
22 -y+1/2,x+1/2,z+1/2
23 y+1/2,-x+1/2,z+1/2
24 y+1/2,x+1/2,-z
25 -x+1/2,-y+1/2,-z+1/2
26 -x+1/2,y+1/2,z
27 x+1/2,-y+1/2,z
28 x+1/2,y+1/2,-z+1/2
29 y+1/2,x+1/2,z
30 y+1/2,-x+1/2,-z+1/2
31 -y+1/2,x+1/2,-z+1/2
32 -y+1/2,-x+1/2,z

loop_
_atom_site_label
_atom_site_type_symbol
_atom_site_symmetry_multiplicity
_atom_site_Wyckoff_label
_atom_site_fract_x
_atom_site_fract_y
_atom_site_fract_z
_atom_site_occupancy
W1 W 4 b 0.00000 0.50000 0.25000 1.00000
Cs1 Cs 8 h 0.18892 0.68892 0.00000 1.00000
Cs2 Cs 4 a 0.00000 0.00000 0.25000 1.00000
O1 O 16 l 0.62510 0.12510 0.16680 1.00000
H1 H 4 c 0.00000 0.00000 0.00000 1.00000

# end of cif

data_Rb3WO4H
_audit_creation_method FINDSYM

_cell_length_a 11.9743502500
_cell_length_b 11.4712919800
_cell_length_c 11.5041410900
_cell_angle_alpha 90.0000000000
_cell_angle_beta 90.0000000000
_cell_angle_gamma 90.0000000000

_symmetry_space_group_name_H-M "P 21/b 21/c 21/a"
_symmetry_Int_Tables_number 61
_space_group.reference_setting '061:-P 2ac 2ab'
_space_group.transform_Pp_abc a,b,c;0,0,0

loop_
_space_group_symop_id
_space_group_symop_operation_xyz
1 x,y,z

```

```
2 x+1/2,-y+1/2,-z
3 -x,y+1/2,-z+1/2
4 -x+1/2,-y,z+1/2
5 -x,-y,-z
6 -x+1/2,y+1/2,z
7 x,-y+1/2,z+1/2
8 x+1/2,y,-z+1/2

loop_
_atom_site_label
_atom_site_type_symbol
_atom_site_symmetry_multiplicity
_atom_site_Wyckoff_label
_atom_site_fract_x
_atom_site_fract_y
_atom_site_fract_z
_atom_site_occupancy
W1 W 8 c 0.74991 0.00791 -0.01757 1.00000
Rb1 Rb 8 c 0.74671 0.22901 0.72928 1.00000
Rb2 Rb 8 c 0.00202 0.78349 -0.00761 1.00000
Rb3 Rb 8 c 0.00245 -0.00693 0.71810 1.00000
O1 O 8 c 0.86839 -0.02153 0.07208 1.00000
O2 O 8 c 0.78097 -0.02617 0.83424 1.00000
O3 O 8 c 0.71730 0.15992 -0.00939 1.00000
O4 O 8 c 0.63217 -0.07532 0.02845 1.00000
H1 H 8 c 0.50535 0.75489 0.25699 1.00000

# end of cif
```

3 Literature

- [1] J. Rodríguez-Carvajal, *Physica B* **1993**, *192*, 55.
- [2] J. Tauc, R. Grigorovici, A. Vanacu, *Phys. Status Solidi* **1966**, *15*, 627.
- [3] R. Dovesi, A. Erba, R. Orlando, C. M. Zicovich-Wilson, B. Civalleri, L. Maschio, M. Rérat, S. Casassa, J. Baima, S. Salustro et al., *Wiley Interdiscip. Rev.-Comput. Mol. Sci.* **2018**, *8*.
- [4] Perdew, Burke, Ernzerhof, *Phys. Rev. Lett.* **1996**, *77*, 3865.
- [5] C. Adamo, V. Barone, *J. Chem. Phys.* **1999**, *110*, 6158.
- [6] F. Weigend, R. Ahlrichs, *Phys. Chem. Chem. Phys.* **2005**, *7*, 3297.
- [7] a) R. E. Stene, B. Scheibe, A. J. Karttunen, W. Petry, F. Kraus, *Eur. J. Inorg. Chem.* **2019**, *2019*, 3672; b) R. E. Stene, B. Scheibe, A. J. Karttunen, W. Petry, F. Kraus, *Eur. J. Inorg. Chem.* **2020**, *2020*, 2260; c) A. J. Karttunen, T. Tynell, M. Karppinen, *J. Phys. Chem. C* **2015**, *119*, 13105.
- [8] H. J. Monkhorst, J. D. Pack, *Phys. Rev. B* **1976**, *13*, 5188.
- [9] a) F. Pascale, C. M. Zicovich-Wilson, F. López Gejo, B. Civalleri, R. Orlando, R. Dovesi, *J. Comput. Chem.* **2004**, *25*, 888; b) C. M. Zicovich-Wilson, F. Pascale, C. Roetti, V. R. Saunders, R. Orlando, R. Dovesi, *J. Comput. Chem.* **2004**, *25*, 1873; c) L. Maschio, B. Kirtman, M. Rérat, R. Orlando, R. Dovesi, *J. Chem. Phys.* **2013**, *139*, 164101.
- [10] a) S. J. Clark, M. D. Segall, C. J. Pickard, P. J. Hasnip, M. I. J. Probert, K. Refson, M. C. Payne, *Z. Kristallogr. – Cryst. Mater.* **2005**, *220*, 567; b) C. J. Pickard, F. Mauri, *Phys. Rev. B* **2001**, *63*; c) J. R. Yates, C. J. Pickard, F. Mauri, *Phys. Rev. B* **2007**, *76*.
- [11] Vanderbilt, *Phys. Rev. B* **1990**, *41*, 7892.
- [12] R. D. Shannon, *Acta Cryst. A* **1976**, *32*, 751.
- [13] P. F. Lang, B. C. Smith, *Dalton Trans.* **2010**, *39*, 7786.
- [14] K. Momma, F. Izumi, *J. Appl. Crystallogr.* **2011**, *44*, 1272.
- [15] Y. Hinuma, G. Pizzi, Y. Kumagai, F. Oba, I. Tanaka, *Band structure diagram paths based on crystallography*, **2016**.
- [16] A. Togo, I. Tanaka **2018**, arXiv:1808.01590v1.
- [17] Y. Hinuma, G. Pizzi, Y. Kumagai, F. Oba, I. Tanaka, *Comput. Mater. Sci.* **2017**, *128*, 140.

8 List of Publications

Published and submitted articles in peer reviewed journals

[6] S. L. Wandelt, A. Karnas, **A. Mutschke**, N. Kunkel, C. Ritter, W. Schnick*, Strontium Nitridoborate Hydride $\text{Sr}_2\text{BN}_2\text{H}$, verified by Single Crystal X-ray and Neutron Powder Diffraction, *submitted*.

[5] **A. Mutschke***, A. Schulz, M. Bertmer, C. Ritter, A. J. Karttunen, G. Kieslich, N. Kunkel*, Expanding the hydride chemistry: antiperovskites $A_3\text{MO}_4\text{H}$ ($A = \text{Rb}, \text{Cs}; M = \text{Mo}, \text{W}$) introducing the transition oxometalate hydrides, *Chem. Sci.* **2022**, *13*, 7773-7779, highlighted as *Chem. Sci. Pick of the Week*.

[4] **A. Mutschke**, Th. Wylezich, A. D. Sontakke, M. Hoelzel, A. Meijerink, N. Kunkel*, $\text{M}\text{CaH}_x\text{F}_{3-x}$ ($M = \text{Rb}, \text{Cs}$): Synthesis, Structure, and Bright, Site-Sensitive Tunable Eu^{2+} Luminescence. *Adv. Optical Mater.* **2021**, *9*, 2002052 (10 pages)

[3] **A. Mutschke**, G. M. Bernard, M. Bertmer, A. J. Karttunen, C. Ritter, V. K. Michaelis, N. Kunkel*, $\text{Na}_3\text{SO}_4\text{H}$ – The First Representative of the Material Class of Sulfate Hydrides, *Angew. Chem. Int. Ed.* **2021**, *60*, 5683-5687

[3] **A. Mutschke**, G. M. Bernard, M. Bertmer, A. J. Karttunen, C. Ritter, V. K. Michaelis, N. Kunkel*, $\text{Na}_3\text{SO}_4\text{H}$ – ein erster Vertreter der Materialklasse der Sulfathydride, *Angew. Chem.* **2021**, *133*, 5747-5751

[2] Th. Wylezich, R. Valois, M. Suta, **A. Mutschke**, C. Ritter, A. Meijerink, A. J. Karttunen, N. Kunkel*, Borate Hydrides as a New Material Class – Structure, Computational Studies and Spectroscopic Investigations on $\text{Sr}_5(\text{BO}_3)_3\text{H}$ and $\text{Sr}_5(^{11}\text{BO}_3)_3\text{D}$, *Chem. Eur. J.* **2020**, *51*, 11742-11750

[1] **A. Mutschke**, Th. Wylezich, C. Ritter, A. Karttunen, N. Kunkel* An unprecedented fully H-Substituted Phosphate Hydride $\text{Sr}_5(\text{PO}_4)_3\text{H}$ Expanding the Apatite Family, *Eur. J. Inorg. Chem.* **2019**, *2019*, 5073-5076

*Corresponding authors

Presentations

[3] $\text{Na}_3\text{SO}_4\text{H}$ – a unique anion combination, ATUMS Annual Meeting, 08.-12.11.2021, Online

[2] Materials design by hydride substitution and hydrogenation reactions, ATUMS Annual Meeting, 9.-13.11.2020, Online

[1] New mixed anionic hydrides and (de)hydrogenation reactions as a materials preparation tool, ATUMS Annual Meeting, 10.-15.11.2019, Canmore, Canada

Poster contributions

[2] **Alexander Mutschke**, Thomas Wylezich, Nathalie Kunkel “Expansion of the hydride chemistry – new materials based on mixed anionic hydrides”, 30th annual meeting of the German crystallographic society (DGK), 14.-17.3.2022, Munich (online)

[1] Samuel Merk, **Alexander Mutschke**, Thomas F. Fässler, “Fast Lithium-Ion Conduction in the Hydride $\text{Li}_3(\text{NH}_2)_2\text{I}_{1-x}(\text{BH}_4)_x$ ($0 \leq x \leq 0.3$)”, 11th Energy Colloquium of the Munich School of Engineering, 28-29.7.2021, Garching

Press release

“When hydrogen glows red” – MLZ, 28.06.2021

<https://mlz-garching.de/englisch/news-und-press/news-articles/when-hydrogen-glows-red.ht>

9 List of Figures

- Figure 1.1.** A covalently bonded metal hydride MH_4 (left) with M consisting of a main group (semi)metal. In contrast on the right: an interstitial metal hydride. TM is equal to a transition or lanthanide metal. In this exemplification the hydrogen atoms are incorporated in the *ccp* of the transition metal atoms. The tetrahedra sites (blue) are fully occupied and the octahedra sites (lime) are statistically occupied by approx. 25% (partially filled spheres), resulting in a non-stoichiometric hypothetical sum formula of $TMH_{2.25}$ 2
- Figure 1.2** Rock salt-type LiH (left) consisting of Li^+ and H^- ions as an example for an ionic, salt-like hydride. A complex hydride $LiBH_4$ (right) with molecular BH_4^- units next to Li^+ ions as an example of a complex hydride. 3
- Figure 1.3** Schematic of the bonding situation in salt-like hydrides. Left: pure ionic interaction; middle: the polarized hydride ion with partially charged domains and right: covalent interaction between the metal and hydride with negative and positive partial charges..... 4
- Figure 1.4.** Crystal structure of the transition metal containing oxide hydride $LaSrCoH_{0.7}O_3$. The coordination sphere of hydride is depicted as a grey octahedron..... 6
- Figure 1.5.** Crystal structure of Ca_2HN with the penetrating Ca-supertetrahedra. The coordination sphere of hydride is depicted as a grey octahedron, nitride in light blue. 7
- Figure 1.6.** Crystal structure of Ba_3AlO_4H . The silicate ions are depicted as blue tetrahedra, HBa_6 octahedra are depicted grey. 8
- Figure 1.7.** Crystal structure of $LiSr_2SiO_4H$ 9
- Figure 1.8.** Crystal structures of $Sr_5(PO_4)_3H$ with lilac phosphate tetrahedra (left) and $Sr_5(BO_3)_3H$ with trigonal planar olive borate ions (right). The coordination sphere of hydride is shown as colourless trigonal planar species respectively. 10
- Figure 1.9.** Crystal structure of Ca_2BN_2H . HCa_4 tetrahedra are illustrated grey..... 10
- Figure 1.10.** Crystal structures of $Ca_6Cr_2N_6H$ (left) and Ba_3CrN_3H (right). The coordination sphere of hydrogen is depicted as grey polyhedra respectively. $[Cr_2N_6]^{11-}$ ions are light blue, $[CrN_3]^{5-}$ ions are shown as colourless, trigonal planar units. 11
- Figure 1.11.** Crystal structure of the ideal cubic perovskite structure with AX_{12} cuboctahedron (light blue) and BX_6 octahedron (grey). 12

- Figure 1.12.** Left: orthorhombic perovskite structure (FeGdO₃-type) in the space group *Pnma* (62) and right: a tetragonal perovskite structure in the SrZrO₃-type (*I4/mcm*, 140). 13
- Figure 1.13.** Left: 6H-stacking polytype perovskite *P6₃/mmc* (194), right: 9R-stacking polytype perovskite *R3m* (166). The hexagonal und cubic close packing layers are marked with *h* and *c* respectively. 14
- Figure 1.14.** Crystal structure of tetragonal antiperovskites with complex anions. Left tetragonal K₃(SO₄)F-type (*I4/mcm*, 140), right tetragonal Ag₃CrO₄Cl-type (*P4/nmm*, 129, O2). The complex anions are depicted as blue tetrahedra. The colour codes are kept identical to the normal perovskite structure, illustrating the analogy of the octahedra. 15
- Figure 1.15.** Crystal structure of the mineral Kogarkoite, Na₃SO₄F, space group *P2₁/m* (11), depicted as a 4x4 supercell to point out the 9R-stacking perovskite polytype analogy. SO₄²⁻ tetrahedra are depicted yellow, FNa₆ octahedra purple. 16
- Figure 1.16.** A macroscopic depiction of a luminescent particle (left) and the detailed luminescence process arising in the activator ion depicted as configurational coordinate diagram (right), modified after^[149]. 17
- Figure 1.17** a) configurational coordinate diagram of *f-f* transitions; b) configurational coordinate diagram of *d-f* transitions. 18
- Figure 1.18.** Configurational coordinate diagram of an anomalous luminescence process of Eu²⁺ according to^[154]. 19
- Figure 1.19.** Formation of an impurity trapped exciton with a Eu³⁺ centre according to^[154]. 20
- Figure 1.20.** Schematic illustration of the contributions to the energetic level of the 4*f*⁶5*d*¹ state in transitions of Eu²⁺. An octahedral coordination sphere of Eu²⁺ is illustrated to demonstrate the crystal field splitting effect. Energy levels are not representative of realistic energy levels. 21
- Figure 1.21.** Energy transfer (E.T.) process in a luminescent particle between S and A with a distance R; b) spectral overlap between the emission *g*S (E) of the sensitizer and the absorption *g*A (E) of the activator; c) energy level schemes of the involved states according to^[149]. 22
- Figure 1.22.** Typical decay curves on a logarithmic scale with an exponential decay (1) and a decay curve influenced by energy transfers (2). 23
- Figure 2.1.** Picture of an encapsulated and sealed Ni-alloy ampule, ready to be placed in an oven. Stone wool is placed as buffer between the quartz glass and the ampule. 26
- Figure 2.2** Annealing temperature program for the hardening process of the autoclaves. 27

Figure 2.3. Picture of the disassembled autoclave (left) for reactions under hydrogen pressure. The assembled autoclave with the crucibles and reactants inside is depicted in the middle, ready to be loaded with hydrogen pressure. The hydrogen-loaded autoclave, placed in a tube furnace with stone wool for isolation is depicted on the right. A burst protection is adjusted in front. 28

Figure 2.4. Tungsten carbide (grey) and zirconium dioxide (yellow) beakers with 10 balls each for mechanochemical reactions. Placed beaker in the planetary mill, ready to be started. 28

Figure 3.1. X-ray diffraction patterns of $\text{RbCaH}_x\text{F}_{3-x}$ and the refined cell parameters a plotted in dependency of the hydride content x in the mixed phase. Background reflections caused by the grease to fixate the samples within the capton foils are marked with an asterisk. 36

Figure 3.2. X-ray diffraction patterns of $\text{CsCaH}_x\text{F}_{3-x}$ and the refined cell parameters a plotted in dependency of the hydride content x in the mixed phase. Background reflections caused by the grease to fixate the samples within the capton foils are marked with an asterisk, reflections originating from Cs_2CaH_4 are marked with a rhombus. 37

Figure 3.3. Rietveld refinement plot of $\text{CsCaD}_{1.5}\text{F}_{1.5}$ based on co-refinement of neutron and X-ray diffraction data. Bragg markers from top to bottom: $\text{CsCaD}_{1.5}\text{F}_{1.5}$ (97.04(7) wt%), CaD_2 , (2.15(9) wt%), CaO (0.43(20) wt%), CaF_2 (0.39(22) wt%). $R_p = 5.10\%$, $R_{wp} = 6.53\%$, $R_{\text{Bragg}} = 3.15\%$, $X^2 = 4.97$ 38

Figure 3.4. Pictures of encapsulated samples of $\text{CsCaH}_x\text{F}_{3-x}:\text{Eu}^{2+}$ ($x \leq 2.5$). Top shows the ampoules under daylight and the bottom picture the corresponding luminescence upon 376 nm UV irradiation. From left to right: $x = 0, 0.25, 0.5, 0.75, 1.0, 1.5, 2.0$, and 2.5 39

Figure 3.5. PL spectra of $\text{CsCaH}_x\text{F}_{3-x}:\text{Eu}^{2+}$ at an excitation wavelength of 380 nm. 39

Figure 3.6. Decay curves of $\text{CsCaH}_x\text{F}_{3-x}:\text{Eu}^{2+}$ monitored at several emission maxima wavelengths with excitation wavelength of 375 nm. Whereas $\text{CsCaF}_3:\text{Eu}^{2+}$ shows a monoexponential behaviour, the decay curves of monitored emission bands of the mixed phases deviate from a monoexponential behaviour. 40

Figure 3.7. a) and b): PL spectra of $\text{CsCaH}_2\text{F}:\text{Eu}^{2+}$ with several different dopant concentrations (0.5 mol%, 1 mol% and 10 mol% in respect to Ca^{2+}). Arrows mark the intensity change of the emission bands with increasing dopant concentrations. c) monitored decay curves of different emission bands of the samples with varying dopant concentrations. The colour codes are kept the same as depicted for the PL spectra. 41

Figure 3.8. PL and PLE spectra of $\text{CsCaH}_2\text{F}:\text{Eu}^{2+}$ prepared by both dopant methods in comparison to the PL and PLE spectrum of $\text{CsCaH}_2\text{F}:\text{Eu}^{2+}$ doped with 10 mol% Eu^{2+} . The arrow marks the vanishing emission band. 42

- Figure 4.1.** p-XRD patterns of the synthesis products with the respective set autoclave temperatures. The vertical bars represent simulated Bragg reflections: blue $\text{Na}_3\text{SO}_4\text{H}$, red Na_2SO_4 (*Cmcm*) and green Na_2S 44
- Figure 4.2** Crystal structure of $\text{Na}_3\text{SO}_4\text{H}$. Simplistic unit cell with ellipsoids (90% probability) left and depiction with Na_6H octahedra as an antiperovskite-like structure right. Sulfate tetrahedra are depicted yellow. 44
- Figure 4.3.** Rietveld refinement of $\text{Na}_3\text{SO}_4\text{D}$. Diffraction data acquired at the D2B at the ILL. Bragg markers from top to bottom $\text{Na}_3\text{SO}_4\text{D}$ (92.2(9) wt.%), Na_2SO_4 (*Cmcm*) (6.3(7) wt.%), NaD (1.5(2) wt.%). $R_p = 1.70\%$ $R_{wp} = 3.63\%$, $R_{exp} = 3.63\%$, $\chi^2 = 1.00$ 45
- Figure 4.4.** Left: FT-IR spectra of $\text{Na}_3\text{SO}_4\text{H}$ and $\text{Na}_3\text{SO}_4\text{D}$ with simulated spectra (DFT-PBE0 level of theory) below. Right: Raman spectra of $\text{Na}_3\text{SO}_4\text{H}$ and $\text{Na}_3\text{SO}_4\text{D}$ with the corresponding simulated spectra (DFT-PBE0 level of theory) below. 46
- Figure 4.5.** a) Room temperature ^1H MAS NMR spectrum of $\text{Na}_3\text{SO}_4\text{H}$, acquired with a spinning frequency of 10.0 kHz, $B_0 = 9.4$ T, b) ^{23}Na NMR spectrum of $\text{Na}_3\text{SO}_4\text{H}$, the deconvolution is traced in blue below the experimental spectrum. 47
- Figure 4.6.** Electronic band structure of $\text{Na}_3\text{SO}_4\text{H}$ and projected density of states at the DFT-PBE0 level of theory. 48
- Figure 4.7.** p-XRD pattern of $\text{Rb}_3\text{MoO}_4\text{H}$ obtained after a synthesis attempt at too high reaction temperatures. The vertical bars represent simulated Bragg reflections: red $\text{Rb}_3\text{MoO}_4\text{H}$, blue Molybdenum and green RbH . Asterisks mark a further not assignable side phase. 51
- Figure 4.8.** p-XRD pattern of $\text{Cs}_3\text{MoO}_4\text{H}$ obtained after a synthesis attempt at a too low reaction temperature. The vertical bars represent simulated Bragg reflections of the indexable compounds: red $\text{Cs}_3\text{MoO}_4\text{H}$, blue Cs_2MoO_4 , and green CsH 51
- Figure 4.9.** p-XRD pattern of $\text{Rb}_3\text{WO}_4\text{H}$ obtained after a synthesis attempt at a too high reaction temperature. The vertical bars represent simulated Bragg reflections of $\text{Rb}_3\text{WO}_4\text{H}$, asterisks marks unassignable impurities. 52
- Figure 4.10.** Schematic of the tetragonal phases with the $\text{K}_3\text{SO}_4\text{F}$ structure type along the *c*-axis (left) and *a/b*-plane (right). A_6H octahedra are depicted lilac, the oxometalate tetrahedral orange. 53
- Figure 4.11.** Crystal structure of $\text{Rb}_3\text{WO}_4\text{H}$ in *a*-direction (left) and *b*-direction (right). HRb_6 octahedra are depicted lilac, tungstate tetrahedra orange. 54
- Figure 4.12.** Experimental Raman spectra of the tetragonal crystallizing phases with the respective simulated spectra (DFT-PBE0 level of theory) depicted below. 56

- Figure 4.13.** Experimental Raman spectrum of $\text{Rb}_3\text{WO}_4\text{H}$ with the simulated spectrum (DFT-PBE0 level of theory) depicted below. 56
- Figure 4.14.** Room temperature ^2H MAS NMR spectra of the four phases. The spectra were acquired with spinning frequencies of 5 kHz and a magnetic field strength of $B_0 = 17.6$ T.... 57
- Figure 4.15.** Electronic band structure of the tetragonal phases with the respective projected density of states at the DFT-PBE0 level of theory. a) $\text{Rb}_3\text{MoO}_4\text{H}$, b) $\text{Cs}_3\text{MoO}_4\text{H}$ and c) $\text{Cs}_3\text{WO}_4\text{H}$ 58
- Figure 4.16.** Tauc-plot of $\text{Cs}_3\text{WO}_4\text{H}$ determined by UV-VIS absorption spectroscopy. The blue vertical dashed lines indicate the region considered for the linear fit. A direct band gap of 3.66 eV is determined and matches the predicted band gap of 3.56 eV..... 59
- Figure 4.17.** Electronic band structure of $\text{Rb}_3\text{WO}_4\text{H}$ with the projected density of states at the DFT-PBE0 level of theory..... 59
- Figure 4.18.** Temperature dependent p-XRD patterns of $\text{Rb}_3\text{WO}_4\text{H}$. Individual patterns were measured in 20 K steps. Arrows mark emerging and diminishing differences between the RT and low temperature phase patterns..... 60
- Figure 4.19.** Left: contour plot of the temperature dependent X-ray diffraction data of $\text{Rb}_3\text{WO}_4\text{H}$. The approximate phase transition region is marked with a dashed line. Right: DSC curve with the peaks corresponding to the low temperature phase transitions. 61
- Figure 4.20.** Comparison of the low temperature phase p-XRD pattern (left) with the RT p-XRD pattern (right). Due to Rb-fluorescence, a large background is visible. 61
- Figure 4.21.** Rietveld refinement plot of $\text{Rb}_3\text{WO}_4\text{D}$ based on neutron data collected from the D2B ILL at 4K. $R_p = 8.17\%$, $R_{wp} = 9.98\%$, $R_{exp} = 0.86\%$, $\chi^2 = 136$ 62
- Figure 4.22.** P-XRD measurement of the sample obtained by the attempted synthesis of $\text{K}_3\text{MoO}_4\text{H}$. Vertical red bars resemble simulated Bragg reflections of a structure adapted from rhombohedral $\text{Na}_3\text{SO}_4\text{F}$. Asterisks mark molybdenum reflections. Rhombuses mark unknown reflections. 63
- Figure 4.23.** Rietveld refinement plot of $\text{K}_3\text{MoO}_4\text{H}$. Greyed-out areas were cut out during refinement. $R_p = 12.4\%$, $R_{wp} = 16.5\%$, $R_{exp} = 1.24\%$, $\chi^2 = 178$ 64
- Figure 4.24.** Left: proposed crystal structure of $\text{K}_3\text{MoO}_4\text{H}$. Right: depiction as antiperovskite with HK_6 octahedra in lilac and molybdate ions in orange. 64
- Figure 11.1.** Rietveld refinement plot of RbCaHF_2 . $R_p = 2.00\%$, $R_{wp} = 3.04\%$, $R_{Bragg} = 1.68\%$, $R_{exp} = 2.38\%$, $\chi^2 = 1.63$ 187

Figure 11.2. Rietveld refinement plot of the attempted synthesis of CsCaH₃. Bragg markers from top to bottom: CsCaH₃ (31.6(4) wt%), Cs₂CaH₄ (45.6(5) wt%), and CaH₂ (22.8(4) wt%). $R_p = 4.05\%$, $R_{wp} = 5.94\%$, $R_{Bragg} = 3.70\%$, $R_{exp} = 3.91\%$, $\chi^2 = 2.31$. The asterisk marks an unknown side phase excluded from refinement. 187

Figure 11.3. Rietveld refinement plot of Rb₃MoO₄D (*I4/mcm*, 140) based on neutron diffraction data acquired from the D2B at room temperature. The grey area was cut out during refinement as this reflection corresponds to an unknown side phase. Bragg markers from top to bottom: Rb₃MoO₄D (89.3(7) wt.%), Rb₂MoO₄ (*Pnam*) (6.2(3) wt.%), RbD (*Fm3m*) (4.6(1) wt.%). The corresponding determined crystal structure with ellipsoids (90% probability) is depicted on the right. 189

Figure 11.4. Rietveld refinement plot of Cs₃MoO₄D (*I4/mcm*, 140) based on neutron diffraction data acquired from the D2B at room temperature. Bragg markers from top to bottom: Cs₃MoO₄D (90.3(10) wt.%), Cs₂MoO₄ (*Pnma*) (9.7(1) wt.%). The corresponding, determined crystal structure with ellipsoids (90% probability) is depicted on the right. 190

Figure 11.5. Rietveld refinement plot of Cs₃WO₄D (*I4/mcm*, 140) based on powder neutron diffraction data acquired from the D2B at room temperature. Bragg markers Cs₃WO₄D. A schematic of the corresponding determined crystal structure is depicted on the left. Ellipsoid probability 90%. 191

Figure 11.6. Rietveld refinement plot of Rb₃WO₄D (*Pbca*, 61) at room temperature based on powder neutron diffraction data acquired from the D2B at room temperature. Bragg markers Rb₃WO₄D. A schematic of the corresponding determined crystal structure is depicted on the left. Ellipsoid probability 90%. 193

Figure 11.7. Rietveld refinement plot of Rb₃MoO₄D (*I4/mcm*, 140) based on neutron diffraction data acquired from the D2B at 4K. The grey area was cut out during refinement as this reflection corresponds to an unknown side phase. Bragg markers from top to bottom: Rb₃MoO₄D (89.2(4) wt.%), Rb₂MoO₄ (*Pnam*) (6.6(2) wt.%), RbD (*Fm3m*) (4.2(3) wt.%). The corresponding determined crystal structure with ellipsoids (90% probability) is depicted on the right. 194

Figure 11.8. Rietveld refinement plot of Cs₃MoO₄D (*I4/mcm*, 140) based on neutron diffraction data acquired from the D2B at 4K. Bragg markers from top to bottom: Cs₃MoO₄D (90.6(4) wt.%), Cs₂MoO₄ (*Pnma*) (9.4(1) wt.%). The corresponding, determined crystal structure with ellipsoids (90% probability) is depicted on the right. 196

Figure 11.9. Rietveld refinement plot of Cs₃WO₄D (*I4/mcm*, 140) based on powder neutron diffraction data acquired from the D2B at 4K. Bragg markers Cs₃WO₄D. A schematic of the corresponding determined crystal structure is depicted on the left. Ellipsoid probability 90%. 198

10 List of Tables

Table 2.1. List of chemicals used in this thesis.	25
Table 3.1. Crystallographic data of CsCaD _{1.28} F _{1.72} obtained by joint Rietveld refinement of neutron and X-ray diffraction data.	38
Table 4.1 Crystallographic data of Na ₃ SO ₄ D obtained by Rietveld refinement of neutron diffraction data.....	45
Table 4.2. Overview of the crystal structures.	53
Table 4.3. Calculated total and Gibbs free energies of Rb ₃ MoO ₄ H and Rb ₃ WO ₄ H at the DFT-PBE0 level of theory in both crystallographic modifications.....	54
Table 4.4. Determined Goldschmidt tolerance factors.	55
Table 4.5. Crystallographic data obtained by Rietveld refinement of Rb ₃ WO ₄ D.	62
Table 4.6. Crystallographic data of K ₃ MoO ₄ H obtained from Rietveld refinement.	64
Table 11.1. Rietveld refinement parameters of Na ₃ SO ₄ D determined from powder neutron diffraction data acquired from the D2B at room temperature.	188
Table 11.2. Rietveld refinement parameters of Rb ₃ MoO ₄ D determined from powder neutron diffraction data acquired from the D2B at room temperature.	189
Table 11.3. Crystallographic data of Rb ₃ MoO ₄ D determined from Rietveld refinement of room temperature neutron diffraction data.	190
Table 11.4. Rietveld refinement parameters of Cs ₃ MoO ₄ D determined from powder neutron diffraction data acquired from the D2B at room temperature.	190
Table 11.5. Crystallographic data of Cs ₃ MoO ₄ D determined from Rietveld refinement of room temperature neutron diffraction data.	191
Table 11.6. Rietveld refinement parameters of Cs ₃ WO ₄ D determined from powder neutron diffraction data acquired from the D2B at room temperature.	192
Table 11.7. Crystallographic data of Cs ₃ WO ₄ D determined from Rietveld refinement of RT neutron diffraction data.	192

- Table 11.8.** Rietveld refinement parameters of $\text{Rb}_3\text{WO}_4\text{D}$ determined from Rietveld refinement of powder neutron diffraction data acquired from the D2B at room temperature. 193
- Table 11.9.** Crystallographic data of $\text{Rb}_3\text{WO}_4\text{D}$ determined from Rietveld refinement of RT neutron diffraction data. 194
- Table 11.10.** Rietveld refinement parameters of $\text{Rb}_3\text{MoO}_4\text{D}$ determined from powder neutron diffraction data acquired from the D2B at 4K. 195
- Table 11.11.** Crystallographic data of $\text{Rb}_3\text{MoO}_4\text{D}$ determined from Rietveld refinement of neutron diffraction data acquired at 4K. 195
- Table 11.12.** Rietveld refinement parameters of $\text{Cs}_3\text{MoO}_4\text{D}$ determined from powder neutron diffraction data acquired from the D2B at 4K. 196
- Table 11.13.** Crystallographic data of $\text{Cs}_3\text{MoO}_4\text{D}$ determined from Rietveld refinement of neutron diffraction data acquired at 4K. 197
- Table 11.14.** Rietveld refinement parameters of $\text{Cs}_3\text{WO}_4\text{D}$ determined from powder neutron diffraction data acquired from the D2B at 4K. 198
- Table 11.15.** Crystallographic data of $\text{Cs}_3\text{WO}_4\text{D}$ determined from Rietveld refinement of neutron diffraction data acquired at 4K. 199

11 Appendix

11.1 Rietveld refinement plots and additional crystallographic data

RbCaHF₂

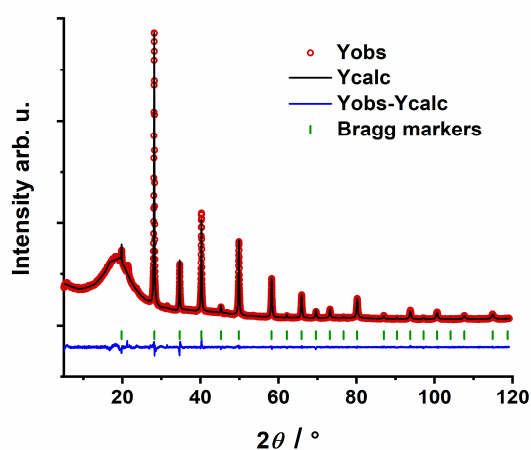


Figure 11.1. Rietveld refinement plot of *RbCaHF₂*. $R_p = 2.00\%$, $R_{wp} = 3.04\%$, $R_{Bragg} = 1.68\%$, $R_{exp} = 2.38\%$, $\chi^2 = 1.63$.

CsCaH₃

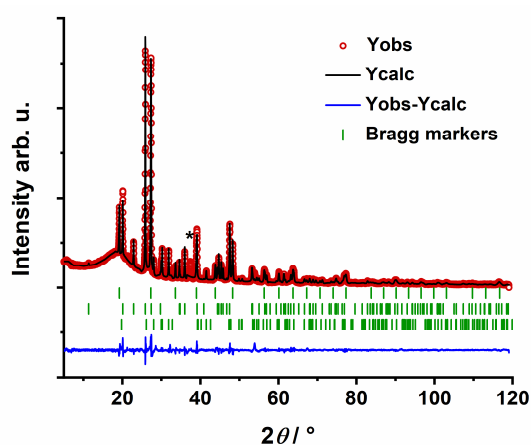


Figure 11.2. Rietveld refinement plot of the attempted synthesis of *CsCaH₃*. Bragg markers from top to bottom: *CsCaH₃* (31.6(4) wt%), *Cs₂CaH₄* (45.6(5) wt%), and *CaH₂* (22.8(4) wt%). $R_p = 4.05\%$, $R_{wp} = 5.94\%$, $R_{Bragg} = 3.70\%$, $R_{exp} = 3.91\%$, $\chi^2 = 2.31$. The asterisk marks an unknown side phase excluded from refinement.

*Na₃SO₄D***Table 11.1.** Rietveld refinement parameters of Na₃SO₄D determined from powder neutron diffraction data acquired from the D2B at room temperature.

Na₃SO₄D	
Space group	<i>P4/nmm</i> (129, O2)
Calculated density [g/cm ³]	2.328
Step scan increment	0.05
2θ range (°)	10 - 158
Wavelength (Å)	1.594
Number of profile points	2960
Temperature (K)	298
Program	Fullprof
Shape parameter η	0.471(14)
Caglioti parameters (<i>U</i> , <i>V</i> , <i>W</i>)	<i>U</i> = 0.166(4) <i>V</i> = -0.353(7) <i>W</i> = 0.323(4)
Number of reflections	160
Number of refined parameters	116
<i>R</i> _{Bragg}	2.84%
<i>R</i> _p	1.70%
<i>R</i> _{wp}	3.63%
<i>R</i> _{exp}	3.63%
Goodness of fit (<i>χ</i> ²)	1.00%

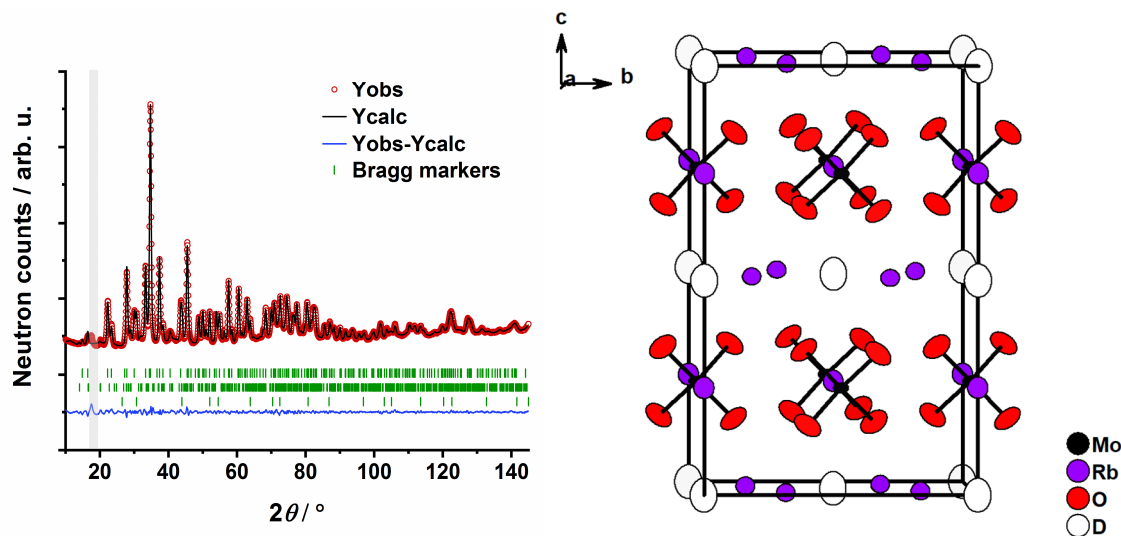
Rb₃MoO₄D (RT)

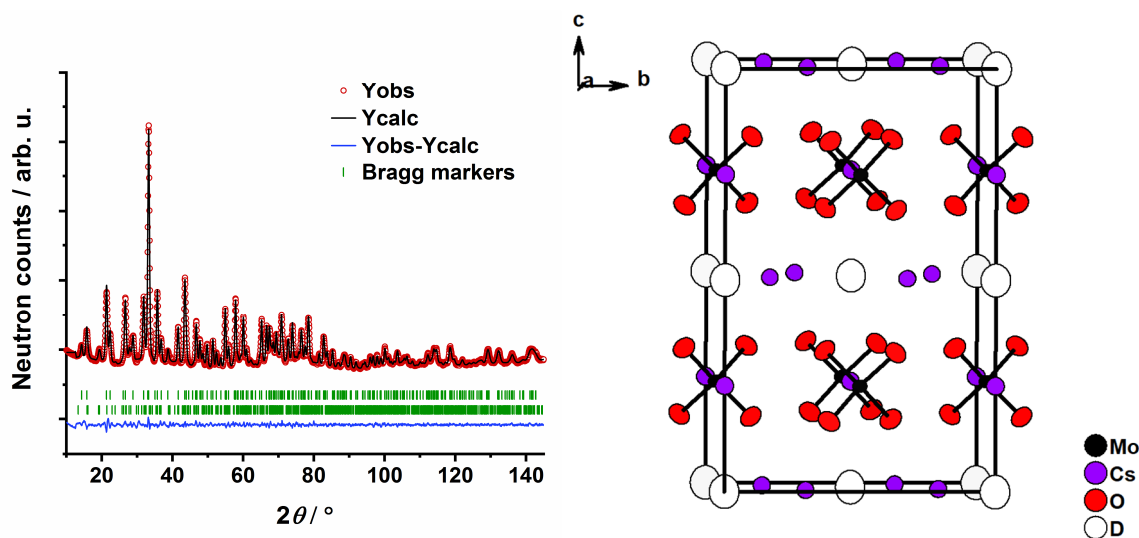
Figure 11.3. Rietveld refinement plot of $\text{Rb}_3\text{MoO}_4\text{D}$ ($I4/mcm$, 140) based on neutron diffraction data acquired from the D2B at room temperature. The grey area was cut out during refinement as this reflection corresponds to an unknown side phase. Bragg markers from top to bottom: $\text{Rb}_3\text{MoO}_4\text{D}$ (89.3(7) wt.%), Rb_2MoO_4 ($Pnam$) (6.2(3) wt.%), RbD ($Fm\bar{3}m$) (4.6(1) wt.%). The corresponding determined crystal structure with ellipsoids (90% probability) is depicted on the right.

Table 11.2. Rietveld refinement parameters of $\text{Rb}_3\text{MoO}_4\text{D}$ determined from powder neutron diffraction data acquired from the D2B at room temperature.

$\text{Rb}_3\text{MoO}_4\text{D}$	
Space group	$I4/mcm$ (140)
Calculated density [g/cm^3]	3.655
Step scan increment	0.05
2θ range ($^\circ$)	10 - 158
Wavelength (\AA)	1.594
Number of profile points	2960
Temperature (K)	298
Program	Fullprof
Shape parameter η	0.539 (10)
Caglioti parameters (U , V , W)	$U = 0.484(17)$ $V = -0.510(19)$ $W = 0.395(1)$
Number of reflections	230
Number of refined parameters	112
R_{Bragg}	2.84%
R_p	1.49%
R_{wp}	2.03%
R_{exp}	0.65%
Goodness of fit (χ^2)	9.60%

Table 11.3. Crystallographic data of $\text{Rb}_3\text{MoO}_4\text{D}$ determined from Rietveld refinement of room temperature neutron diffraction data.

Cell parameters						
$a = 7.8620(3) \text{ \AA}$, $c = 12.2998(5) \text{ \AA}$; $a/b=1.00$, $b/c=0.6392$						
$V = 760.26(5) \text{ \AA}^3$						
Atom	Wyckoff position	Site	x/a	y/b	z/c	
Mo	4b	-42m	0	$\frac{1}{2}$	$\frac{1}{4}$	
Rb1	8h	$m2m$	0.19049(13)	$x + \frac{1}{2}$	0	
Rb2	4a	422	0	0	$\frac{1}{4}$	
O1	16l	m	0.12924(13)	$x + \frac{1}{2}$	0.66646(17)	
D1	4c	$4/m$	0	0	0	
Anisotropic displacement parameters [\AA^2]						
Atom	U_{11}	U_{22}	U_{33}	U_{12}	U_{13}	U_{23}
Mo1	0.0227(9)	0.0227(9)	0.0095(14)	0.00000	0.00000	0.00000
Rb1	0.0298(7)	0.0298(7)	0.0267(11)	-0.0054(9)	0.00000	0.00000
Rb2	0.0357(11)	0.0357(11)	0.0399(18)	0.00000	0.00000	0.00000
O1	0.0581(10)	0.0581(10)	0.0450(11)	-0.0184(10)	0.0222(6)	0.0222(6)
D1	0.0363(10)	0.0363(10)	0.0565(20)	0.00000	0.00000	0.00000

 $\text{Cs}_3\text{MoO}_4\text{D}$ (RT)**Figure 11.4.** Rietveld refinement plot of $\text{Cs}_3\text{MoO}_4\text{D}$ ($I4/mcm$, 140) based on neutron diffraction data acquired from the D2B at room temperature. Bragg markers from top to bottom: $\text{Cs}_3\text{MoO}_4\text{D}$ (90.3(10) wt.%), Cs_2MoO_4 ($Pnma$) (9.7(1) wt.%). The corresponding, determined crystal structure with ellipsoids (90% probability) is depicted on the right.**Table 11.4.** Rietveld refinement parameters of $\text{Cs}_3\text{MoO}_4\text{D}$ determined from powder neutron diffraction data acquired from the D2B at room temperature.

$\text{Cs}_3\text{MoO}_4\text{D}$	
Space group	$I4/mcm$ (140)
Calculated density [g/cm^3]	4.319
Step scan increment	0.05
2θ range ($^\circ$)	10 - 158
Wavelength (\AA)	1.594
Number of profile points	2960
Temperature (K)	298
Program	Fullprof

Shape parameter η	0.541(12)
Caglioti parameters (U , V , W)	$U = 0.352(10)$ $V = -0.497(13)$ $W = 0.393(5)$
Number of reflections	258
Number of refined parameters	98
R_{Bragg}	1.60
R_p	1.18
R_{wp}	1.57
R_{exp}	0.83
Goodness of fit (χ^2)	3.59

Table 11.5. Crystallographic data of $\text{Cs}_3\text{MoO}_4\text{D}$ determined from Rietveld refinement of room temperature neutron diffraction data.

Cell parameters						
$a = 8.2113(2) \text{ \AA}$, $c = 12.7893(4) \text{ \AA}$; $a/b=1.00$, $b/c= 0.6420$						
$V = 833.70(4) \text{ \AA}^3$						
Atom	Wyckoff position	Site	x/a	y/b	z/c	
Mo	4b	-42m	0	$\frac{1}{2}$	$\frac{1}{4}$	
Cs1	8h	$m2m$	0.18705(16)	$x + \frac{1}{2}$	0	
Cs2	4a	422	0	0	$\frac{1}{4}$	
O1	16l	m	0.12348(11)	$x + \frac{1}{2}$	0.66890(11)	
D1	4c	4/m	0	0	0	
Anisotropic displacement parameters [\AA^2]						
Atom	U_{11}	U_{22}	U_{33}	U_{12}	U_{13}	U_{23}
Mo1	0.0209(8)	0.0209(8)	0.0154(12)	0.00000	0.00000	0.00000
Cs1	0.0275(7)	0.0275(7)	0.0272(13)	-0.0032(9)	0.00000	0.00000
Cs2	0.0308(10)	0.0308(10)	0.0304(18)	0.00000	0.00000	0.00000
O1	0.0421(7)	0.0421(7)	0.0376(9)	-0.0162(9)	0.0100(5)	0.0100(5)
D1	0.0487(11)	0.0487(11)	0.063(2)	0.00000	0.00000	0.00000

$\text{Cs}_3\text{WO}_4\text{D}$ (RT)

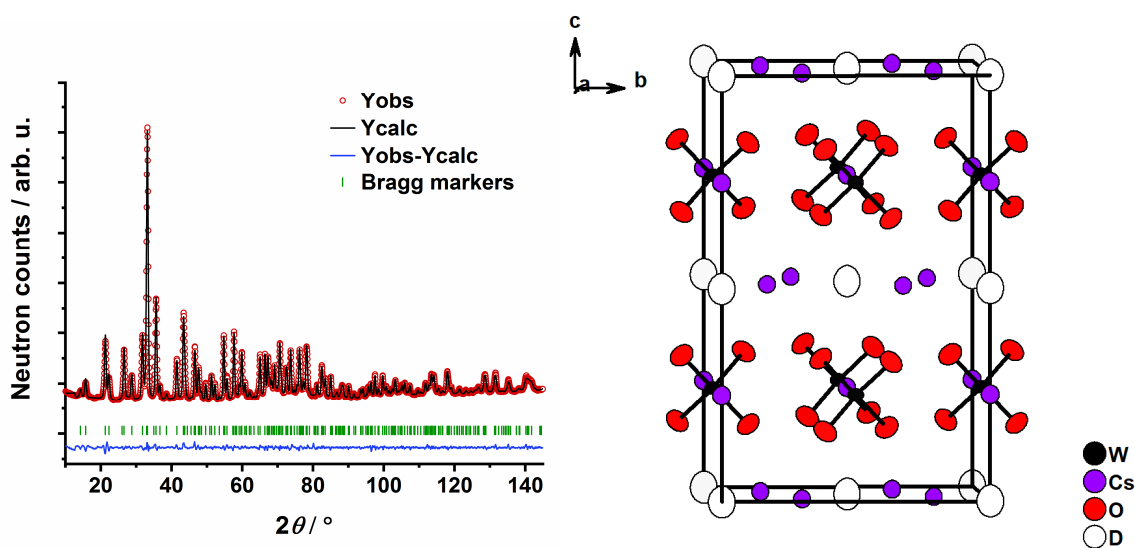


Figure 11.5. Rietveld refinement plot of $\text{Cs}_3\text{WO}_4\text{D}$ ($I4/mcm$, 140) based on powder neutron diffraction data acquired from the D2B at room temperature. Bragg markers $\text{Cs}_3\text{WO}_4\text{D}$. A schematic of the corresponding determined crystal structure is depicted on the left. Ellipsoid probability 90%.

Table 11.6. Rietveld refinement parameters of Cs₃WO₄D determined from powder neutron diffraction data acquired from the D2B at room temperature.

Cs₃WO₄D	
Space group	<i>I4/mcm</i> (140)
Calculated density [g/cm ³]	4.954
Step scan increment	0.05
2θ range (°)	10 - 158
Wavelength (Å)	1.594
Number of profile points	2960
Temperature (K)	298
Program	Fullprof
Shape parameter η	0.478(10)
Caglioti parameters (<i>U</i> , <i>V</i> , <i>W</i>)	<i>U</i> = 0.263(6) <i>V</i> = -0.474(10) <i>W</i> = 0.386(4)
Number of reflections	260
Number of refined parameters	73
<i>R</i> _{Bragg}	2.03
<i>R</i> _p	1.53
<i>R</i> _{wp}	2.04
<i>R</i> _{exp}	0.87
Goodness of fit (<i>X</i> ²)	5.46

Table 11.7. Crystallographic data of Cs₃WO₄D determined from Rietveld refinement of RT neutron diffraction data.

Cell parameters						
a = 8.2331(2) Å, c = 12.8289(3) Å; a/b=1.00, b/c= 0.6418						
V = 869.58(4) Å ³						
Atom	Wyckoff position	Site	x/a	y/b	z/c	
W	4b	-42 <i>m</i>	0	½	¼	
Cs1	8h	<i>m2m</i>	0.18917(12)	<i>x</i> + ½	0	
Cs2	4a	422	0	0	¼	
O1	16l	<i>m</i>	0.12355(9)	<i>x</i> + ½	0.66889(9)	
D1	4c	4/ <i>m</i>	0	0	0	
Anisotropic displacement parameters [Å²]						
Atom	U₁₁	U₂₂	U₃₃	U₁₂	U₁₃	U₂₃
W1	0.0249(8)	0.0249(8)	0.0143(12)	0.00000	0.00000	0.00000
Cs1	0.0279(6)	0.0279(6)	0.0299(10)	0.0023(7)	0.00000	0.00000
Cs2	0.0320(9)	0.0320(9)	0.0322(14)	0.00000	0.00000	0.00000
O1	0.0484(6)	0.0484(6)	0.0417(7)	-0.0184(7)	0.0132(4)	0.0132(4)
D1	0.0405(8)	0.0405(8)	0.0562(15)	0.00000	0.00000	0.00000

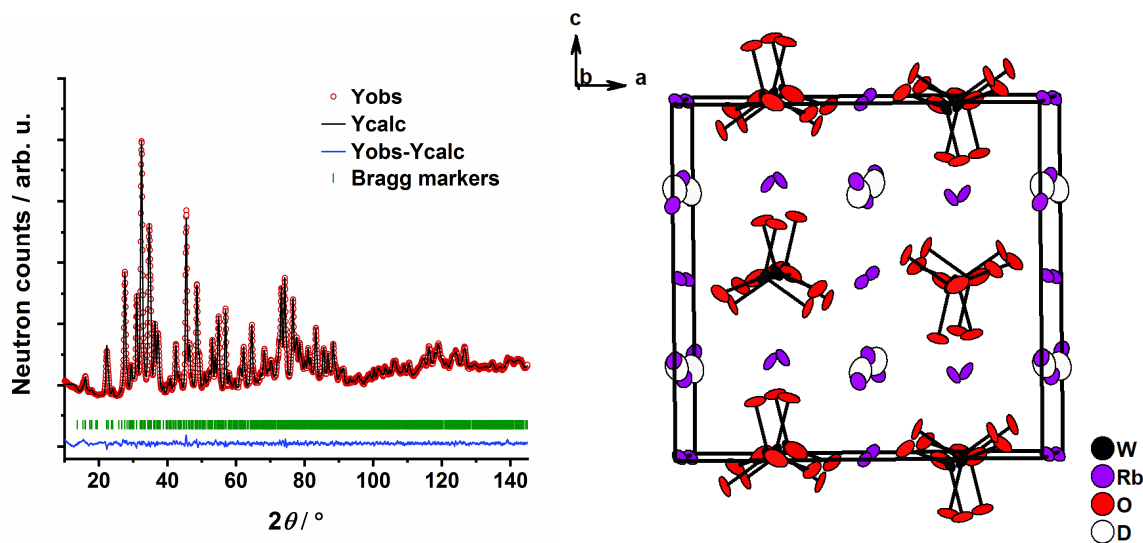
Rb_3WO_4D (RT)

Figure 11.6. Rietveld refinement plot of Rb_3WO_4D ($Pbca$, 61) at room temperature based on powder neutron diffraction data acquired from the D2B at room temperature. Bragg markers Rb_3WO_4D . A schematic of the corresponding determined crystal structure is depicted on the left. Ellipsoid probability 90%.

Table 11.8. Rietveld refinement parameters of Rb_3WO_4D determined from Rietveld refinement of powder neutron diffraction data acquired from the D2B at room temperature.

Rb_3WO_4D	
Space group	$Pbca$ (61)
Calculated density [g/cm^3]	4.322
Step scan increment	0.05
2θ range ($^\circ$)	10 - 158
Wavelength (\AA)	1.594
Number of profile points	2960
Temperature (K)	298 K
Program	Fullprof
Shape parameter η	0.540(10)
Caglioti parameters (U , V , W)	$U = 0.348(11)$ $V = -0.527(14)$ $W = 0.405(5)$
Number of reflections	1610
Number of refined parameters	140
R_{Bragg}	1.60
R_p	1.08
R_{wp}	1.44
R_{exp}	0.86
Goodness of fit (χ^2)	2.77

Table 11.9. Crystallographic data of $\text{Rb}_3\text{WO}_4\text{D}$ determined from Rietveld refinement of RT neutron diffraction data.

Cell parameters						
a = 11.9262(3) Å, b = 11.3972(5) Å, c = 11.4492(5) Å; a/b=1.0464 b/c=0.9955 c/a=0.9600						
V = 1556.24(10) Å ³						
Atom	Wyckoff position	Site	x/a	y/b	z/c	
W1	8c	1	0.7464(7)	0.0054(4)	-0.0149(4)	
Rb1	8c	1	0.7464(4)	0.2334(4)	0.7289(3)	
Rb2	8c	1	-0.0009(4)	0.7822(4)	-0.0062(5)	
Rb3	8c	1	0.0003(4)	-0.0078(4)	0.7188(3)	
O1	8c	1	0.8660(5)	-0.0224(5)	0.0730(5)	
O2	8c	1	0.7823(5)	-0.0226(5)	0.8365(4)	
O3	8c	1	0.7173(5)	0.1588(4)	-0.0086(5)	
O4	8c	1	0.6318(6)	-0.0766(5)	0.0303(4)	
D1	8c	1	0.5068(6)	0.7562(5)	0.2585(9)	
Anisotropic displacement parameters [Å ²]						
Atom	U ₁₁	U ₂₂	U ₃₃	U ₁₂	U ₁₃	U ₂₃
W1	0.0181(20)	0.016(2)	0.030(3)	-0.008(3)	-0.011(3)	-0.004(3)
Rb1	0.0243(18)	0.035(3)	0.037(3)	0.003(2)	-0.018(3)	0.0047(19)
Rb2	0.029(4)	0.027(2)	0.028(2)	0.003(2)	-0.0096(20)	-0.002(2)
Rb3	0.032(4)	0.017(2)	0.041(3)	0.004(3)	0.007(2)	0.008(2)
O1	0.016(4)	0.064(4)	0.055(4)	0.008(3)	-0.021(3)	0.006(3)
O2	0.065(5)	0.053(4)	0.015(3)	-0.022(3)	0.013(3)	-0.013(2)
O3	0.071(5)	0.032(3)	0.044(3)	0.026(3)	-0.024(3)	0.004(3)
O4	0.047(4)	0.051(4)	0.038(4)	-0.021(4)	0.022(3)	-0.012(3)
D1	0.0542(19)	0.042(3)	0.077(4)	0.023(3)	0.007(3)	-0.008(4)

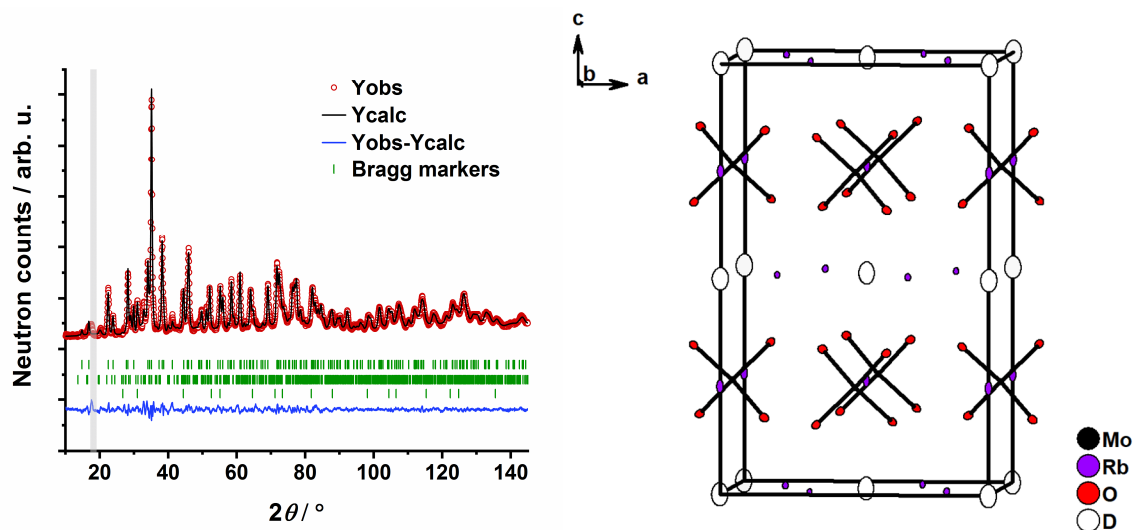
 $\text{Rb}_3\text{MoO}_4\text{D}$ (4K)**Figure 11.7.** Rietveld refinement plot of $\text{Rb}_3\text{MoO}_4\text{D}$ ($I4/mcm$, 140) based on neutron diffraction data acquired from the D2B at 4K. The grey area was cut out during refinement as this reflection corresponds to an unknown side phase. Bragg markers from top to bottom: $\text{Rb}_3\text{MoO}_4\text{D}$ (89.2(4) wt.%), Rb_2MoO_4 ($Pnam$) (6.6(2) wt.%), RbD ($Fm\bar{3}m$) (4.2(3) wt.%). The corresponding determined crystal structure with ellipsoids (90% probability) is depicted on the right.

Table 11.10. Rietveld refinement parameters of Rb₃MoO₄D determined from powder neutron diffraction data acquired from the D2B at 4K.

Rb₃MoO₄D	
Space group	<i>I4/mcm</i> (140)
Calculated density [g/cm ⁻³]	3.804
Step scan increment	0.05
2θ range (°)	10 - 158
Wavelength (Å)	1.594
Number of profile points	2960
Temperature (K)	4
Program	Fullprof
Shape parameter η	0.593(17)
Caglioti parameters (<i>U</i> , <i>V</i> , <i>W</i>)	<i>U</i> = 0.365(19) <i>V</i> = -0.115(35) <i>W</i> = 0.411(12)
Number of reflections	225
Number of refined parameters	76
<i>R</i> _{Bragg}	2.84
<i>R</i> _p	3.85
<i>R</i> _{wp}	5.05
<i>R</i> _{exp}	1.63
Goodness of fit (<i>χ</i> ²)	9.65

Table 11.11. Crystallographic data of Rb₃MoO₄D determined from Rietveld refinement of neutron diffraction data acquired at 4K.

Cell parameters						
a = 7.6853(3) Å c = 12.3320(7) Å, b/c = 0.6232						
V = 728.38(5) Å ³						
Atom	Wyckoff position	Site	x/a	y/b	z/c	
Mo	4b	-4 <i>m</i>	0	½	¼	
Rb1	8h	<i>m2m</i>	0.18285(16)	<i>x</i> + ½	0	
Rb2	4a	422	0	0	¼	
O1	16l	<i>m</i>	0.13102(15)	<i>x</i> + ½	0.66651(17)	
D1	4c	4/ <i>m</i>	0	0	0	
Anisotropic displacement parameters [Å²]						
Ato	U ₁₁	U ₂₂	U ₃₃	U ₁₂	U ₁₃	U ₂₃
Mo1	0.0042(11)	0.0042(11)	0.0042(16)	0.00000	0.00000	0.00000
Rb1	0.0031(6)	0.0031(6)	0.0059(11)	0.0021(8)	0.00000	0.00000
Rb2	0.0045(9)	0.0045(9)	0.0189(17)	0.00000	0.00000	0.00000
O1	0.0083(6)	0.0083(6)	0.0076(10)	-0.0046(7)	-0.0015(5)	-0.0015(5)
D1	0.0179(11)	0.0179(11)	0.038(2)	0.00000	0.00000	0.00000

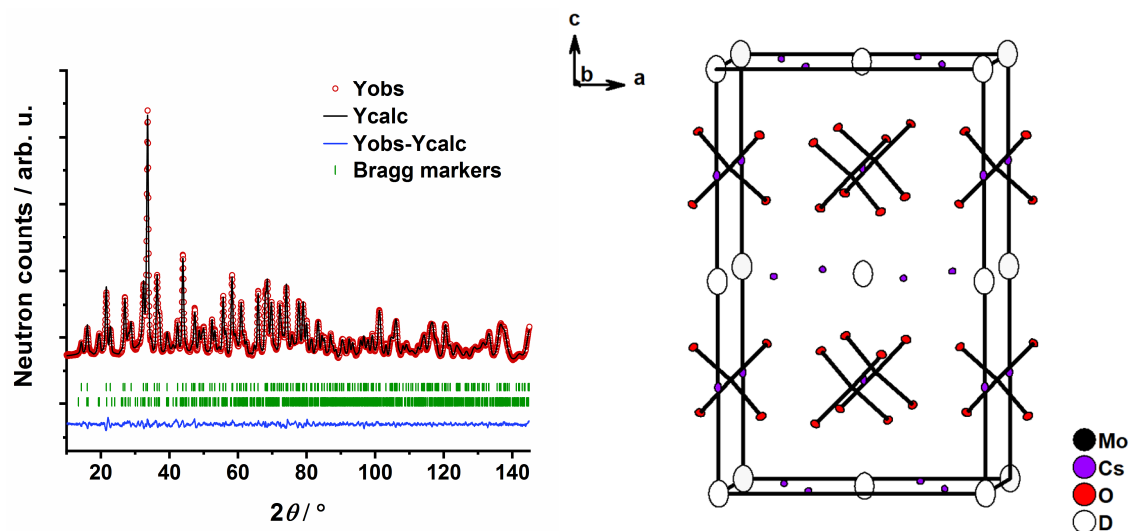
Cs_3MoO_4D (4K)

Figure 11.8. Rietveld refinement plot of Cs_3MoO_4D ($I4/mcm$, 140) based on neutron diffraction data acquired from the D2B at 4K. Bragg markers from top to bottom: Cs_3MoO_4D (90.6(4) wt.%), Cs_2MoO_4 ($Pnma$) (9.4(1) wt.%). The corresponding, determined crystal structure with ellipsoids (90% probability) is depicted on the right.

Table 11.12. Rietveld refinement parameters of Cs_3MoO_4D determined from powder neutron diffraction data acquired from the D2B at 4K.

Cs_3MoO_4D	
Space group	$I4/mcm$ (140)
Calculated density [g/cm^3]	4.467
Step scan increment	0.05
2θ range ($^\circ$)	10 - 158
Wavelength (\AA)	1.594
Number of profile points	2960
Temperature (K)	4
Program	Fullprof
Shape parameter η	0.487(15)
Caglioti parameters (U, V, W)	$U = 0.405(9)$ $V = -0.416(14)$ $W = 0.396(5)$
Number of reflections	251
Number of refined parameters	103
R_{Bragg}	1.53
R_p	1.62
R_{wp}	2.06
R_{exp}	0.85
Goodness of fit (χ^2)	5.86

Table 11.13. Crystallographic data of Cs₃MoO₄D determined from Rietveld refinement of neutron diffraction data acquired at 4K.

Cell parameters						
a = 8.0697(2) Å, c = 12.8026(4) Å; a/b=1.00, b/c= 0.6303						
833.70(4) Å ³						
Atom	Wyckoff position	Site	x/a	y/b	z/c	
Mo	4b	-42 <i>m</i>	0	½	¼	
Cs1	8h	<i>m2m</i>	0.18171(15)	<i>x</i> +½	0	
Cs2	4a	422	0	0	¼	
O1	16l	<i>m</i>	0.12602(11)	<i>x</i> +½	0.66837(11)	
D1	4c	4/ <i>m</i>	0	0	0	
Anisotropic displacement parameters [Å²]						
Atom	U₁₁	U₂₂	U₃₃	U₁₂	U₁₃	U₂₃
Mo1	0.0018(8)	0.0018(8)	0.0042(13)	0.00000	0.00000	0.00000
Cs1	0.0054(6)	0.0054(6)	0.0047(13)	-0.0035(8)	0.00000	0.00000
Cs2	0.0051(9)	0.0051(9)	0.0109(16)	0.00000	0.00000	0.00000
O1	0.0097(5)	0.0097(5)	0.0074(7)	-0.0062(7)	0.0020(4)	0.0020(4)
D1	0.0296(10)	0.0296(10)	0.055(2)	0.00000	0.00000	0.00000

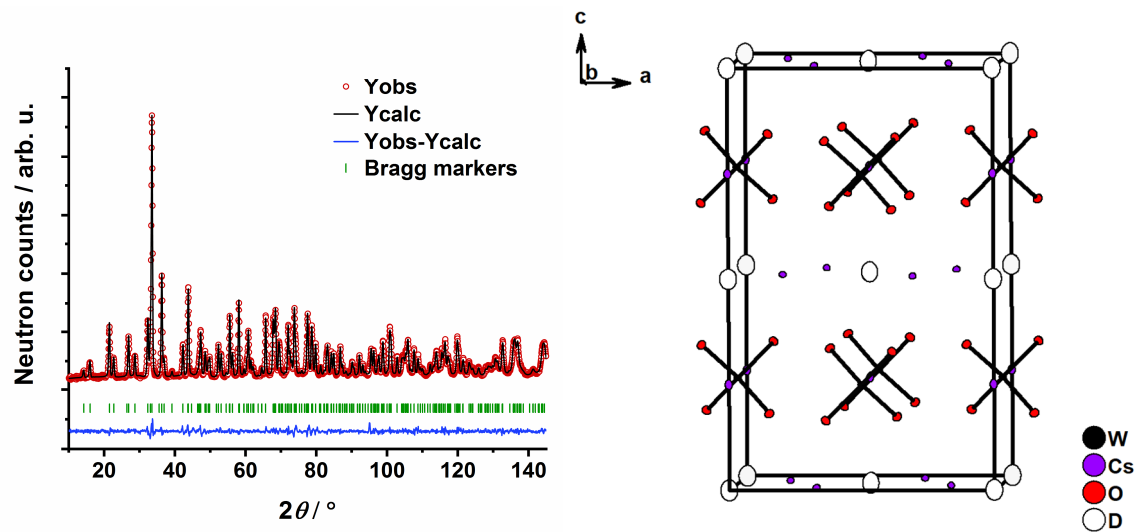
Cs_3WO_4D (4K)

Figure 11.9. Rietveld refinement plot of Cs_3WO_4D ($I4/mcm$, 140) based on powder neutron diffraction data acquired from the D2B at 4K. Bragg markers Cs_3WO_4D . A schematic of the corresponding determined crystal structure is depicted on the left. Ellipsoid probability 90%.

Table 11.14. Rietveld refinement parameters of Cs_3WO_4D determined from powder neutron diffraction data acquired from the D2B at 4K.

Cs_3WO_4D	
Space group	$I4/mcm$ (140)
Calculated density [g/cm^3]	5.132
Step scan increment	0.05
2θ range ($^\circ$)	10 - 158
Wavelength (\AA)	1.594
Number of profile points	2960
Temperature (K)	4
Program	Fullprof
Shape parameter η	0.502(13)
Caglioti parameters (U, V, W)	$U = 0.111(3)$ $V = -0.148(7)$ $W = 0.188(3)$
Number of reflections	252
Number of refined parameters	77
R_{Bragg}	2.69
R_p	4.13
R_{wp}	5.20
R_{exp}	2.01
Goodness of fit (χ^2)	6.71

Table 11.15. Crystallographic data of Cs₃WO₄D determined from Rietveld refinement of neutron diffraction data acquired at 4K.

Cell parameters						
a = 8.0843(1) Å, c = 12.8448(2) Å; a/b=1.00, b/c= 0.6294 839.48(2) Å ³						
Atom	Wyckoff position	Site	x/a	y/b	z/c	
W	4b	-42m	0	½	¼	
Cs1	8h	m2m	0.18395(14)	x +½	0	
Cs2	4a	422	0	0	¼	
O1	16l	m	0.12679(10)	x +½	0.66857(10)	
D1	4c	4/m	0	0	0	
Anisotropic displacement parameters [Å²]						
Atom	U₁₁	U₂₂	U₃₃	U₁₂	U₁₃	U₂₃
W1	0.0068(9)	0.0068(9)	0.0014(13)	0.00000	0.00000	0.00000
Cs1	0.0059(5)	0.0059(5)	0.0048(9)	-0.0016(7)	0.00000	0.00000
Cs2	0.0063(7)	0.0063(7)	0.0114(14)	0.00000	0.00000	0.00000
O1	0.0096(3)	0.0096(3)	0.0087(6)	-0.0031(6)	0.0016(4)	0.0016(4)
D1	0.0224(8)	0.0224(8)	0.0343(16)	0.00000	0.00000	0.00000